

e efficiency.

# Electron performance measurements with the ATLAS detector using the 2010 LHC proton-proton collision data

The ATLAS Collaboration

Received: October 14, 2011 / Revised version: February 17, 2012

**Abstract.** Detailed measurements of the electron performance of the ATLAS detector at the LHC are reported, using decays of the  $Z$ ,  $W$  and  $J/\psi$  particles. Data collected in 2010 at  $\sqrt{s}=7$  TeV are used, corresponding to an integrated luminosity of almost  $40 \text{ pb}^{-1}$ . The inter-alignment of the inner detector and the electromagnetic calorimeter, the determination of the electron energy scale and resolution, and the performance in terms of response uniformity and linearity are discussed. The electron identification, reconstruction and trigger efficiencies, as well as the charge misidentification probability, are also presented.

## 1 Introduction

The precise determination of the electron performance of the ATLAS detector at the LHC is essential both for Standard Model measurements and for searches for Higgs bosons and other new phenomena. Physics processes of prime interest at the LHC are expected to produce electrons from a few GeV to several TeV. Many of them, such as Higgs-boson production, have small cross-sections and suffer from large background, typically from jets of hadrons. Therefore an excellent electron identification capability, with high efficiency and high jet rejection rate, is required over a broad energy range to overcome the low signal-to-background ratio. For example, in the moderate transverse energy region  $E_T = 20 - 50$  GeV a jet-rejection factor of about  $10^5$  is desirable to extract a pure signal of electrons above the residual background from jets faking electrons. In the central region up to  $|\eta| < 2.5$ , this challenge is faced by using a powerful combination of detector technologies: silicon detectors, a transition radiation tracker and a longitudinally layered electromagnetic calorimeter system with fine lateral segmentation.

A further strength of the ATLAS detector is its ability to reconstruct and identify electrons outside the tracking coverage up to  $|\eta| < 4.9$ . This brings several advantages. For example, it improves the sensitivity of the measurement of forward-backward asymmetry, and therefore the weak mixing angle, in  $Z \rightarrow ee$  events, and it enlarges the geometrical acceptance of searches for Higgs bosons and other new particles.

To realize the full physics potential of the LHC, the electron energy and momentum must be precisely measured. Stringent requirements on the alignment and on the calibration of the calorimeter come, for example, from the goal of a high-precision  $W$  mass measurement.

This paper describes the measurements of the electron energy scale and resolution and of the efficiency to trigger, reconstruct and identify electrons using  $Z \rightarrow ee$ ,  $W \rightarrow ee$  and  $J/\psi \rightarrow ee$  events observed in the data collected in 2010 at a centre-of-mass energy of  $\sqrt{s} = 7$  TeV, corresponding to an integrated luminosity of almost  $40 \text{ pb}^{-1}$ . As the available statistics are significantly lower for isolated electrons from  $J/\psi \rightarrow ee$  decays and these electrons are also more difficult to extract, only a subset of the measurements were performed in this channel.

The structure of the paper is the following. In Section 2, a brief reminder of the inner detector and calorimeter system is presented. The data and Monte Carlo (MC) samples used in this work are summarized in Section 3. Section 4 starts with the introduction of the trigger, reconstruction and identification algorithms and then proceeds by presenting the inclusive single and dielectron spectra in Subsection 4.5. The inter-alignment of the inner detector and the electromagnetic (EM) calorimeter is discussed in Subsection 4.6. The in-situ calibration of the electron energy scale is described in Section 5 followed by its performance in terms of resolution, linearity in energy, and uniformity in  $\phi$ . The measurement of the electron selection efficiencies with the tag-and-probe technique is presented in Section 6. The identification efficiency determination is discussed in detail in Subsection 6.2, and the differences observed between data and MC predictions are attributed to imperfections of the MC description of the main discriminating variables. The reconstruction efficiency is reported in Subsection 6.4, followed by the charge misidentification probability in Subsection 6.5, and the trigger efficiency in Subsection 6.6. Conclusions and an outlook are given in Section 7.

## 2 The ATLAS detector

A complete description of the ATLAS detector is provided in Ref. [1].

ATLAS uses a right-handed coordinate system with its origin at the nominal  $pp$  interaction point at the centre of the detector. The positive  $x$ -axis is defined by the direction from the interaction point to the centre of the LHC ring, with the positive  $y$ -axis pointing upwards, while the beam direction defines the  $z$ -axis. The azimuthal angle  $\phi$  is measured around the beam axis and the polar angle  $\theta$  is the angle from the  $z$ -axis. The pseudorapidity is defined as  $\eta = -\ln \tan(\theta/2)$ .

The inner detector (ID) provides a precise reconstruction of tracks within  $|\eta| < 2.5$ . It consists of three layers of pixel detectors close to the beam-pipe, four layers of silicon microstrip detector modules with pairs of single-sided sensors glued back-to-back (SCT) providing eight hits per track at intermediate radii, and a transition radiation tracker (TRT) at the outer radii, providing about 35 hits per track (in the range  $|\eta| < 2.0$ ). The TRT offers substantial discriminating power between electrons and charged hadrons over a wide energy range (between 0.5 and 100 GeV) via the detection of X-rays produced by transition radiation. The inner-most pixel vertexing layer (also called the  $b$ -layer) is located just outside the beam-pipe at a radius of 50 mm. It provides precision vertexing and significant rejection of photon conversions through the requirement that a track has a hit in this layer.

A thin superconducting solenoid, contributing 0.66 radiation length at normal incidence to the amount of passive material before the EM calorimeter, surrounds the inner detector and provides a 2 T magnetic field.

The electromagnetic calorimeter system is separated into two parts: a presampler detector and an EM calorimeter, a lead-liquid-argon (LAr) detector with accordion-shaped kapton electrodes and lead absorber plates. The EM calorimeter has three longitudinal layers (called *strip*, *middle* and *back* layers) and a fine segmentation in the lateral direction of the showers within the inner detector coverage. At high energy, most of the EM shower energy is collected in the middle layer which has a lateral granularity of  $0.025 \times 0.025$  in  $\eta \times \phi$  space. The first (*strip*) layer consists of finer-grained strips in the  $\eta$ -direction with a coarser granularity in  $\phi$ . It offers discrimination against multiple photon showers (including excellent  $\gamma - \pi^0$  separation), a precise estimation of the pseudorapidity of the impact point and, in combination with the middle layer, an estimation of the photon pointing direction [2]. These two layers are complemented by a presampler detector placed in front with a granularity of  $0.025 \times 0.1$  covering only the range  $|\eta| < 1.8$  to correct for energy lost in the material before the calorimeter, and by the back layer behind, which collects the energy deposited in the tail of very high energy EM showers. The transition region between the barrel (EMB) and endcap (EMEC) calorimeters,  $1.37 < |\eta| < 1.52$ , has a large amount of material in front of the first active calorimeter layer. The endcap EM calorimeters are divided into two wheels, the outer (EMEC-OW) and the inner (EMEC-IW) wheels covering

the ranges  $1.375 < |\eta| < 2.5$  and  $2.5 < |\eta| < 3.2$ , respectively.

Hadronic calorimeters with at least three longitudinal segments surround the EM calorimeter and are used in this context to reject hadronic jets. The forward calorimeters (FCal) cover the range  $3.1 < |\eta| < 4.9$  and also have EM shower identification capabilities given their fine lateral granularity and longitudinal segmentation into three layers.

## 3 Data and Monte Carlo samples

The results are based on the proton-proton collision data collected with the ATLAS detector in 2010 at  $\sqrt{s}=7$  TeV. After requiring good data-quality criteria, in particular those concerning the inner detector and the EM and hadronic calorimeters, the total integrated luminosity used for the measurements is between 35 and  $40 \text{ pb}^{-1}$  depending on the trigger requirements.

The measurements are compared to expectations from MC simulation. The  $Z \rightarrow ee$ ,  $J/\psi \rightarrow ee$  and  $W \rightarrow ee$  MC samples were generated by PYTHIA [3] and processed through the full ATLAS detector simulation [4] based on GEANT4 [5]. To study the effect of multiple proton-proton interactions different pile-up configurations with an average about two interactions per beam crossing were also simulated.

In addition, MC samples were produced with additional passive material in front of the EM calorimeter representing a conservative estimate of the possible increases in the material budget based on various studies using collision data, including studies of track reconstruction efficiency [6, 7, 8, 9], the measurement of the photon conversion rate [10], studies of the energy flow in the EM calorimeter [11], EM shower-shape variables and the energy to momentum ratio. In these samples, the amounts of additional material with respect to the nominal geometry, expressed in units of radiation length ( $X_0$ ) and given at normal incidence, are  $0.05X_0$  in the inner detector,  $0.2X_0$  in its services,  $0.15X_0$  at the end of the SCT and TRT endcaps and at the ID endplate,  $0.05X_0$  between barrel presampler detector and the strip layer of the EM calorimeter, and  $0.1X_0$  in front of the LAr EM barrel calorimeter in the cryostat.

The distribution of material as a function of  $\eta$  in front of the presampler detector and the EM calorimeter is shown on the left of Figure 1 for the nominal and extra-material geometries. The contributions of the different detector elements up to the ID boundaries, including the services and thermal enclosures, are detailed on the right.

The peak in the amount of material before the electromagnetic calorimeter at  $|\eta| \approx 1.5$ , corresponding to the transition region between the barrel and endcap EM calorimeters, is due to the cryostats, the corner of the barrel electromagnetic calorimeter, the inner detector services and the tile scintillator. The sudden increase of material at  $|\eta| \approx 3.2$ , corresponding to the separation between the endcap calorimeters and the FCal, is mostly due to the

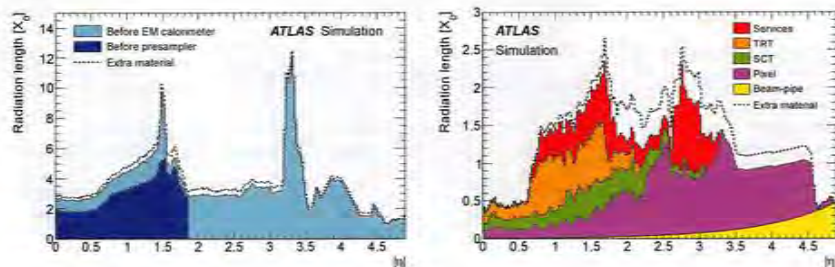


Fig. 1. Amount of material, in units of radiation length  $X_0$ , traversed by a particle as a function of  $\eta$ : (left) material in front of the presampler detector and the EM calorimeter, and (right) material up to the ID boundaries. The contributions of the different detector elements, including the services and thermal enclosures are shown separately by filled color areas. The extra material used for systematic studies is indicated by dashed lines. The primary vertex position has been smeared along the beamline.

cryostat that acts also as a support structure. It runs almost projective at the low radius part of EMEC IW.

## 4 Electron trigger, reconstruction and identification

### 4.1 Trigger

The ATLAS trigger system [12] is divided into three levels. The hardware-based first-level trigger (L1) performs a fast event selection by searching for high- $p_T$  objects and large missing or total energy using reduced granularity data from the calorimeters and the muon system and reduces the event rate to a maximum of 75 kHz. It is followed by the software-based second-level trigger (L2) and event filter (EF), collectively referred to as the high-level trigger (HLT). The reconstruction at L2 is seeded by the L1 result. It uses, with full granularity and precision, all the available detector data (including the information from the inner detector) but only in the regions identified by the L1 as Regions of Interest (RoI). After L2 selection, the event rate is about 3 kHz. In the EF, more complex algorithms seeded by the L2 results and profiting from offline-like calibration and alignment are used to reduce the event rate to about 200 Hz.

At L1, electromagnetic objects are selected if the total transverse energy deposited in the EM calorimeter in two adjacent towers of  $\Delta\eta \times \Delta\phi = 0.1 \times 0.1$  size is above a certain threshold. Fast calorimeter and tracking reconstruction algorithms are deployed at L2. The L2 calorimeter reconstruction is very similar to the offline algorithm, with the notable difference that clusters are seeded by the highest  $E_T$  cell in the middle calorimeter layer instead of applying the full offline sliding-window algorithm described in Subsection 4.2. The L2 track reconstruction algorithm was developed independently to fulfill the more

stringent timing requirements. The EF uses the offline reconstruction and identification algorithms described in Subsections 4.2 and 4.4. It applies similar (typically somewhat looser) cuts in order to remain fully efficient for objects identified offline.

During the 2010 proton-proton collision data taking period, the trigger menu continuously evolved in order to fully benefit from the increasing LHC luminosity. Initially, the trigger relied on the L1 decision only while the HLT decisions were recorded but not used to reject events. As the luminosity increased, the HLT began actively rejecting events with higher and higher  $E_T$  thresholds and more stringent selections. A detailed description of the trigger configuration and selection criteria applied in 2010 can be found in Refs. [12,13].

### 4.2 Reconstruction

Electron reconstruction [14] in the central region of  $|\eta| < 2.47$  starts from energy deposits (clusters) in the EM calorimeter which are then associated to reconstructed tracks of charged particles in the inner detector.

To reconstruct the EM clusters, seed clusters of longitudinal towers with total transverse energy above 2.5 GeV are searched for by a *sliding-window* algorithm. The window size is  $3 \times 5$  in units of  $0.025 \times 0.025$  in  $\eta \times \phi$  space, corresponding to the granularity of the calorimeter middle layer. The cluster reconstruction is expected to be very efficient for true electrons. In MC simulations, the efficiency is about 95% at  $E_T > 5$  GeV and 100% for electrons with  $E_T > 15$  GeV from  $W$  and  $Z$  decays.

In the tracking volume of  $|\eta| < 2.5$ , reconstructed tracks extrapolated from their last measurement point to the middle layer of the calorimeter are very loosely matched to the seed clusters. The distance between the track impact point and the cluster position is required to

*reco*  
" EM 3x5  
track  
↓  
cluster  
rebuilding  
3x7  
mostly @ small &  
energy loss

satisfy  $\Delta\eta < 0.05$ . To account for bremsstrahlung losses, the size of the sign corrected  $\Delta\phi$  window is 0.1 on the side where the extrapolated track bends as it traverses the solenoidal magnetic field and is 0.05 on the other side. An electron is reconstructed if at least one track is matched to the seed cluster. In the case where several tracks are matched to the same cluster, tracks with silicon hits are preferred, and the one with the smallest  $\Delta R = \sqrt{\Delta\eta^2 + \Delta\phi^2}$  distance to the seed cluster is chosen.

The electron cluster is then rebuilt using  $3 \times 7$  ( $5 \times 5$ ) longitudinal towers of cells in the barrel (endcaps). These lateral cluster sizes were optimized to take into account the different overall energy distributions in the barrel and endcap calorimeters. The cluster energy is then determined [2] by summing four different contributions: (1) the estimated energy deposit in the material in front of the EM calorimeter, (2) the measured energy deposit in the cluster, (3) the estimated external energy deposit outside the cluster (lateral leakage), and (4) the estimated energy deposit beyond the EM calorimeter (longitudinal leakage). The four terms are parametrised as function of the measured cluster energies in the presampler detector (where it is present) and in the three EM calorimeter longitudinal layers based on detailed simulation of energy deposition in both active and inactive material in the relevant detector systems. The good description of the detector in the MC simulation is therefore essential in order to correctly reconstruct the electron energy.

The four-momentum of *central electrons* is computed using information from both the final cluster and the best track matched to the original seed cluster. The energy is given by the cluster energy. The  $\phi$  and  $\eta$  directions are taken from the corresponding track parameters at the vertex.

In the *forward region*,  $2.5 < |\eta| < 4.9$ , where there are no tracking detectors, the electron candidates are reconstructed only from energy deposits in the calorimeters by grouping neighbouring cells in three dimensions, based on the significance of their energy content with respect to the expected noise. These *topological clusters* [15] have a variable number of cells in contrast to the fixed-size sliding-window clusters used in the central region. The direction of *forward electrons* is defined by the barycentre of the cells belonging to the cluster. The energy of the electron is determined simply by summing the energies in the cluster cells and is then corrected for energy loss in the passive material before the calorimeter. An electron candidate in the forward region is reconstructed only if it has a small hadronic energy component and a transverse energy of  $E_T > 5$  GeV.

### 4.3 Requirements on calorimeter operating conditions

The quality of the reconstructed energy of an electron object relies on the conditions of the EM calorimeter. Three types of problems arose during data taking that needed to be accounted for at the analysis level:

- Failures of electronic front-end boards (FEBs). A few percent of the cells are not read out because they are connected to non-functioning FEBs, on which the active part (VCSEL) of the optical transmitter to the readout boards has failed [16]. As this can have an important impact on the energy reconstruction in the EM calorimeter, the electron is rejected if part of the cluster falls into a dead FEB region in the EM calorimeter strip or middle layer. If the dead region is in the back layer or in the presampler detector, which in general contain only a small fraction of the energy of the shower, the object is considered good and an energy correction is provided at the reconstruction level.

- High voltage (HV) problems. A few percent of the HV sectors are operated under non-nominal high voltage, or have a zero voltage on one side of the readout electrode (for redundancy, each side of an EM electrode, which is in the middle of the LAr gap, is powered separately) [16]. In the very rare case when a part of the cluster falls into a dead high-voltage region, the cluster is rejected. Non-nominal voltage conditions increase the equivalent noise in energy but do not require special treatment for the energy reconstruction.

- Isolated cells producing a high noise signal or no signal at all. These cells are masked at the reconstruction level, so that their energy is set to the average of the neighbouring cells. Nonetheless an electron is rejected, if any of the cells in its core, defined as the  $3 \times 3$  cells in the middle layer, is masked.

The loss of acceptance due to these object quality requirements was about 6% per electron on average dominated by losses due to non-functioning FEBs (replaced during the 2010/2011 LHC winter shutdown).

These requirements are also applied to the MC samples when performing comparisons with data. Nonetheless, differences arise between data and MC, induced for example by the treatment of clusters around dead FEBs. While the barycentre of such clusters tends to be shifted in the data, this behaviour is not fully reproduced by MC when the dead area has not been simulated. The total uncertainty on the loss of acceptance is estimated to be about 0.4% per electron.

### 4.4 Identification

The baseline electron identification in the central  $|\eta| < 2.47$  region relies on a cut-based selection using calorimeter, tracking and combined variables that provide good separation between isolated or non-isolated signal electrons, background electrons (primarily from photon conversions and Dalitz decays) and jets faking electrons. The cuts can be applied independently. Three reference sets of cuts have been defined with increasing background rejection power: *loose*, *medium* and *tight* [14] with an expected jet rejection of about 500, 5000 and 50000, respectively, based on MC simulation. Shower shape variables of the EM calorimeter middle layer and hadronic leakage variables are used in the *loose* selection. Variables from the

Table 1. Definition of variables used for loose, medium and tight electron identification cuts for the central region of the detector with  $|\eta| < 2.47$ .

Type	Description	Name
<b>Loose selection</b>		
Acceptance	$ \eta  < 2.47$	
Hadronic leakage	Ratio of $E_T$ in the first layer of the hadronic calorimeter to $E_T$ of the EM cluster (used over the range $ \eta  > 0.8$ and $ \eta  > 1.37$ )	$R_{had}$
	Ratio of $E_T$ in the hadronic calorimeter to the EM cluster (used over the range $ \eta  > 0.8$ and $ \eta  < 1.37$ )	$R_{had}$
Middle layer of EM calorimeter	Ratio of the energy in $3 \times 7$ cells over the energy in $7 \times 7$ cells centred at the electron cluster position	$R_\eta$
	Lateral shower width, $\sqrt{(\sum E_i \eta_i^2)/(\sum E_i) - (\langle \eta_i \rangle)^2}/(\sum E_i)$ , where $E_i$ is the energy and $\eta_i$ is the pseudorapidity of cell $i$ and the sum is calculated within a window of $3 \times 5$ cells	$w_{\eta 2}$
<b>Medium selection (includes loose)</b>		
Strip layer of EM calorimeter	Shower width, $\sqrt{(\sum E_i (i - i_{max})^2)/(\sum E_i)}$ , where $i$ runs over all strips in a window of $\Delta\eta \times \Delta\phi \approx 0.0625 \times 1.5$ corresponding typically to 20 strips in $\Delta\eta$ and $i_{max}$ is the index of the highest-energy strip	$w_{\eta 1}$
	Ratio of the energy difference between the largest and second largest energy deposits in the cluster over the sum of these energies	$E_{ratio}$
Track quality	Number of hits in the pixel detector ( $\geq 1$ )	$n_{pixel}$
	Number of hits in the pixel and SCT detectors ( $\geq 7$ )	$n_{SI}$
Track-cluster matching	Transverse impact parameter ( $ d_0  < 5$ mm)	$d_0$
	$\Delta\eta$ between the cluster position in the strip layer and the extrapolated track ( $\Delta\eta < 0.01$ )	$\Delta\eta$
<b>Tight selection (includes medium)</b>		
Track-cluster matching	$\Delta\phi$ between the cluster position in the middle layer and the extrapolated track ( $ \Delta\phi  < 0.02$ )	$\Delta\phi$
	Ratio of the cluster energy to the track momentum	$E/p$
	Tighter $\Delta\eta$ requirement ( $ \Delta\eta  < 0.005$ )	$\Delta\eta$
Track quality	Tighter transverse impact parameter requirement ( $ d_0  < 1$ mm)	$d_0$
TRT	Total number of hits in the TRT	$n_{TRT}$
	Ratio of the number of high-threshold hits to the total number of hits in the TRT	$f_{HT}$
Conversions	Number of hits in the b-layer ( $\geq 1$ )	$n_{BL}$
	Veto electron candidates matched to reconstructed photon conversions	

EM calorimeter strip layer, track quality requirements and track-cluster matching are added to the *medium* selection. The *tight* selection adds  $E/p$ , particle identification using the TRT, and discrimination against photon conversions via a b-layer hit requirement and information about reconstructed conversion vertices [17]. Table 1 lists all variables used in the *loose*, *medium* and *tight* selections. The cuts are optimised in 10 bins of cluster  $\eta$  (defined by calorimeter geometry, detector acceptances and regions of increasing material in the inner detector) and 11 bins of cluster  $E_T$  from 5 GeV to above 80 GeV.

Electron identification in the forward  $2.5 < |\eta| < 4.9$  region, where no tracking detectors are installed, is based solely on cluster moments<sup>1</sup> and shower shapes [14]. These

<sup>1</sup> The cluster moment of degree  $n$  for a variable  $x$  is defined as:

$$\langle x^n \rangle = \frac{\sum_i E_i x_i^n}{\sum_i E_i}, \quad (1)$$

where  $i$  runs over all cells of the cluster.

provide efficient discrimination against hadrons due to the good transverse and longitudinal segmentation of the calorimeters, though it is not possible to distinguish between electrons and photons. Two reference sets of cuts are defined, *forward loose* and *forward tight* selections. Table 2 lists the identification variables.

#### 4.5 Inclusive single and dielectron spectra

To illustrate the electron identification performance, the left of Figure 2 shows the  $E_T$  distribution of all electron candidates passing the *tight* identification cuts and having  $|\eta| < 2.47$  excluding the transition region,  $1.37 < |\eta| < 1.52$ . The data sample was collected by single electron triggers with varying thresholds. The Jacobian peak at  $E_T \approx 40$  GeV from  $W$  and  $Z$  decays is clearly visible above the sum of contributions from semi-leptonic decays of beauty and charm hadrons, electrons from photon conversions and hadrons faking electrons.

*act rejection*  
EH INT  
CAL  
SDS  
goes  
goes

Table 2. Definition of variables used for *forward loose* and *forward tight* electron identification cuts for the  $2.5 < |\eta| < 4.9$  region of the detector.

Type	Description	Name
<b>Forward loose selection</b>		
Acceptance	$2.5 <  \eta  < 4.9$	
Shower depth	Distance of the shower barycentre from the calorimeter face measured along the shower axis	$\lambda_{centre}$
Longitudinal second moment	Second moment of the distance of each cell to the shower centre in the longitudinal direction ( $\lambda_z$ )	$\langle \lambda^2 \rangle$
Transverse second moment	Second moment of the distance of each cell to the shower centre in the transverse direction ( $\lambda_t$ )	$\langle r^2 \rangle$
<b>Forward tight selection (includes forward loose)</b>		
Maximum cell energy	Fraction of cluster energy in the most energetic cell	$f_{max}$
Normalized lateral moment	$w_2$ is the second moment of $r_t$ setting $r_t = 0$ for the two most energetic cells, while $w_{max}$ is the second moment of $r_t$ setting $r_t = 4$ cm for the two most energetic cells, and $r_t = 0$ for the others	$\frac{w_2}{w_2 + w_{max}}$
Normalized longitudinal moment	$l_2$ is the second moment of $\lambda_t$ setting $\lambda_t = 0$ for the two most energetic cells, while $l_{max}$ is the second moment of $\lambda_t$ setting $\lambda_t = 10$ cm for the two most energetic cells and $\lambda_t = 0$ for the others	$\frac{l_2}{l_2 + l_{max}}$

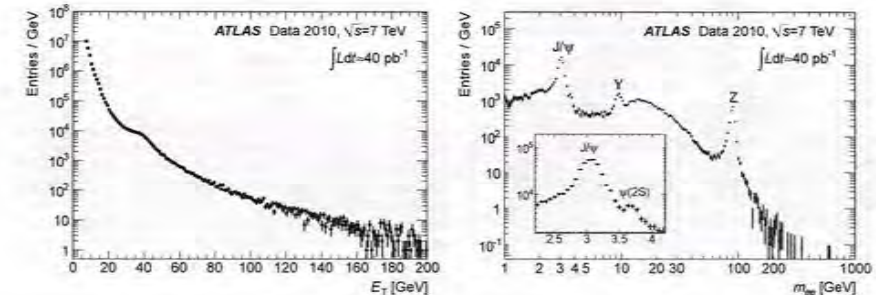


Fig. 2. (left)  $E_T$  distribution of electron candidates passing the *tight* identification cuts for events selected by single electron triggers with varying  $E_T$  thresholds. Data with  $E_T < 20$  GeV correspond to lower integrated luminosity values and were rescaled to the full luminosity. (right) Reconstructed dielectron mass distribution of electron candidate pairs passing the *tight* identification cuts for events selected by low  $E_T$  threshold dielectron triggers. The number of events is normalised by the bin width. Errors are statistical only.

The measurement of known particles decaying into electron final states is an important ingredient in order to calibrate and measure the performance of the detector. The dielectron mass spectrum is plotted on the right of Figure 2 using a selection of unscaled, low  $E_T$  threshold dielectron triggers. Both electrons are required to pass the *tight* selection, to be of opposite sign, and to have  $E_T > 5$  GeV and  $|\eta| < 2.47$ . The  $J/\psi$ ,  $Y$  and  $Z$  peaks are clearly visible, and evidence for the  $\psi(2S)$  meson is also apparent. The shoulder in the region of  $m_{ee} \approx 15$  GeV is caused by the kinematic selection.

#### 4.6 Inter-alignment of the inner detector and the electromagnetic calorimeter

A global survey of the positions of the LAr cryostats and of the calorimeters inside them was performed with an accuracy of about 1–2 mm during their integration and installation in the ATLAS cavern<sup>2</sup>. Since the intrinsic accuracy of the EM calorimeter shower position measurement is expected to be about 200  $\mu$ m for high energy electrons[1],

<sup>2</sup> Measurements were performed when warm and predictions are used to estimate the calorimeter positions inside the cryostats when cold.

accurate measurements of the in-situ positions of the EM calorimeters are prerequisites to precise matching of the extrapolated tracks and the shower barycentres.

For most ATLAS analyses using track-cluster matching cuts (as described in Table 1), or photon pointing, a precision of the order of 1 mm is sufficient. A precision as good as  $100 \mu\text{m}$  is very valuable to improve bremsstrahlung recovery for precision measurements, such as the  $W$  mass measurement.

The relative positions of the four independent parts of the EM calorimeter (two half-barrels and two endcaps) were measured with respect to the inner detector position, assuming that the ID itself is already well-aligned. About 300000 electron candidates with  $p_T > 10 \text{ GeV}$ , passing the *medium* identification cuts, were used.

The comparison of the cluster position and the extrapolated impact point of the electron track on the calorimeter provides a determination of the calorimeter translations and tilts with respect to their nominal positions. A correction for the sagging of the calorimeter absorbers (affecting the azimuthal measurement of the cluster) has been included for the barrel calorimeter with an amplitude of 1 mm. The derived alignment constants are then used to correct the electron cluster positions.

To illustrate the improvements brought by this first alignment procedure, the  $\Delta\eta$  track-cluster matching variable used in electron reconstruction and identification is shown in Figure 3. Here, a sample of electron candidates collected at the end of the 2010 data taking period with  $p_T > 20 \text{ GeV}$ , passing the *medium* identification cuts and requirements similar to the ones described in Subsection 5.1.1 to select  $W$  and  $Z$  candidates, is used. The two-peak structure for  $-2.47 < \eta < -1.52$  visible on the left is due to the transverse displacement of the endcap by about 5 mm which is then corrected by the alignment procedure. On the right of Figure 3,  $\Delta\phi$  for the barrel  $-1.37 < \eta < 0$  is also shown. After including corrections for sagging, a similar precision is reached in  $\phi$  in the endcaps, as well. After the inter-alignment, the *tight* track-cluster matching cuts ( $|\Delta\eta| < 0.005$  and  $|\Delta\phi| < 0.02$ ) can be applied with high efficiency.

These inter-alignment corrections are applied for all datasets used in the following sections.

## 5 Electron energy scale and resolution

### 5.1 Electron energy-scale determination

The electromagnetic calorimeter energy scale was derived from test-beam measurements. The total uncertainty is 3% in the central region covering  $|\eta| < 2.47$ , and it is 5% in the forward region covering  $2.5 < |\eta| < 4.9$ . The dominant uncertainty, introduced by the transfer of the test-beam results to the ATLAS environment, comes from the LAr absolute temperature normalization in the test beam cryostat.

Even with the limited statistics of  $Z \rightarrow ee$  and  $J/\psi \rightarrow ee$  decays available in the 2010 dataset, the well known

masses of the  $Z$  and  $J/\psi$  particles can be used to improve considerably the knowledge of the electron energy scale and to establish the linearity of the response of the EM calorimeter. An alternative strategy to determine the electron energy scale is to study the ratio of the energy  $E$  measured by the EM calorimeter and the momentum  $p$  measured by the inner detector,  $E/p$ . This technique gives access to the larger statistics of  $W \rightarrow ee$  events but depends on the knowledge of the momentum scale and therefore the alignment of the inner detector.

The strategy to calibrate the EM calorimeter is described in Refs. [2, 18]. It was validated using test-beam data [19, 20, 21]. The energy calibration is divided into three steps:

1. The raw signal extracted from each cell in ADC counts is converted into a deposited energy using the electronic calibration of the EM calorimeter [18, 22, 23].
2. MC-based calibration [2] corrections are applied at the cluster level for energy loss due to absorption in the passive material and leakage outside the cluster as discussed in Subsection 4.2. For the central region,  $|\eta| < 2.47$ , additional fine corrections depending on the  $\eta$  and  $\phi$  coordinates of the electron are made to compensate for the energy modulation as a function of the impact point.
3. The in-situ calibration using  $Z \rightarrow ee$  decays determines the energy scale and intercalibrates, as described in Subsection 5.1.1, the different regions of the calorimeters covering  $|\eta| < 4.9$ .

For calibrated electrons with transverse energy larger than  $20 \text{ GeV}$ , the ratio between the reconstructed and the true electron energy is expected to be within 1% of unity for almost all pseudorapidity regions. The energy resolution is better than 2% for  $E_T > 25 \text{ GeV}$  in the most central region,  $|\eta| < 0.6$ , and only exceeds 3% close to the transition region of the barrel and endcap calorimeters where the amount of passive material in front of the calorimeter is the largest.

This section describes the in-situ measurement of the electron energy scale and the determination of the energy resolution. The in-situ calibration is performed using  $Z \rightarrow ee$  decays both for central and forward electrons. The linearity of response versus energy is cross-checked in the central region using  $J/\psi \rightarrow ee$  and  $W \rightarrow ee$  decays, but only with limited accuracy. Due to the modest  $Z \rightarrow ee$  statistics in the 2010 data sample, the intercalibration is performed only among the calorimeter sectors in  $\eta$ . The non-uniformities versus  $\phi$  are much smaller, as expected. They are shown in Subsection 5.1.5.

#### 5.1.1 Event selection

High- $E_T$  electrons from  $Z$  and  $W$  decays are collected using EM triggers requiring a transverse energy above about  $15 - 17 \text{ GeV}$  in the early data taking periods and a high-level trigger also requiring *medium* electron identification criteria in later periods. Low- $E_T$  electrons from  $J/\psi$  are

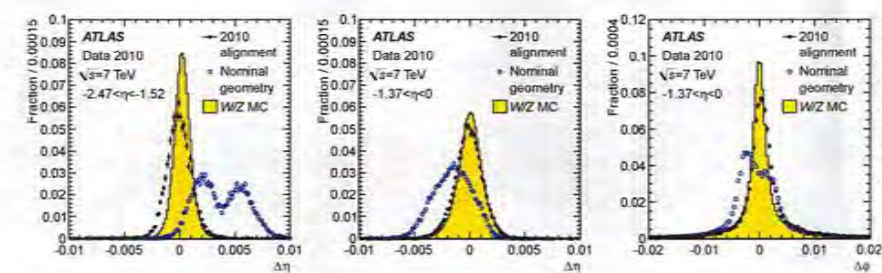


Fig. 3. Track-cluster matching variables of electron candidates from  $W$  and  $Z$  decays for reconstruction with nominal geometry and after the 2010 alignment corrections have been applied: (left)  $\Delta\eta$  distributions for  $-2.47 < \eta < -1.52$  and (middle)  $-1.37 < \eta < 0$ ; (right)  $\Delta\phi$  distributions for  $-1.37 < \eta < 0$ . The MC prediction with perfect alignment is also shown.

selected by a mixture of low  $E_T$  threshold EM triggers depending on the data taking period. All events must have at least one primary vertex formed by at least 3 tracks.

Electrons are required to be within  $|\eta| < 2.47$  excluding the transition region of  $1.37 < |\eta| < 1.52$  for central, and within  $2.5 < |\eta| < 4.9$  for forward candidates. Electrons from  $W$  and  $Z$  (resp.  $J/\psi$ ) decays must have  $E_T > 20 \text{ GeV}$  (resp.  $E_T > 5 \text{ GeV}$ ).

For central-central  $Z$  selection, the *medium* identification cut is applied for both electrons, and for the central-forward  $Z$  selection, a central *tight* and a forward *loose* electron are required. To suppress the larger background *tight-tight* pairs are selected for the  $J/\psi$  analysis. For  $Z$  and  $J/\psi$  selections in the central region, only oppositely charged electrons are considered (no charge information is available in the forward region). The dielectron invariant mass should be in the range  $80 - 100 \text{ GeV}$  for  $Z \rightarrow ee$  and  $2.5 - 3.5 \text{ GeV}$  for  $J/\psi \rightarrow ee$  candidates.

For the  $W$  selection, a *tight* electron is required with additional cuts applied on jet cleaning [24], missing transverse momentum  $E_T^{\text{miss}} > 25 \text{ GeV}$  and transverse mass<sup>3</sup>  $m_T > 40 \text{ GeV}$ .  $Z \rightarrow ee$  events are suppressed by rejecting events containing a second *medium* electron.

In total, about 10000 central-central  $Z$  and 3100 central-forward  $Z$  candidates are selected in the reconstructed dielectron mass range  $m_{ee} = 80 - 100 \text{ GeV}$ . The number of  $J/\psi$  candidates is about 8500 in the mass range  $m_{ee} = 2.5 - 3.5 \text{ GeV}$ . The largest statistics, about 123000 candidates, comes from  $W$  decays.

The amount of background contamination is estimated from data to be about 1% for the central-central electron pairs and 14% for the central-forward electron pairs for the  $Z \rightarrow ee$  selection. It is significantly higher, 23%, for

<sup>3</sup> The transverse mass is defined as

$$m_T = \sqrt{2E_T^e E_T^{\text{miss}}(1 - \cos(\phi^e - \phi^{\text{miss}}))},$$

where  $E_T^e$  is the electron transverse energy,  $E_T^{\text{miss}}$  is the missing transverse momentum,  $\phi^e$  is the electron direction and  $\phi^{\text{miss}}$  is the direction of  $E_T^{\text{miss}}$  in  $\phi$ .

the  $J/\psi \rightarrow ee$  selection. It amounts to 7% for the  $W \rightarrow ee$  selection.

#### 5.1.2 Energy-scale determination using dielectron decays of $Z$ and $J/\psi$ particles

Any residual miscalibration for a given region  $i$  is parametrised by

$$E^{\text{meas}} = E^{\text{true}}(1 + \alpha_i), \quad (2)$$

where  $E^{\text{true}}$  is the true electron energy,  $E^{\text{meas}}$  is the energy measured by the calorimeter after MC-based energy-scale correction, and  $\alpha_i$  measures the residual miscalibration. The  $\alpha$  energy-scale correction factors are determined by a fit minimizing the negative unbinned log-likelihood [2]:

$$-\ln L_{\text{tot}} = \sum_{i,j} \sum_{k=1}^{N_{ij}^{\text{events}}} -\ln L_{ij} \left( \frac{m_k}{1 + \frac{\alpha_i + \alpha_j}{2}} \right), \quad (3)$$

where the indices  $i, j$  denote the regions considered for the calibration with one of the electrons from the  $Z \rightarrow ee$  decay being in region  $i$  and the other in region  $j$ ,  $N_{ij}^{\text{events}}$  is the total number of selected  $Z \rightarrow ee$  decays with electrons in regions  $i$  and  $j$ ,  $m_k$  is the measured dielectron mass in a given decay, and  $L_{ij}(m)$  is the probability density function (pdf) quantifying the compatibility of an event with the  $Z$  lineshape. This pdf template is obtained from PYTHIA MC simulation and smoothed to get a continuous distribution. Since the experimental distribution of the dielectron invariant mass depends strongly on the cluster  $\eta$  of the two electrons, mainly due to the material in front of the calorimeter, the pdf is produced separately for different bins in  $|\eta|$  of the two electron clusters.

The procedure described above was applied to the full 2010 dataset in 58  $\eta$  bins over the full calorimeter coverage of  $|\eta| < 4.9$  and is considered as the *baseline calibration* method. The resulting  $\alpha$  values are shown on the left of

Figure 4. They are within  $\pm 2\%$  in the barrel region and within  $\pm 5\%$  in the forward regions. The rapid variations with  $\eta$  occur at the transitions between the different EM calorimeter systems as indicated in Figure 4. The variations within a given calorimeter system are due to several effects related to electronic calibration, high-voltage corrections (in particular in the endcaps<sup>4</sup>), additional material in front of the calorimeter, differences in the calorimeter and presampler energy scales, and differences in lateral leakage between data and MC.

The same procedure was applied using  $J/\psi \rightarrow ee$  events to determine the electron energy scale. The resulting  $\alpha$  values are in good agreement with the  $Z \rightarrow ee$  measurement and the observed small differences are used in the following to estimate the uncertainty specific to low- $E_T$  electrons.

### 5.1.3 Systematic uncertainties

The different sources of systematic uncertainties affecting the electron energy-scale measurement are summarized in Table 3 and discussed below:

- **Additional material** The imperfect knowledge of the material in front of the EM calorimeter affects the electron energy measurement since the deposited energy in any additional material is neither measured, nor accounted for in the MC-based energy calibration. Nonetheless, if additional material were present in data, the  $\alpha$  correction factors extracted from  $Z \rightarrow ee$  events would restore the electron energy scale on average. However, electrons from  $Z$  decays have an  $E_T$  spectrum with a mean value around 40 GeV. For other values of  $E_T$ , a residual uncertainty arises due to the extrapolation of the calibration corrections, as passive material affects lower-energy electrons more severely. This effect is estimated in two steps. First the calibration procedure is applied on a  $Z \rightarrow ee$  MC sample produced, as explained in Section 3, with a dedicated geometry model with additional material in front of the calorimeters using the nominal MC sample to provide the reference  $Z$  lineshape, as performed on data. Then the non-linearity is measured using MC truth information by comparing the most probable value of the  $E_{\text{reco}}/E_{\text{truth}}$  distributions between the nominal MC and the one with additional material in bins of electron  $E_T$ . The systematic uncertainty varies from  $-2\%$  to  $+12\%$ . As expected and by construction, it vanishes for  $E_T \sim 40$  GeV corresponding to the average electron  $E_T$  in the  $Z \rightarrow ee$  sample. This dominant uncertainty is therefore parametrised as a function of  $E_T$  for the different  $\eta$  regions.

- **Low- $E_T$  electrons** The energy-scale calibration results obtained for  $J/\psi \rightarrow ee$  and  $Z \rightarrow ee$  decays can

be compared. As shown on the right of Figure 4, the  $\alpha$  correction factors extracted using  $J/\psi \rightarrow ee$  decays after applying the baseline calibration using  $Z \rightarrow ee$  decays are within 1% of unity, despite the very different  $E_T$  regimes of the two processes (the mean electron  $E_T$  in the  $J/\psi$  selection is about 9 GeV). This demonstrates the good linearity of the EM calorimeter and also that the amount of material before the calorimeter is modelled with reasonable accuracy. Nonetheless, a 1% additional uncertainty is added for electrons with  $E_T = 10$  GeV, decreasing linearly to 0% for  $E_T = 20$  GeV.

Note, that the systematic uncertainties affecting the  $J/\psi \rightarrow ee$  calibration are evaluated in the same manner as described here for the  $Z \rightarrow ee$  analysis and are shown in Figure 4. The dominant uncertainty comes from the imperfect knowledge of the material in front of the calorimeter and varies between 0.2% in the central barrel and 1% close to the transition region between the barrel and endcap calorimeters.

- **Presampler detector energy scale** The sensitivity of the calibration to the measured presampler energy is significant because it is used to correct for energy lost upstream of the active EM calorimeter. Since the in-situ calibration only fixes one overall scale, it cannot correct for any difference between the presampler detector and the EM calorimeter energy scales. By comparing the energy deposited in the presampler by electrons from  $W \rightarrow e\nu$  decays between data and MC simulation, one can extract an upper limit<sup>5</sup> on the presampler detector energy-scale uncertainty: it is about 5% in the barrel and 10% in the endcap regions up to  $|\eta| = 1.8$ . The impact on the electron energy scale due to the uncertainty on the presampler energy scale depends on  $\eta$  via the distribution of material in front of the calorimeter and on  $E_T$ , since the fraction of energy deposited in the presampler decreases as the electron energy increases. For very high- $E_T$  electrons, this uncertainty should decrease asymptotically to zero. As for the material uncertainty, the  $\alpha$  coefficients extracted from  $Z \rightarrow ee$  data correct the electron energy scale on average for any bias on the presampler energy scale (giving by construction no bias at  $E_T \sim 40$  GeV) but will not improve the response linearity in energy. The largest uncertainty is 1.4%, found for the region  $1.52 < |\eta| < 1.8$  and for  $E_T = 1$  TeV (due to the large extrapolation from  $E_T = 40$  GeV to this energy).

- **Calorimeter electronic calibration and cross-talk** Cells belonging to different sampling layers in the EM calorimeters may have slightly different energy scales due to cross-talk and uncertainties arising from an imperfect electronic calibration. The uncertainties on the energy scale relative to the middle layer for cells in the strip and back layers of the calorimeter are es-

<sup>4</sup> The form of the accordion in the endcap varies as a function of the radius. This implies a variation in the size of the LAr gap. Even though the HV is varied as a function of the radius to compensate this, the compensation is not perfect and residual effects are present.

<sup>5</sup> As this limit is extracted from data-MC comparisons, it will include contributions from the uncertainty on the material and therefore lead to some double-counting of this material uncertainty.

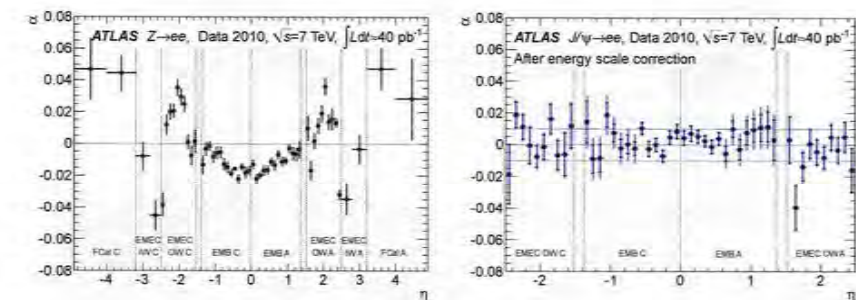


Fig. 4. The energy-scale correction factor  $\alpha$  as a function of the pseudorapidity of the electron cluster derived from fits (left) to  $Z \rightarrow ee$  data and (right) to  $J/\psi \rightarrow ee$  data. The uncertainties of the  $Z \rightarrow ee$  measurement are statistical only. The  $J/\psi \rightarrow ee$  measurement was made after the  $Z \rightarrow ee$  calibration had been applied. Its results are given with statistical (inner error bars) and total (outer error bars) uncertainties. The boundaries of the different detector parts defined in Section 2 are indicated by dotted lines.

timated to be 1% and 2%, respectively [25, 26]. Using the same method as discussed above for the presampler detector energy scale, the uncertainty on the strip layer energy scale is found to be 0.1% for all  $\eta$  and  $E_T$ , while it is negligible on the back layer energy scale (as the energy deposited there is small).

- **Non-linearities in the readout electronics** The readout electronics provide a linear response to typically 0.1% [27]. This is taken as a systematic uncertainty on the extrapolation of the electron energy scale extracted from  $Z \rightarrow ee$  events to higher energies.

- **Requirements on calorimeter operating conditions** To check the possible bias due to these requirements, a tighter veto was applied on electrons falling close to dead regions and electrons in regions with non-nominal high voltage were excluded. No significant effect is observed for the barrel and endcap calorimeters, while differences of 0.6 – 0.8% are seen in the forward region.

- **Background and fit range** The effect of the background, predominantly from jets, on the extracted  $\alpha$  values was studied by tightening the electron selection thereby decreasing the amount of background significantly. In addition, the fit range was also changed from  $80 - 100$  GeV to  $75 - 105$  GeV and  $85 - 95$  GeV. The resulting uncertainty due to the electron selection is +0.1% in the barrel region and reaches +1% in the forward region, while due to the fit range it is 0.1% in the barrel region and grows to 0.6% in the forward region. These uncertainties are treated as uncorrelated.

- **Pile-up** The effect of pile-up is studied by determining the  $\alpha$  coefficients as a function of the number of reconstructed primary vertices (from 1 to 4). The average ( $\langle \alpha \rangle$ ) increases very slightly with the number of primary vertices and a systematic uncertainty of 0.1% is assigned.

- **Possible bias of the method** The bias of the method is assessed by repeating the fit procedure on simulated data, resulting in a systematic uncertainty of 0.1% (0.2%) in the central (forward) region. Moreover, the results of alternative fit methods were compared on data and agree within 0.1 – 0.5% (0.8 – 1.0%). This is added as an additional uncertainty due to possible biases of the method.

- **Theoretical inputs** In the extraction of the  $\alpha$  coefficients from the data, the MC simulation, which uses a certain model of the  $Z$  lineshape, serves as a reference. Uncertainties related to the imperfect physics modelling of QED final state radiation, of the parton density functions in the proton, and of the underlying event are found to be negligible.

To summarize, the overall systematic uncertainty on the electron energy scale is a function of  $E_T$  and  $\eta$ . It is illustrated in Figure 5 for two  $\eta$ -regions. For central electrons with  $|\eta| < 2.47$ , the uncertainty varies from 0.3% to 1.6%. The systematic uncertainties are smallest for  $E_T = 40$  GeV, typically below 0.4%. Below  $E_T = 20$  GeV, the uncertainty grows linearly with decreasing  $E_T$  and slightly exceeds 1% at  $E_T = 10$  GeV. For forward electrons with  $2.5 < |\eta| < 4.9$ , the uncertainties are larger and vary between 2% and 3%.

### 5.1.4 Energy-scale determination using $E/p$ measurements

A complementary in-situ calibration method compares the energy  $E$  measured by the electromagnetic calorimeter to the momentum  $p$  measured by the inner detector. It allows to take advantage of the larger statistics of  $W \rightarrow e\nu$  decays.

The ratio  $E/p$  is shown on the left of Figure 6 for electrons selected in the barrel EM calorimeter in  $W \rightarrow e\nu$

**Table 3.** Systematic uncertainties (in %) on the electron energy scale in different detector regions.

	Barrel	Endcap	Forward
Additional material	$E_T$ - and $\eta$ -dependent, from -2% to +1.2%		
Low- $E_T$ region	$E_T$ -dependent, from 1% at 10 GeV to 0% at 20 GeV		
Presampler energy scale	$E_T$ - and $\eta$ -dependent, 0–1.4%		
Strip layer energy scale	0.1	0.1	0.1
Electronic non-linearity	0.1	0.1	0.1
Object quality requirements	<0.1	<0.1	0.6–0.8
Background and fit range	0.1	0.3	1.2
Pile-up	0.1	0.1	0.1
Bias of method	0.1	0.1–0.5	0.8–1.0

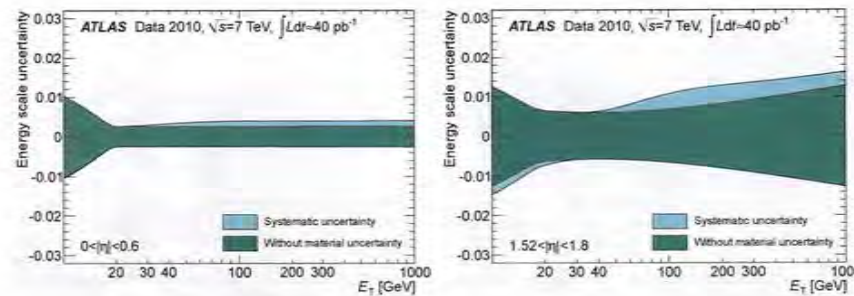


**Fig. 5.** Total systematic uncertainty on the electron energy scale (left) for the region  $|\eta| < 0.6$  which has the smallest uncertainty, and (right) for  $1.52 < |\eta| < 1.8$  which has the largest uncertainty within the central region. The uncertainty is also shown without the contribution due to the amount of additional material in front of the EM calorimeters.

events,  $E/p$  is close to unity, with a significant tail at large values due to Bremsstrahlung occurring in the inner detector. The core of the distribution can be described by a Gaussian whose width corresponds to the measurement error due to both the EM cluster energy and the track curvature resolutions.

The unbinned  $E/p$  distributions are fitted by a Crystal Ball function [28,29] and the most probable value,  $\bar{E}/p$ , is extracted. The fit range,  $0.9 < E/p < 2.2$ , was chosen to be fully contained within the  $E_T$ - and  $\eta$ -dependent lower (0.7–0.8) and upper (2.5–5.0) cuts applied in the *tight* electron selection. The correction factors  $\alpha_{E/p}$  are then derived by

$$\widehat{E/p}_{\text{data}} = \widehat{E/p}_{\text{MC}}(1 + \alpha_{E/p}). \quad (4)$$

On the right of Figure 6 the  $\eta$  dependence of the  $\alpha_{E/p}$  coefficients measured using electrons and positrons from  $W \rightarrow e\nu$  decays are shown after the baseline calibration had been applied. As expected,  $\alpha_{E/p} \approx 0$  within about 1%. The fluctuations are larger in the endcaps, where the results are poorer.

The dominant systematic uncertainties on the measured  $\alpha_{E/p}$  values arise from the fit procedure, (0.1–0.9)%.

### 5.1.5 Energy response uniformity and linearity

The azimuthal uniformity of the calorimeter response is studied using both the dielectron invariant mass distributions of  $Z \rightarrow ee$  events and the  $E/p$  distributions of  $W \rightarrow e\nu$  events, after applying the  $\eta$ -dependent baseline calibration. The results are shown in Figure 7 for two  $\eta$  regions. They demonstrate a  $\phi$  non-uniformity of less than about 1%.

The linearity of the calorimeter response is studied, after applying the  $\eta$ -dependent baseline calibration, by determining the  $\alpha$  coefficients in bins of electron energy.

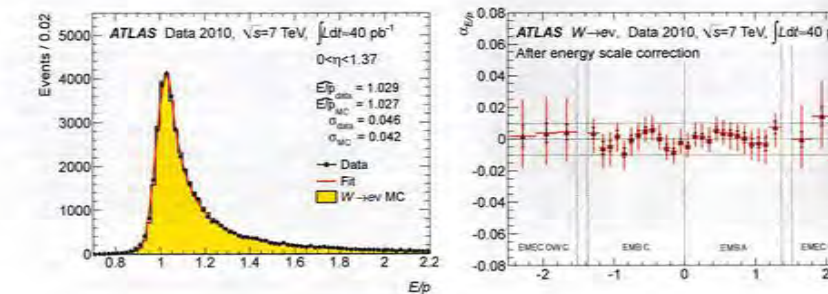


**Fig. 6.** (left)  $E/p$  distributions of electrons and positrons from  $W \rightarrow e\nu$  decays for  $0 < \eta < 1.37$  in data (full circles with statistical error bars) and  $W \rightarrow e\nu$  MC (filled histogram). The result of the fit with a Crystal Ball function to the data is also shown (full line). The most probable value ( $\bar{E}/p$ ) and the Gaussian width ( $\sigma$ ) of the fitted Crystal Ball function are given both for the data and the signal MC. (right) The  $\alpha_{E/p}$  energy-scale correction factors derived from fits to  $E/p$  distributions of  $W \rightarrow e\nu$  electron and positron data, after the baseline calibration had been applied. The inner error bars show the statistical uncertainty, while the outer error bars indicate the total uncertainty. The boundaries of the different detector parts defined in Section 2 are indicated by dotted lines.

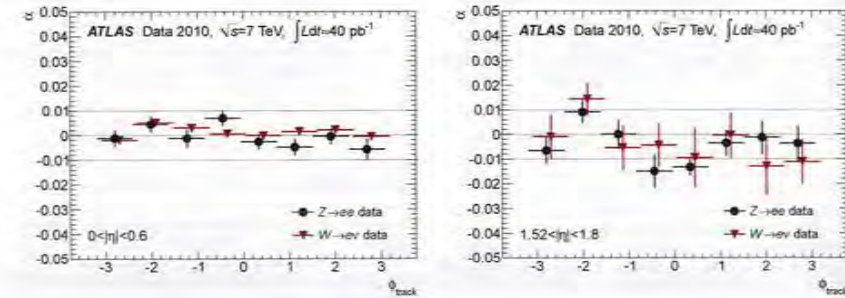


**Fig. 7.** The  $\alpha$  energy-scale correction factor as a function of the electron track  $\phi$  for (left)  $|\eta| < 0.6$  and (right)  $1.52 < |\eta| < 1.8$  determined by the baseline calibration using  $Z \rightarrow ee$  decays (circles) and by the  $E/p$  method using  $W \rightarrow e\nu$  decays (triangles). Errors are statistical only.

The  $Z \rightarrow ee$  results are complemented at low energy by a  $J/\psi \rightarrow ee$  calibration point as shown in Figure 8 for two regions: on the left the region  $|\eta| < 0.8$  which has the smallest uncertainties, and on the right the region  $1.52 < |\eta| < 1.8$  which is affected by the largest material uncertainties. Compared to  $E_T$  independent calibration, calibration factors obtained as a function of  $E_T$  are more sensitive to the description of the energy resolution. This effect was estimated by varying the energy resolution in MC simulation within its uncertainty and was found to be about 0.1% in the central region and up to 0.8% in the forward region. All measurements are found to be within the uncertainty bands assigned to the electron energy scale.

### 5.2 Electron energy resolution

The fractional energy resolution in the calorimeter is parametrised as

$$\frac{\sigma_E}{E} = \frac{a}{\sqrt{E}} \oplus \frac{b}{E} \oplus c. \quad (5)$$

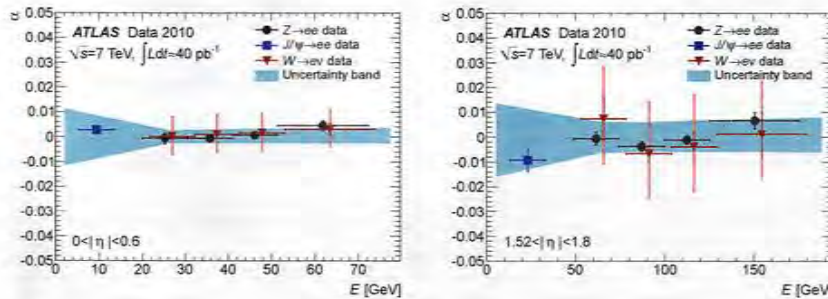


**Fig. 8.** The  $\alpha$  energy-scale correction factor as a function of the electron energy for (left)  $|\eta| < 0.6$  and (right)  $1.52 < |\eta| < 1.8$  determined by the baseline calibration method using  $Z \rightarrow ee$  (circles) and  $J/\psi \rightarrow ee$  (square) decays and by the  $E/p$  method described in Subsection 5.1.4 using  $W \rightarrow e\nu$  decays (triangles). For the  $Z \rightarrow ee$  data points, the inner error bar represents the statistical uncertainty and the outer gives the combined error when bin migration effects are also included. The error on the  $J/\psi \rightarrow ee$  measurements are statistical only. The band represents the systematic errors on the energy scale for the baseline calibration method as discussed in Table 3. For the  $E/p$  method, the inner error bar represents the statistical and the outer the total uncertainty.

Here  $a$ ,  $b$  and  $c$  are  $\eta$ -dependent parameters:  $a$  is the sampling term,  $b$  is the noise term and  $c$  is the constant term. Great care was taken during the construction of the calorimeter to minimise all sources of energy response non-uniformity, since any non-uniformity has a direct impact on the constant term of the energy resolution. The construction tolerances and the electronic calibration system ensure that the calorimeter response is locally uniform, with a local constant term below 0.5% [20] over regions of typical size  $\Delta\eta \times \Delta\phi = 0.2 \times 0.4$ . These regions are expected to be intercalibrated in situ to 0.5% achieving a global constant term<sup>6</sup> around 0.7% for the EM calorimeter, which is well within the requirement driven by physics needs, for example the  $H \rightarrow \gamma\gamma$  sensitivity [18].

To extract the energy resolution function from data, more statistics are needed than available in the 2010 data sample. Therefore, only the constant term is determined here from a simultaneous analysis of the measured and predicted dielectron invariant mass resolution from  $Z \rightarrow ee$  decays, taking the sampling and noise terms from MC simulations.

As shown in Figure 9, the measured dielectron mass distribution of electrons coming from  $J/\psi \rightarrow ee$  decays is in good agreement with the MC prediction (both for the mean and the width). Since the electron energy resolution at these low energies is dominated by the contribution from the sampling term, it is assumed that the term  $a$  is well described, within a 10% uncertainty, as a function of  $\eta$  by the MC simulation. The noise term has a significant

contribution only at low energies. Moreover, its effect on the measurement of the constant term cancels out to first order, since the noise description in the MC simulation is derived from calibration data runs. The above assumptions lead to the formula:

$$c_{\text{data}} = \sqrt{2 \cdot \left( \left( \frac{\sigma}{m_Z} \right)^2_{\text{data}} - \left( \frac{\sigma}{m_Z} \right)^2_{\text{MC}} \right) + c_{\text{MC}}^2}, \quad (6)$$

where  $c_{\text{MC}}$  is the constant term of about 0.5% in the MC simulation. The parameter  $c_{\text{data}}$  is an effective constant term which includes both the calorimeter constant term and the effect of inhomogeneities due to possible additional material.  $m_Z$  denotes the  $Z$  mass [30], and  $\sigma$  is the Gaussian component of the experimental resolution.

The resolutions are derived from fits to the invariant mass distributions using a Breit-Wigner convolved with a Crystal Ball function in the mass range  $80 - 100$  GeV for central-central events and in the mass range  $75 - 105$  GeV for central-forward events. The Breit-Wigner width is fixed to the measured  $Z$  width [30], and the experimental resolution is described by the Crystal Ball function. Figure 10 shows the invariant mass distributions of the selected  $Z \rightarrow ee$  decays: the measured Gaussian components of the experimental resolution are always slightly worse than those predicted by MC, with the smallest deviation observed for barrel-barrel events (top left) and the largest one for central-EMEC-IW events (bottom left).

In central-forward events the two electrons belong to different detector regions. Therefore, when extracting the constant term in the forward region, a smearing is applied to the central electrons using the results of the barrel-barrel and endcap-endcap measurements.

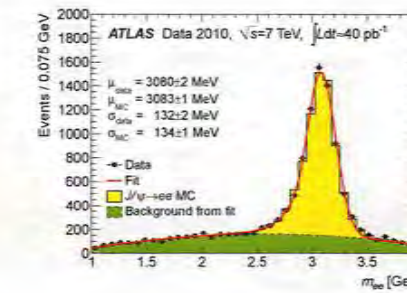


**Fig. 9.** Reconstructed dielectron mass distribution for  $J/\psi \rightarrow ee$  decays, as measured after applying the baseline  $Z \rightarrow ee$  calibration. The data (full circles with statistical error bars) are compared to the sum of the MC signal (light filled histogram) and the background contribution (darker filled histogram) modelled by a Chebyshev polynomial. The mean ( $\mu$ ) and the Gaussian width ( $\sigma$ ) of the fitted Crystal Ball function are given both for data and MC.

**Table 4.** Measured effective constant term  $c_{\text{data}}$  (see Eq. 6) from the observed width of the  $Z \rightarrow ee$  peak for different calorimeter  $\eta$  regions.

Sub-system	$\eta$ -range	Effective constant term, $c_{\text{data}}$
EMB	$ \eta  < 1.37$	$1.2\% \pm 0.1\% \text{ (stat)} \pm 0.5\% \text{ (syst)}$
EMEC-OW	$1.52 <  \eta  < 2.47$	$1.8\% \pm 0.4\% \text{ (stat)} \pm 0.4\% \text{ (syst)}$
EMEC-IW	$2.5 <  \eta  < 3.2$	$3.3\% \pm 0.2\% \text{ (stat)} \pm 1.1\% \text{ (syst)}$
FCal	$3.2 <  \eta  < 4.9$	$2.5\% \pm 0.4\% \text{ (stat)} \pm 1.0\% \text{ (syst)}$

The results obtained for the effective constant term are shown in Table 4. Several sources of systematic uncertainties are investigated. The dominant uncertainty is due to the uncertainty on the sampling term, as the constant term was extracted assuming that the sampling term is correctly reproduced by the simulation. To assign a systematic uncertainty due to this assumption, the simulation was modified by increasing the sampling term by 10%. The difference in the measured constant term is found to be about 0.4% for the EM calorimeter and 1% for the forward calorimeter. The uncertainty due to the fit procedure was estimated by varying the fit range. The uncertainty due to pile-up was investigated by comparing simulated MC samples with and without pile-up and was found to be negligible.

## 6 Efficiency measurements

In this section, the measurements of electron selection efficiencies are presented using the tag-and-probe method [31, 32].  $Z \rightarrow ee$  events provide a clean environment to study all components of the electron selection efficiency discussed in this paper. In certain cases, such as identification or trigger efficiency measurements, the statistical power of the results is improved using  $W \rightarrow e\nu$  decays, as well. To extend the reach towards lower transverse energies,

$J/\psi \rightarrow ee$  decays are also used to measure the electron identification efficiency. However the available statistics of  $J/\psi \rightarrow ee$  events after the trigger requirements in the 2010 data sample are limited and do not allow a precise separation of the isolated signal component from b-hadron decays and from background processes.

### 6.1 Methodology

A measured electron spectrum needs to be corrected for efficiencies related to the electron selection in order to derive cross-sections of observed physics processes or limits on new physics. This correction factor is defined as the product of different efficiency terms. For the case of a single electron in the final state one can write:

$$C = \epsilon_{\text{event}} \cdot \alpha_{\text{reco}} \cdot \epsilon_{ID} \cdot \epsilon_{\text{trig}} \cdot \epsilon_{\text{isol}}. \quad (7)$$

Here  $\epsilon_{\text{event}}$  denotes the efficiency of the event preselection cuts, such as primary vertex requirements and event cleaning.  $\alpha_{\text{reco}}$  accounts for the basic reconstruction efficiency to find an electromagnetic cluster and to match it loosely to a reconstructed charged particle track in the fiducial region of the detector and also for any kinematic and geometrical cuts on the reconstructed object itself.  $\epsilon_{ID}$  denotes the efficiency of the identification cuts relative to reconstructed electron objects.  $\epsilon_{\text{trig}}$  stands for the

<sup>6</sup> The long-range constant term is the residual miscalibration between the different calorimeter regions, and the global constant term is the quadratic sum of the local and long-range constant terms.

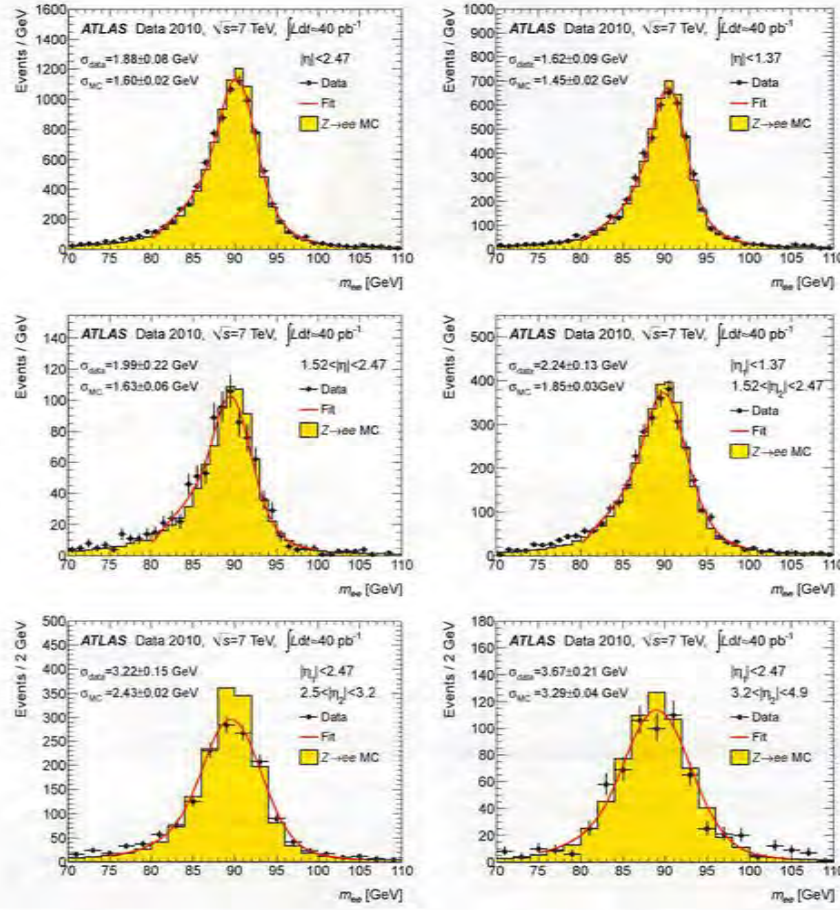


**Fig. 10.** Reconstructed dielectron mass distributions for  $Z \rightarrow ee$  decays for different pseudorapidity regions after applying the baseline  $Z \rightarrow ee$  calibration. The transition region  $1.37 < |\eta| < 1.52$  is excluded. The data (full circles with statistical error bars) are compared to the signal MC expectation (filled histogram). The fits of a Breit-Wigner convolved with a Crystal Ball function are shown (full lines). The Gaussian width ( $\sigma$ ) of the Crystal Ball function is given both for data and MC simulation.

$C = \epsilon_{ev} \cdot \epsilon_{rec} \cdot \epsilon_{ID} \cdot \epsilon_{trig} \cdot \epsilon_{isol}$

primary vertex  $n \geq 3$   
loose matching  
 $E_T > 40$  GeV  
select on

the trigger efficiency with respect to all reconstructed and identified electron candidates.  $\epsilon_{isol}$  is the efficiency of any isolation requirement, if applied, limiting the presence of other particles (tracks, energy deposits) close to the identified electron candidate.

In this paper, three of the above terms are studied: the dominant term of  $\epsilon_{rec}$  that accounts for the efficiency to loosely match a reconstructed track fulfilling basic quality criteria to a reconstructed cluster, the identification efficiency  $\epsilon_{ID}$ , and the trigger efficiency  $\epsilon_{trig}$  for the most important single electron triggers used in physics analyses based on 2010 data.

Note that the above decomposition is particularly useful as it allows the use of data-driven measurements of the above independent efficiency terms, such as the ones presented in this paper using the tag-and-probe (T&P) technique, in physics analyses, and therefore limits the reliance on MC simulation. This is usually done by correcting the MC predicted values of the above efficiency terms for a given physics process in bins (of typically  $E_T$  and  $\eta$ ) by the measured ratios of the data to MC efficiencies in the T&P sample in the same bins. The range of validity of this method depends on the kinematic parameters of the electrons used in the physics analysis itself and on more implicit observables such as the amount of jet activity in the events considered in the analysis with respect to that observed in the T&P sample.

The T&P method aims to select a clean and unbiased sample of electrons, called probe electrons, using selection cuts, called tag requirements, primarily on other objects in the event. The efficiency of any selection cut can then be measured by applying it to the sample of probe electrons. In the following, a well-identified electron is used as the tag in the  $Z \rightarrow ee$  and  $J/\psi \rightarrow ee$  measurements and high missing transverse momentum is used in the  $W \rightarrow ev$  measurements.

For most efficiency measurements presented here, the contamination of the probe sample by background (for example hadrons faking electrons, or electrons from heavy flavour decays, or electrons from photon conversions) requires the use of some background estimation technique (usually a side-band or a template fit method). The number of electron candidates is then independently estimated both at the probe level and at the level where the probe passes the cut of interest. The efficiency is then equivalent to the fraction of probe candidates passing the cut of interest.

Depending on the background subtraction method, different formulae for computing the statistical uncertainties on the efficiency measurements have been used as discussed in Ref. [33]. These formulae are approximate but generally conservative. When no background subtraction is necessary, the simple binomial formula is replaced by a Bayesian evaluation of the uncertainty.

The statistics available with the full 2010 dataset are not sufficient to measure any of the critical efficiency components as a function of two parameters, so the measurements are performed separately in bins of  $\eta$  and  $E_T$  of the probe. The bins in  $\eta$  are adapted to the detector geometry,

try, while the  $E_T$ -binning corresponds to the optimization bins of the electron identification cuts.

## 6.2 Electron identification efficiency in the central region

The measurements of the efficiency of electron identification with the predefined sets of requirements, called *medium* and *tight* and described in Table 1, were performed on three complementary samples of  $W \rightarrow ev$ ,  $Z \rightarrow ee$  and  $J/\psi \rightarrow ee$  events. While the electrons from  $W \rightarrow ev$  and  $Z \rightarrow ee$  decays are typically well-isolated, the  $J/\psi \rightarrow ee$  signal is a mix of isolated and non-isolated electrons. Both prompt ( $pp \rightarrow J/\psi X'$ ) and non-prompt ( $b \rightarrow J/\psi X'$ ) production contribute, and in the latter case the electrons from the  $J/\psi \rightarrow ee$  decay are typically accompanied by other particles from the decay of the b-hadron. This, coupled with the higher background levels in the low- $E_T$  region, makes the  $J/\psi$  analysis more demanding. The measurements cover the central region of the EM calorimeter within the tracking acceptance,  $|\eta| < 2.47$ , and the electron transverse energy range  $E_T = 4 - 50$  GeV. Electrons in the forward region,  $2.5 < |\eta| < 4.9$ , are discussed in Subsection 6.3.

### 6.2.1 Probe selection

The three data samples were obtained using a variety of triggers:

1.  $W \rightarrow ev$  decays are collected using a set of  $E_T^{\text{miss}}$  triggers. These triggers had an increasing  $E_T^{\text{miss}}$  threshold from approximately 20 GeV initially at low luminosity to 40 GeV at the highest luminosities obtained in 2010. The total number of unbiased electron probes in this sample after background subtraction amounts to about 27500.
2.  $Z \rightarrow ee$  decays are obtained using a set of single inclusive electron triggers with an  $E_T$  threshold of 15 GeV. The total number of unbiased electron probes in this sample is about 14500 after background subtraction.
3.  $J/\psi \rightarrow ee$  decays are selected using a set of low- $E_T$  single electron triggers with thresholds between 5 and 10 GeV. Towards the end of 2010, these triggers had to be heavily prescaled and a different trigger was used, requiring an electromagnetic cluster with  $E_T > 4$  GeV in addition to the single electron trigger. The total number of unbiased electron probes in this sample amounts to about 6000 after background subtraction. As already noted, they are a mix of isolated and non-isolated electrons from prompt and non-prompt  $J/\psi$  decays, respectively, with their fractions depending on the transverse energy bin.

Only events passing data-quality criteria, in particular concerning the inner detector and the calorimeters, are considered. At least one reconstructed primary vertex with at least three tracks should be present in the

event. Additional cuts were applied to minimise the impact of beam backgrounds and to remove electron candidates pointing to problematic regions of the calorimeter readout as discussed in Subsection 4.3.

Unbiased samples of electron probes, with minimal background under the signal, were obtained by applying stringent cuts to the trigger object in the event (a neutrino in the case of  $W \rightarrow e\nu$  decays and one of the two electrons in the case of  $Z \rightarrow ee$  and  $J/\psi \rightarrow ee$  decays), which is thus the tag, and by selecting the electron probe following very loose requirements on the EM calorimeter cluster and the matching track:

- In the case of  $W \rightarrow e\nu$  decays, simple kinematic requirements were made:  $E_T^{\text{miss}} > 25$  GeV and  $m_T > 40$  GeV. For the fake electron background from multijet events, there is usually a strong correlation in the transverse plane between the azimuthal angle of the  $E_T^{\text{miss}}$  vector and that of one of the highest  $E_T$  reconstructed jets. Thus a large rejection against fake electrons from hadrons or photon conversions can be obtained by requiring  $E_T^{\text{miss}}$  isolation: the difference between the azimuthal angles of the missing transverse momentum and any jet having  $E_T > 10$  GeV was required to be  $\Delta\phi > 2.5$  for the baseline analysis. This  $\Delta\phi$  threshold was varied between 0.7 and 2.5 to assess the sensitivity of the measurements to the level of background under the  $W \rightarrow e\nu$  signal.
- In the case of  $Z \rightarrow ee$  (resp.  $J/\psi \rightarrow ee$ ) decays, the tag electron was required to have  $E_T > 20$  (resp. 5) GeV, to match the corresponding trigger object, and to pass the *tight* electron identification requirements. The identification requirements were varied between the *medium* and *tight* selections to evaluate the sensitivity of the measurements to the level of background under the  $Z \rightarrow ee$  and  $J/\psi \rightarrow ee$  signal. The probe electron was required to be of opposite charge to the tag electron. In the  $J/\psi \rightarrow ee$  selection, to address the case of high- $E_T$  electrons that would often produce close-by EM showers in the calorimeter, the distance in  $\Delta R$  between the two electron clusters was required to be larger than 0.1. All tag-probe pairs passing the cuts were considered.
- The probe electron was required to have  $|\eta| < 2.47$ , and  $E_T > 15$  GeV for  $W \rightarrow e\nu$ ,  $E_T > 15$  GeV for  $Z \rightarrow ee$ , and  $E_T > 4$  GeV for  $J/\psi \rightarrow ee$  decays.
- To reject beam-halo muons producing high-energy bremsstrahlung clusters in the EM calorimeter in the data sample collected by  $E_T^{\text{miss}}$  triggers for the  $W \rightarrow e\nu$  channel, certain track quality requirements have to be applied on the electron probes: the electron tracks should have at least one pixel hit and a total of at least seven silicon (pixel plus SCT) hits. These cuts have been applied in all three selections,  $W \rightarrow e\nu$ ,  $Z \rightarrow ee$  and  $J/\psi \rightarrow ee$ . Their efficiency is measured separately using  $Z \rightarrow ee$  events as described in Subsection 6.4.
- The same procedure is applied to the MC simulation, with in addition a reweighting of the MC to reproduce the pile-up observed in data as well as the proper mixture of the various triggers. Figure 11 shows the transverse energy

distributions of the probes for each of the three channels and, for completeness since the  $W \rightarrow e\nu$  channel relies on an orthogonal trigger based on  $E_T^{\text{miss}}$ , the transverse mass distribution for the  $W \rightarrow e\nu$  selected probes. In order to compare these distributions to those expected from a signal MC, *tight* identification cuts have been applied to the probes resulting in very high purity in the case of the  $W \rightarrow e\nu$  and  $Z \rightarrow ee$  channels. In the case of the  $J/\psi \rightarrow ee$  channel however, some background remains even at this stage, as can be seen from the excess of probes in data compared to MC at low  $E_T$ . The small differences seen between data and MC distributions in the  $W \rightarrow e\nu$  measurement arise primarily from the imperfections of the modelling of the  $E_T^{\text{miss}}$ -triggers in simulation.

### 6.2.2 Background subtraction

The next step in the analysis is to use a discriminating variable to estimate the signal and background contributions in each  $E_T$  or  $\eta$  bin. This variable should ideally be uncorrelated to the electron identification variables.

#### Dielectron mass for the $Z \rightarrow ee$ and $J/\psi \rightarrow ee$ channels

The reconstructed dielectron mass is the most efficient discriminating variable to estimate the signal and background contributions in the selected sample of electron probes from  $Z \rightarrow ee$  and  $J/\psi \rightarrow ee$  decays. The signal integration ranges, typically  $80 < m_{ee} < 100$  GeV for the  $Z \rightarrow ee$  channel and  $2.8 < m_{ee} < 3.2$  GeV for the  $J/\psi \rightarrow ee$  channel, were chosen to balance the possible bias of the efficiency measurement and the systematic uncertainty on the background subtraction.

In the  $Z \rightarrow ee$  channel, which has more events and lower background contamination, the efficiency measurements in  $\eta$ -bins (for transverse energies  $20 < E_T < 50$  GeV) were performed with a simple same-sign background subtraction. For both channels, the shape of the background under the dielectron mass peak depends strongly on the  $E_T$ -bin due to kinematic threshold effects. Therefore for the measurements in  $E_T$ -bins (integrated over  $|\eta| < 2.47$  and excluding the overlap region  $1.37 < |\eta| < 1.52$ ), the background subtraction is performed as follows.

- In the  $Z \rightarrow ee$  channel, a two-component fit with a signal contribution plus a background contribution is performed in each bin to the  $m_{ee}$  distribution over typical fit mass ranges of  $40 < m_{ee} < 160$  GeV. The signal contribution is modelled either by a Breit-Wigner distribution convolved with a parametrisation of the low-mass tail, arising mostly from material effects, by a Crystal Ball function, or by a template obtained from  $Z \rightarrow ee$  MC simulation. For the background contribution a variety of fit functions were considered. In the  $Z \rightarrow ee$  measurement, an exponential and a single-sided exponential convolved with a Gaussian are used.
- In the case of the  $J/\psi \rightarrow ee$  selection, where the background contamination is highest, the amount and

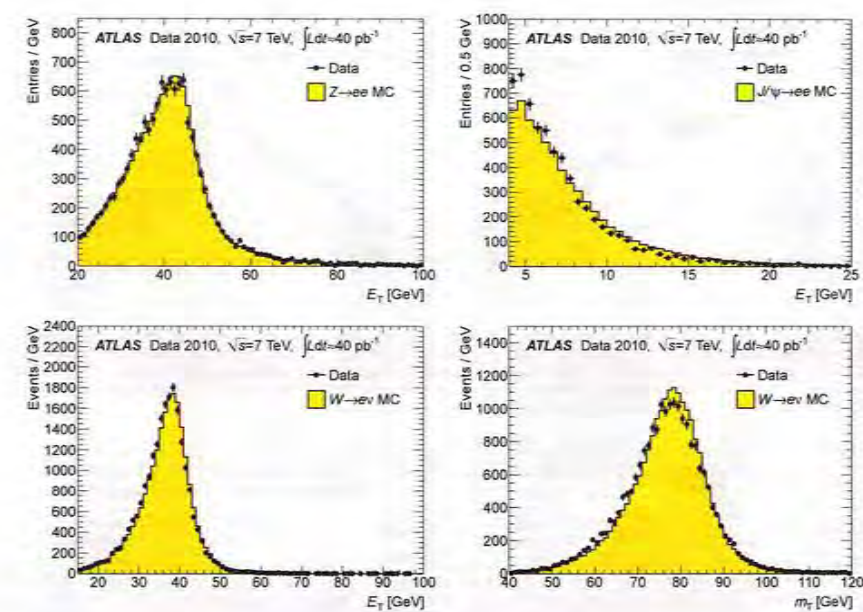
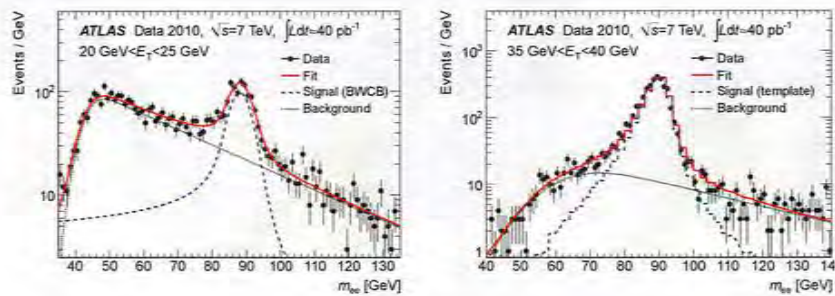


Fig. 11. Transverse energy spectra, compared between data and MC, for the selected electron probes passing *tight* identification cuts for the (top left)  $Z \rightarrow ee$ , (top right)  $J/\psi \rightarrow ee$ , and (bottom left)  $W \rightarrow ee$  channels, together with (bottom right) the transverse mass distribution for the  $W \rightarrow e\nu$  channel. The data points are plotted as full circles with statistical error bars, and the MC prediction, normalised to the number of data entries, as a filled histogram.

shape of the background vary significantly with the  $E_T$  of the probe, and depend strongly on the selection criteria applied to the probe. Therefore, the fit described above, and applied typically over  $1.8 < m_{ee} < 4$  GeV, contains a third component, which is based on the spectrum of same-sign pairs in the data. Use of the same-sign sample has the advantage that it describes the shape of a large fraction of the background (random combinations of fake or real electrons), in particular in the signal region. The remaining background is modelled on each side of the signal region by an exponential, a Landau function or a Chebyshev polynomial. Examples of the fit results are shown in Figure 12 for the  $Z \rightarrow ee$  and in Figure 13 for the  $J/\psi \rightarrow ee$  measurement.

**Calorimeter isolation for the  $W \rightarrow e\nu$  channel** The  $W \rightarrow e\nu$  sample is selected with very stringent  $E_T^{\text{miss}}$  requirements. There is only a limited choice of observables to discriminate the isolated electron signal from the residual background from jets. One suitable observable, which is

nevertheless slightly correlated with some of the electron identification variables, is the energy isolation measured in the calorimeter. This isolation variable, denoted hereafter  $I_{\Delta R=0.4}$ , is computed over a cone of half-angle  $\Delta R = 0.4$  as follows. The transverse energies of all EM and hadronic calorimeter cells are summed except for those which are in the  $5 \times 7$  EM calorimeter cells in  $\Delta\eta \times \Delta\phi$  space around the cluster barycentre. This sum is normalised to the transverse energy of the EM cluster to yield  $I_{\Delta R=0.4}$ . For isolated electrons, the  $I_{\Delta R=0.4}$  distribution is expected to peak at values close to zero, with a width determined by the combination of electronic noise, shower leakage, underlying event and pile-up contributions. For the background from jets, a much wider distribution is expected reaching values well beyond unity. The signal region is defined by requiring that the calorimeter isolation be below a certain threshold, typically 0.4. The residual background in the signal region is estimated using template distributions derived from data by requiring that the electron probes fail certain electron identification cuts. The obtained templates are normalized in the background region, above the



**Fig. 12.** The distributions of the dielectron invariant mass of  $Z \rightarrow ee$  candidate events, before applying electron identification cuts on the probe electron, in the  $E_T$ -range (left) 20–25 GeV and (right) 35–40 GeV. The data distribution (full circles with statistical error bars) is fitted with the sum (full line) of a signal component (dashed line) modelled by a Breit-Wigner convolved with a Crystal Ball function (BWCB) on the left or by a MC template on the right, and a background component (dotted line) chosen here as an exponential decay function convolved with a Gaussian.

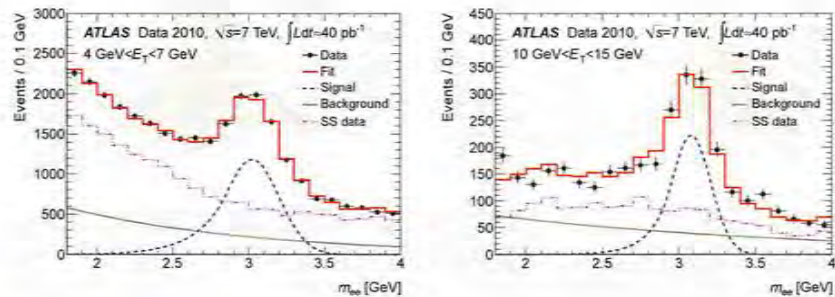


**Fig. 13.** The distributions of the dielectron invariant mass of  $J/\psi \rightarrow ee$  candidate events, before applying electron identification cuts on the probe electron, in the  $E_T$ -range (left) 4–7 GeV and (right) 10–15 GeV. The data distribution (full circles with statistical error bars) is fitted with the sum (full line) of a signal component (dashed line) described by a Crystal Ball function and two background components, one taken from same-sign pairs in the data (dash-dotted line) and the remaining background modelled by an exponential function (dotted line).

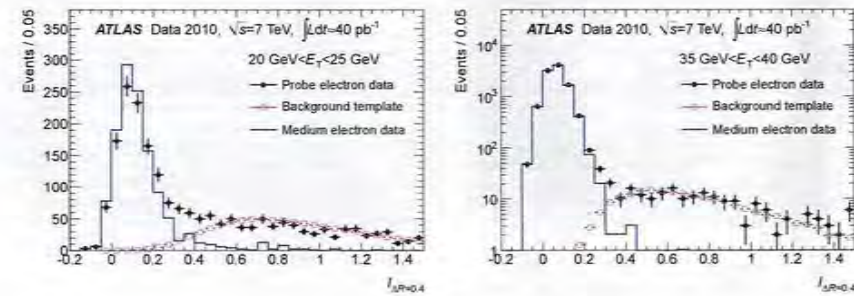
chosen isolation threshold, to the number of selected electron probes.

Figure 14 shows the  $I_{\Delta R=0.4}$  distribution for the data in two regions of phase space: a low- $E_T$  bin,  $20 < E_T < 25$  GeV, where the background contribution is high, and the  $E_T$  bin,  $35 < E_T < 40$  GeV, which has the largest fraction of the signal statistics and a very high signal-to-background ratio.

**Samples obtained after background subtraction** Once the background subtraction procedure has been well defined, the next step in the process of measuring the effi-

cencies of the electron identification criteria (relative to electron reconstruction with additional track silicon hit requirements, as described above) is to define the total numbers of signal probes before and after applying the identification cuts, together with their statistical and systematic uncertainties. The ratios of these two numbers in each  $E_T$ -bin or  $\eta$ -bin are the efficiencies measured in data.

Table 5 shows several examples of the numbers of signal and background probes and of the corresponding signal-to-background ratios ( $S/B$ ) for the three channels and for selected  $E_T$ -bins. The  $S/B$  ratios were found to be fairly uniform as a function of  $\eta$  for a given channel and  $E_T$ -bin. In contrast, as expected, the  $S/B$  ratios im-



**Fig. 14.** The distributions of the calorimeter isolation variable,  $I_{\Delta R=0.4}$  for the  $W \rightarrow ee$  data sample for (left)  $20 < E_T < 25$  GeV and (right)  $35 < E_T < 40$  GeV. The full circles with statistical error bars correspond to the probe electrons before applying any identification cuts. The open squares show the corresponding background template, derived from data, normalised to the probe electron data in the region  $I_{\Delta R=0.4} > 0.4$ . To illustrate the expected shape of the  $W \rightarrow ee$  signal, the distributions obtained for electron probes passing the *medium* identification cuts and normalised to the calculated  $W \rightarrow ee$  signal are shown by full histograms.

**Table 5.** Numbers of signal and background probes and signal-over-background ratios ( $S/B$ ), in different  $E_T$  ranges, for the  $W \rightarrow ee$ ,  $Z \rightarrow ee$ , and  $J/\psi \rightarrow ee$  channels. The errors are statistical only.

$E_T$ [GeV]	$W \rightarrow ee$			$Z \rightarrow ee$		$J/\psi \rightarrow ee$	
	15–20	20–25	35–40	20–25	40–45	4–7	15–20
Signal	$455 \pm 20$	$1040 \pm 30$	$10090 \pm 100$	$870 \pm 40$	$3710 \pm 60$	$3900 \pm 90$	$155 \pm 15$
Background	$60 \pm 10$	$140 \pm 20$	$35 \pm 6$	$460 \pm 20$	$160 \pm 20$	$3330 \pm 190$	$120 \pm 20$
$S/B$	$7.3 \pm 1.0$	$7.3 \pm 1.1$	$290 \pm 50$	$1.9 \pm 0.1$	$24 \pm 3$	$1.2 \pm 0.1$	$1.3 \pm 0.3$

prove considerably for high- $E_T$  electrons from  $W \rightarrow ee$  and  $Z \rightarrow ee$  decay. The  $S/B$  ratios for the  $W \rightarrow ee$  channel are considerably higher than for the  $Z \rightarrow ee$  channel partly due to the higher  $W$  cross-section and partly because of the more stringent kinematic cuts applied to the neutrino tag (high  $E_T^{\text{miss}}$  and  $E_T^{\text{miss}}$  isolation) than to the electron tag in the  $Z \rightarrow ee$  case. Such stringent kinematic cuts were not applied to the  $Z \rightarrow ee$  channel because of limited statistics. At the much lower  $E_T$ -values covered by the  $J/\psi \rightarrow ee$  channel, the  $S/B$  ratios are of order unity before applying any electron identification cuts and therefore the systematic uncertainties from the background subtraction procedure will be larger than for the  $W \rightarrow ee$  and  $Z \rightarrow ee$  channels, as shown in Subsection 6.2.3.

### 6.2.3 Systematic uncertainties

The dominant systematic uncertainties on the efficiency measurements described above are linked to the background subtraction from the probe samples, especially before applying the electron identification cuts. The background level under the signal was varied substantially to verify the stability of the background subtraction proce-

dure, mostly by varying the cuts applied to the tag component of the event. Furthermore, the background subtraction method itself was also varied. The following sources of systematic uncertainties were considered:

- Background level** The tag requirements (such as the electron identification level, *medium* or *tight*, for  $Z \rightarrow ee$  and  $J/\psi \rightarrow ee$ , and the  $E_T^{\text{miss}}$  and electron isolation, for  $W \rightarrow ee$  and  $Z \rightarrow ee$ , respectively), were varied to induce variations of the background level under the signal.

- Discriminating variable used in the background estimation** Several analysis choices were varied to estimate the uncertainty due to the discriminating variable chosen (calorimeter isolation for  $W \rightarrow ee$  and invariant mass for  $Z \rightarrow ee$  and  $J/\psi \rightarrow ee$ ): the size of the signal window; the definition of the side-band region used for background subtraction for the  $\eta$ -dependent efficiencies in the  $Z \rightarrow ee$  channel; the signal and background models (functions or templates) used in the fits for the  $E_T$ -dependent efficiencies in the  $Z \rightarrow ee$  and  $J/\psi \rightarrow ee$  channels; the definition of the isolation variable and the normalization region for the background template distributions for the  $W \rightarrow ee$  channel.

**Possible bias related to the method of the background subtraction** The possible bias from the correlations between the discriminating variable and the efficiencies themselves in the case of calorimeter isolation for the  $W \rightarrow e\nu$  channel was studied by changing the selection used when producing the background isolation template (trigger stream, selection cuts). Also, wherever feasible the possible bias of the efficiency extraction method (in particular the background subtraction) was also studied by repeating the measurements on simulated data and comparing the results to the MC truth. Typically, these *closure tests* were performed by mixing a high-statistics simulated signal sample and a background contribution with the background shape taken from a control region in data. The signal-to-background ratios were estimated from data and varied within reasonable limits. Any observed bias (defined as the difference of the measured and the true MC value in the test) was taken as an additional systematic uncertainty.

All combinations of the above variations were used to extract the efficiency, yielding about a hundred distinct measurements for each channel and for each kinematic bin. Given the complexity of the background subtraction procedure and the variety of kinematic configurations studied, no single preferred method for background subtraction could be defined. The central value of the measured efficiency was therefore defined as the mean of the distribution of all the efficiency values obtained through these variations and the systematic uncertainty was defined as the root mean square of the distributions. The statistical error is the mean of the statistical errors of all measurements corresponding to these analysis configurations.

Other potential sources of uncertainty were also checked but led to negligible contributions to the overall systematic uncertainty on the measurements:

- the impact of the energy-scale corrections discussed in Subsection 5.1 of this paper;
- the charge-dependence of the efficiencies in the  $W \rightarrow e\nu$  measurement;
- the time-dependence of the efficiencies in the  $W \rightarrow e\nu$  measurement;
- the size of the dead regions in the EM calorimeter;
- the amount of pile-up considered in the simulation.

When comparing the measured efficiencies with MC predictions, uncertainties related to the composition of the T&P sample potentially also need to be considered. In the case of the  $J/\psi \rightarrow ee$  channel, the uncertainties on the **fraction of non-prompt  $J/\psi$  decays** [34] in the probe sample, which depend both on the kinematic bin and on the trigger conditions, are important. The uncertainties linked to the trigger, reconstruction and identification efficiencies of the non-prompt contribution are included. The effect of the modelling of the **mixture of triggers** used in the  $W \rightarrow e\nu$  and  $J/\psi \rightarrow ee$  channels was also studied. It is negligible in the  $W \rightarrow e\nu$  case.

Table 6 illustrates the main components of the measurement uncertainties on the efficiency of the *tight* electron identification cuts for a few typical  $E_T$ -bins and for

each channel. These uncertainties are somewhat larger than those for the *medium* cuts. The total uncertainties are computed as the quadratic sum of the statistical and the total systematic uncertainties. In the  $Z \rightarrow ee$  and  $J/\psi \rightarrow ee$  measurements, the total systematic uncertainty is obtained by adding linearly the closure test biases to the quadratic sum of all other components.

#### 6.2.4 Measured efficiencies

The efficiencies of the *medium* and *tight* electron identification cuts as a function of  $E_T$  and  $\eta$  are shown in Figures 15, 16 and 17, respectively, for the  $W \rightarrow e\nu$ ,  $Z \rightarrow ee$  and  $J/\psi \rightarrow ee$  channels. For the  $J/\psi \rightarrow ee$  channel, only the measurements in four bins of  $E_T$  are presented due to the limited statistics, especially in the endcaps. For the  $W \rightarrow e\nu$  and  $Z \rightarrow ee$  channels, the measured efficiencies are compared directly to those expected from the MC simulations, whereas, for the  $J/\psi \rightarrow ee$  channel, the measured efficiencies are compared to a weighted average of the efficiencies expected from prompt and non-prompt  $J/\psi$  production. As the *tight* cuts rely on tracking information, their performance is quite sensitive to interactions of electrons in the inner detector material. Their efficiency versus  $\eta$  is expected to be much less uniform than that of the *medium* cuts.

The observed differences between data and MC are discussed in terms of differences in electron identification variables in Subsection 6.2.5, in particular for the calorimeter shower shapes (used in the *medium* and *tight* selections) and for the ratio of high-threshold transition radiation hits to all hits in the TRT detector (used in the *tight* selection).

Overall, the  $\eta$  dependence of the identification efficiency is in good agreement between data and MC, with the most important deviations seen around the transition region between the barrel and endcap calorimeters. Larger differences are seen as a function of  $E_T$ , especially in the  $W \rightarrow e\nu$  measurement, where the efficiency appears to decrease more at low  $E_T$  for data than for MC. More data are needed to properly understand this result.

The  $E_T$ -dependence of the efficiencies in the case of the  $J/\psi \rightarrow ee$  measurements is in good agreement between data and MC. The shape can be attributed to the combination of the increasing contribution of non-isolated electrons from non-prompt  $J/\psi$  production (for which the efficiency decreases with  $E_T$  and is significantly lower at all  $E_T$  than for electrons from prompt  $J/\psi$  production) and to the rapidly improving efficiency for isolated electrons from prompt  $J/\psi$  production as  $E_T$  increases in this low- $E_T$  range.

To check the consistency of the measurements, the electron and positron identification efficiency from the  $W \rightarrow e\nu$  sample is compared, in Figure 18, for *medium* cuts as a function of  $E_T$  and for *tight* cuts as a function of  $\eta$ . Only statistical uncertainties are shown. The systematic uncertainties are in general significantly larger and correlated to some extent between the electron and positron measurements in the same  $E_T$ - or  $\eta$ -bin.

**Table 6.** Relative uncertainties (in %) on the measured efficiencies of the *tight* electron identification for  $W \rightarrow e\nu$ ,  $Z \rightarrow ee$  and  $J/\psi \rightarrow ee$  decays for a few typical  $E_T$  bins (integrated over the full  $\eta$ -range). For the  $J/\psi \rightarrow ee$  channel, the uncertainties affecting the MC prediction for the efficiency are also given.

$E_T$ range (GeV)	$W \rightarrow e\nu$			$Z \rightarrow ee$			$J/\psi \rightarrow ee$		
	15-20	20-25	35-40	20-25	40-45	4-7	7-15	20	
Statistics	3.0	1.7	0.3	3.5	0.9	2.5	9.9		
Background level	1.2	1.3	0.3	4.4	0.9	2.2	3.1		
Discriminating variable (nature, shape, range)	4.8	1.9	0.3	3.3	1.5	4.9	9.6		
Possible bias of background subtraction	3.7	0.6	0.1	1.7	1.8	3.6	3.1		
Total	7.1	3.1	0.5	8.0	3.6	9.3	16.5		
MC statistics							0.2	0.8	
Non-prompt $J/\psi$							5.2	7.7	
Trigger mixture							5.1	2.4	
MC total							7.3	8.1	

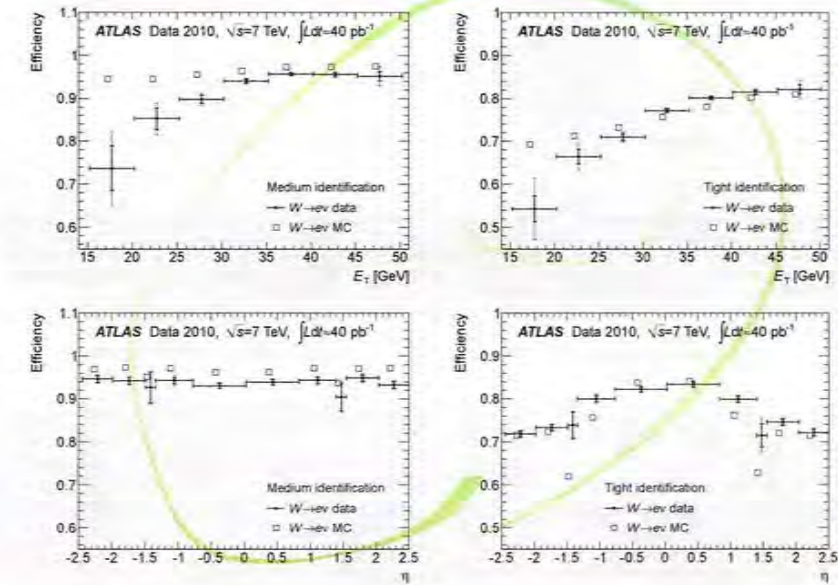


**Fig. 15.** Electron identification efficiencies measured from  $W \rightarrow e\nu$  events and predicted by MC for (left) medium and (right) tight identification as a function of  $E_T$  and integrated over  $|\eta| < 2.47$  excluding the transition region  $1.37 < |\eta| < 1.52$  and (bottom) of  $\eta$  and integrated over  $20 < E_T < 50$  GeV. The results for the data are shown with their statistical (inner error bars) and total (outer error bars) uncertainties. The statistical error on the MC efficiencies plotted as open squares is negligible. For clarity, the data and MC points are slightly displaced horizontally in opposite directions.

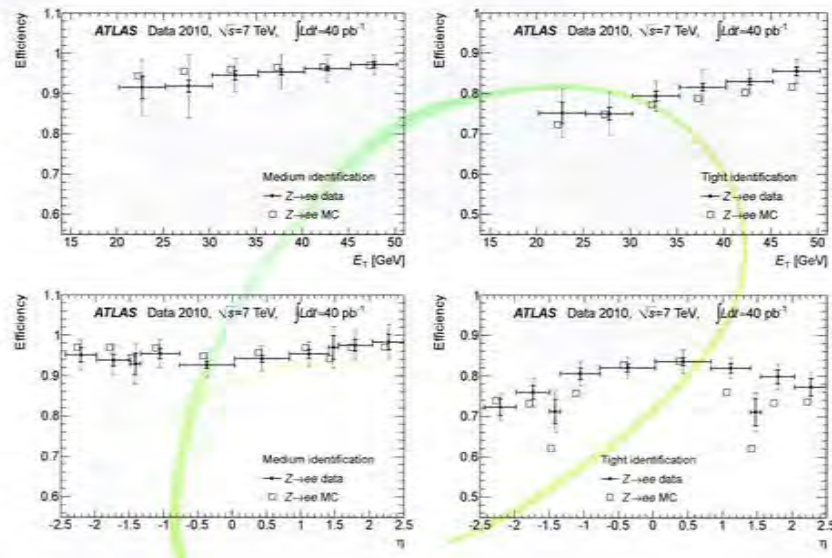


**Fig. 16.** Electron identification efficiencies measured from  $Z \rightarrow ee$  events and predicted by MC for (left) *medium* and (right) *tight* identification as a function (top) of  $E_T$  and integrated over  $|\eta| < 2.47$  excluding the transition region  $1.37 < |\eta| < 1.52$  and (bottom) of  $\eta$  and integrated over  $20 < E_T < 50$  GeV. The results for the data are shown with their statistical (inner error bars) and total (outer error bars) uncertainties. The statistical error on the MC efficiencies plotted as open squares is negligible. For clarity, the data and MC points are slightly displaced horizontally in opposite directions.

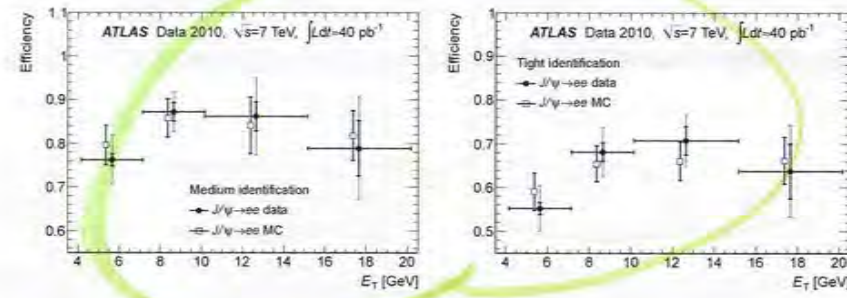


**Fig. 17.** Electron identification efficiencies measured from  $J/\psi \rightarrow ee$  events and predicted by MC for (left) *medium* and (right) *tight* identification as a function of  $E_T$  and integrated over  $|\eta| < 2.47$  excluding the transition region  $1.37 < |\eta| < 1.52$ . The results for the data are shown with their statistical (inner error bars) and total (outer error bars) uncertainties. The MC predictions are a weighted average of the efficiencies expected for prompt and non-prompt  $J/\psi$  production as explained in the text. The total error on the MC efficiencies plotted as open squares is also shown. For clarity, the data and MC points are slightly displaced horizontally in opposite directions.

The identification efficiency is expected to be higher for positrons than for electrons, since there are about 40% more positrons produced than electrons from  $W$  decays. Although the charge misidentification probability due to material effects is itself charge independent, the higher rate of  $W^+ \rightarrow e^+ \nu$  will induce more charge-misidentified probes in the electron sample than in the positron sample. The lower identification efficiency of these charge-misidentified electrons and positrons, also as a consequence of the material effects, leads to the expected difference in efficiency. This difference is estimated in MC simulation to be as large as 3% at high  $\eta$ -values where the amount of material is larger.

Since the dominant systematic uncertainties on the measurement arise from background subtraction and the number of events in the electron channel is smaller to start with, somewhat higher total uncertainties are observed in the measurements for electrons than for positrons. Small disagreements between data and MC in some  $\eta$ -bins indicate that there might be some contribution also from residual misalignment effects in the inner detector. The discrepancies observed in these few bins have, therefore, been added in quadrature to the total uncertainty for the charge-averaged measurements. It is expected that, with more data and improved inner-detector alignment constants, these discrepancies will be reduced.

The measurements for the  $J/\psi \rightarrow ee$  channel have also been repeated for the *medium* identification criteria for different ranges of the measured pseudo-proper time, defined as

$$\tau_0 = \frac{L_{xy} \cdot m}{p_T}, \quad (8)$$

where  $L_{xy}$  is the distance between the primary vertex and the extrapolated common vertex of the two electron candidates in the transverse plane,  $m$  is the reconstructed dielectron mass, and  $p_T$  is the reconstructed transverse momentum of the  $J/\psi$  candidate. Restricting the allowed pseudo-proper time to low (resp. high) values will improve the purity of the sample in terms of prompt (resp. non-prompt)  $J/\psi$  decays. The results of these measurements for the two highest statistics  $E_T$ -bins are compared in Figure 19 to the MC expectations for the weighted prompt plus non-prompt sample. The efficiencies expected for pure prompt and non-prompt  $J/\psi$  production are also shown. The efficiencies increase by several percent as the fraction of non-prompt decays decrease. The data show the same trend but more statistics are needed to measure clearly the variation of the efficiency with the fraction of decays from prompt  $J/\psi$  production in the data, and ultimately to separate the prompt and non-prompt  $J/\psi$  samples in the electron channel.

The  $W \rightarrow ee$  and  $Z \rightarrow ee$  samples cover very similar  $E_T$  and  $\eta$ -ranges, but they are not identical, so the one-dimensional identification efficiencies presented here are not expected to be exactly equal for a given bin in each channel. The measured identification efficiencies, integrated over  $\eta$  and for  $20 < E_T < 50$  GeV, are given in Table 7. Within their respective total uncertainties, the

departures from the expected MC efficiencies observed for  $W \rightarrow ee$  and  $Z \rightarrow ee$  decays are compatible.

In contrast, the overlap between the  $W \rightarrow ee$  and  $J/\psi \rightarrow ee$  samples is limited to the  $E_T$ -range between 15 and 20 GeV, a region in which both samples suffer from quite low statistics and from large systematic uncertainties of about 10%. Moreover, the  $J/\psi \rightarrow ee$  efficiency is the weighted average of prompt and non-prompt  $J/\psi$  decays, where only the former should be comparable to the electron efficiency obtained from  $W \rightarrow ee$  decays. As the  $\eta$ -distributions of the two samples are not as similar as those of electrons from  $W \rightarrow ee$  and  $Z \rightarrow ee$  decays, the measured and expected identification efficiencies and their ratios are compared in the 15 – 20 GeV  $E_T$ -bin in Table 8, but only over a limited  $\eta$ -range,  $|\eta| < 0.8$ . The MC efficiencies for  $W$  and prompt  $J/\psi$  production agree within a few percent. The measurement uncertainties are however still too large to draw firm conclusions.

### 6.2.5 Electron identification variables

The efficiencies measured in data and predicted by MC simulation presented in Figures 15, 16 and 17 manifest some marked differences. These differences are related to discrepancies in electron identification variables. In this section, the distributions of calorimeter shower shapes and of the high threshold hit fraction in the TRT are discussed.

**Shower-shape distributions** Lateral shower shapes in the EM calorimeter (listed in Table 1) play a crucial role in *medium* electron identification. They are extracted by the T/P method using  $Z \rightarrow ee$  events in bins of the probe  $E_T$ , with tag requirements and probe definition as described in Section 6.2. The residual background, which could distort the measured distributions, is removed on a statistical basis using the technique of Ref. [35]. The method assigns a weight to each event based on a likelihood fit to the  $m_{ee}$  distribution in the range of 40 – 180 GeV. These weights are then used to build the shape distributions. In order to obtain unbiased results, the correlations between the discriminating variable ( $m_{ee}$ ) and the extracted variables (shower shapes) need to be negligible. This was verified using MC simulation.

To obtain bin-by-bin systematic uncertainties on the extracted electron shower shapes, different models for the signal and background dielectron-mass distributions were investigated as in the efficiency measurement.

The background subtraction method was validated by a closure test performed on MC events by applying the same procedure as used for the data. For some distributions, the observed bias is of the same order as the systematic uncertainty due to the choice of fit functions. The total bin-by-bin systematic uncertainties are calculated as the sum of these two uncertainties and are  $E_T$  dependent. They amount to 1 – 5% in the  $E_T$ -bin 25 – 30 GeV, and to 1 – 3% in the bin 40 – 50 GeV, depending on the shape variable. With the 2010 dataset, the total uncertainty is dominated by the statistical uncertainty.

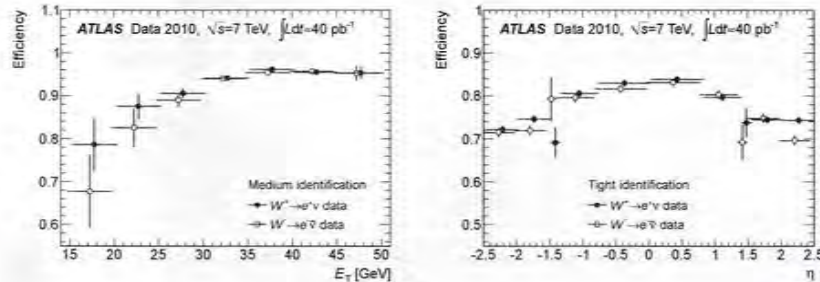


**Fig. 18.** Electron identification efficiencies measured separately for positrons (full circles) and electrons (open circles) from  $W \rightarrow ee$  events (left) for *medium* identification as a function of  $E_T$  and integrated over  $|\eta| < 2.47$  excluding the transition region  $1.37 < |\eta| < 1.52$  and (right) for *tight* identification as a function of  $\eta$  and integrated over  $20 < E_T < 50$  GeV. The results are shown with statistical uncertainties only. For clarity, the electron and positron data points are slightly displaced horizontally in opposite directions.

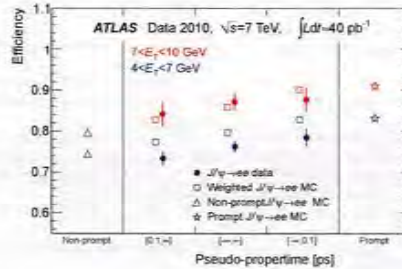


**Fig. 19.** Electron identification efficiencies measured from  $J/\psi \rightarrow ee$  events and predicted by MC for *medium* identification for two  $E_T$  ranges:  $4 < E_T < 7$  GeV (lower points) and  $7 < E_T < 10$  GeV (higher points) for different ranges of pseudo-proper time. The left-most open triangles show the MC efficiencies for a pure non-prompt  $J/\psi$  sample, while the right-most open stars show them for a pure prompt  $J/\psi$  sample integrated over all pseudo-proper time values. The MC predictions plotted as open squares in the middle are weighted averages of the efficiency values expected for prompt and non-prompt  $J/\psi$  production as explained in the text. The results for the data are shown with statistical uncertainties only. For clarity, the data and MC points are slightly displaced horizontally in opposite directions.

**Table 7.** *Medium* and *tight* identification efficiencies (in %) measured in the  $W \rightarrow ee$  and  $Z \rightarrow ee$  channels, integrated over  $|\eta| < 2.47$  excluding the transition region between barrel and endcap EM calorimeters at  $1.37 < |\eta| < 1.52$  and over  $20 < E_T < 50$  GeV. The measured data efficiencies are given together with the expected efficiencies from MC simulation and with their ratios. For the data measurements and for the ratios, the first error corresponds to the statistical uncertainty and the second to the systematic uncertainty. For the MC expectations, the statistical uncertainties are negligible.

Selection	Channel	Data [%]	MC [%]	Ratio
Medium	$W \rightarrow ee$	$94.1 \pm 0.2 \pm 0.6$	96.9	$0.971 \pm 0.002 \pm 0.007$
	$Z \rightarrow ee$	$94.7 \pm 0.4 \pm 1.5$	96.3	$0.984 \pm 0.004 \pm 0.015$
Tight	$W \rightarrow ee$	$78.1 \pm 0.2 \pm 0.6$	77.5	$1.009 \pm 0.003 \pm 0.007$
	$Z \rightarrow ee$	$80.7 \pm 0.5 \pm 1.5$	78.5	$1.028 \pm 0.006 \pm 0.016$

Wishful new  
0.942  
0.785

**Table 8.** *Medium* and *tight* identification efficiencies (in %) measured in the  $W \rightarrow ee$  and  $J/\psi \rightarrow ee$  channels, integrated over  $|\eta| < 0.8$  and  $15 < E_T < 20$  GeV. The measured data efficiencies are given together with the expected efficiencies from MC simulation and their ratios. The MC efficiencies for the  $J/\psi \rightarrow ee$  channel are obtained as a weighted average of the expected prompt and non-prompt components (see text). For completeness, the expected MC efficiencies for a pure sample of  $J/\psi \rightarrow ee$  decays from prompt  $J/\psi$  production are also given. For the data measurements and for the ratios, the first error corresponds to the statistical uncertainty and the second to the systematic uncertainty. For the MC expectations, the statistical uncertainties are negligible.

Selection	Channel	Data [%]	MC [%]	Ratio	MC [%] prompt $J/\psi$
Medium	$W \rightarrow ee$	$75.8 \pm 8.8 \pm 8.1$	94.9	$0.80 \pm 0.09 \pm 0.07$	
	$J/\psi \rightarrow ee$	$80.0 \pm 7.3 \pm 10.2$	81.9	$0.98 \pm 0.09 \pm 0.14$	92.9
Tight	$W \rightarrow ee$	$61.9 \pm 6.0 \pm 7.0$	78.3	$0.79 \pm 0.08 \pm 0.09$	
	$J/\psi \rightarrow ee$	$68.1 \pm 7.3 \pm 9.0$	69.1	$0.99 \pm 0.11 \pm 0.15$	78.3

97.8  
64.3

The extracted electron shower shapes from data are compared to the MC prediction in Figure 20. There are significant differences visible for all extracted variables. The distributions of the strip and middle layer shapes are wider and are also shifted in data towards the background region. As a result, somewhat lower *medium* efficiencies are observed in data compared to MC. Currently, work is ongoing to refine the calorimeter simulation to achieve a better description of the shower shape distributions.

### 6.3 Electron identification efficiency in the forward region

The efficiency of electron identification in the forward region outside the tracking acceptance is studied using  $Z \rightarrow ee$  events, in two bins of pseudorapidity:  $2.5 < |\eta| < 3.2$  corresponding to EMEC-IW and  $3.2 < |\eta| < 4.9$  corresponding to the FCAL detectors.

#### 6.3.1 Probe selection and background subtraction

The tag electron is required to be a *central tight* electron with  $E_T > 25$  GeV and  $|\eta| < 2.47$  excluding the transition region  $1.37 < |\eta| < 1.52$ , while the probe is a *forward* electron candidate with  $E_T > 20$  GeV and  $2.5 < |\eta| < 4.9$ . With this selection, a total of 5469 pairs in the  $m_{ee}$  range 59–124 GeV are found in the EMEC-IW, while 3429 pairs are found in the range 50–160 GeV in the FCAL.

The background is subtracted using an unbinned maximum likelihood fit to the dielectron invariant mass. The same methodology is used as in Subsection 6.2. The signal is modelled either by a Breit-Wigner convolved with a Crystal Ball function or by a MC template. The background is described either by a template from data requiring that the pair fails certain selection cuts or by different analytical functions.

**High threshold TRT hits** The *tight* identification cuts listed in Table 1 rely on more stringent matching cuts between the inner detector and EM calorimeter measurements and on additional measurements in the inner detector. In particular, an advantage of the ATLAS detector is the capability of the TRT to discriminate against hadronic fakes over  $|\eta| < 2.0$  using information on the ratio of high threshold transition radiation hits over all hits ( $f_{HTR}$ ).

Figure 21 shows the  $f_{HTR}$  distribution in two  $\eta$ -regions for electron candidates from  $Z \rightarrow ee$  decays, selected by a T&P analysis and having momenta in the range 10–100 GeV, where the probability for producing high-threshold hits (HT) from transition radiation (TR) in the TR straws is uniform. This probability is in the range of 0.2–0.25, to be compared with about 0.05 for pion candidates in the same momentum range [36].

The HT probability for electrons varies with the radiator type, therefore it is expected to be different in the barrel and endcap regions. It also depends on the varying incidence angle of the charged particles on the straws. The observed HT probability as a function of  $\eta$  is not modelled perfectly in the barrel TRT by the MC simulation, but the largest effect is the higher than predicted HT probability in the TR endcap wheels. For  $|\eta| > 1.0$ , the HT probability in data is measured to be significantly higher than in MC, resulting in a better than expected electron identification performance.

#### 6.3.2 Results

Table 9 presents the measured and expected efficiency values. The electron identification efficiency in the forward region is not perfectly reproduced by MC. This can be

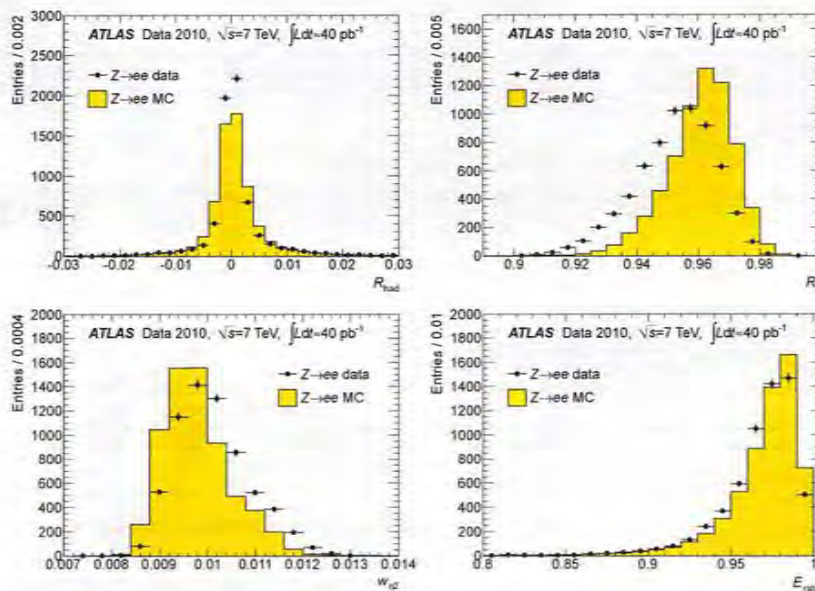


Fig. 20. Electron shower shapes from  $Z \rightarrow ee$  events for probe electrons in the range  $E_T = 40 - 50$  GeV: (top left)  $R_{\text{had}}$  hadronic leakage, (top right)  $R_\eta$  and (bottom left)  $w_{92}$  middle-layer variables, (bottom right)  $E_{\text{ratio}}$  strip-layer variable. The data points are plotted as full circles with error bars, representing the total statistical and systematic uncertainties. The MC predictions, normalised to the number of data entries, are shown by filled histograms.

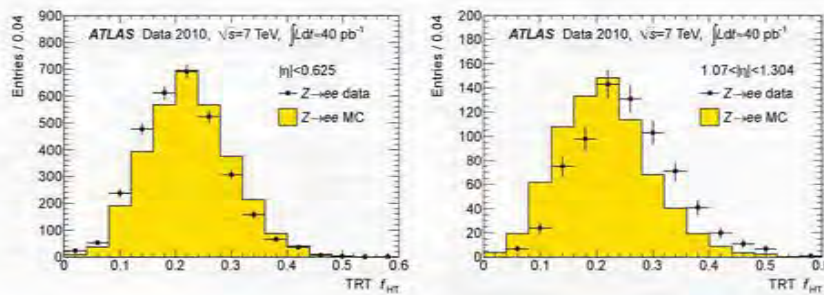


Fig. 21. Distributions of the fraction of high-threshold hits in the TRT measured from  $Z \rightarrow ee$  data and compared to MC prediction for (left)  $|\eta| < 0.625$  and (right)  $1.07 < |\eta| < 1.304$ . The data points are plotted as full circles with statistical error bars, while the MC predictions, normalised to the number of data entries, are shown as filled histograms.

Table 9. Identification efficiencies (%) in the forward region measured from  $Z \rightarrow ee$  events integrated over  $E_T > 20$  GeV and over  $2.5 < |\eta| < 3.2$  for EMEC-IW and over  $3.2 < |\eta| < 4.9$  for FCal. The measured data efficiencies are given together with the expected efficiencies from MC simulation and with their ratios. For the data measurements and for the ratios, the first error corresponds to the statistical and the second to the systematic uncertainty. For the MC expectations, the statistical uncertainties are about 0.1%.

Detector	Selection	Data [%]	MC [%]	Ratio
EMEC-IW	Forward loose	$83.1 \pm 1.3 \pm 4.6$	90.7	$0.916 \pm 0.014 \pm 0.051$
	Forward tight	$58.2 \pm 1.4 \pm 3.6$	72.8	$0.800 \pm 0.019 \pm 0.050$
FCal	Forward loose	$87.5 \pm 2.6 \pm 7.2$	89.0	$0.983 \pm 0.029 \pm 0.081$
	Forward tight	$53.2 \pm 2.3 \pm 4.3$	59.4	$0.896 \pm 0.038 \pm 0.072$

explained by the observation that the showers are broader and longer in data. The origin of these discrepancies is under investigation.

#### 6.4 Reconstruction efficiency of central electrons

In this section, the electron reconstruction efficiencies are studied with respect to sliding-window clusters in the EM calorimeter using  $Z \rightarrow ee$  decays following the methodology of Subsection 6.2. The reconstruction efficiency defined this way measures the combined electron track reconstruction and track-cluster matching efficiencies.

##### 6.4.1 Probe selection and background subtraction

To measure the electron reconstruction efficiency with or without the additional requirements on the number of silicon hits on the associated track introduced in Subsection 6.2.1, the requirements on the probe electron are released to consider all sliding-window EM clusters. Using *tight tag* electrons having  $E_T = 20 - 50$  GeV, this leads to almost 20000 probes, with 500 – 4000 per pseudorapidity bin. The S/B ratio in the dielectron mass range  $80 < m_{ee} < 100$  GeV varies from about 1 (for *medium* tags) to 6 – 10 (for *tight isolated* tags).

As for the identification efficiency measurement, the average of measurements, made with different configurations of the background level and the size of the signal window in the dielectron mass, was used to assess the reconstruction efficiencies. In particular, *medium* or *tight* tags, with or without track or cluster isolation requirements, and with or without a cut on the transverse impact parameter significance, and five different integration ranges are considered. The root mean square of these 80 measurements is assigned as the systematic error on the reconstruction efficiency due to the stability of the background estimation on data.

The potential biases of the background subtraction method were also studied in a MC closure test. The best closure was achieved using an exponential shape to describe the background and a Breit-Wigner convolved with a Crystal Ball function (to account for detector effects) to model the signal. The difference between the efficiency estimated using such a fit and the true efficiency is considered as an additional systematic uncertainty. The largest

bias found in any  $\eta$  bin is taken for all bins. It amounts to 1.5% (0.5%) when the requirements on silicon hits on the track are (not) required.

##### 6.4.2 Results and pseudorapidity dependence

The measured reconstruction efficiency in data, shown in Figure 22, is compatible with the MC predictions, though slightly higher values are observed in data, especially in the region  $0.8 < |\eta| < 2.01$  when requirements on the numbers of silicon hits on the track are applied. The globally averaged efficiencies in the full pseudorapidity range of  $|\eta| < 2.47$  are given in Table 10. The efficiency loss due to requirements on the numbers of silicon hits is smaller than 3% in the barrel and reaches almost 10% in the highest  $|\eta|$  bins.

The results for the data are shown with their statistical (inner error bars) and total (outer error bars) uncertainties. The statistical error on the MC efficiencies is negligible.

#### 6.5 Charge misidentification probability

Mismeasurement of the charge happens primarily when the electron interacts early in the detector and the EM shower produces several high  $p_T$  tracks. The primary track is then either not available or a different subsequent track is matched to the EM cluster. The charge misidentification probability,  $\epsilon_{\text{Qmisd}}$ , is defined as the fraction of electrons with incorrectly measured charge with respect to all electrons, and depends on the applied electron identification cuts. In particular, track quality cuts decrease  $\epsilon_{\text{Qmisd}}$  significantly.

In this study  $\epsilon_{\text{Qmisd}}$  is investigated comparing same-sign pairs to all (same-sign and opposite-sign) pairs in  $Z \rightarrow ee$  events at four levels of electron identification: reconstruction, silicon hit requirements on the track as defined in Subsection 6.2.1, and the standard *medium* and *tight* selections.

##### 6.5.1 Probe selection and background subtraction

To ensure a well measured tag electron charge, the tag is confined to the barrel region of  $|\eta| < 1.37$ . No correction is applied for the misidentification of the *tight* central

**Table 10.** Efficiency (in %) for electron reconstruction only and with requirements on the number of silicon hits on the track, measured from  $Z \rightarrow ee$  events, integrated over  $20 < E_T < 50$  GeV and over  $|\eta| < 2.47$ , excluding the transition region between barrel and endcap EM calorimeters at  $1.37 < |\eta| < 1.52$ . The measured data efficiencies are given together with the expected efficiencies from MC simulation and with their ratios. For the data measurements and for the ratios, the first error corresponds to the statistical uncertainty and the second one to the systematic uncertainty. For the MC expectations, the statistical uncertainties are negligible.

Selection	Data [%]	MC [%]	Ratio
Electron reconstruction	$98.7 \pm 0.1 \pm 0.2$	98.3	$1.005 \pm 0.001 \pm 0.002$
Track silicon hit requirements	$94.3 \pm 0.2 \pm 0.8$	93.1	$1.013 \pm 0.002 \pm 0.008$

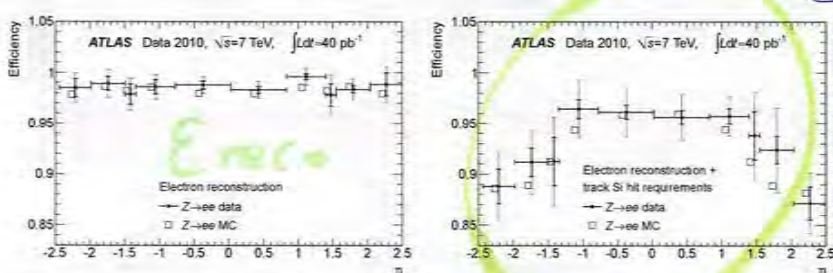


**Fig. 22.** Reconstruction efficiency measured from  $Z \rightarrow ee$  events and predicted by MC as a function of the cluster pseudorapidity and integrated over  $20 < E_T < 50$  GeV (left) for electron reconstruction only and (right) after applying requirements on the number of silicon hits on the track. The results for the data are shown with their statistical (inner error bars) and total (outer error bars) uncertainties. The statistical error on the MC efficiencies plotted as open squares is negligible. For clarity, the data and MC points are slightly displaced horizontally in opposite directions.

tag electron. This increases the measured probability with respect to the “true” value by about 0.2%.

The selection of same-sign pairs favours background over signal. This is especially problematic when studying  $\epsilon_{\text{QmisID}}$  at early stages of electron identification. Additional requirements beyond the standard  $Z \rightarrow ee$  selection described in Subsection 6.2.1 are necessary. To extract the central value for  $\epsilon_{\text{QmisID}}$ , a low missing transverse momentum of  $E_T^{\text{miss}} < 25$  GeV is required, reducing significantly the  $W \rightarrow ee$  background. To assess the systematic uncertainty due to background contamination, four other variants of the selection were studied with different requirements on  $E_T^{\text{miss}}$ , calorimeter isolation and the tag  $E_T$ . With the standard  $Z \rightarrow ee$  selection, about 1000 probes are found, with a S/B ratio of 0.34, in the same-sign sample at the reconstruction level in the full pseudorapidity range. Applying the  $E_T^{\text{miss}}$  and calorimeter isolation cuts, the S/B ratio improves to 0.74 but the number of probes drops to 550. The available statistics is much more limited at *medium* (100–140 same-sign pairs) and *tight* (about 40 same-sign pairs) identification levels, where S/B = 5.5–8 is achieved.

The remaining background is subtracted by a template method at early identification stages where the available statistics is sufficient, and by a side-band method at the *medium* and *tight* identification levels. For the

fit, the background template is derived from data events where the tag electron candidate fires an EM trigger (with no trigger-level electron identification) but fails both the *medium* offline selection and the isolation cut. The signal template is obtained from  $Z \rightarrow ee$  MC. The number of signal events is counted within  $75 < m_{ee} < 100$  GeV.

The systematic uncertainties are estimated by varying the tag requirements, the signal and background templates (or the side-bands), and the  $m_{ee}$  signal window, in a way similar to that described in Subsection 6.2.

### 6.5.2 Results and pseudorapidity dependence

The results for globally averaged charge misidentification probabilities are summarised in Table 11. Overall the data-MC agreement is good. The measurement in the data tends to be slightly lower than the MC prediction.

The same techniques are applied in bins of electron probe pseudorapidity. The results are displayed in Figure 23 at the two extreme levels of selection: after electron reconstruction only and after *tight* identification.

The measurements are repeated separately for the cases of positive (negative) tag electrons, measuring  $\epsilon_{\text{QmisID}}$  predominantly for true negative (positive) probes.

**Table 11.** Charge misidentification probabilities (in %) at different levels of electron identification from  $Z \rightarrow ee$  events, integrated over  $|\eta| < 2.47$  excluding the transition region between barrel and endcap EM calorimeters at  $1.37 < |\eta| < 1.52$  and over  $E_T > 20$  GeV. The measured data efficiencies are given together with the expected efficiencies from MC simulation. For the data measurements, the first error corresponds to the statistical uncertainty and the second one to the systematic uncertainty. For the MC expectations, the statistical uncertainties are negligible.

Selection	Data [%]	MC [%]
Electron reconstruction	$2.17 \pm 0.25 \pm 0.28$	2.73
Track silicon hit requirements	$1.13 \pm 0.21 \pm 0.16$	1.28
Medium identification	$1.04 \pm 0.11 \pm 0.14$	1.20
Tight identification	$0.37 \pm 0.07 \pm 0.11$	0.50

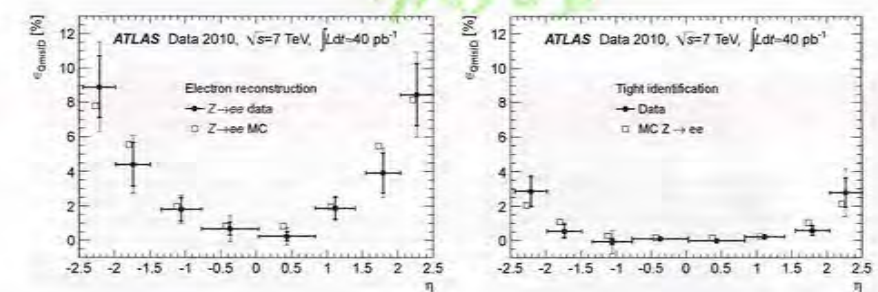


**Fig. 23.** Electron charge misidentification probability measured from  $Z \rightarrow ee$  events as a function of pseudorapidity and integrated over  $E_T > 20$  GeV (left) after electron reconstruction and (right) after *tight* selection. Data points are shown with statistical (inner error bars) and total uncertainties (outer error bars). The MC expectation is indicated by open squares. For clarity, the data and MC points are slightly displaced horizontally in opposite directions.

The results for the different charges agree within uncertainties.

These measurements, even if limited in precision, do not show any significant difference between the charge misidentification probability in data and MC. An  $\epsilon_{\text{QmisID}}$  of about 0.5% is observed in the barrel and up to 8% at high  $\eta$  for candidates at the reconstruction level. The measured probability decreases to about 0.2% in the barrel and around 2% in the endcaps after *tight* identification cuts.

### 6.6 Electron trigger efficiency

The trigger efficiency is defined as the fraction of identified offline electrons that fire a given trigger. Here, the *medium* and *tight* selections are considered as offline benchmarks, for which the most commonly used triggers were designed to have close to 100% efficiency in the plateau  $E_T$ -region, starting typically about 5 GeV above the trigger threshold. The main sources of inefficiency are readout problems of the L1 system, lower reconstruction efficiency (especially for tracking) at trigger level due to timing con-

straints, and small differences of the electron identification variables between trigger and offline [12,13].

In 2010, events with high- $p_T$  electrons were primarily selected by the *e15\_medium* and *e20\_loose* triggers, which require an electron candidate reconstructed at the event filter (EF) level with  $E_T > 15$  and 20 GeV passing the *medium* and *loose* identification cuts, respectively. In this section, their efficiency measurements using  $W \rightarrow ee$  and  $Z \rightarrow ee$  decays are reported.

#### 6.6.1 Probe selection

To measure the trigger efficiency, electron probes in the range  $E_T > 15$  GeV are checked for a match to an EF electron fulfilling the trigger selection. The angular distance  $\Delta R$  between the trigger and offline electron candidates is computed using the tracking variables. It is required to be smaller than 0.15. This loose cut results in a 100% matching efficiency. Note that, while all three levels of the trigger have to be implicitly satisfied, no particular matching is required between the offline electron and L1 or L2 trigger objects.

$W \rightarrow e\nu$  and  $Z \rightarrow ee$  candidates are selected following Subsection 6.2. The *medium* or *tight* requirement on the probe electron candidate increases significantly the purity of the sample. For example, in the  $Z \rightarrow ee$  channel the background fraction of *tight-medium* pairs is below 1%. Therefore, no background subtraction is applied when obtaining the central values of the trigger efficiency measurements.

Systematic uncertainties due to the tag requirements, the  $m_{ee}$  requirement in the probe definition for the  $Z \rightarrow ee$  channel, the background contamination, the energy-scale uncertainty and the trigger-offline matching requirement have been studied and found to be less than 0.1% in total.

### 6.6.2 Results and $E_T$ dependence

Figure 24 shows the trigger efficiency as a function of the offline  $E_T$  of *tight* probe electrons for the e15\_medium and e20\_loose triggers. As expected, both triggers are very efficient in the plateau region starting 5 GeV above the trigger threshold.

The integrated efficiencies in the plateau region are summarized in Table 12 together with the data/MC efficiency ratios. As correctly predicted by the MC, the trigger efficiency is slightly higher with respect to the offline *tight* selection than to the *medium* one. This is mainly due to the  $E/p$  cut present in the *tight* selection: it rejects electrons with a large amount of bremsstrahlung radiation which are less efficiently reconstructed by the fast L2 tracking algorithm. The  $W$  and  $Z$  results are compatible for all four trigger-offline selection combinations.

The small difference in the trigger efficiency behaviour between data and MC could be explained by the presence of dead L1 trigger towers,<sup>7</sup> not simulated in MC (typically well below the per mille level), differences at the few % level in the electron energy-scale calibration introduced by the offline data reprocessing, and differences in the distribution of identification variables between data and MC as discussed in Subsection 6.2.5.

## 7 Conclusions

The performance of the ATLAS detector for electrons in 2010 was presented, using  $W \rightarrow e\nu$ ,  $Z \rightarrow ee$  and  $J/\psi \rightarrow ee$  decays in  $pp$  collision data.

An inter-alignment of the inner detector and the EM calorimeter has been performed and resulted in a track-cluster matching accuracy close to the MC expectation. Further improvements are in progress, in particular for  $\phi$  in the endcap regions covering  $1.52 < |\eta| < 2.47$ .

The electron energy scale has been determined in bins of pseudorapidity with a precision of 0.3–1.6% in the central region over  $|\eta| < 2.47$  and 2–3% in the forward regions over  $2.5 < |\eta| < 4.9$ , with a residual non-uniformity in  $\phi$  below 1% in the central region. After applying the

2010 in-situ calibration, the constant term of the energy resolution is measured to be  $(1.2 \pm 0.1(\text{stat}) \pm 0.3(\text{syst}))\%$  in the barrel EM calorimeter covering  $|\eta| < 1.37$ , increasing to 1.8% in the endcaps and to about 3% in the forward regions. With the additional statistics being collected in 2011, the energy-scale will be determined in  $(\eta, \phi)$  bins and the knowledge of the material in front of the calorimeter will be improved. The EM calorimeter constant term should therefore be determined more accurately and should decrease towards its design value of 0.7%.

Precise measurements as a function of  $\eta$  and  $E_T$  have been performed for a variety of components of the electron selection efficiency in the central region over  $|\eta| < 2.47$ . The electron identification efficiency has been measured with a total accuracy better than 1% for the highest-statistics bin of  $E_T = 35–40$  GeV using  $W \rightarrow e\nu$  events, and to about 10% for the lowest-statistics bin of  $E_T = 15–20$  GeV using  $W \rightarrow e\nu$  and  $J/\psi \rightarrow ee$  events.

The differences between calorimeter shower shapes measured in data and predicted by MC have been an ongoing topic of study since the first runs collecting cosmic-ray events [37,38]. These are now precisely measured for  $|\eta| < 2.47$  using the  $Z \rightarrow ee$  channel which allows to extract unbiased distributions for the electron probes.

Other important components of the electron selection efficiency have been determined with good accuracy in the  $Z \rightarrow ee$  channel, even though they are more difficult to extract: the electron reconstruction efficiency, the efficiency of the track silicon hit requirements, and the probability of electron charge misidentification. The trigger efficiency measurements have established very high plateau efficiencies of the electron triggers used in 2010.

In the forward region over  $2.5 < |\eta| < 4.9$ , despite the difficulty of the measurements without any tracking information and with non-optimal EM calorimeter measurements, the clear signal observed from  $Z \rightarrow ee$  decays has been used to also measure the electron identification efficiencies with reasonable accuracy. The disagreements between data and MC are found to be larger in this region.

In parallel, work is ongoing to measure precisely the material in the detector and to refine the description of the detector material, the simulation of the EM shower development in the calorimeter, and the transition radiation production in the TRT. This will ultimately improve the description of the data by the MC.

The accuracy of all efficiency measurements will benefit from the much larger statistics available in 2011. Two-dimensional measurements in  $(E_T, \eta)$  space with finer  $\eta$  granularity will be obtained with accuracies better than 1%, allowing a more precise identification of the sources of the different  $E_T$ -dependence of the efficiencies in data and MC.

In the low- $E_T$  range, the  $J/\psi \rightarrow ee$  measurements require a substantial increase in statistics to measure the reconstruction and identification efficiencies in the low- $E_T$  region, important for Higgs-boson searches. In this region, the material effects are large, the energies are closer to the

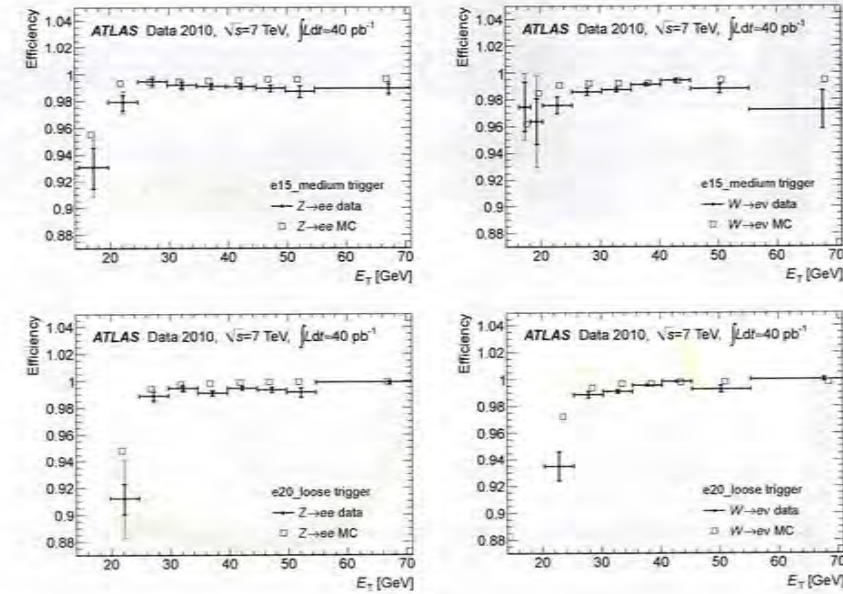


Fig. 24. Efficiency with respect to offline *tight* electrons for (top) e15\_medium and (bottom) e20\_loose triggers measured from (left)  $Z \rightarrow ee$  and (right)  $W \rightarrow ee$  events as a function of the offline electron  $E_T$  and integrated over  $|\eta| < 2.47$  excluding the transition region between the barrel and endcap EM calorimeters. The results for the data are shown with their statistical (inner error bars) and total (outer error bars) uncertainties. The statistical error on the MC efficiencies plotted as open squares is negligible. For clarity, the data and MC points are slightly displaced horizontally in opposite directions.

Table 12. Efficiency (in %) for the e15\_medium (e20\_loose) trigger measured from  $W \rightarrow e\nu$  and  $Z \rightarrow ee$  events, integrated over  $|\eta| < 2.47$  excluding the transition region between barrel and endcap EM calorimeters at  $1.37 < |\eta| < 1.52$  and over  $E_T > 20$  (25) GeV. The measured data efficiencies are given together with the expected efficiencies from MC simulation and with their ratios. For the data measurements and for the ratios, the error corresponds to the statistical uncertainty. The systematic errors are below 0.1%. For the MC expectations, the statistical uncertainties are negligible.

Trigger	Probe	Channel	Data [%]	MC [%]	Ratio
e15_medium	Offline medium	$W \rightarrow e\nu$	$98.48 \pm 0.08$	$98.76$	$0.997 \pm 0.001$
		$Z \rightarrow ee$	$98.67 \pm 0.10$	$99.24$	$0.994 \pm 0.001$
	Offline tight	$W \rightarrow e\nu$	$98.96 \pm 0.07$	$99.30$	$0.997 \pm 0.001$
		$Z \rightarrow ee$	$99.02 \pm 0.09$	$99.54$	$0.995 \pm 0.001$
e20_loose	Offline medium	$W \rightarrow e\nu$	$99.28 \pm 0.05$	$99.52$	$0.998 \pm 0.001$
		$Z \rightarrow ee$	$99.11 \pm 0.08$	$99.73$	$0.994 \pm 0.001$
	Offline tight	$W \rightarrow e\nu$	$99.42 \pm 0.05$	$99.69$	$0.997 \pm 0.001$
		$Z \rightarrow ee$	$99.33 \pm 0.08$	$99.83$	$0.995 \pm 0.001$

<sup>7</sup> These dead L1 trigger towers were repaired in the 2010–2011 LHC winter shutdown.

reconstruction threshold, and the identification cuts are stringent.

In the high- $E_T$  range, above that explored in this paper, much higher statistics of  $W \rightarrow e\nu$  and  $Z \rightarrow ee$  decays are required to extend the measurements to a region important for exotic searches where the efficiencies are expected to become asymptotically flat with  $E_T$ .

Overall, the performance of the ATLAS inner detector and EM calorimeters has been firmly established using the limited electron statistics from  $W$ ,  $Z$  and  $J/\psi$  decays obtained in 2010 at  $\sqrt{s} = 7$  TeV corresponding to about  $40\text{ pb}^{-1}$ . The agreement between the measurements in data and the predictions of the MC is generally good, leading to only small corrections of the MC electron performance estimates in physics analyses.

## 8 Acknowledgements

We thank CERN for the very successful operation of the LHC, as well as the support staff from our institutions without whom ATLAS could not be operated efficiently.

We acknowledge the support of ANPCyT, Argentina; YerPhI, Armenia; ARC, Australia; BMWF, Austria; ANAS, Azerbaijan; SSTC, Belarus; CNPq and FAPESP, Brazil; NSERC, NRC and CFI, Canada; CERN; CONICYT, Chile; CAS, MOST and NSFC, China; COLCIENCIAS, Colombia; MDM, CR, MPO, CR and VSC, CR, Czech Republic; DNRF, DNSRC and Lundbeck Foundation, Denmark; ARTEMIS, European Union; IN2P3-CNRS, CEA-DSM/IRFU, France; GNAS, Georgia; BMBF, DFG, HGF, MPG and AvH Foundation, Germany; GSRT, Greece; IFE, MINERVA, GIF, DIP and Benoziyo Center, Israel; INFN, Italy; MEXT and JSPS, Japan; CNRST, Morocco; FOM and NWO, Netherlands; RCN, Norway; MNiSW, Poland; GRICES and FCT, Portugal; MEROY (MECTS), Romania; MES of Russia and ROSATOM, Russian Federation; JINR, MSTD, Serbia; MSSR, Slovakia; ARRS and MVZT, Slovenia; DST/NRF, South Africa; MICINN, Spain; SRC and Wallenberg Foundation, Sweden; SER, SNSF and Cantons of Bern and Geneva, Switzerland; NSC, Taiwan; TAEK, Turkey; STFC, the Royal Society and Leverhulme Trust, United Kingdom; DOE and NSF, United States of America.

The crucial computing support from all WLCG partners is acknowledged gratefully, in particular from CERN and the ATLAS Tier-1 facilities at TRIUMF (Canada), NDGF (Denmark, Norway, Sweden), CC-IN2P3 (France), KIT/GridKA (Germany), INFN-CNAF (Italy), NL-T1 (Netherlands), PIC (Spain), ASGC (Taiwan), RAL (UK) and BNL (USA) and in the Tier-2 facilities worldwide.

## References

1. The ATLAS Collaboration, *The ATLAS Experiment at the CERN Large Hadron Collider*, JINST 3 (2008) S08003.
2. The ATLAS Collaboration, *Expected performance of the ATLAS experiment : detector, trigger and physics*, CERN-OPEN-2008-20, arXiv:0801.0512 [hep-ex].
3. T. Sjöstrand, S. Mrenna, and P. Z. Skands, *Pythia 6.4 Physics and Manual*, JHEP 0805 (2008) 026, arXiv:hep-ph/0603175.
4. The ATLAS Collaboration, *The ATLAS Simulation Infrastructure*, Eur. Phys. J. C70 (2010) 823–874, arXiv:1005.4563 [physics.ins-det].
5. S. Agostinelli et al., *CERNlib: A simulation toolkit*, Nucl. Instrum. Meth. A506 (2003) 250–303.
6. The ATLAS Collaboration, *Charged-particle multiplicities in pp interactions at  $\sqrt{s} = 900$  GeV measured with the ATLAS detector at the LHC*, Phys. Lett. B688 (2010) 21–42, arXiv:1003.3128 [hep-ex].
7. The ATLAS Collaboration, *Charged-particle multiplicities in pp interactions measured with the ATLAS detector at the LHC*, New J. Phys. 13 (2011) 053033, arXiv:1012.5104 [hep-ex].
8. The ATLAS Collaboration, *Study of the Material Budget in the ATLAS Inner Detector with  $K_S^0$  decay in collision data at  $\sqrt{s} = 900$  GeV*, ATLAS-CONF-2010-019.
9. The ATLAS Collaboration, *A measurement of the material in the ATLAS inner detector using secondary hadronic interactions*, JINST 7 (2012) P01033, arXiv:1110.6194 [hep-ex].
10. The ATLAS Collaboration, *Photon conversion at  $\sqrt{s} = 900$  GeV measured with the ATLAS detector*, ATLAS-CONF-2010-007.
11. The ATLAS Collaboration, *Probing the material in front of the ATLAS electromagnetic calorimeter with energy flow from  $\sqrt{s} = 7$  TeV minimum bias events*, ATLAS-CONF-2010-037.
12. The ATLAS Collaboration, *Performance of the ATLAS Trigger System in 2010*, Eur. Phys. J. C72 (2012) 1849, arXiv:1110.1530 [hep-ex].
13. The ATLAS Collaboration, *Performance of the Electron and Photon Trigger in p-p Collisions at  $\sqrt{s} = 7$  TeV with the ATLAS Detector at the LHC*, ATLAS-CONF-2011-114.
14. ATLAS Collaboration, *Expected electron performance in the ATLAS experiment*, ATL-PHYS-PUB-2011-006.
15. W. Lampl et al., *Calorimeter Clustering Algorithms : Description and Performance*, ATL-LARG-PUB-2008-002.
16. The ATLAS Collaboration, *Readiness of the ATLAS Liquid Argon Calorimeter for LHC Collisions*, Eur. Phys. J. C70 (2010) 723–753, arXiv:0912.2642 [physics.ins-det].
17. The ATLAS Collaboration, *Expected photon performance in the ATLAS experiment*, ATL-PHYS-PUB-2011-007.
18. The ATLAS Collaboration, *ATLAS detector and physics performance: Technical Design Report, Vol. 1*, Technical Design Report ATLAS, CERN, Geneva, 1999, CERN/LHCC 99-14, ATLAS TDR 14.
19. M. Aharrouche et al., *Energy linearity and resolution of the ATLAS electromagnetic barrel calorimeter in an electron test-beam*, Nucl. Instrum. Meth. A568 (2006) 601–623, arXiv:physics/0508012.
20. J. Colas et al., *Response Uniformity of the ATLAS Liquid Argon Electromagnetic Calorimeter*, Nucl. Instrum. Meth. A568 (2006) 429–455, arXiv:0709.1094 [physics.ins-det].
21. M. Aharrouche et al., *Measurement of the response of the ATLAS liquid argon barrel calorimeter to electrons at the 2004 combined test-beam*, Nucl. Instrum. Meth. A614 (2010) 400–432.
22. B. Aubert et al., *Performance of the ATLAS electromagnetic calorimeter end-cap module 0*, Nucl. Instrum. Meth. A500 (2003) 178–201.
23. B. Aubert et al., *Performance of the ATLAS electromagnetic calorimeter barrel module 0*, Nucl. Instrum. Meth. A500 (2003) 202–231.
24. The ATLAS Collaboration, *Data-quality requirements and event cleaning for jets and missing transverse energy reconstruction with the ATLAS detector in Proton-Proton collisions at a center-of-mass energy of  $\sqrt{s} = 7$  TeV*, ATLAS-CONF-2010-036.
25. D. Banfi et al., *Cell response equalization of the ATLAS electromagnetic calorimeter without the direct knowledge of the ionization signals*, J. Instrum. 1 (2006) P08001.
26. C. Collard et al., *Prediction of signal amplitude and shape for the ATLAS electromagnetic calorimeter*, ATL-LARG-PUB-2007-010.
27. H. Abreu et al., *Performance of the electronic readout of the ATLAS liquid argon calorimeters*, JINST 5 (2010) P09003.
28. M.J. Oreiglia, *A study of the reactions  $\gamma + \gamma \rightarrow \gamma\gamma\gamma$* , Ph.D. thesis, SLAC-R-235 (1980), Appendix D.
29. J.E. Geiser, *Charmonium spectroscopy from radiative decay of the  $J/\psi$  and  $\psi'$* , Ph.D. thesis, SLAC-R-255 (1982), Appendix F.
30. The ALEPH, DELPHI, L3, OPAL and SLD Collaborations, *Precision electroweak measurements on the  $Z$  resonance*, Physics Reports 427 (2006) 257–454, arXiv:hep-ex/0509008.
31. The CDF Collaboration, *First measurement of inclusive  $W$  and  $Z$  cross sections from Run II of the Fermilab Tevatron Collider*, Phys. Rev. Lett. 94 (2005) 091803, arXiv:hep-ex/0405078.
32. The D0 Collaboration, *Measurement of the shape of the boson rapidity distribution for  $pp \rightarrow Z/\gamma^* \rightarrow e^+e^- + X$  events produced at  $\sqrt{s} = 1.96$  TeV*, Phys. Rev. D76 (2007) 012003, arXiv:hep-ex/0702026.
33. C. Blocker, *Treatment of Errors in Efficiency Calculations*, CDF/MEMO/STATISTICS/PUBLIC/7168, 2004.
34. The ATLAS Collaboration, *Measurement of the differential cross-sections of inclusive, prompt and non-prompt  $J/\psi$  production in proton-proton collisions at  $\sqrt{s} = 7$  TeV*, Nucl. Phys. B850 (2011) 387–444, arXiv:1104.3038 [hep-ex].
35. M. Pivk and F.R. Le Diberder, *ePlot : a statistical tool to unfold data distributions*, Nucl. Instrum. Meth. A555 (2005) 356–369, arXiv:physics/0402083.
36. The ATLAS Collaboration, *Particle identification performance of the ATLAS Transition Radiation Tracker*, ATLAS-CONF-2011-128.
37. The ATLAS Collaboration, *Studies of the performance of the ATLAS detector using cosmic-ray muons*, Eur. Phys. J. C71 (2011) 1593, arXiv:1011.5665 [physics.ins-det].
38. The ATLAS Collaboration, *Performance of the ATLAS Detector using First Collision Data*, JHEP 1009 (2010) 056, arXiv:1005.5254 [hep-ex].

$\langle 2.47 [20, 50] \rangle$

red  
 $A_2$

$$0.943 \times 0.942 \\ 0.785$$

Max value

• 2012 relection  $v_h$

pile up  $\approx 5\%$

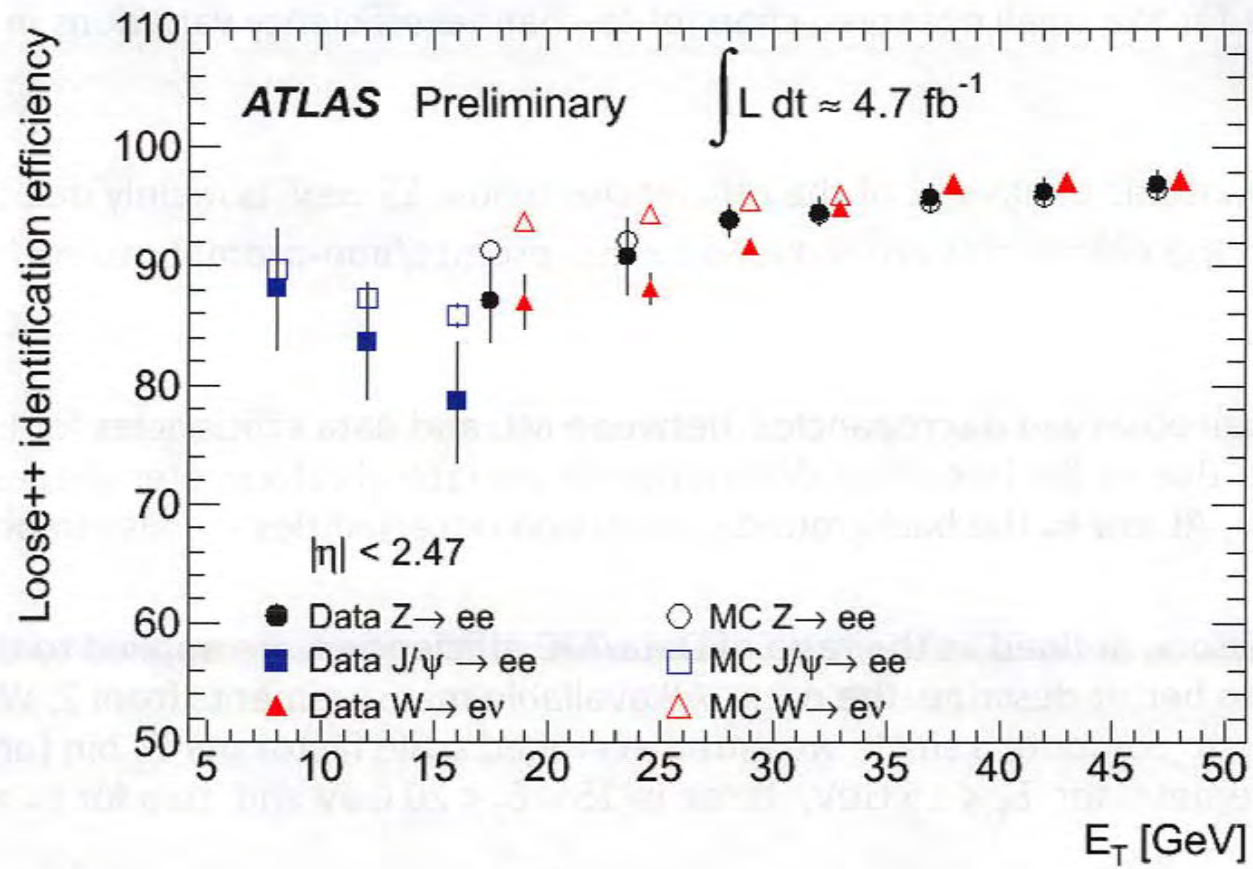
time  $\approx 2\text{ days}$

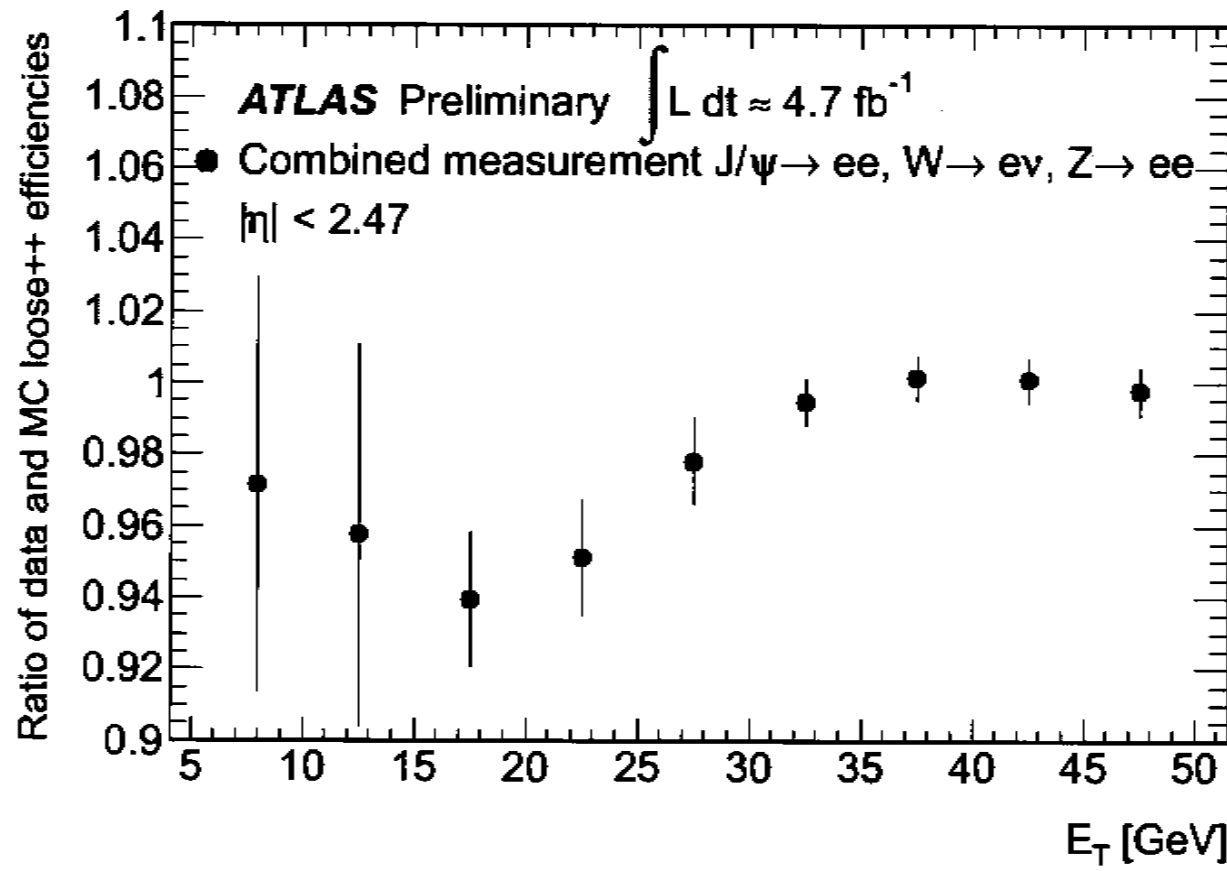
## Identification efficiency measurement for electrons with transverse energy between 7 and 50 GeV

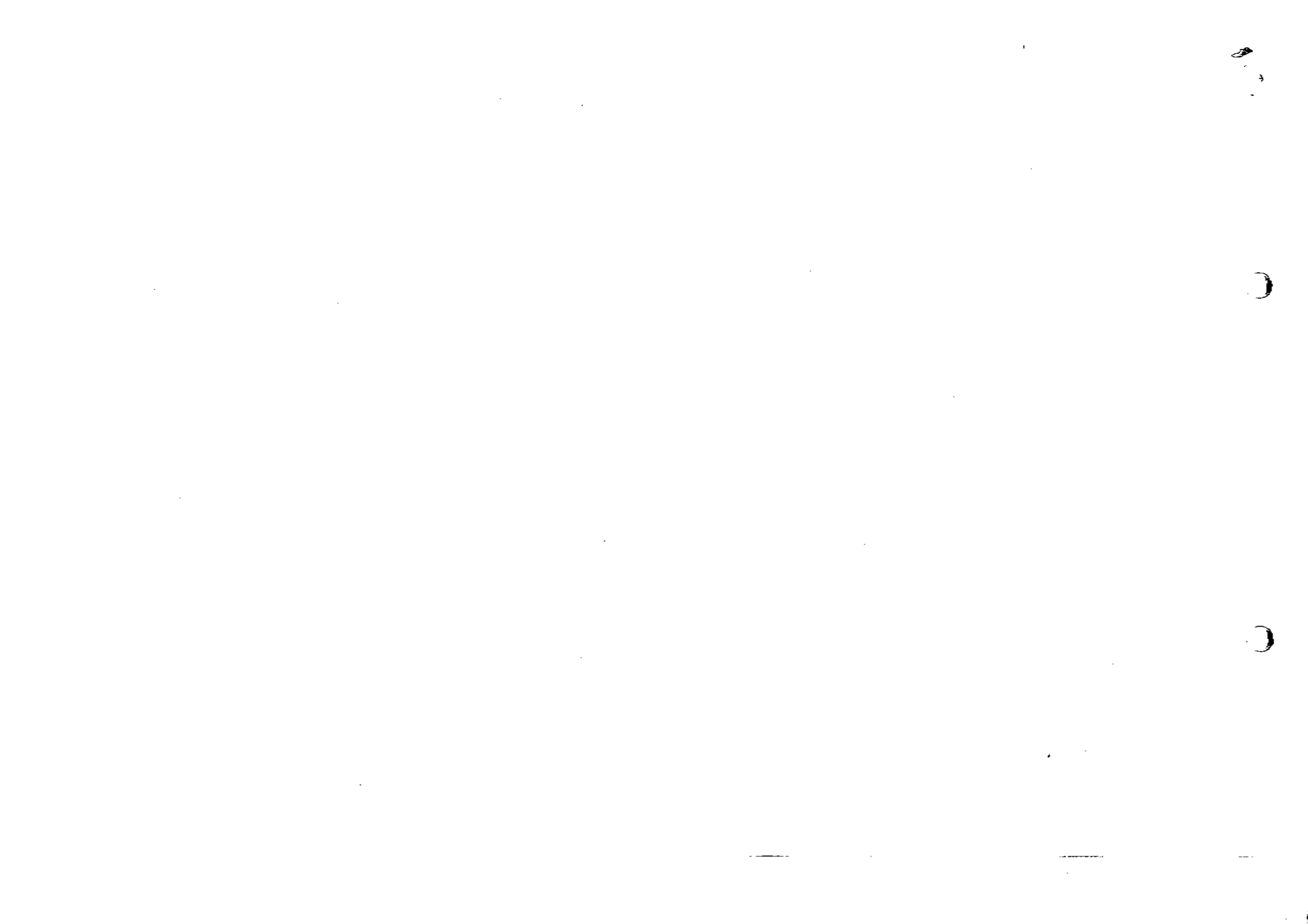
- 1) The electron identification efficiency is defined with respect to a reconstructed calorimeter cluster with a good-quality track pointing into it (see point 10). The measured efficiency is obtained with the so-called “tag-and-probe” method applied to  $Z \rightarrow e^+e^-$ ,  $W \rightarrow e\nu$  and  $J/\psi \rightarrow e^+e^-$  samples, as explained in detail in the ATLAS electron performance paper <http://arxiv.org/abs/1110.3174>.
- 2) The full 2011 dataset is used, representing an integrated luminosity of  $\sim 4.7 \text{ fb}^{-1}$ . Results are shown for electron transverse energies ( $E_T$ ) between 7 and 50 GeV and they are compared to Monte Carlo expectations obtained by applying Tag and Probe method to  $Z \rightarrow e^+e^-$ ,  $W \rightarrow e\nu$  and  $J/\psi \rightarrow e^+e^-$  Pythia samples. Electrons from  $W$  and  $Z$  provide measurements from 15 to 50 GeV, while the transverse energy region from 4 to 20 GeV is probed by the  $J/\psi$  decays. These results are extracted from  $\sim 1.6\text{M}$   $Z \rightarrow e^+e^-$ ,  $\sim 2.3\text{M}$   $W \rightarrow e\nu$  and  $\sim 63\text{k}$   $J/\psi \rightarrow e^+e^-$  events. Efficiency is shown for one of the reference criteria set, so-called Loose++, combining calorimetric shower shapers and loose track-cluster matching requirements.

- 3) The mainstream inclusive electron triggers with a  $E_T$  threshold of 20-25 GeV are used to select  $Z \rightarrow e^+e^-$  events with one unbiased electron. A set of dedicated triggers requiring significant missing transverse energy together with a calorimeter cluster with  $E_T > 13\text{GeV}$  having a good-quality track pointing into it, are setup to allow collecting unbiased electrons from W decays. Dedicated end-of-fall triggers are also used to collect  $J/\psi$  decays, combining one tightly selected electron accompanied by a second electron above a low  $E_T$  threshold, with the invariant mass of the pair between 1 and 5 GeV.
- 4)  $J/\psi$  are produced mainly directly (promptly) and also in the decay of B-hadrons (non-promptly), leading to electrons with different identification efficiencies. The measured efficiency of  $J/\psi$  probe electrons is compared to a MC prediction computed as the weighted mean of prompt and non-prompt simulated decays, as explained in detail in reference <http://arxiv.org/abs/1110.3174>. The results presented here are obtained from the sub-sample of  $J/\psi$  with short reconstructed lifetime which reduces the uncertainty arising from the residual non-prompt component.
- 5) The MC events are reweighted to reproduce the pileup and trigger conditions that correspond to the data. Systematic errors in data points take into account of background subtraction and fitting procedure uncertainties. In the case of the  $J/\psi$  decays, an additional uncertainty for the prompt-non prompt mixing is also included.

- 6) Efficiencies are shown as a function of the electron transverse energy, integrating over the  $|\eta| < 2.47$  range. Kinematical differences between the three channels may account for the small observed channel-to-channel efficiency variations in a given  $E_T$  range.
- 7) Non-monotonic behaviour of the efficiencies below 15 GeV is mainly due to the fact that  $J/\psi$  efficiencies are reduced by the prompt/non-prompt mixing (see point 4).
- 8) The small observed discrepancies between MC and data efficiencies for  $E_T < \sim 25$  GeV are due to the imperfect description of the lateral calorimeter shapes by Geant4. At low  $E_T$  the background subtraction uncertainties are also important.
- 9) Scale factors, defined as the ratio of Data/MC efficiencies, are applied to the MC events to better describe the data. All available measurements from Z, W and  $J/\psi$  are used to compute a single weighted averaged scale factor per  $E_T$  bin (one measurement for  $E_T < 15$  GeV, three in  $15 < E_T < 20$  GeV and two for  $E_T > 25$  GeV).
- 10) The reconstruction and track quality efficiency has been measured with  $Z \rightarrow e^+e^-$  decays to be  $\sim 95\%$  in the range from 15 to 50 GeV. It is well modelled by the simulation with a  $\sim 1\%$  uncertainty.







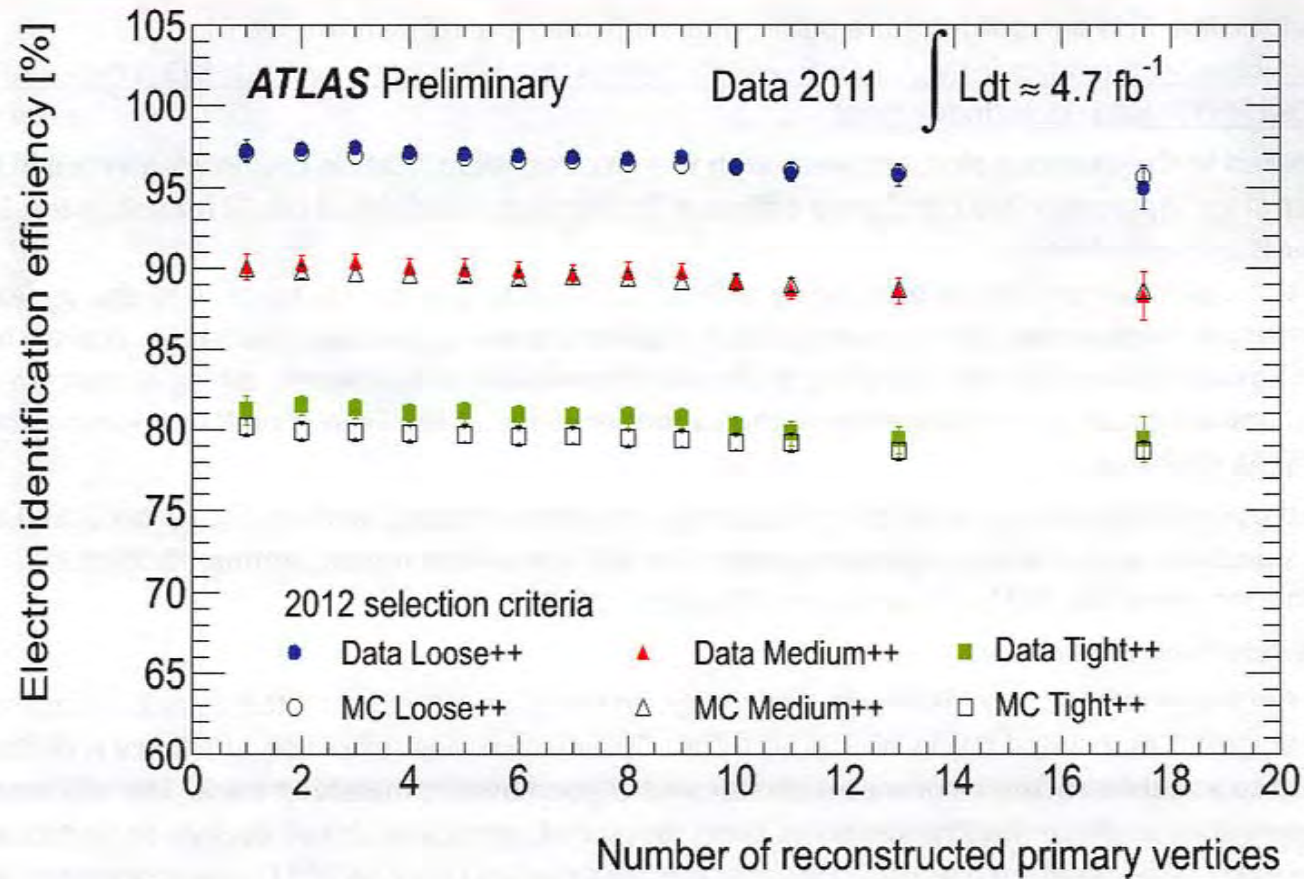
## Electron identification efficiency dependence on pileup (update)

- 1) This plot (slide 2) is an update of the public plot available here (shown in slide 3):  
<https://atlas.web.cern.ch/Atlas/GROUPS/PHYSICS/EGAMMA/PublicPlots/20110512/EfficiencyPileup/ATL-COM-PHYS-2011-1636/index.html>
- 2) Compared to the previous plot, obtained with the electron identification cuts implemented in the trigger after September 2011 and used offline, a further optimised set of cuts<sup>(\*)</sup> for use in the 2012 trigger is presented here.  
<sup>(\*)</sup> This re-optimisation is done by relaxing criteria sensitive to pile-up (i.e. fraction of energy leaking in the hadronic calorimeter) and compensating by tightening pile-up robust criteria (i.e. lateral shower shape variables using the first sampling of the electromagnetic calorimeter), taking advantage of fine lateral and longitudinal segmentation of the calorimeter and of the Transition Radiation capability of the ATLAS detector
- 3) This re-optimisation allows to largely mitigate the efficiency dependence on pile-up observed with the 2011 selection, with a similar rejection power. The MC simulation models within ~0.5% this dependence over the 2011 dataset range of pileup activity.
- 4) More details on the analysis:

The number of primary vertices increases with the pileup. In this plot, a reconstructed vertex is required to have at least 3 associated tracks with  $p_T > 0.4$  GeV. The electron identification efficiency is defined with respect to a reconstructed calorimeter cluster with a good quality matching track. The efficiency corresponding to these requirements has been measured, using also  $Z \rightarrow ee$  decays, to be ~95% and is only weakly dependent on pile-up (~1% variation over the full range of 2011 pile-up activity). The measured identification efficiency, shown as a function of the number of primary vertices in the event, is obtained with the so-called “tag-and-probe” method applied to the  $Z \rightarrow e^+e^-$  sample, as described in the electron performance paper <http://arxiv.org/abs/1110.3174>.

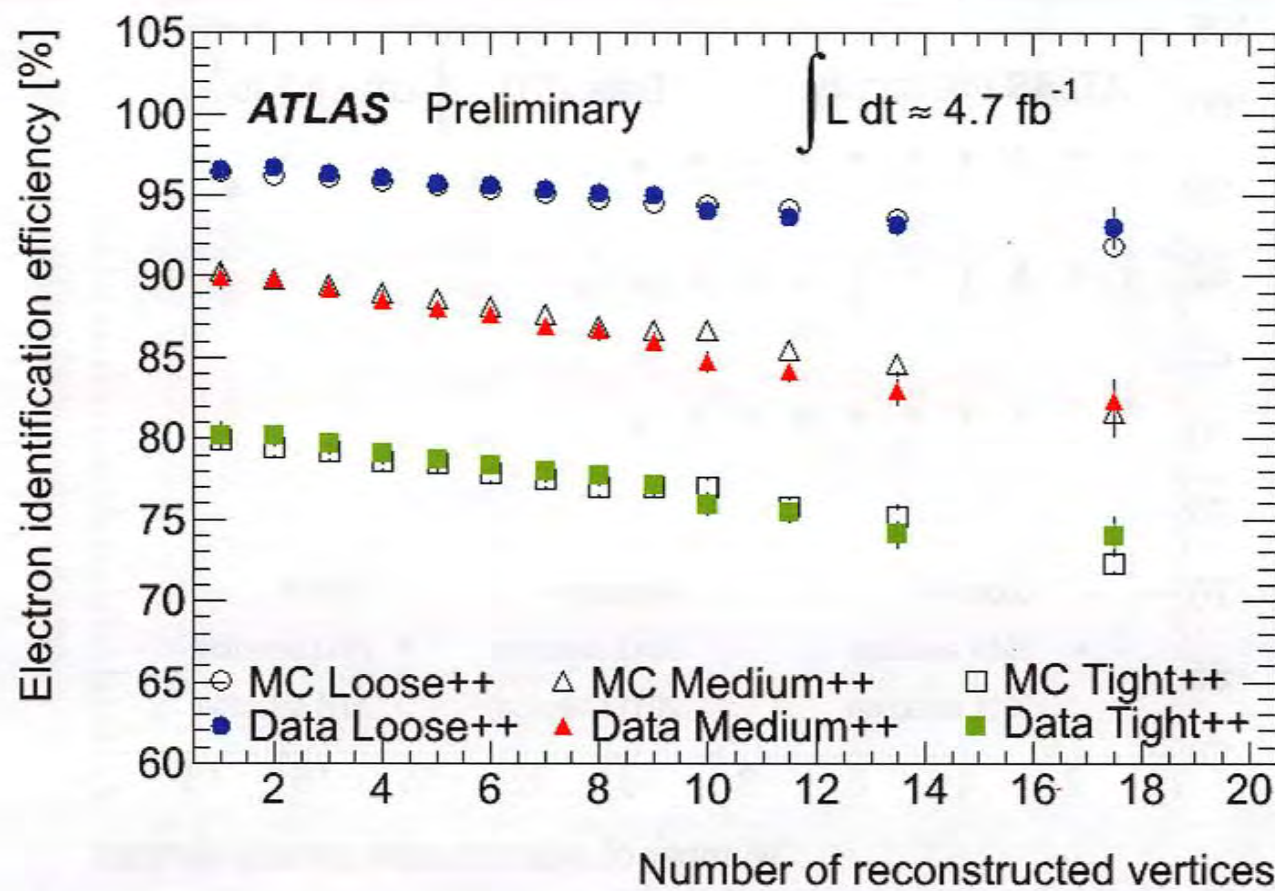
The full 2011 dataset is used (full symbols), representing an integrated luminosity of ~4.7 fb<sup>-1</sup>. Results are shown for electron transverse energies between 20-50 GeV and they are compared to Monte Carlo expectations (open symbols) obtained by applying the same tag- and-probe technique to a Pythia  $Z \rightarrow e^+e^-$  sample

## Electron identification efficiency dependence on pileup (update)



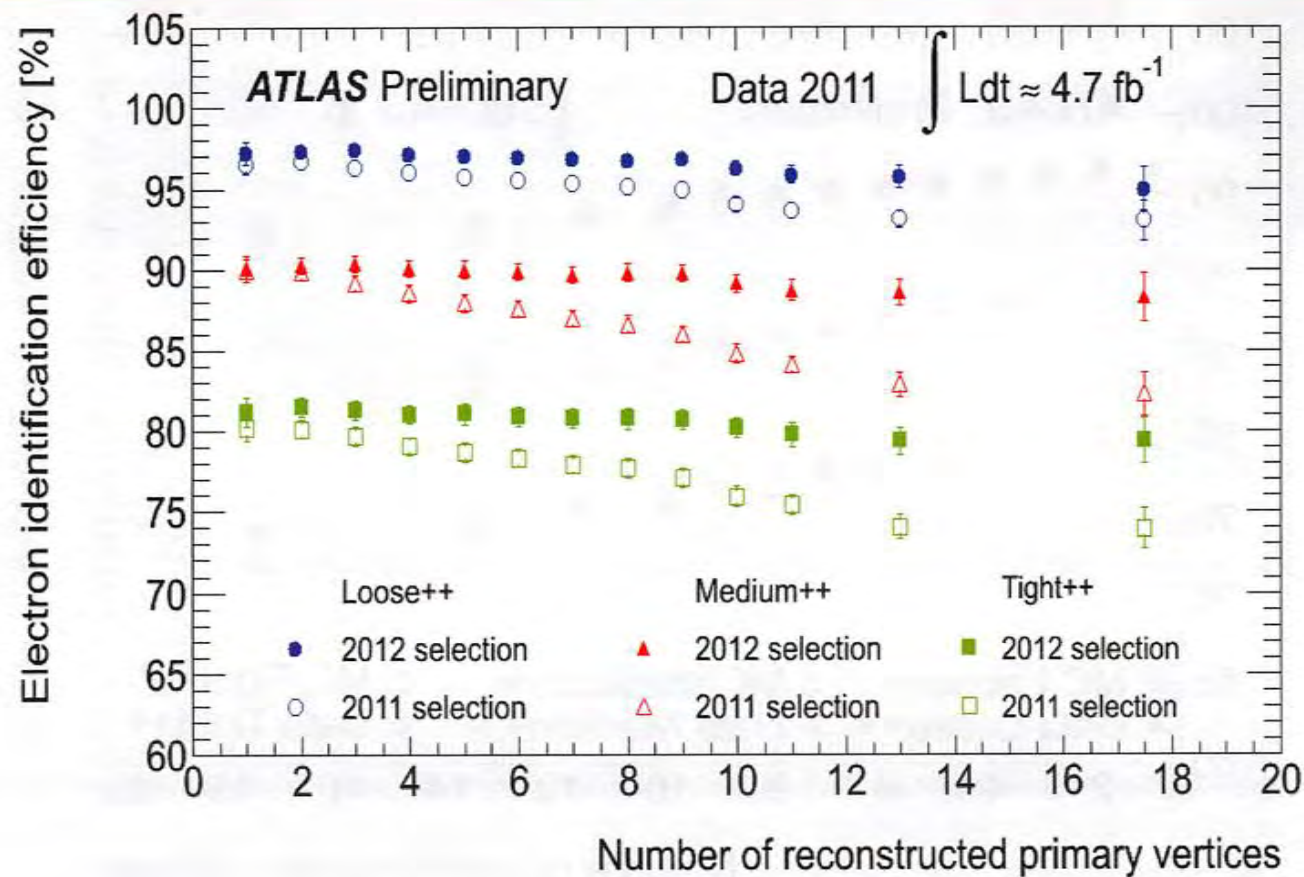
Efficiencies are shown for different number of reconstructed primary vertices, going from 1 to 10 in bins of unit size and then wider bins 11-12, 13-14 and 15-20.

**Plot already public, using the identification menu implemented in 2011 trigger**



<https://atlas.web.cern.ch/Atlas/GROUPS/PHYSICS/EGAMMA/PublicPlots/20110512/EfficiencyPileup/ATL-COM-PHYS-2011-1636/index.html>

## Electron identification efficiency dependence on pileup (addendum)



This plot shows the data measurements using re-optimised 2012 selection criteria (filled points, from plot in slide 2) superimposed with those using 2011 selection (open points, from plot in slide 3).

## Electron reconstruction efficiency

The reconstruction efficiency of electrons is defined with respect to electromagnetic clusters built using a sliding window algorithm. The combined electron track reconstruction and the track-cluster matching are measured using the so-called „Tag and Probe“ method utilizing  $Z \rightarrow e^+e^-$  events, described in more detail in [1]. The cluster building efficiency for such electrons is close to 1.

For the 2011 measurement, the full data sample at  $\sqrt{s}=7$  TeV with an integrated luminosity of  $\int L=4.7 \text{ fb}^{-1}$  has been used, while for the 2012 measurement the first  $\int L \sim 770 \text{ pb}^{-1}$  at  $\sqrt{s}=8$  TeV has been utilized.

For the 2012 data taking, the electron reconstruction algorithm has been improved with respect to 2011. This uses an electron hypothesis track reconstruction which allows for Bremsstrahlung losses in the pattern recognition, where previously only multiple scattering was considered. A Gaussian Sum Filter (GSF) algorithm to re-fit all tracks associated to electromagnetic clusters and a more performant track-cluster matching are used, which allows to recover electron candidates that suffered large energy losses due to Bremsstrahlung emissions.

Fig. 1) The reconstruction efficiency (including the requirements on the track quality, namely that the number of pixel hits and silicon hits – the sum of pixel and SCT hits – exceed 1 and 7 respectively) is shown as a function of the pseudorapidity  $\eta$  for electrons with transverse energy between 30 and 50 GeV, for data (filled markers) and MC (open markers) from 2011 (red up triangles) and 2012 (blue down triangles). The total (statistical and systematic) uncertainty is displayed.

Over this  $E_T$  range, the absolute increase in reconstruction efficiency in 2012 as compared to 2011 – for both data and MC - is  $\sim 1\%$  in the barrel region of the calorimeter and  $\sim 5\%$  in the endcaps (where there is more material in front of the calorimeter, hence more electrons undergo bremsstrahlung emissions).

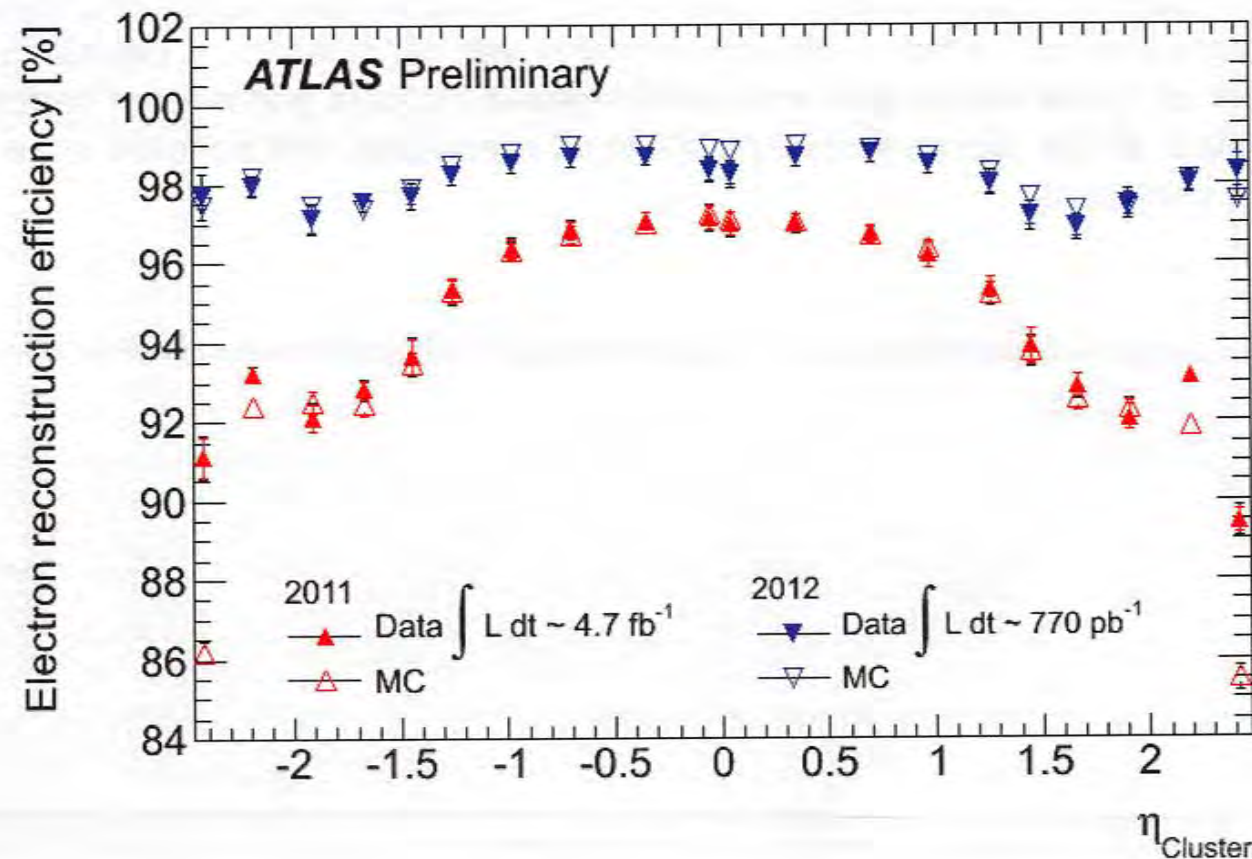
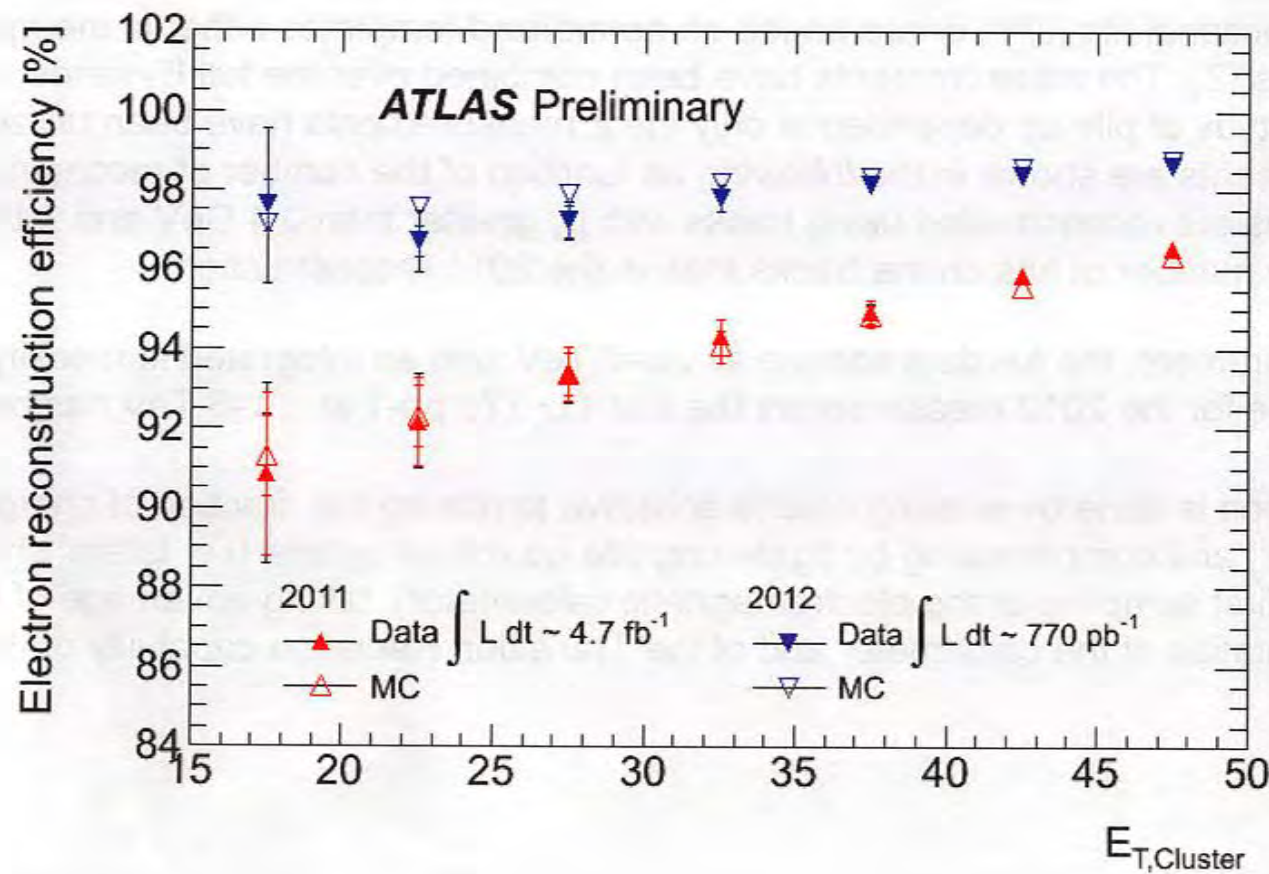


Fig. 2) The reconstruction efficiency (including the requirements on the track quality, namely that the number of pixel hits and silicon hits – the sum of pixel and SCT hits – exceed 1 and 7 respectively) is shown as a function of the electron transverse energy, for data (filled markers) and MC (open markers) from 2011 (red up triangles) and 2012 (blue down triangles). The total (statistical and systematic) uncertainty is displayed. Electrons reconstructed in the calorimeter transition region  $1.37 < |\eta| < 1.52$  are not taken into account.

Averaging over the pseudorapidity coverage of the central calorimeter ( $|\eta| < 2.47$ ), the absolute increase in reconstruction efficiency in 2012 as compared to 2011 – for both data and MC - is  $\sim 2\%$  for the high  $E_T$  region and up to 6-8% for the low  $E_T$  ( $< 20$  GeV) region, which is particularly important for searches using low momentum leptons.



## Electron identification efficiency

In order to mitigate the impact of the harsher pile-up conditions of 2012 data taking, the electron identification criteria have been re-optimized (\*) with respect to the ones used in 2011. Four sets of identification criteria are employed for 2012 data taking, called „Loose“, „Medium“ and „Tight“ (in order of decreasing efficiency and increasing background rejection) and “multiLepton” (developed in the context of searches with multi lepton final state analyses, exploiting specific cuts on high/low brem categories using GSF information).

The electron identification efficiency (defined with respect to reconstructed electrons having a good quality track pointing to an EM cluster) has been measured using the so-called „Tag and Probe“ method utilizing  $Z \rightarrow e^+e^-$  and  $J/\Psi \rightarrow e^+e^-$  events (see ). Backgrounds are either subtracted using functional fits ( $J/\Psi$ ) or are based on normalized templates either in the mass or the isolation distributions ( $Z$ ). The measurements have been combined over the full  $E_T$  range, spanning from 7-50 GeV. For the study of pile-up dependence only the  $Z$  measurements have been utilized. The efficiency measurements are shown in the following as function of the number of reconstructed primary vertices. The vertices are reconstructed using tracks with  $p_T$  greater than 0.4 GeV and with tighter requirements on the number of hits on the tracks than in the 2011 reconstruction.

For the 2011 measurement, the full data sample at  $\sqrt{s}=7$  TeV with an integrated luminosity of  $\int L=4.7$  fb $^{-1}$  has been used, while for the 2012 measurement the first  $\int L \sim 770$  pb $^{-1}$  at  $\sqrt{s}=8$  TeV has been utilized.

(\*) This re-optimisation is done by relaxing criteria sensitive to pile-up (i.e. fraction of energy leaking in the hadronic calorimeter) and compensating by tightening pile-up robust criteria (i.e. lateral shower shape variables using the first sampling of the electromagnetic calorimeter), taking advantage of fine lateral and longitudinal segmentation of the calorimeter and of the Transition Radiation capability of the ATLAS detector

Fig. 3) The identification efficiency for the Loose, Medium and Tight set of cuts is shown as a function of the number of reconstructed primary vertices within a range from 2 to 20. The data efficiency measurement (full markers) is flat within 2-3% and is modelled by the MC simulation (open markers) over the full range better than within 0.5% for Loose and Tight identification criteria (in blue and green). For the Medium criteria, the data/MC agreement is better than 2% and is flat as a function of the number of primary vertices.

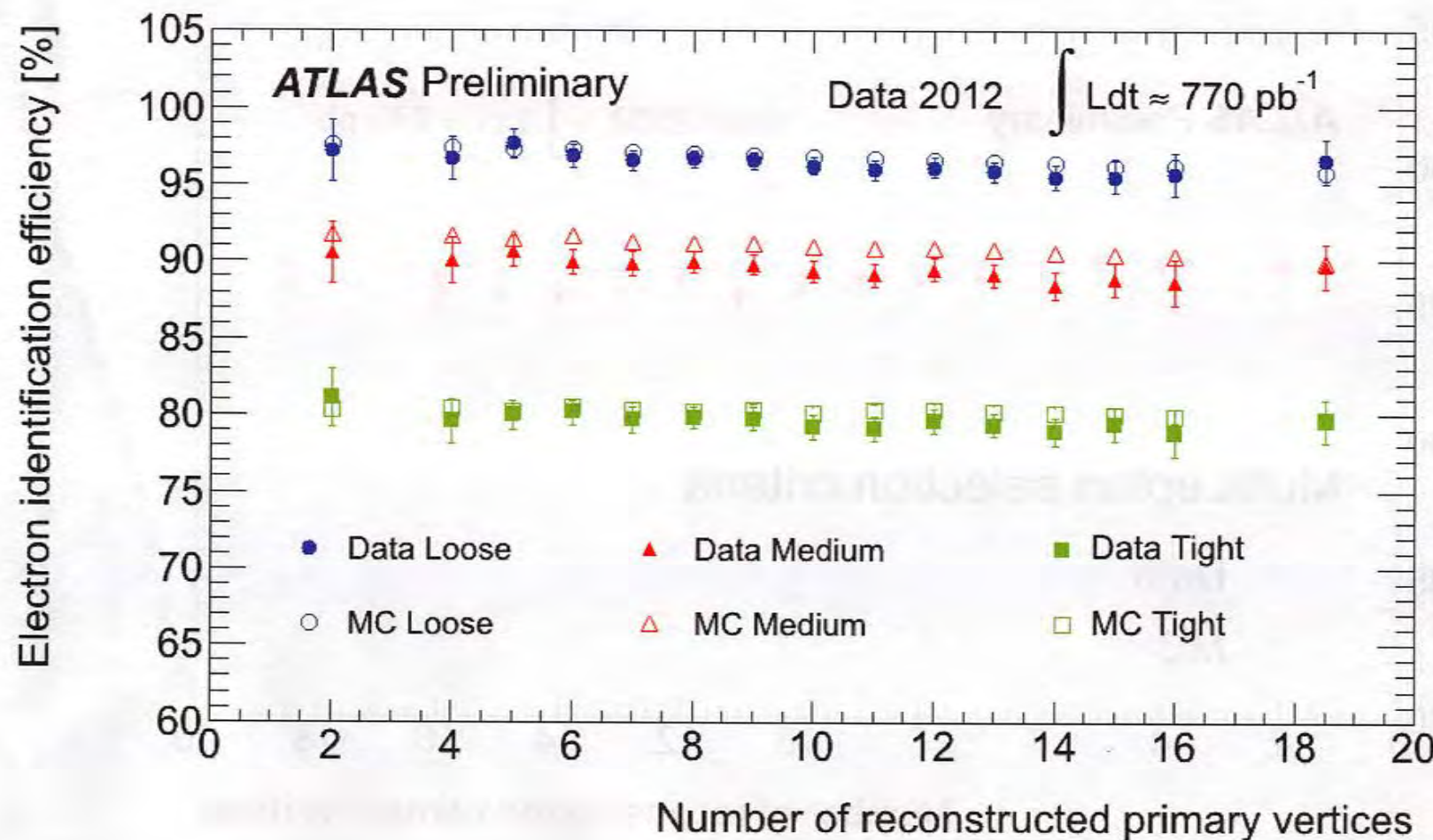


Fig. 4) The identification efficiency measurement for the „MultiLepton“ selection criteria is shown as function of the number of reconstructed primary vertices within a range from 2 to 20. The data efficiency measurement (full triangles) is flat within 2% and is modelled by the MC simulation (open triangles) over the full range better than within 0.5%.

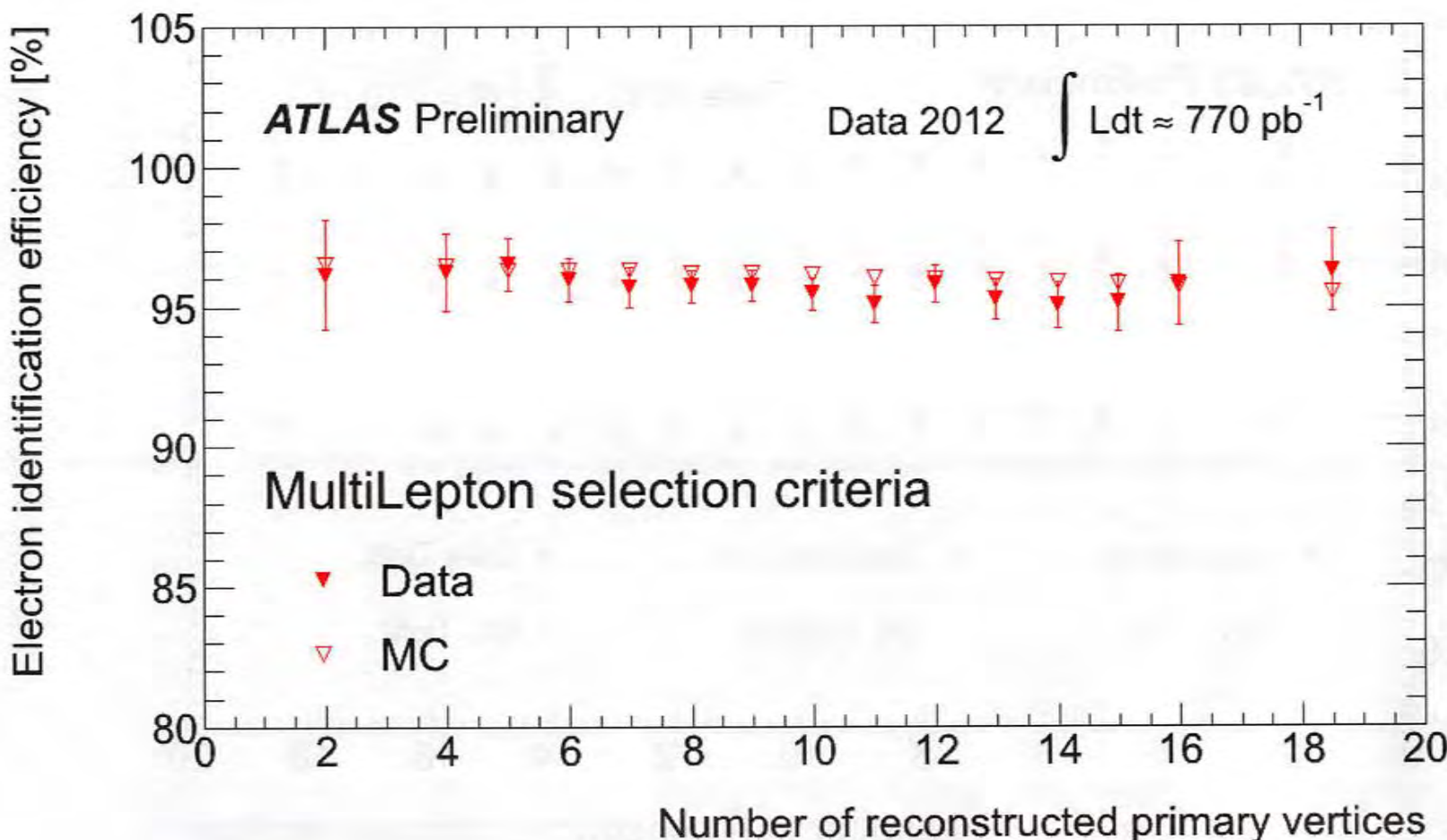
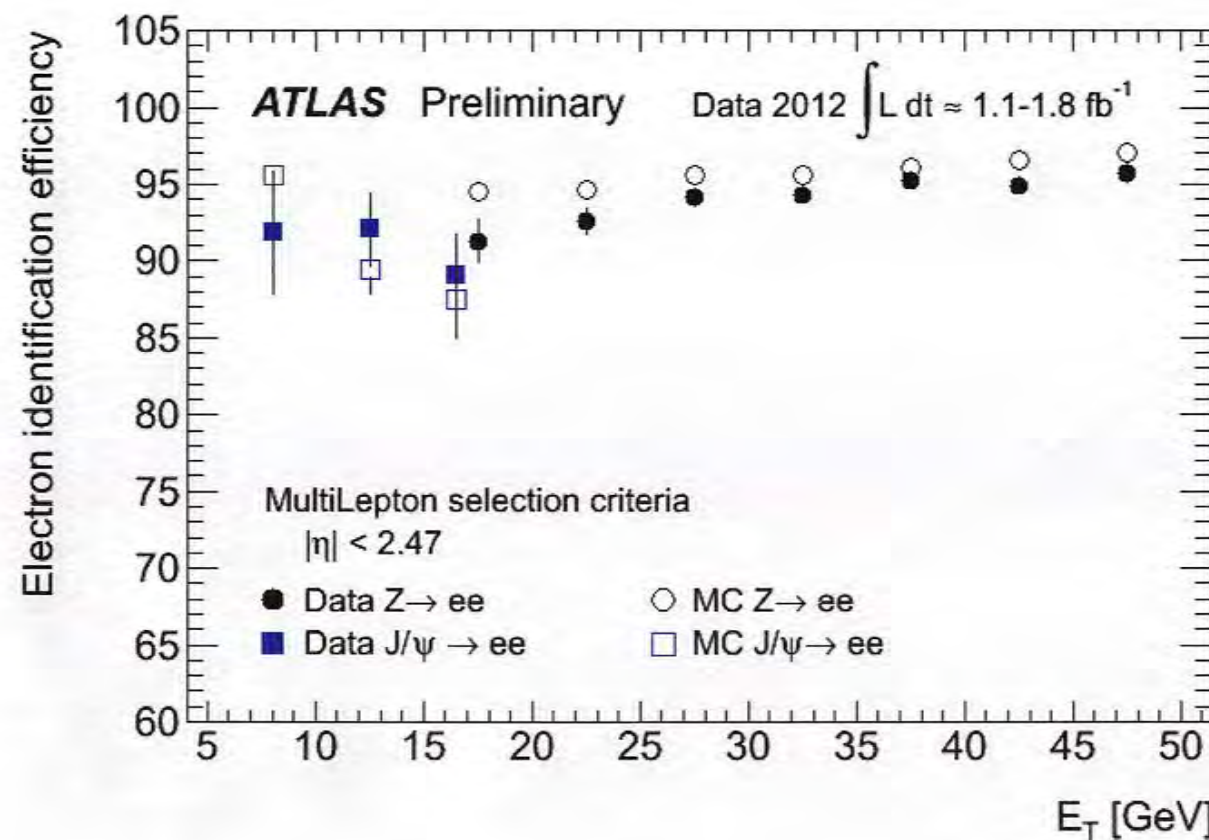
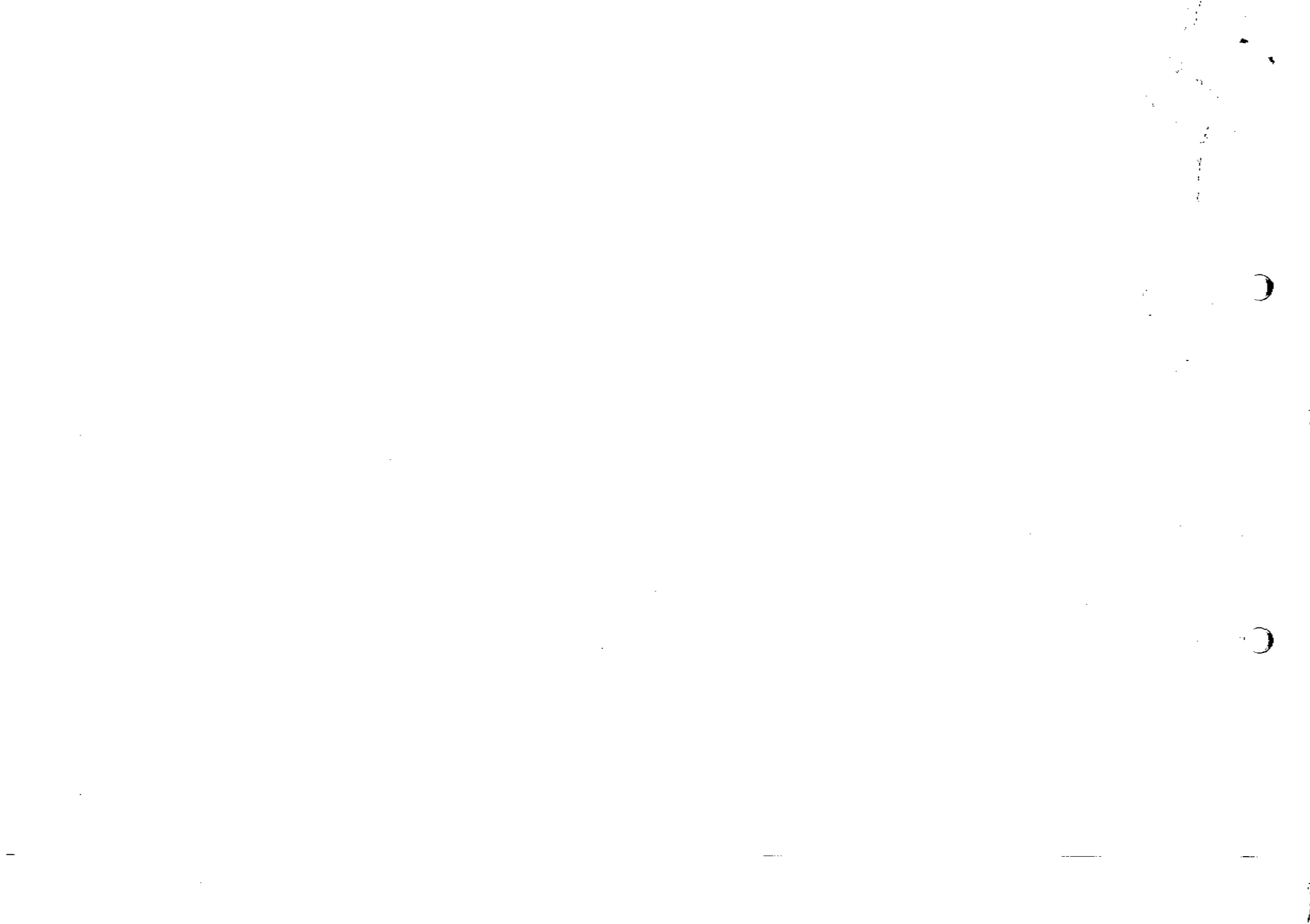


Fig. 5) The identification efficiency measurement for the „MultiLepton“ selection criteria is shown as a function of the electron transverse energy and averaged over the pseudorapidity range of the central calorimeter ( $|\eta| < 2.47$ ). Data efficiencies for  $J/\psi$  and  $Z$  Tag and Probe measurements (blue and black full markers) are compared to the MC efficiencies (open markers). The efficiency measurement is flat as a function of  $E_T$  within  $\sim 5\%$ . The measured efficiency from  $J/\psi$  Tag and Probe method must be compared to the MC prediction computed as the weighted mean of prompt and non-prompt simulated decays, as explained in detail in reference <http://arxiv.org/abs/1110.3174>. The results presented here are obtained from the sub-sample of  $J/\psi$  with short reconstructed pseudo-proper time which reduces the uncertainty arising from the residual non-prompt component. The MC/data agreement is better than 4% for low  $E_T$  and better than 0.5-1% at high  $E_T$ .







## ATLAS NOTE

ATLAS-CONF-2012-047

May 18, 2012



### Improved electron reconstruction in ATLAS using the Gaussian Sum Filter-based model for bremsstrahlung

The ATLAS Collaboration

#### Abstract

The behavior of high-energy electrons in the ATLAS Inner Detector is dominated by radiative energy losses (bremsstrahlung) as they traverse matter. These can be significant considering the substantial amount of material that the Inner Detector contains and can give rise to deviations from the original charged particle's path as it propagates through the magnetic field. As a result, significant inefficiencies, both during the electron trajectory reconstruction and in the determination of the corresponding track parameters in the bending plane, can be observed. In this note, we present a modification of the electron reconstruction in ATLAS that uses track refitting with the Gaussian Sum Filter (GSF) algorithm, with the aim of improving the estimated electron track parameters. The performance of this new scheme is compared to that of the existing standard electron reconstruction, for electron transverse energies between 7 GeV and 80 GeV.

© Copyright 2012 CERN for the benefit of the ATLAS Collaboration.  
Reproduction of this article or parts of it is allowed as specified in the CC-BY-3.0 license.

## 1 Introduction

An electron can lose a significant amount of its initial energy due to bremsstrahlung energy losses when interacting with the material it traverses. This is particularly relevant with modern tracking detector designs, based on semiconductor technologies developed for optimal performance in stringent environments such as those at the LHC. Such tracking detectors are characterized by non-uniformly distributed material with high concentrations at specific radial positions. While the detector elements themselves contribute very little to the overall material budget, the requirements for on-detector electronics, power distribution, cooling and mechanical support add significantly to it. Because of the electron's small mass, radiative losses can be substantial, resulting in alterations of the curvature of the electron's trajectory when it propagates through a magnetic field and hence of the electron track.

The ATLAS [1] Inner Detector allows the measurement of the trajectories of charged particles over five units in pseudorapidity,  $|\eta| < 2.5$ , as well as the determination of their production vertices. It comprises three sub-systems: a silicon Pixel Detector at low radius providing three space points per track, a Semiconductor Tracker (SCT) providing four measurements in two stereo coordinates and a Transition Radiation Tracker (TRT) providing track-following and electron identification capability up to  $|\eta| = 2.0$ . The whole tracker is surrounded by a solenoidal magnet with a central field of 2 T. The overall material distribution of the ATLAS Inner Detector is shown in Fig. 1, illustrating significant increases at higher pseudorapidities.

The electron reconstruction scheme used for the 2010 and 2011 publications of ATLAS results employs the same tracking algorithm for all charged particles, with all tracks fitted using a pion particle hypothesis to estimate the material effects. The lack of special treatment for bremsstrahlung effects results in inefficiencies in reconstructing the electron trajectory. It also results in the degradation of the estimated track parameters, increasing with the amount of material encountered. This has a strong dependence on the electron pseudorapidity. By taking into account bremsstrahlung losses (and the resulting alteration of the track curvature) by using the Gaussian Sum Filter (GSF) [2, 3] approach, the estimated electron track parameters are expected to be improved.

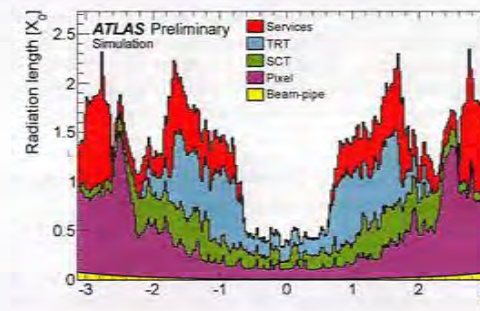


Figure 1: Distribution of the Inner Detector material thickness given separately for each sub-detector as a function of the pseudorapidity  $\eta$  reflecting the Inner Detector description implemented in the current ATLAS simulation. The material of the Pixel and SCT detectors include the passive material mostly located behind the active silicon sensors. The track-refitting technique presented in this note has been developed primarily to account for the radiative energy losses due to this material.

A two-step programme is underway in ATLAS to improve electron reconstruction: first to correct all track parameters associated to electron candidates by performing bremsstrahlung *refitting* prior to electron reconstruction and identification, and eventually to perform bremsstrahlung *recovery* at the initial step of the electron trajectory formation to allow for more efficient track reconstruction. Correcting for bremsstrahlung effects will also mean that track-to-calorimeter matching will use a better defined track, the electron four-momentum vector will be better determined and particle identification tools will benefit from those improvements. Such a procedure would eventually allow for more optimal electron identification in analyses, thereby potentially recovering significant efficiency losses, especially at low transverse momentum.

This note describes the results of the first step, namely applying, prior to electron reconstruction and identification, a bremsstrahlung refit with the GSF algorithm to tracks already associated to electron candidates. The impact on the determination of track parameters and more global combined-parameters involving the calorimeter, will be presented. In Section 2, a brief overview of the Gaussian Sum Filter approach and the new electron reconstruction scheme are presented. The effects on the reconstructed track parameters are discussed in Section 3, and more global parameters involving the electromagnetic calorimeter are reviewed in Section 4. Finally, a specific example involving electrons with small transverse momenta is presented in Section 5.

## 2 Electron Reconstruction

Electron candidates are selected by matching reconstructed tracks to clusters formed by the energy deposited in the electromagnetic calorimeter [4, 5]. The reconstruction of a charged-particle track in ATLAS involves determining the particle's trajectory in the tracker from the detector response and then estimating the track parameters that best describe it. The latter include two parameters that give the transverse ( $d_0$ ) and the longitudinal position ( $z_0$ ) of the perigee (impact parameters), two parameters that describe the direction of the charged particle at this point ( $\phi, \theta$ ) and one parameter that provides the inverse track momentum multiplied by the charge ( $q/p$ ). The errors on the track parameters originate from experimental uncertainties due to the intrinsic resolution of the tracker sensors and the interaction of the charged particle with the detector material. The track parameters and their corresponding uncertainties are estimated from the track-fitting process. For muons or pions (neglecting hadronic interactions), an essentially linear least-squares fit using a linearized helical model with scattering angle formulation [6, 7] is used to estimate the trajectory from the set of experimental measurements. Unfortunately in the case of electrons, such an assumption is not valid since their trajectory is affected by energy losses dominated by bremsstrahlung.

A well-known model of the energy loss of electrons due to bremsstrahlung was proposed by Bethe and Heitler [8]. According to this model, the probability density function for an electron to retain a portion  $z = \frac{E_f}{E_i}$  of its initial energy  $E_i$  as its final energy  $E_f$ , is given by [2, 8]:

$$f(z) = \frac{[-\ln z]^{a-1}}{\Gamma(a)}, \quad \text{with } a = t/\ln 2, \quad 0 < z < 1 \quad (1)$$

where  $t$  is the thickness of the material traversed by the electron in units of radiation length  $X_0$ . The expression above needs to be modified in order to account for processes, such as the Landau-Pomeranchuk-Migdal (LPM) or the Ter-Mikaelian effects, that become prominent at electron energies of the order of several GeV or higher [9]. The resulting probability density function cannot be expressed in an analytical form, but it can be implemented numerically in simulation engines like GEANT4 [10] providing the model that describes the radiative energy losses of electrons. Under those conditions, a non-linear fitter may provide better estimations of the track parameters. Such a fitter, based on a generalisation of the Kalman Filter [11], and called the Gaussian Sum Filter (GSF), has been developed in [3]. It assumes that

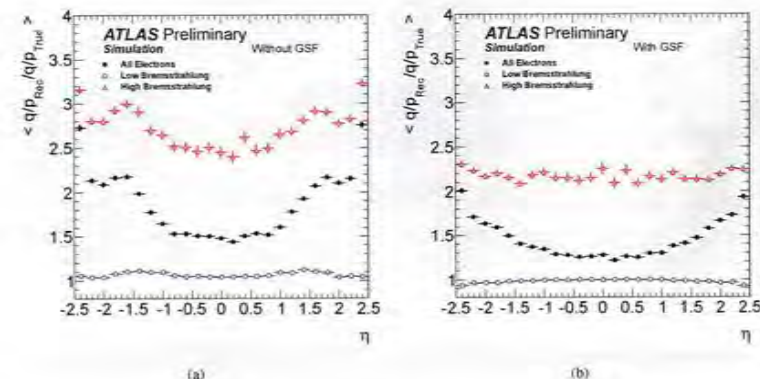


Figure 2: Mean value of the ratio of reconstructed over the true electron inverse momentum times charge ( $q/p$ ) as a function of pseudorapidity for single electrons with transverse momentum between 7 and 80 GeV that lose less than (open points) and greater than (open triangles) 20% of their energy due to bremsstrahlung in the silicon detector and surrounding infrastructure without (a) and with (b) GSF refitting applied. Electrons that suffer significant bremsstrahlung losses dominate the high pseudorapidity regions. This explains the larger dependence with pseudorapidity when all the electrons are averaged (solid points).

the trajectory state can be approximated as a weighted sum of Gaussian functions. The GSF splits the experimental noise into individual Gaussian components and uses the Kalman filter technique in order to process each one. The GSF therefore consists of a number of Kalman filters running in parallel, each one representing a different contribution to the full Bethe-Heitler spectrum. In its current ATLAS implementation, the Gaussian Sum Filter is used to account for the radiative loss effects of electrons as they traverse the silicon trackers. In the case of the Transition Radiation Tracker, it has been found that due to the more homogeneous distribution of the detector material and the lower precision of the measurements, applying the GSF does not result in any appreciable improvements.

Using the GSF, all the tracks with transverse momentum  $p_T > 400$  MeV and  $|\eta| < 2.5$  that are assigned to electrons [5] in an event can be refitted. The resulting new collection of bremsstrahlung-corrected tracks and the corresponding electromagnetic clusters form new inputs to the standard electron reconstruction algorithm. This procedure has several advantages:

1. The approach described above is expected to improve the estimation of bending-plane quantities, as is presented in more detail in Section 3. In particular, their dependence on the amount of material encountered by (and hence the pseudorapidity of) the electron should be significantly reduced as shown in Fig. 2 in the case of simulated single electrons with transverse momenta between 7-80 GeV.
2. The extrapolation of the tracks and their matching to the electromagnetic calorimeter clusters is performed using the re-estimated track parameters. It is therefore expected that in certain cases the track considered as the best match to the electromagnetic cluster will have changed. Some improvements are also possible in the case of the different electron identification categories. This is particularly likely in the case of the so-called “tight” electrons [4, 5] (which make use of both first and second sampling layer calorimeter information, information from the two silicon detectors

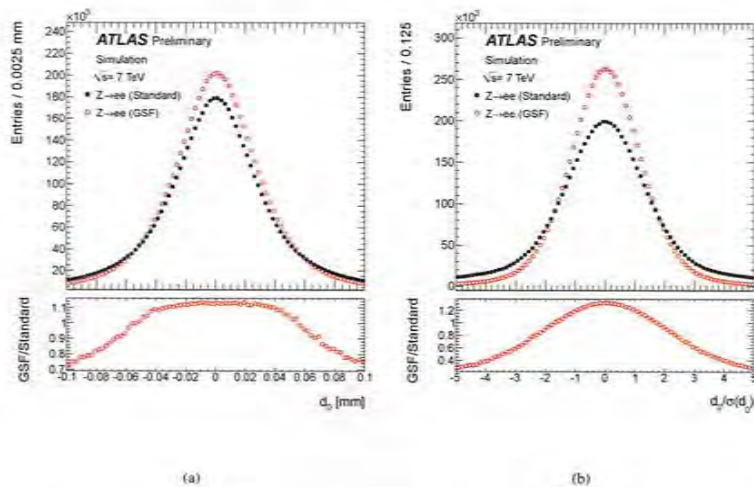


Figure 3: The distribution of the transverse impact parameter resolution (a) and of the transverse impact parameter significance (b) for both GSF (open red) and standard (solid black) truth-matched Monte-Carlo electrons from Z-boson decays. The bottom plots show the ratio of the entries of the GSF and standard electrons per bin.

and the Transition Radiation Tracker,  $E/p$ , as well as matching between tracking and calorimeter  $\eta$  and  $\phi$  position), where several quantities sensitive to bremsstrahlung losses are employed. The above implications are described in more detail in Section 4.

3. The electron four-momentum is computed using the improved estimates of the track parameters. This is particularly beneficial in the case of low- $p_T$  electrons where the contribution to the resolution of the four-momentum of the track parameters is dominant and where the impact of bremsstrahlung losses is more severe. Furthermore the reconstructed invariant masses of resonances decaying into two electrons are also better evaluated. Both of the above are especially relevant in the case of the  $J/\psi$  resonances, where lower energy electrons are involved, as is demonstrated in Section 5.

### 3 Electron Track Parameters

This section focuses on presenting the improvements in the track parameters in the transverse plane. It should be noted that a full account of the radiative energy losses of an electron is practically impossible. Although the track parameters do improve, some bias will always remain. This is especially the case if the electron has lost significant amounts of energy due to bremsstrahlung at low radius inside the ATLAS Inner Detector, e.g. in the first two Pixel Detector layers. Radiative energy losses are expected to only marginally affect the track parameters in the longitudinal plane. For the results presented in this section when simulated data samples are presented, only reconstructed electrons that pass the “loose++” [4, 5] selection and have been associated to the corresponding generator ones, referred to as truth-matched

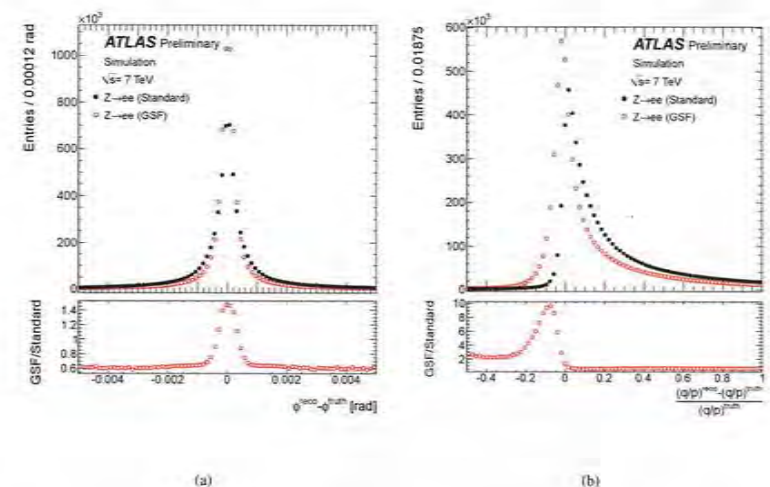


Figure 4: The distribution of the resolution of the track direction  $\phi$  at the perigee (a) and of the relative bias on the track inverse momentum multiplied by the charge  $q/p$  (b), for both GSF (open red) and standard (solid black) truth-matched Monte-Carlo electrons from Z-boson decays. The bottom plots show the ratio of the entries of the GSF and standard electrons per bin.

Monte-Carlo electrons, are used.

### 3.1 Transverse Track Parameters Resolution

The distributions of the transverse track parameters are shown in Figs. 3 and 4 for the case of electrons from Z-boson decays. In Fig. 3(a) the resolution of the transverse impact parameter  $d_0$  is shown. The transverse impact parameter significance  $d_0/\sigma_{d_0}$  is defined as the ratio of the transverse impact parameter  $d_0$  to the error from the track fitting procedure,  $\sigma_{d_0}$ , and is shown in Fig. 3(b). Fig. 4(a) shows the resolution of the track direction  $\phi$  at the perigee. Finally, the relative bias of the track inverse momentum multiplied by the charge  $q/p$  is shown in Fig. 4(b). As expected, there is a clear improvement in the resolution of all the bending-plane track parameters when radiative losses are accounted for during the track fitting. This could potentially have important implications in physics analyses, for example in the Higgs-boson searches via its decay into two Z-bosons with at least one of the latter subsequently decaying into two electrons. Here, the final-state electrons resulting from the Higgs-boson decay sequence can be separated from those originating from heavy-quark decays by a cut on the transverse impact parameter significance since electrons from heavy quark decay are expected to have large true  $d_0$  values, whereas the true transverse impact parameter of electrons from Z decays should be zero. Equally important is the dependence of the transverse track parameters resolution width (or of the mean relative bias in the case of the track  $q/p$ ) on the electron pseudorapidity  $\eta$  or transverse momentum  $p_T$  as shown in Figs. 5 and 6. At larger pseudorapidities, the amount of material encountered by the electron increases, resulting in increased degradation of the reconstructed track parameters. As is evident in Fig. 5, accounting for the

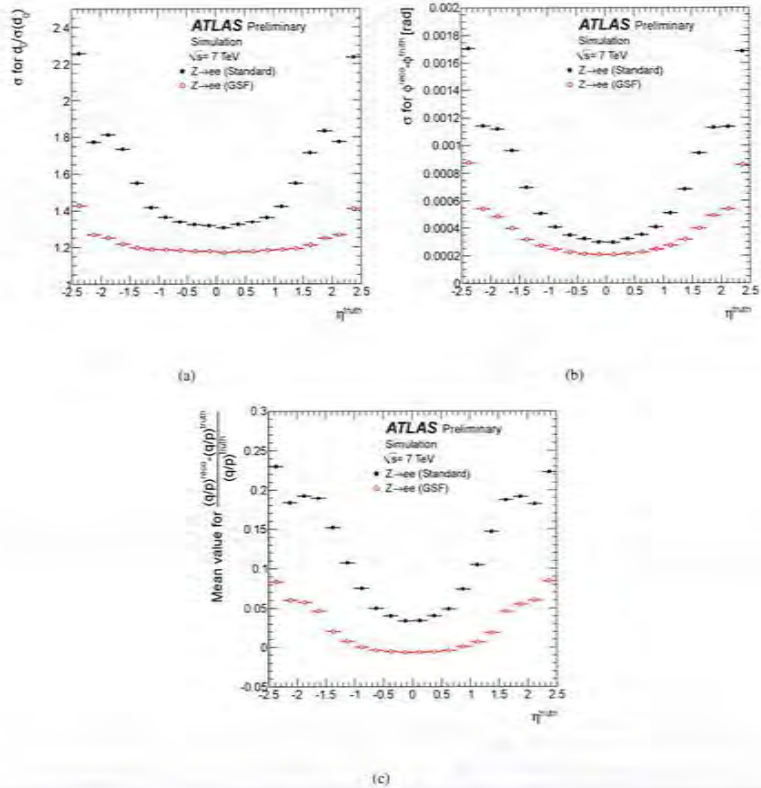


Figure 5: The dependence on the pseudorapidity  $\eta$  of the width of the transverse impact parameter significance (a), of the width of the resolution of the track direction at the perigee  $\phi$  (b), and of the mean relative bias of the track inverse momentum multiplied by the charge  $q/p$  (c), for GSF (open red) and standard (solid black) truth-matched Monte-Carlo electrons from Z-boson decays.

bremsstrahlung losses during the track fitting reduces these effects. In addition, the mean relative bias on the reconstructed electron track inverse momentum multiplied by the charge ( $q/p$ ) is reduced.

### 3.2 Comparison with Data for the Transverse Impact Parameter Significance

In data, electrons produced by heavy-quark or Z-boson decays can be arranged in two separate samples and then be used to check how well the simulation describes the reconstructed transverse impact parameter significance when the bremsstrahlung corrections are included. Electrons from  $b$ -hadron decays are

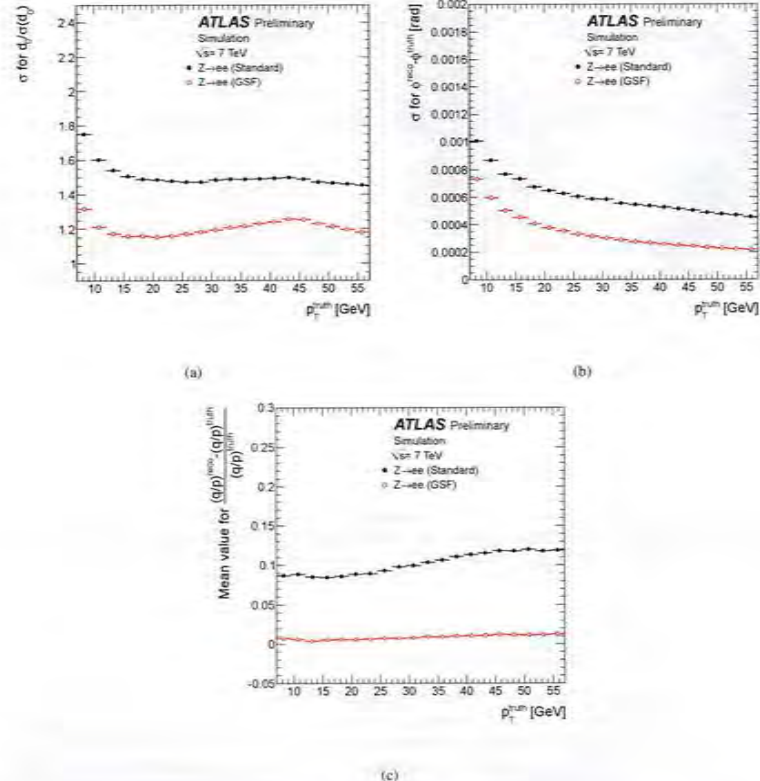


Figure 6: The dependence on the transverse momentum  $p_T$  of the width of the transverse impact parameter significance (a), of the width of the resolution of the track direction at the perigee  $\phi$  (b), and of the mean relative bias of the track inverse momentum multiplied by the charge  $q/p$  (c), for GSF (open red) and standard (solid black) truth-matched Monte-Carlo electrons from Z-boson decays.

selected in data events where either a Z-boson [12] or a  $t\bar{t}$  pair (through the dilepton channel [13]) has already been identified. At least one b-tagged jet with  $p_T > 25$  GeV is required in the event. One can then look for additional electrons in the selected events that have a well-reconstructed cluster matched to a track, with  $p_T > 7$  GeV and  $|\eta| < 2.47$  and pass the “loose++” selection criteria. These electrons are required to lie within a cone  $\Delta R < 0.5$  around the tagged jet. On the other hand, electrons from Z-boson decays are identified using a tag-and-probe approach. The tag electron is an isolated electron that passes the “tight” selection, while the probe electron is only required to pass the “loose++” selection, using the criteria defined in [4,5]. The two electrons are required to have opposite charges and to have an invariant

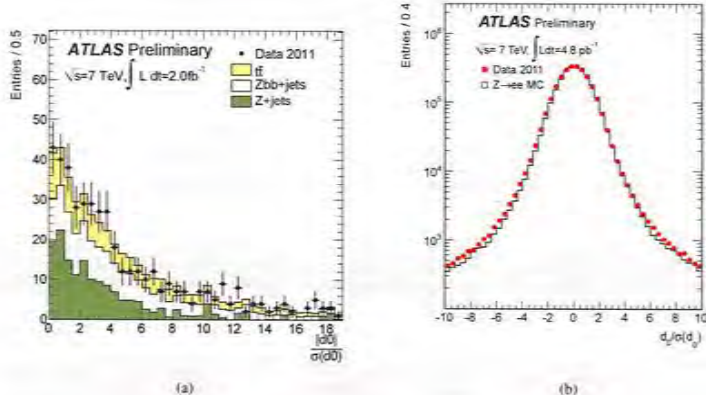


Figure 7: Comparison between data and simulation of the reconstructed transverse impact parameter significance for GSF-reconstructed electrons from heavy-quark decays (a) (where due to the limited statistics the absolute value of the transverse impact parameter significance is used instead) and from Z-boson decays (b). The small shift visible between the MC and the data distributions in the latter plot is due to a feature in the ATLAS simulation that is unrelated to the bremsstrahlung treatment studied in this note.

mass within 15 GeV from that of the Z-boson. The distribution of the reconstructed transverse impact parameter significance for electrons refitted using the GSF in data is shown in Fig. 7. The agreement between the data and the simulation is very good.

#### 4 Electron Combined-Parameter Performance

Combined parameters are computed using the selected electron tracks as described in Section 3 and the associated calorimeter information via the track-to-calorimeter matching criteria. The ATLAS Liquid-Argon Electromagnetic Calorimeter extends to a pseudorapidity of  $|\eta| = 3.2$ . Over the  $|\eta| < 2.5$  range covered by the tracker, it makes precision measurements with three sampling depths. The combined parameters discussed in this section include the calorimeter energy to track momentum ratio ( $E/p$ ), and the difference in the extrapolated track impact point to the second sampling of the calorimeter  $\phi$  cluster barycentre position ( $\Delta\phi_2$ ). The latter has been multiplied by the charge sign so that the impact point difference is independent of the particle charge. They are used in the electron identification algorithms, particularly in the so-called “tight++” identification [4, 5], which makes use of both first and second sampling layer calorimeter information, information from the two silicon detectors and the Transition Radiation Tracker,  $E/p$ , as well as matching between tracking and calorimeter  $\eta$  and  $\phi$  position.

The following subsections show comparisons of the GSF-refitted simulated electrons to the standard-reconstructed electrons as well as comparisons between simulation and collision data of GSF-refitted electrons from Z-boson decays. One example is also shown for prompt  $J/\psi \rightarrow ee$  data, to illustrate the good data to Monte Carlo agreement of GSF electrons at lower energies.

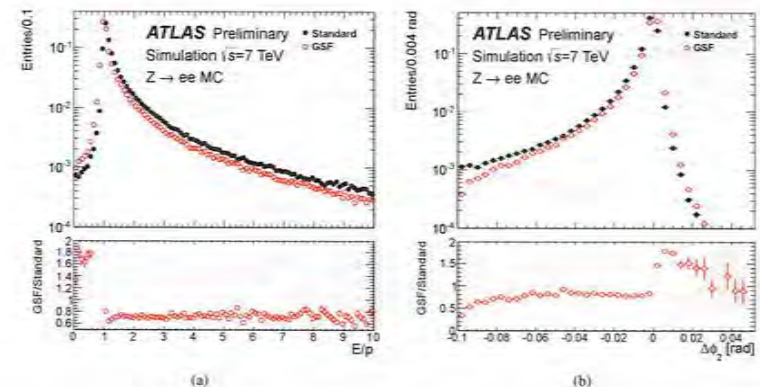


Figure 8: The distributions of the calorimeter energy to track momentum ratio ( $E/p$  in (a)) and of the azimuthal  $\phi$  difference between the extrapolated track and the corresponding cluster position as measured in the second sampling of the calorimeter ( $\Delta\phi_2$  in (b)), for truth-matched Monte-Carlo GSF (open red) and standard (solid black) electrons. The GSF-to-standard ratio is given below:

#### 4.1 Combined Track-Calorimeter Parameters

Distributions of  $E/p$  and  $\Delta\phi_2$  for truth-matched simulated electrons from Z decays are shown in Fig. 8, as well as the dependence of their means on  $\eta$  in Fig. 9. The GSF-refitted electrons are better centred at  $E/p = 1$  and  $\Delta\phi_2 = 0$  with smaller radiative tails than the standard electrons candidates. The  $\eta$  dependence of the mean of the distributions is noticeably flattened, implying lesser sensitivity to material effects in the case of the GSF-refitted electrons. Figure 10 illustrates the good agreement between data and simulation for the  $E/p$  variable for the case of reconstructed electrons in the electromagnetic calorimeter outer barrel ( $0.8 < |\eta| < 1.37$ ). Figure 11 shows an equivalent plot for  $J/\psi \rightarrow ee$  events which represent electrons with fairly low energies in the range  $7 \text{ GeV} < E_T < 15 \text{ GeV}$  where, as discussed earlier in this note, radiative energy losses are more pronounced.

#### 4.2 Electron Identification Efficiencies

Since the GSF-refitted tracks and their associated calorimeter cluster information form the new input to the electron identification algorithm, electron identification efficiencies are expected to improve. The “tight++” electron identification efficiency with respect to Monte-Carlo truth information is shown in Fig. 12 as a function of electron  $\eta$ . Electrons refitted with GSF show an improvement in the electron identification efficiency of over 5% at high  $|\eta|$ . The improvement as a function of transverse momentum is approximately 2% at 15 GeV and 0.5% at 70 GeV. The “tight++” selection requirements used in the plots shown have been optimised for the older standard electrons. Further improvement might be achieved by reoptimising these requirements when the new GSF-refitted tracks are used.

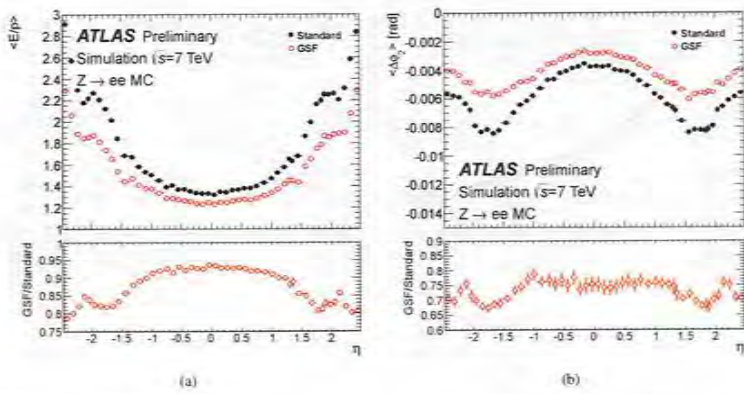


Figure 9: The dependence on the pseudorapidity  $\eta$  of the mean calorimeter energy to track momentum ratio ( $E/p$ , in (a)) and of the mean difference of extrapolated track  $\phi$  to the cluster  $\phi$  position as measured in the second sampling of the calorimeter ( $\Delta\phi_2$  in (b)), for truth-matched Monte-Carlo GSF (open red) and standard (solid black) electrons. The GSF-to-standard ratio is given below.

#### 4.3 Choice of Tracks Matched to Clusters

It is instructive to see how often a different track is matched to the calorimeter cluster as a result of the GSF-refitting, compared to the standard tracking. This information is shown in Fig. 13 as a function of  $\eta$ . In the central  $\eta$  region, a new track is rarely selected, but this choice is changed in approximately 5% of the cases at high  $|\eta|$ . Matching to different tracks is largely independent of  $p_T$ , averaging approximately 0.8% over the entire  $p_T$  kinematic range.

### 5 $J/\psi$ Invariant Mass Shape with GSF-refitted Electrons

The greatest improvements in electron reconstruction after implementing bremsstrahlung correction techniques are expected at low ( $\lesssim 15$  GeV) transverse energies. The  $J/\psi$  meson ( $m_{J/\psi} = 3069.9$  MeV [14]) provides an abundant source of low energy di-electron final states, and is therefore a testbed tool for validation studies of these bremsstrahlung-aware reconstruction tools. In addition to an increase in the reconstruction and identification efficiencies, gains in the resolution of electron kinematic quantities will lead to improvements in the accuracy of the parent  $J/\psi$  four-vector. As a result, the position of the peak of the parent invariant mass distribution should be more accurate, which could be important in the measurement of the mass of new particles (e.g. exotic new quarkonia states). The mass resolution is also expected to improve, which is particularly desirable for the separation of closely spaced states such as the  $\Upsilon(1S)$ ,  $\Upsilon(2S)$  and  $\Upsilon(3S)$ . Other indirect benefits may also be seen in physics measurements that are reliant on angular distributions (e.g. polarisation), or those which are sensitive to bin migrations (such as differential cross-sections). Aside from the best-fit values for the kinematic variables, an improvement is also expected in the covariance matrix for the four-vectors benefiting, for example, the vertex position fits and lifetime measurements.

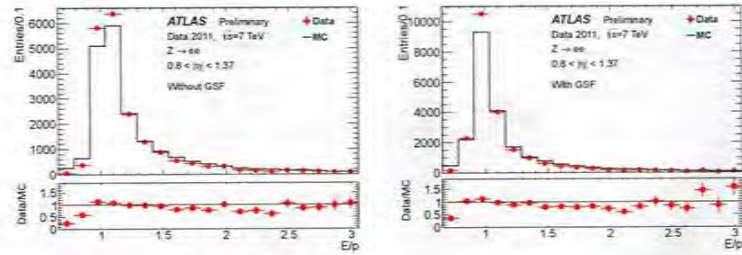


Figure 10: Comparison of the data to a simulation of the calorimeter energy to track momentum ratio ( $E/p$ ), for  $0.8 < |\eta| < 1.37$  using standard (left plot) and GSF (right plot) tracking for  $Z \rightarrow ee$  candidate electrons with reconstructed electron energy  $15 \text{ GeV} < E_T < 25 \text{ GeV}$ .

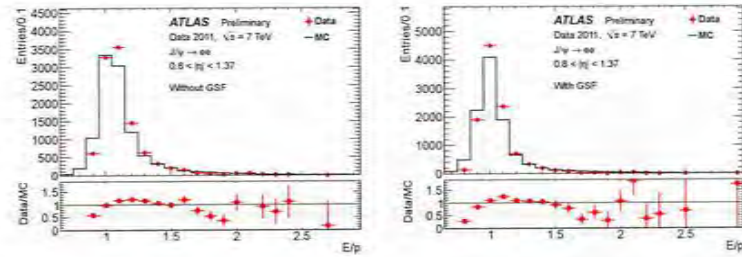


Figure 11: Comparison of the data to a simulation of the calorimeter energy to track momentum ratio ( $E/p$ ), for  $0.8 < |\eta| < 1.37$  using standard (left plot) and GSF (right plot) tracking for  $J/\psi \rightarrow ee$  candidate electrons with reconstructed electron energy  $7 \text{ GeV} < E_T < 15 \text{ GeV}$ .

#### 5.1 $J/\psi$ Candidate Selection

This study uses a Monte-Carlo data sample of about 5 million prompt  $J/\psi$  produced by the PYTHIA 6 [15] generator (which uses the MRST LO<sup>\*</sup> [16] parton distribution functions) with an ATLAS-specific tune [17]. *Prompt* refers to those  $J/\psi$  directly produced in the primary (hard) interaction, or from the decay of excited charmonium states (e.g.  $\chi_{c1} \rightarrow \gamma J/\psi$ ). A non-prompt  $J/\psi$  sample was also initially studied, but showed similar results to the prompt sample and so is not discussed here. A subset of the full 2011 collision data-set (approximately 37 million events recorded early during the data-taking campaign and combining all contributing electron triggers) is also included in the analysis for comparison with the simulation. For both the data and simulation samples, events were processed with (1) the standard electron reconstruction algorithm and (2) the modified algorithm where the GSF is used to refit all tracks associated to each electromagnetic cluster, leaving the track-cluster matching and identification criteria unchanged.

A standard candidate selection is employed, which requires two opposite-sign reconstructed electrons, each with an associated track containing at least 6 silicon hits (with at least one of these in the

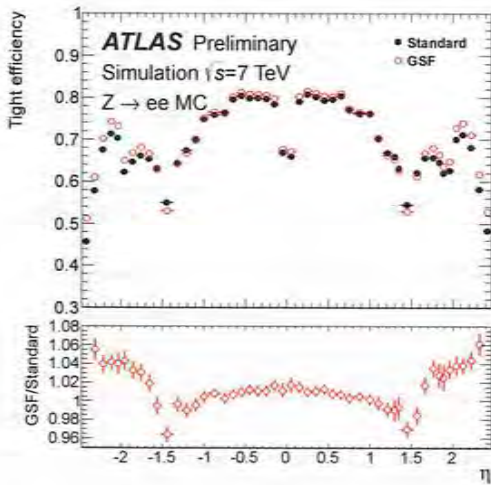


Figure 12: The “tight++” electron identification efficiency with respect to Monte-Carlo truth as a function of  $\eta$ , for GSF (open red) and standard (solid black) electrons. The GSF-to-standard ratio is given below.

pixel detector). Both electrons are required to fulfil the “tight” electron identification criteria. For each  $J/\psi \rightarrow ee$  decay candidate passing these selections, the two electron tracks are then fitted to a common vertex with the requirement on the fit quality that  $\chi^2_{\text{vertexfit}} < 200$ . Precise knowledge of the position of the vertex is essential in any attempt to separate prompt from non-prompt  $J/\psi$ . The resulting vertex-refitted tracks and their corresponding covariance matrices are then used to construct the  $J/\psi$  four-vector and covariance matrix, from which the invariant mass and uncertainty ( $m_{e^+e^-}$  and  $\delta m_{e^+e^-}$ , respectively) are calculated.

## 5.2 Results and Discussion

The invariant mass distributions for the prompt simulation sample are shown in Fig. 14(a), with the results for the standard electron reconstruction and reconstruction using GSF track fitting, normalized to the same number of entries, overlaid for comparison. The shape of the curve for the GSF-refitted electrons is much more symmetrical about its peak value, which is in addition closer to the PDG value of 3096.9 MeV [14]. A tail to the left of the peak remains due to the inability of the GSF algorithm to account for bremsstrahlung losses when the photon emission occurs very close to the electron production vertex, but as can be seen in the figure, the resolution is indeed narrower when using GSF refitting. These trends are also reflected in the results for the collision data sample (Fig. 14(b)). The distribution for the data also includes a secondary, smaller peak at the  $\psi(2S)$  mass, which is slightly more visible for the GSF reconstruction.

The evolution of the mass shape with the pseudorapidity of the electrons is another point of interest. In Fig. 15(b), the invariant mass for the GSF-refitted Monte-Carlo  $J/\psi$  sample is displayed as a function

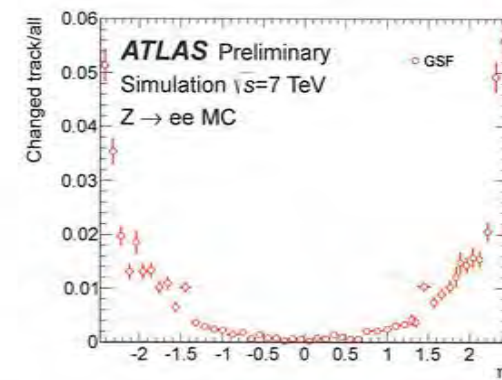


Figure 13: Fraction of Monte-Carlo electron candidates for which a different track was matched to the calorimeter cluster as a result of GSF-refitting (compared to the original track selection for standard tracking) as a function of  $\eta$ .

of the parent  $J/\psi$  rapidity. The width of the distributions is strongly dependent on the rapidity, but the position of the peak is more stable than in the case of the standard electron reconstruction (Fig. 15(a)). The observed poorer resolution in the forward regions is as expected, since for these trajectories there is generally more material in the detector and less coverage by the tracking elements.

To quantify the shapes of the GSF distributions, binned maximum-likelihood fits were performed using the Crystal Ball (CB) function for the signal peak and a second order Chebychev polynomial to describe the background. The intrinsic width of the mass distributions is a function of the rapidity (see Fig. 15(b)). An accurate description of the signal shape across the entire rapidity range would require several CB curves to account for this. This complication was avoided by restricting the rapidity range of the  $J/\psi$  candidates to  $|y| < 0.1$ , where the width is essentially constant. For the collision data sample, a second CB was used to describe the  $\psi(2S)$  resonance. The fits for the two samples are given in Fig. 16, with values for the peak parameter  $m_{J/\psi}$  of 3105–3107 MeV, and having consistent widths. Though the position of the mean is slightly above the PDG value (by approximately 10 MeV), it is a clear improvement over the peak value for standard electron reconstruction, which is at approximately 3020 MeV. The widths measured in these fits using the GSF algorithm (73 and 85 MeV for simulation and data, respectively) are much narrower compared to the results when using calorimeter measurements of transverse energy on similar data samples (typically  $\gtrsim 110$  MeV). For comparison, distributions for  $J/\psi \rightarrow \mu^+\mu^-$  decays are symmetric and have a width of about 50 MeV [18]. The success of the CB fits here in describing the peak shape is encouraging, as it is important for accurate extraction of yields for cross-section measurements.

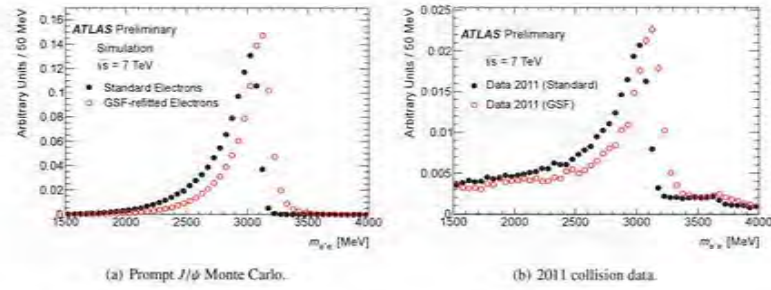


Figure 14: The  $e^+e^-$  invariant mass distributions for prompt  $J/\psi$  simulation (a) and 2011 collision data samples (b).

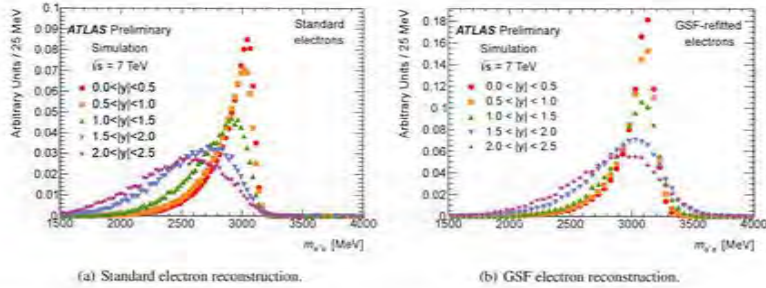


Figure 15: The invariant mass distributions as a function of the combined  $e^+e^-$  rapidity for the standard (a) and GSF reconstruction (b) of simulated  $J/\psi$  decays. While the widths of the distributions clearly increase in the more forward  $\eta$  regions, the GSF algorithm successfully stabilises the position of the peak.

## 6 Summary and Conclusions

A modification of the ATLAS electron reconstruction scheme, that uses track refitting with the Gaussian Sum Filter (GSF) algorithm to account for the effects of bremsstrahlung, is presented in this note. It is demonstrated that this procedure leads to an improved estimation of bending-plane quantities such as the transverse impact parameter significance, track angular direction at the perigee  $\phi$ , and the inverse momentum multiplied by the charge  $q/p$ . Distributions of combined track and calorimeter parameters such as the calorimeter energy to track momentum ratio,  $E/p$ , as well as the difference in extrapolated track impact point to the calorimeter second sampling  $\phi$  cluster barycentre position,  $\Delta\phi_2$ , are observed to be narrower and less dependent on the amount of material traversed by the electron, which is a function of the electron pseudorapidity, being larger at large  $|\eta|$ . Improvements on the order of up to 5% for electron identification efficiency at large  $|\eta|$  in the endcap regions are also demonstrated. Significant improvements are observed in the invariant mass mean and width of  $J/\psi \rightarrow ee$  since the electron four-momentum is computed using the better-estimated track parameters. This note concludes the first phase of a two-step programme in ATLAS to improve the electron reconstruction aiming at correcting all tracks

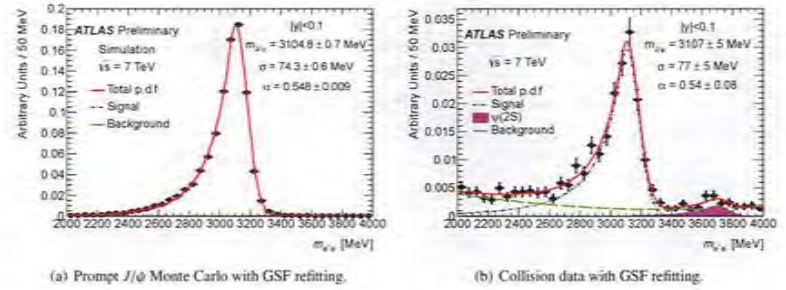


Figure 16: The mass distributions for the GSF-refitted prompt  $J/\psi$  Monte Carlo (a) and collision data samples (b) restricted to a rapidity range  $|\eta| < 0.1$  and fitted using a single Crystal Ball function for the signal (dashed blue line) and a second order Chebyshev polynomial (dashed green line) for the background. In the case of the real data, a second CB function was required to account for the  $\psi(2S)$  (purple filled area). The overall fit is shown in red. The resulting Crystal Ball fit parameters,  $m_{J/\psi}$ ,  $\sigma$  and  $\alpha$ , are displayed with their uncertainties on the plot.

associated to electron candidates by performing bremsstrahlung refitting prior to electron reconstruction and identification. It will be followed by a bremsstrahlung recovery at the initial step of reconstruction, making it the new default electron reconstruction scheme in ATLAS.

## References

- [1] ATLAS Collaboration, G. Aad et al., *The ATLAS Experiment at the CERN Large Hadron Collider*, JINST **3** (2008) S08003.
- [2] R. Fruehwirth, *A Gaussian-mixture approximation of the Bethe-Heitler model of electron energy loss by bremsstrahlung*, Comp. Phys. Comm. **154** (2003) 131.
- [3] T. M. Atkinson, PhD thesis, The University of Melbourne, 2006.
- [4] ATLAS Collaboration, *Electron performance measurements with the ATLAS detector using the 2010 LHC proton-proton collision data*, Eur. Phys. J. **C72** (2012) 1909.
- [5] ATLAS Collaboration, *Expected electron performance in the ATLAS experiment*, ATLAS-PHYS-PUB-2011-006 (2011).
- [6] ATLAS Collaboration, T. Cornelissen et al., *Concepts, Design and Implementation of the ATLAS New Tracking (NEWT)*, ATLAS-SOFT-PUB-2007-007 (2007).
- [7] ATLAS Collaboration, *Expected Performance of the ATLAS Experiment - Detector, Trigger and Physics*, arXiv:0901.0512 [physics.hep-ex].
- [8] H. Bethe and W. Heitler, *The Quantum Theory of Radiation*, Proc. R. Soc. **A146** (1934) 83.
- [9] A. Schaelicke et al., *Improved Description of Bremsstrahlung for High-Energy Electrons in Geant4*, IEEE Nucl. Sci. Symp. Conf. Rec. **N37-1** (2008) 2788.

- [10] The GEANT4 Collaboration, S. Agostinelli et al., *GEANT4: A simulation toolkit*, Nucl. Instrum. Meth. **A506** (2003) 250.
- [11] R. Fruehwirth, *Application of Kalman filtering to track and vertex fitting*, Nucl. Instrum. Meth. **A262** (1987) 444.
- [12] ATLAS Collaboration, *Measurement of the cross-section for b-jets produced in association with a Z-boson at  $\sqrt{s} = 7$  TeV with the ATLAS detector*, Phys. Lett. B **706** (2012) 295.
- [13] ATLAS Collaboration, *Measurement of the top quark pair production cross section in pp collisions at  $\sqrt{s} = 7$  TeV in dilepton final states with ATLAS*, ATLAS-CONF-2011-100 (2011).
- [14] K. Nakamura et al., *Review of Particle Physics*, Physical Review G **37** (2010) 075021.
- [15] T. Sjostrand, S. Mrenna, and P. Z. Skands, *PYTHIA 6.4 Physics and Manual*, JHEP **0605** (2006) 026.
- [16] A. Sherstnev and R. S. Thorne, *Parton Distributions for LO Generators*, EPJC **55** (2008) 553.
- [17] ATLAS Collaboration, *ATLAS tunes of PYTHIA6 and Pythia 8 for MCII*, ATLAS-PHYS-PUB-2011-009 (2011).
- [18] ATLAS Collaboration, *Measurement of the differential cross-sections of inclusive, prompt and non-prompt J/ $\psi$  production in proton-proton collisions at  $\sqrt{s} = 7$  TeV*, Nuclear Physics B **850** (2011) no. 3, 387 – 444.

## A Additional Distributions

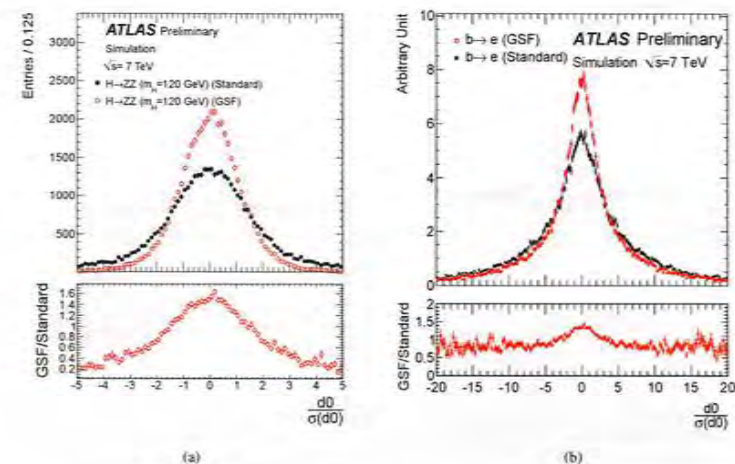


Figure 17: Truth-matched Monte Carlo distribution of the transverse impact parameter significance for both GSF and standard reconstructed electrons from 120 GeV Standard Model Higgs-boson decays (a) and heavy-quark (b) decays. The bottom plots shows the ratio of the entries of the GSF and standard electrons per bin of  $d_0/\sigma_{d_0}$ .

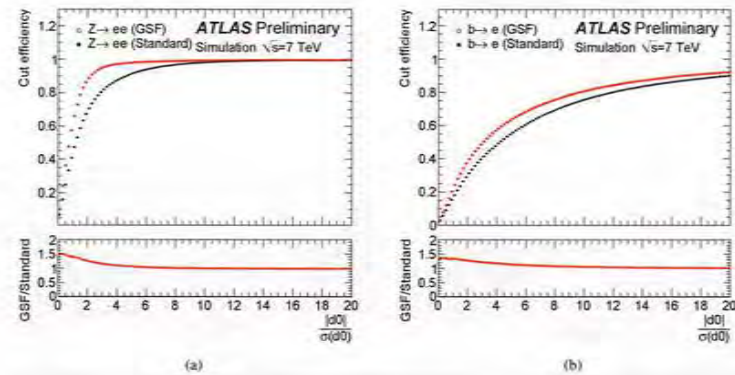


Figure 18: Efficiency for selecting electrons from simulated Z-boson (a) and heavy-quark (b) decays as a function of different requirements on the absolute value of the transverse impact parameter significance.

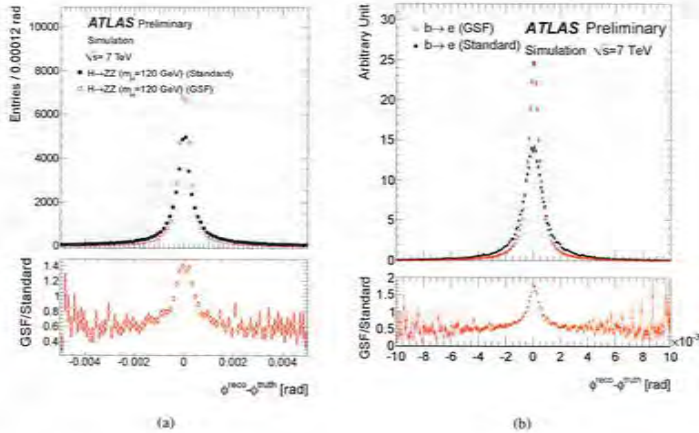


Figure 19: The resolution of the reconstructed electron track direction angle  $\phi$  at the perigee for GSF (open red) and standard (solid black) reconstructed simulated electrons from 120 GeV Standard Model Higgs-boson (a) and from heavy-quark decays (b). The bottom plots shows the ratio of the entries of the GSF and standard electrons.

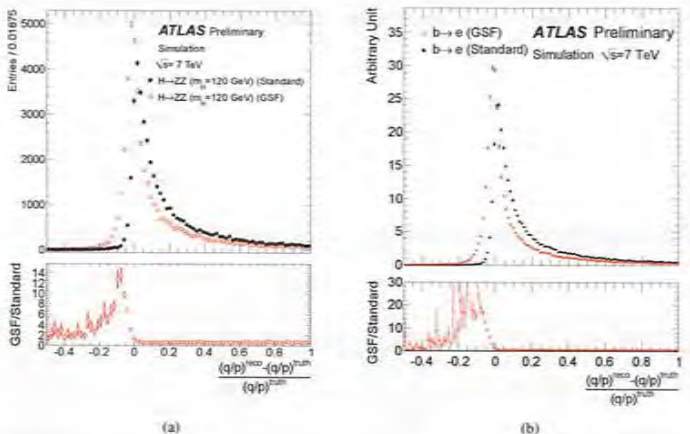


Figure 20: The relative bias of the reconstructed electron track inverse momentum  $1/p$  at the perigee multiplied by the charge  $q$  for both GSF (open red) and standard (solid black) reconstructed simulated electrons from 120 GeV Standard Model Higgs-boson decays (a) and from heavy-quark decays (b). In each case the bottom plot shows the ratio of the entries of the GSF and standard electrons per bin of the relative  $q/p$  bias.

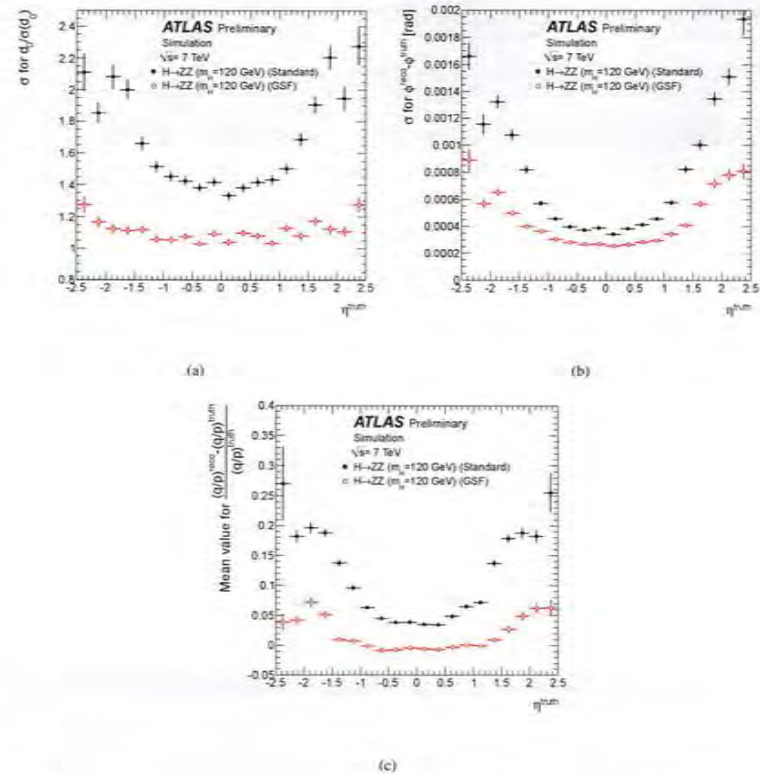


Figure 21: The transverse impact parameter significance pull width (a), the resolution width of the track direction angle  $\phi$  at the perigee (b) and the mean relative bias of the inverse track momentum multiplied by the charge  $q/p$  (c), for truth-matched Monte Carlo electrons as a function of the pseudorapidity  $\eta$  for both GSF (open red) and standard (solid black) reconstructed electrons from 120 GeV Standard Model Higgs-boson decays.

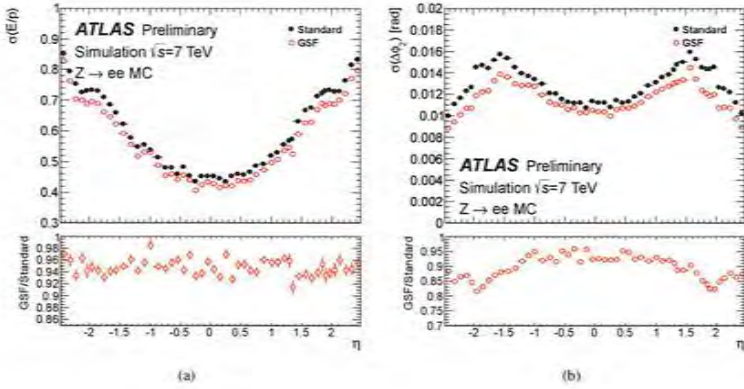


Figure 22: Truth-matched Monte-Carlo distributions of the width ( $\sigma$ ) of the calorimeter energy to track momentum ratio ( $E/p$ ) (a) and of the mean difference of extrapolated track  $\phi$  to the cluster  $\phi$  position as measured in the second sampling of the calorimeter ( $\Delta\phi_2$ ) (b) as a function of  $\eta$ , for GSF (open red) and for standard (solid black) electrons. The GSF-to-standard ratio is given below.

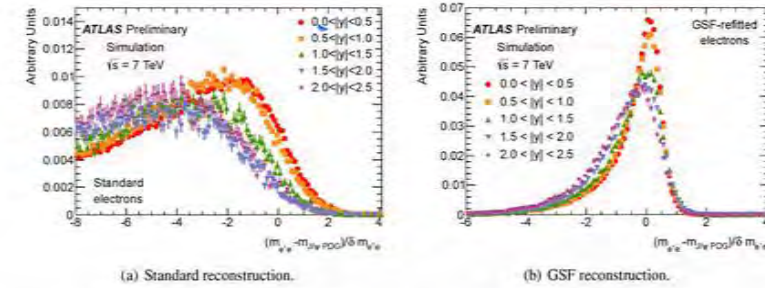


Figure 24: The pull distribution of the di-electron invariant mass, for the standard (a) and GSF (b) reconstruction of MC electrons from  $J/\psi$  decays as a function of the candidate  $J/\psi$  rapidity. Ideally, the distributions should be a Gaussian function centered at zero with unity width in the core, though a tail on the negative side is expected. The results for the GSF are less dependent on rapidity and far closer to the desired distribution than those for the standard reconstruction.

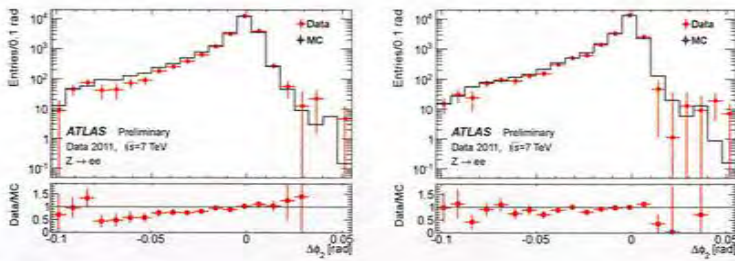
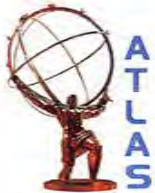


Figure 23: Data comparison to simulation of the extrapolated track  $\phi$  to the cluster  $\phi$  position as measured in the second sampling of the calorimeter ( $\Delta\phi_2$ ), for  $0.8 < |\eta| < 1.37$  (left plot) and  $1.52 < |\eta| < 2.0$  (right plot) for  $Z \rightarrow ee$  candidate GSF electrons with reconstructed electron energy  $15 \text{ GeV} < E_T < 25 \text{ GeV}$ .

०

०



## ATLAS NOTE

April 18, 2011



### Expected electron performance in the ATLAS experiment

The ATLAS collaboration

#### Abstract

We describe the latest improvements in electron reconstruction and identification and give an update on the expected electron performance of the ATLAS detector. All results presented in this note are based on Monte-Carlo simulation studies. They indicate that with a good understanding of the combined inner detector and calorimeter performance, powerful reconstruction software and a detailed material description in front of the calorimeter, a rejection of  $10^5$  against jets and background electrons from photon conversions can be achieved with an electron efficiency of 71% for  $p_T > 20$  GeV. A very high purity electron sample can therefore be obtained in this  $p_T$  range.

## Contents

<b>1</b>	<b>Introduction</b>	<b>1</b>
<b>2</b>	<b>The ATLAS electromagnetic calorimeter and inner detector</b>	<b>2</b>
<b>3</b>	<b>Electron and photon trigger</b>	<b>2</b>
3.1	Electron and Photon Trigger Selection . . . . .	3
3.2	Expected E/ $\gamma$ trigger performance . . . . .	4
<b>4</b>	<b>Electron reconstruction algorithm</b>	<b>6</b>
<b>5</b>	<b>Cuts-based optimisation for electron identification</b>	<b>8</b>
5.1	Definition and optimisation of “loose” and “medium” electron selection . . . . .	9
5.2	Definition and optimisation of electron “tight” selection . . . . .	9
<b>6</b>	<b>Recent changes in electron identification (based on the 2009/2010 LHC data-taking runs)</b>	<b>19</b>
<b>7</b>	<b>Electron isolation algorithm</b>	<b>20</b>
<b>8</b>	<b>Expected electron reconstruction and identification performance</b>	<b>20</b>
8.1	High $p_T$ electrons: Standard Model processes . . . . .	22
8.1.1	Results of standard selection . . . . .	22
8.1.2	Results on recent modification of identification (based on 2009/2010 Run) . . . . .	26
8.1.3	Possible further improvements of the tight selection . . . . .	26
8.2	High $p_T$ electrons: Beyond the Standard Model processes . . . . .	27
8.3	Low $p_T$ electrons from J/ $\psi$ . . . . .	27
<b>9</b>	<b>Forward algorithm in high <math>\eta</math> electron studies</b>	<b>28</b>
9.1	Optimisation . . . . .	29
9.2	Expected performance . . . . .	31
<b>10</b>	<b>Conclusion</b>	<b>31</b>

## 1 Introduction

Estimating the nature and relative contributions of the main backgrounds to measurements in final states with isolated electrons at the LHC over the full detector acceptance is of crucial importance. The background to isolated electrons include electrons from heavy flavors and background electrons from Dalitz decays or photon conversions originating from neutral pion decays and jets. It has been shown that in the case of inclusive electron searches, a rejection of  $10^5$  against jets and background electrons is required to bring the background safely below the level of single isolated electrons, which is about two orders of magnitude worse than at the Tevatron [1]. At the same time, a high and uniform efficiency over the full  $p_T$  and  $\eta$  range is necessary<sup>1</sup>. To achieve this, the combination of inner detector and calorimeter information, a powerful reconstruction software as well as a detailed material description in front of the calorimeter are essential. This note describes the latest status of the reconstruction and identification

<sup>1</sup>In the right-handed ATLAS coordinate system, the pseudorapidity  $\eta$  is defined as  $\eta = -\ln[\tan(\theta/2)]$ , where the polar angle  $\theta$  is measured with respect to the LHC beamline. The azimuthal angle  $\phi$  is measured with respect to the  $x$ -axis, which points towards the center of the LHC ring. The  $z$ -axis is parallel to the anti-clockwise beam viewed from above. Transverse momentum and energy are defined as  $p_T = p \sin \theta$  and  $E_T = E \sin \theta$ , respectively.

algorithms as well as the expected performance on physics processes. The performance numbers quoted in this note are mostly based on simulated samples at  $\sqrt{s} = 10$  TeV and are calculated in the absence of pile-up. Updated numbers on efficiency and rejection related to recent changes in the identification selection are given for samples at  $\sqrt{s} = 7$  TeV. The difference between 7 TeV and 10 TeV samples is expected to be small for efficiency and rejection estimates over the whole phase space. We will focus on cuts-based electron identification as opposed to more complex multivariate identification tools that are described elsewhere [2].

Electron trigger performance is described in Section 3. In the following sections the improvements in reconstruction are discussed followed by the offline identification cut optimisation strategy, chosen variables and cut values. Section 6 describes the most recent changes in electron identification based on the 2009/2010 LHC data-taking runs. Section 7 is dedicated to the calorimeter and tracking isolation and the final sections to the estimated efficiency and rejection for known and hypothetical physics processes covering the detector  $p_T$  and  $\eta$  acceptance.

## 2 The ATLAS electromagnetic calorimeter and inner detector

The ATLAS electromagnetic (EM) calorimeter has a fine segmentation in both the lateral ( $\eta \times \phi$  space) and longitudinal directions of the showers. At high energy, most of the EM shower energy is collected in the second layer which has a lateral granularity of  $0.025 \times 0.025$  in  $\eta \times \phi$  space. The first layer consists of finer-grained strips in the  $\eta$ -direction (with a coarser granularity in  $\phi$ ), which offer excellent  $\gamma - x^0$  discrimination. These two layers are complemented by a presampler layer placed in front with coarse granularity to correct for energy lost in the material before the calorimeter, and by a back layer behind, which enables a correction to be made for the tail of very highly energetic EM showers. The transition region between the barrel and end-cap EM calorimeters,  $1.37 < |\eta| < 1.52$ , is expected to have poorer performance because of the large amount of material in front of the first active calorimeter layers. The presampler layer covers only the range  $|\eta| < 1.8$ . The end-cap EM calorimeters (EMEC) are divided into two wheels, the outer and inner wheels covering the ranges  $1.375 < |\eta| < 2.5$  and  $2.5 < |\eta| < 3.2$ , respectively. The forward calorimeters (FCal) cover the range  $3.1 < |\eta| < 4.9$  and also provide some EM shower identification thanks to their longitudinal segmentation into three layers as well as the different absorber material used (copper for the layer closest to the interaction point and tungsten for the other two).

The ATLAS inner detector provides precise track reconstruction over  $|\eta| < 2.5$ . It consists of three layers of pixel detectors close to the beam-pipe, four layers of silicon microstrip detectors (SCT) providing eight hits per track at intermediate radii, and a transition radiation tracker (TRT) at the outer radii, providing about 35 hits per track (in the range  $|\eta| < 2.0$ ). The TRT also provides substantial discriminating power between electrons and pions over a wide energy range (between 0.5 and 100 GeV). The pixel vertexing layer (also called the b-layer) is located just outside the beam-pipe at a radius of 50 mm, and provides precision vertexing and significant rejection of photon conversions (through a requirement of a track with a hit in this layer).

## 3 Electron and photon trigger

The ATLAS trigger system is divided into three levels. The hardware based first level trigger (L1) performs a preliminary selection using reduced granularity data from the calorimeter and dedicated muon chamber information. It operates within a latency of  $2.5 \mu\text{s}$ , designed for an average output rate of 75 kHz, with an upper limit of 100 kHz. Further event selection is done by the software based second level trigger (L2) and Event Filter (EF), collectively referred to as the High Level Trigger (HLT). The

reconstruction at L2 is seeded by the L1 result and uses the full granularity of the ATLAS subdetectors. The processed data are contained in the regions of the detector identified by the L1 as Regions of Interest (RoI) and corresponds to about 1.4 % of the data of each detector. The L2 is designed to give an output rate of less than 2 kHz with a mean processing time of 40 ms. Upon an L2 accept all the detector data are combined together into a single data block in a process called event-building. The EF has a latency of 4 s. The event rate is further reduced to about 200 Hz. Seeded by the L2 results, more complex algorithms, profiting from offline-like calibration and alignment can be used.

### 3.1 Electron and Photon Trigger Selection

At L1, photons and electrons are selected using calorimeter information with a reduced granularity which is given by the so-called Trigger Tower (TT), with a size of  $\Delta\eta \times \Delta\phi = 0.1 \times 0.1$ . RoIs are formed for each identified electromagnetic object and information on the  $\eta$  and  $\phi$  position and the energy threshold passed are associated to them. The L1 cluster size is  $4 \times 4$  trigger towers.

L2 is seeded by these L1 RoIs. At this stage full granularity data are available. Fast calorimeter and tracking reconstruction algorithms are deployed. The default calorimeter reconstruction works in a similar way as the offline algorithms (the offline algorithms will be described in the next section). The main difference to the offline is the cluster seed finding step which is done using the most energetic cell in the second EM layer at L2 while in the offline reconstruction the sliding window algorithm is used. Cluster building, calibration and cluster corrections are the same as in the offline reconstruction. For tracking purposes three different tracking algorithms are available: SiTrack, IdScan and TRTSegFinder. SiTrack and IdScan have been developed in an independent way from the offline track reconstruction to fulfill the more stringent requirements at L2 concerning timing and complexity. TRTSegfinder has been ported from the offline into L2. Detailed information about these algorithms can be found in [2]. The main characteristics are:

- IdScan: fast pattern recognition is done by first determining the z-position of the interaction point along the beam axis and then performing combinatorial tracking only inside groups of space points that point back to that determined position.
- SiTrack: the formation of track seeds is done using all possible pairing of space points coming from the innermost two layers. Each seed is extrapolated to the beam line using a straight line approximation and a transverse impact parameter cut is applied. Each remaining seed is then extrapolated to the following silicon layers and extensions to the track are selected applying a cut on the distance between the outer space point and the extrapolated seed. The full track is then formed from the union of the space points from all the merged extensions and a track refit is done after removal of duplicate tracks.
- TRTSegFinder: TRT track reconstruction is based on the Hough-transform [3] (histogramming) method. In the initialisation step, a set of trajectories in the  $\phi - R(Z)$  space is calculated in the barrel (endcap) TRT taking into account the value of the local magnetic field. Then a histogram is filled for each event with the TRT hit positions. Track candidates are identified from peaks in this histogram. At least 8 hits are required for a track candidate which in addition has to fulfill track quality criteria such as number of unique hits (hits belonging to only one track) and the ratio of hits to number of straws crossed by the trajectory. In the final step drift information is used by tuning the parameters so that the track lies on the maximum number of drift circle positions.

The performance of SiTrack and IdScan in simulation is similar. However, differences in performance very likely will occur during data taking due to e.g. the effects from dead and noisy channels. In initial running all three will be run to ensure minimal trigger losses with respect to offline. In the software

release used for these studies, the main electron chains use an ‘or’ between SiTrack and IdScan. The EF uses the offline reconstruction algorithms. Due to timing constraints, Bremsstrahlung recovery is not performed. Non-essential parts for the identification of  $e/\gamma$  candidates, such as the four-momentum builder, are not run. The electron and photon identification performed at the trigger level is similar to the offline identification (the offline identification selection will be described later). The cuts used at the EF level are harmonised to the offline ones. However, unlike the offline identification cuts, the trigger level cuts are not  $p_T$  dependent. The cuts for the trigger selection are taken from the offline selection in the  $p_T$  bin corresponding to the trigger threshold. At L2 only a subset of the offline/EF selection criteria is used and the optimisation is done in such a way that the cuts are looser than the EF ones. For the first physics runs, the so called primary or main triggers to be used and their physics motivations are summarised in Table 1.

Signature	Motivation
2e5.medium	$J/\psi \rightarrow ee, Y \rightarrow ee$ , Drell-Yan production
e10.medium	$e^\pm$ from b,c decays, E/p studies
g20.loose	direct photon production, jet calibration using $\gamma$ -jet events, high- $p_T$ physics, e-no track trigger
e20.loose	high- $p_T$ physics, $Z \rightarrow ee, W \rightarrow e\nu$
em105.passHLT	New physics, check for possible problems

Table 1: Summary of the main electron and photon triggers envisaged for the first physics run at  $L \approx 10^{31} \text{cm}^{-2}\text{s}^{-1}$  together with their physics motivation. The terminology used for the trigger signature column in the table is the following: “2e5.medium” for example stands for 2 electron objects with a  $p_T$  greater than 5 GeV and “medium” identification requirements (the electron identification criteria is explained in Section 5); “g20.loose” describes a single photon trigger with a threshold of 20 GeV and “loose” identification requirements; “em105.passHLT” is a trigger that looks for energy deposits greater than 105 GeV in the electromagnetic calorimeter, “passHLT” meaning that there is no requirements (no selection) at the high level trigger.

### 3.2 Expected $E/\gamma$ trigger performance

For the first physics run a luminosity of  $L = 10^{31} \text{cm}^{-2}\text{s}^{-1}$  was assumed at a center of mass energy of 10 TeV. In the meantime the center of mass energy for initial running has been reduced to 7 TeV. Table 2 shows the expected trigger rates for the primary  $e/\gamma$  triggers at 10 TeV. At 7 TeV, the cross sections of the backgrounds and Standard Model physics channels are about 30% lower with the exception of minimum bias events, which only decrease by about 10%. The uncertainties on the QCD jet production from MC is of the order of 2-3%. Fig. 1 shows the electron trigger efficiency as a function of  $E_T$  and  $|\eta|$  for the primary triggers foreseen at  $L = 10^{31} \text{cm}^{-2}\text{s}^{-1}$ . The efficiencies in the plateau region are also given in Table 3. The trigger losses with respect to offline are of the order of 1% and to a large extent occur in the barrel/endcap crack region. At L2, the e5.medium and e10.medium losses are mainly arising from the calorimeter selections, tracks which were not found by the L2 Si-based tracking algorithms (especially in the end-cap region) and by losses due to the cluster-track matching cuts in  $\eta$  and  $\phi$ .

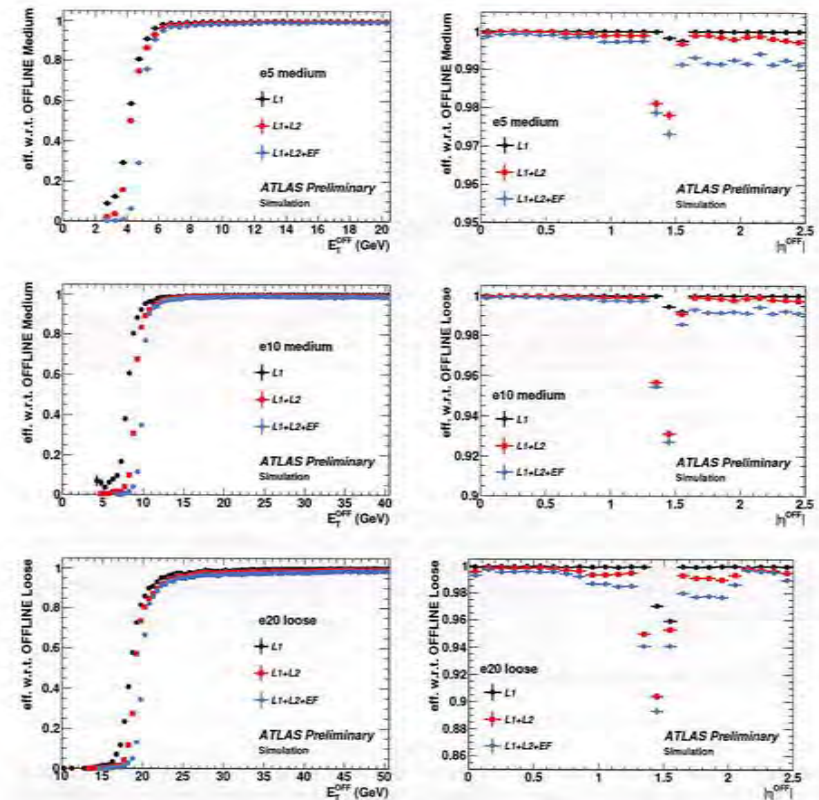


Figure 1: Trigger efficiencies at L1, L2 and EF as a function of the generated electron  $E_T$  (left) and  $|\eta|$  (right) for the signatures e5.medium, e10.medium and e20.loose. The efficiencies are obtained using single electrons from a sample with  $0.5 < E_T < 80$  GeV and are normalised with respect to offline electrons with  $E_T > 5, 10$  or  $20$  GeV passing the medium (for e5.medium and e10.medium) or loose (for e20.loose) set of electron identification cuts in the  $\eta$  range -2.5 to 2.5 (see section 5 for details on offline identification selection). For the  $|\eta|$  plot single electrons with an offline  $E_T > 10, 15$  or  $25$  GeV (from the top to the bottom plot) were chosen to show the efficiency in the plateau.

Level	2e5_medium	e10_medium	g20_loose	e20_loose	em105_passHLT
L1	1850 Hz	2370 Hz	130 Hz	130 Hz	< 1 Hz
L2	76 Hz	184 Hz	55 Hz	23 Hz	< 1 Hz
EF	1.3 Hz	18.4 Hz	10.5 Hz	2.9 Hz	< 1 Hz

Table 2: Expected trigger rates for the primary triggers to be run at  $L = 10^{31} \text{cm}^{-2}\text{s}^{-1}$  assuming collisions at 10 TeV center of mass energy. These numbers were obtained from a sample of 130k of enhanced bias data (minimum bias events filtered by the lowest L1 thresholds).

Level	e5_medium	e10_medium	e20_loose
L1	99.99 $\pm$ 0.002%	99.95 $\pm$ 0.004%	99.68 $\pm$ 0.01%
L2	99.76 $\pm$ 0.01%	99.47 $\pm$ 0.01%	98.89 $\pm$ 0.02%
EF	99.44 $\pm$ 0.01%	99.2 $\pm$ 0.01%	98.28 $\pm$ 0.02%

Table 3: Expected trigger efficiencies for the primary triggers to be run at  $L = 10^{31} \text{cm}^{-2}\text{s}^{-1}$  as obtained from a single electron data sample with a flat distribution in pseudorapidity ( $|\eta| < 2.5$ ) and a flat energy distribution with  $7 < E_T < 80 \text{ GeV}$ . The efficiencies for e5\_medium and e10\_medium are given with respect to the medium offline selections (see section 5 for details on offline identification selection) with a  $E_T$  threshold which is 5 GeV higher than the cut applied at the EF (e.g. it is 10 GeV for e5\_medium). In the case of e20\_loose the efficiency is given with respect to the loose offline selections. The error given is the statistical error.

Each of these sources of losses occur equally frequently in e5\_medium, however, for e10\_medium, the majority of the L2 losses arise from the cluster-track matching cuts. At EF the losses for these triggers arise mainly from differences in the tracking. In the case of e20\_loose, additional losses of 0.8% occur due to loose offline electron objects associated with a TRT-only track. Thus, these tracks are not reconstructed by the Si-based L2 track algorithms, but are, to a large extent, reconstructed by the TRT based L2 tracking algorithm.

#### 4 Electron reconstruction algorithm

The standard electron reconstruction procedure is based on clusters reconstructed in the electromagnetic calorimeter, which then are associated to tracks of charged particles reconstructed in the Inner Detector. This algorithm has been developed to allow for an optimal reconstruction of the four-momentum of electrons for the full momentum and pseudorapidity range and for any luminosity. Information from both detectors is used to allow electrons to be identified with the lowest possible amount of background, keeping in mind that the optimum between the identification efficiency and background rejection depends on the analysis.

Electron reconstruction begins with the creation of a preliminary set of seed clusters. Seed clusters with energies above 2.5 GeV are formed by a sliding window algorithm, where the seed clusters are  $3 \times 5$  in  $\eta/\phi$  middle layer cell units ( $0.025 \times 0.025$ ). After an energy comparison, duplicate clusters are removed from nearby seed clusters.

In the region of the tracker detectors ( $|\eta| < 2.5$ ), an electron is defined by the existence of one or more reconstructed tracks matched to a seed cluster. The  $\eta$  region above 2.5 will be discussed in Section 9. The track-to-cluster matching thus forms the central part of the electron reconstruction. Reconstructed tracks are matched to seed clusters by extrapolating them from their last measurement point to the second

layer of the calorimeter.

The impact point  $\eta$  and  $\phi$  coordinates are then compared to the corresponding seed cluster  $\eta$  and  $\phi$  in that layer. If their difference is below a certain threshold then the track is considered matched to the cluster. Special care is taken in order to account for Bremsstrahlung losses. To this end, the sign-corrected  $\Delta\phi$  window is larger on the side where the extrapolated track bends as it traverses the tracker magnetic field. In the case of tracks that do not contain silicon hits, the matching is restricted to the  $\phi$  coordinate, due to the fact that the accuracy on the  $\eta$  coordinate, as measured by the TRT, is limited. In this case only a rough track matching, e.g. barrel track matched to a barrel cluster, is required.

It is quite possible (e.g. in the case of electromagnetic showers) that more than one track matches the same seed cluster. In this case all the tracks are retained and ordered according to the quality of their match. The track with the smallest difference  $\Delta R = \sqrt{\Delta\eta^2 + \Delta\phi^2}$  between its impact point on the electromagnetic calorimeter and the seed cluster is considered as the best match. Tracks with silicon hits have priority over tracks without silicon hits, the latter tracks being viewed as more likely to belong to electrons originating from photon conversions. The information related to the track-to-cluster matching is retained for all the tracks assigned to the reconstructed electron object and is used during the particle identification, as described later in this note.

As mentioned above, the track matching is affected by Bremsstrahlung losses which result in an asymmetric sign-dependent  $\Delta\phi$  distribution. Studies have shown that this distribution becomes symmetric if one extrapolates the track from the perigee and uses the cluster energy for the electron momentum. While the extrapolation from the last measurement is used in the track match, the  $\Delta\phi$  value from the extrapolation computed with the latter procedure is stored for each track assigned to the electron object. Using the new extrapolation in the track-to-cluster match remains an option and could be used during any reprocessing campaign.

There is an inherent ambiguity between a prompt electron and a converted photon, since both objects are characterized by the existence of tracks pointing to an electromagnetic cluster. In the current reconstruction strategy, objects that have tracks matched to seed clusters will subsequently be treated as electrons. As a result almost all converted photons will be handled as electrons during this stage of the reconstruction and end up in the electron container. This results in a significant contamination of the electron sample by converted photons but ensures on the other hand a high electron reconstruction efficiency. The particle identification criteria, described later in this note, will be able to select the prompt electrons from the original electron candidate sample. Converted photons which are ambiguous with reconstructed electrons are specifically labeled and can also be found in the photon container (as duplicates).

Electromagnetic showers characterized by tracks matched to the seed cluster are considered as electron candidates. The electromagnetic cluster is then recomputed using a  $3 \times 7$  ( $5 \times 5$ ) sliding window in  $\eta/\phi$  middle layer cell units (end caps). A  $3 \times 5$  seed cluster size is explicitly chosen to be a subset of the final electromagnetic cluster sizes. Several corrections to the reconstructed cluster energy are then applied. Finally the electron four-momentum is computed using in addition the track information from the best track matched to the original seed cluster (keeping links to all tracks matched to the electron in a  $\Delta\eta, \Delta\phi$  window). The energy is computed as a weighted average between the cluster energy and the track momentum. The  $\phi$  and  $\eta$  directions are taken from the corresponding track parameters unless the track contains no silicon hits, in which case  $\eta$  is provided by the cluster  $\eta$ -pointing. In cases where the track has only TRT hits, the  $\phi$  position is taken from the track and the  $\eta$  is provided by cluster  $\eta$ -pointing.

The reconstruction efficiency of low- $p_T$  electrons (a few GeV) can be improved by using the track as a starting point. The track is then extrapolated to the electromagnetic calorimeter and a cluster is built using the track impact point as a seed. This algorithm will not be further described in this note. It is described in detail in [2]. In the case of very forward electrons, where there are no tracking detectors, the electron candidates contain only the electromagnetic calorimeter cluster information.

The most important changes in the electron reconstruction since reference [1] concern the cluster seed finding and track matching. The cluster seed definition was changed to improve the performance at low energy. Moving from  $5 \times 5$  cells in middle layer cell units with a threshold of 3 GeV used in [1] to  $3 \times 5$  cells and 2.5 GeV threshold improves the reconstruction efficiency of low energy clusters and lowers the duplicate cluster rate. The duplicate cluster rates are now below the percent level for both  $Z \rightarrow e^+e^-$  and  $J/\psi \rightarrow e^+e^-$  events, while with the previous cluster definition this was a few percent. The improvements in the cluster-track match concern both the selection criteria and the cuts applied. In reference [1], track candidates were rejected for  $E/p > 10$  and the "best track" was selected to be the one with  $E/p$  closest to 1. The  $E/p$  cut resulted in a few percent inefficiency due to Bremsstrahlung losses mostly at large  $\eta$ . The  $E/p$  cut is now not applied anymore. In addition, only one track match was kept for further analysis. This has now been extended to include all matches in a  $\Delta\eta$ ,  $\Delta\phi$  window, giving priority to tracks with silicon hits. This facilitates the study of complicated topologies.

## 5 Cuts-based optimisation for electron identification

The baseline electron identification in ATLAS relies on cuts using variables that provide good separation between isolated electrons and jets (faking electrons). These variables include calorimeter, tracker and combined calorimeter/tracker information. They can be applied independently and three reference sets of cuts have been defined with increasing background rejection power: loose, medium and tight. Shower shape variables of the second calorimeter layer and hadronic leakage variables are used in the loose selection. First calorimeter layer cuts, track quality requirements and track-cluster matching are added at the level of the medium selection. The tight selection adds  $E/p$ , b-layer hit requirements and the particle identification potential of the TRT. Table 4 gives the list of all variables used in the "loose", "medium" and "tight" selections. To allow for robustness at startup, various changes are made based on the expected level of understanding of the detector performance (changes are given with respect to [2]):

- The cluster track matching and transverse impact parameter requirements are loosened.
- Redundant first layer variables are removed from the selection and new, more discriminant, variables are added.
- All first layer cuts are loosened to account for uncertainties on the material in front of the calorimeter and cross-talk dependence. For compensation, the lateral shower shape cuts in the second layer of the EM calorimeter are tightened as well as the hadronic leakage requirements.
- In addition, the trigger and offline selection have been harmonised in accordance with g20 loose and e10 medium rate requirements (see section 3 for details).

The classification of electron candidates based on Monte-Carlo truth is crucial for any cut optimisation. Truth classification (provided by a common tool in ATLAS) was used for all of the following cut optimisation studies. The categories most commonly considered are:

- Isolated electrons, if they match a true electron originating from a Z or W boson.
- Hadron Fakes, if they do not match a true electron, muon or tau.
- Non-isolated electrons, if they match a true electron originating from b(c)-mesons.
- Background electrons, if they match a true electrons coming from Dalitz decays or coming from a photon. The electrons from photons can be further divided depending upon the origin of the photon, for example the photon may arise from a decay of a neutral pion, from the Bremsstrahlung cascade from a true electron coming from a Z, or from an initial or final state radiation of a Z boson.

### 5.1 Definition and optimisation of "loose" and "medium" electron selection

The shower variables used in the loose and medium selection are given as an input to a multi-variate analysis program (TMVA [4]) in order to perform a cut optimisation in 10 bins of cluster  $\eta$  (defined by calorimeter geometry, detector acceptances and regions of increasing material in the inner detector) and 11 bins of cluster  $E_T$  (from 5 to above 80 GeV). This allows for a proper handling of correlations between variables assuring the highest possible electron efficiency for a given jet rejection (results on efficiency and rejection are given in section 8). The "loose" selection uses the following variables (see also Table 4 for definitions):

- $R_{had}$ ,  $R_{had}$ : The distributions of these variables are shown in Fig. 2 for isolated and non-isolated electrons and all background electron candidates. Fig. 3 highlights the  $E_T$  dependence of this variable. All layers of the hadronic calorimeter are summed in the region  $|\eta| > 0.8$  and  $|\eta| < 1.37$  to compensate for the crack between the barrel and extended barrel of the tiles.
- $w_{\eta 2}$ : The distributions of these variables are shown in Fig. 4 for isolated and non-isolated electrons and all background electron candidates. Fig. 5 highlights the  $E_T$  dependence of this variable.
- $R_\eta$ : The distributions of these variables are shown in Fig. 6 for isolated and non-isolated electrons and all background electron candidates. Fig. 7 highlights the  $E_T$  dependence of this variable.

The "medium" selection adds the following shower variables to the "loose" selection (see also Table 4 for definitions):

- $w_{\text{soft}}$ : The distributions of these variables are shown in Fig. 8 for isolated and non-isolated electrons and all background electron candidates. Fig. 9 highlights the  $E_T$  dependence of this variable.
- $E_{\text{raw}}$ : The distributions of these variables shown in Fig. 10 for isolated and non-isolated electrons and all background electron candidates. Fig. 11 highlights the  $E_T$  dependence of this variable.

The "medium" selection also includes tracking related cuts (shown in Fig. 13 to 12) which are optimised by considering their robustness for first data:

- The cut on the number of pixel-layer hits and on total number of silicon hits are set to  $\geq 1$  and  $\geq 7$  respectively. These values have shown to provide high efficiency with good rejection while being at the same time quite robust.
- Following a similar argument the cut on the  $\Delta\eta$  matching between the extrapolated track and the cluster  $\Delta\eta_1 = |\eta_{\text{calo}}^{\text{layer}} - \eta_{\text{track}}|$  is set to  $\leq 0.01$ . Fig. 13 shows the  $\Delta\eta$  distribution for the different types of electron candidates.
- Finally, the cut on the electron transverse impact parameter  $d_0$  is set to  $\leq 5$  mm.  $d_0$  is calculated with respect to the beam spot.

### 5.2 Definition and optimisation of electron "tight" selection

The tight selection is foreseen to achieve high rejection power. The variables added to the "loose" and "medium" selection in the "tight" definition are shown in Fig. 14 and 15 and defined in Table 4. The variables used and cuts applied are the following:

- $\Delta\phi$  between the cluster position in the second layer of the calorimeter and the extrapolated track. The distribution of this variable is shown in Fig. 14 and the cut value is set to 0.02.
- Cluster energy over track momentum ( $E/p$ ). The distribution of this variable is shown in Fig. 14.

- Total number of TRT hits. The difference between the measured number of hits and the expected average number of hits is required to be within 15 hits. This variable is shown in Fig. 14.
- Fraction of high threshold TRT hits. The distribution of this variable is shown in Fig. 15.
- Electrons matching reconstructed conversion photons are rejected. Details on how photon conversions are reconstructed are given in [5]. Fig. 16 shows the conversion bit for all candidates passing the previous tight cuts.

In addition, the tight selection has stricter  $|\Delta\eta| < 0.005$  and impact parameter cut ( $< 1.0$  mm) than the medium selection.

Type	Description	Variable name
Loose cuts		
Acceptance of the detector	* $ \eta  < 2.47$	
Hadronic leakage	<ul style="list-style-type: none"> <li>* Ratio of <math>E_T</math> in the first layer of the hadronic calorimeter to <math>E_T</math> of the EM cluster (used over the range <math> \eta  &lt; 0.8</math> and <math> \eta  &gt; 1.37</math>)</li> <li>* Ratio of <math>E_T</math> in the hadronic calorimeter to <math>E_T</math> of the EM cluster (used over the range <math> \eta  &gt; 0.8</math> and <math> \eta  &lt; 1.37</math>)</li> </ul>	$R_{had1}$ $R_{had2}$
Second layer of EM calorimeter	<ul style="list-style-type: none"> <li>* Ratio in <math>\eta</math> of cell energies in <math>3 \times 7</math> versus <math>7 \times 7</math> cells.</li> <li>* Lateral width of the shower.</li> </ul>	$R_\eta$ $w_{\eta 2}$
Medium cuts (includes Loose)		
First layer of EM calorimeter	<ul style="list-style-type: none"> <li>* Total shower width.</li> <li>* Ratio of the energy difference associated with the largest and second largest energy deposit over the sum of these energies.</li> </ul>	$w_{jet}$ $E_{ratio}$
Track quality	<ul style="list-style-type: none"> <li>* Number of hits in the pixel detector (<math>\geq 1</math>).</li> <li>* Number of hits in the pixels and SCT (<math>\geq 7</math>).</li> <li>* Transverse impact parameter (<math>&lt; 5</math> mm).</li> </ul>	$d_0$
Track matching	* $\Delta\eta$ between the cluster and the track ( $< 0.01$ ).	$\Delta\eta_1$
Tight cuts (includes Medium)		
b-layer	* Number of hits in the b-layer ( $\geq 1$ ).	
Track matching	<ul style="list-style-type: none"> <li>* <math>\Delta\phi</math> between the cluster and the track (<math>&lt; 0.02</math>).</li> <li>* Ratio of the cluster energy to the track momentum</li> <li>* Tighter <math>\Delta\eta</math> cut (<math>&lt; 0.005</math>)</li> </ul>	$\delta\phi_1$ $E/p$ $\Delta\eta_1$
Track quality	* Tighter transverse impact parameter cut ( $< 1$ mm).	$d_0$
TRT	<ul style="list-style-type: none"> <li>* Total number of hits in the TRT.</li> <li>* Ratio of the number of high-threshold hits to the total number of hits in the TRT.</li> </ul>	
Conversions	* Electron candidates matching to reconstructed photon conversions are rejected	

Table 4: Definition of variables used for loose, medium and tight electron identification cuts for the central region of the detector ( $|\eta| < 2.47$ )

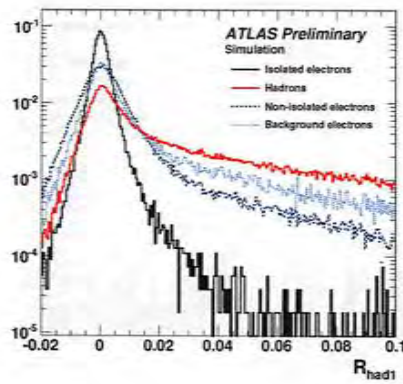


Figure 2: Energy leakage into the first layer of the hadronic calorimeter over cluster  $E_T$  for isolated electrons and the main backgrounds to isolated electron studies.

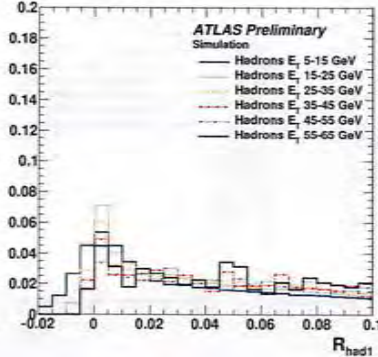
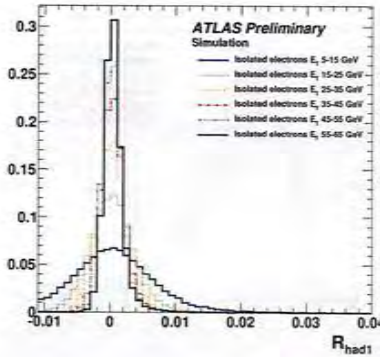


Figure 3: Energy leakage into the hadronic calorimeter over cluster  $E_T$  for isolated electrons (left) and hadrons faking electrons (right) in various  $E_T$  bins

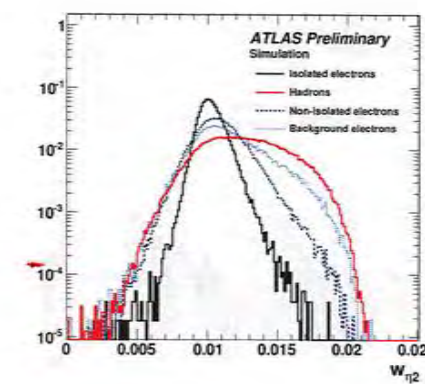


Figure 4: Shower width in the second compartment of the electromagnetic calorimeter for isolated electrons and the main backgrounds to isolated electron studies.

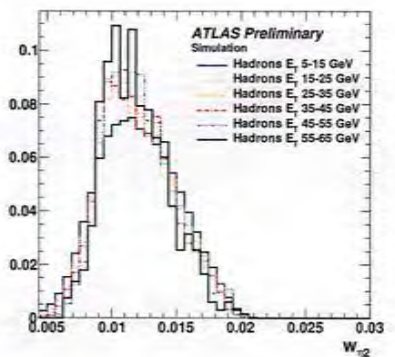
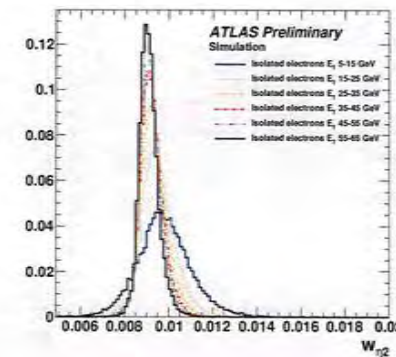


Figure 5: Shower width of isolated electrons (left) and hadrons faking electrons (right) in various cluster  $E_T$  bins

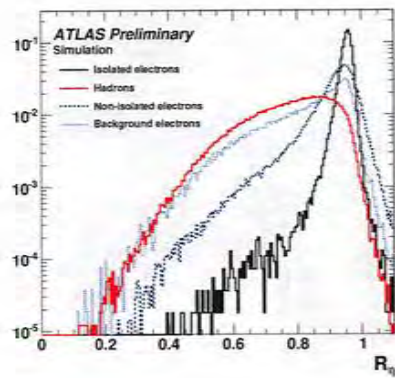


Figure 6: Ratio of energy in 3x7 over 7x7 cells in the second compartment of the electromagnetic calorimeter for isolated electrons and the main backgrounds to isolated electron studies.

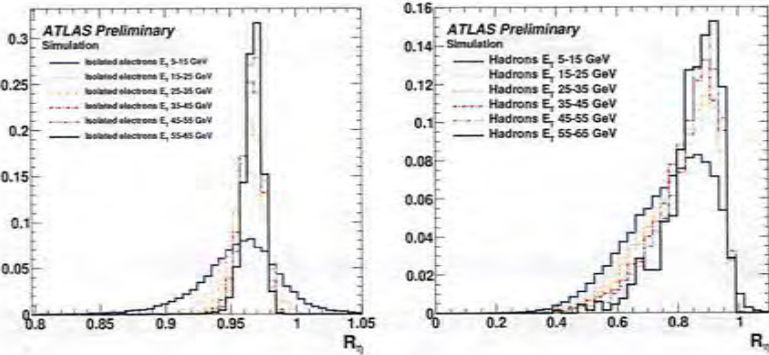


Figure 7: Ratio of energy in 3x7 over 7x7 cells in the second compartment of the electromagnetic calorimeter for isolated electrons (left) and hadrons faking electrons (right) in various  $E_T$  bins

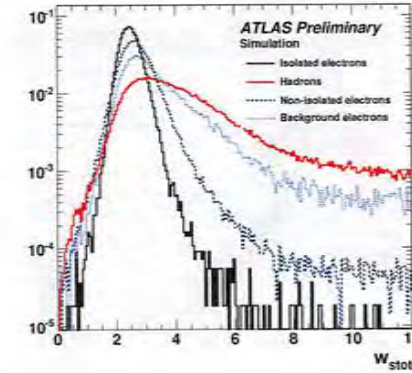


Figure 8: Shower width in the first compartment for isolated electrons and the main backgrounds to isolated electron studies.

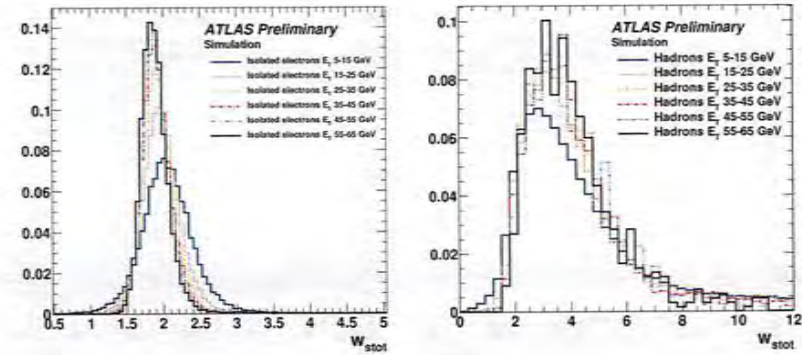


Figure 9: Shower width in the first compartment for isolated electrons (left) and hadrons faking electrons (right) in various  $E_T$  bins

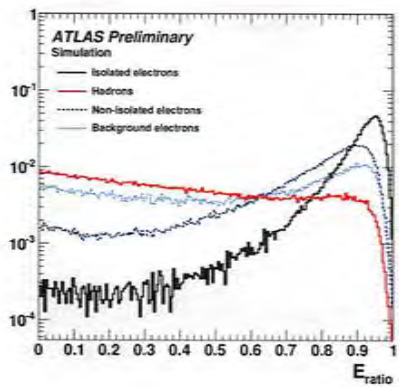


Figure 10: Ratio of the energy difference associated with the largest and second largest energy deposit over the sum of these energies for isolated electrons and the main backgrounds to isolated electron studies.

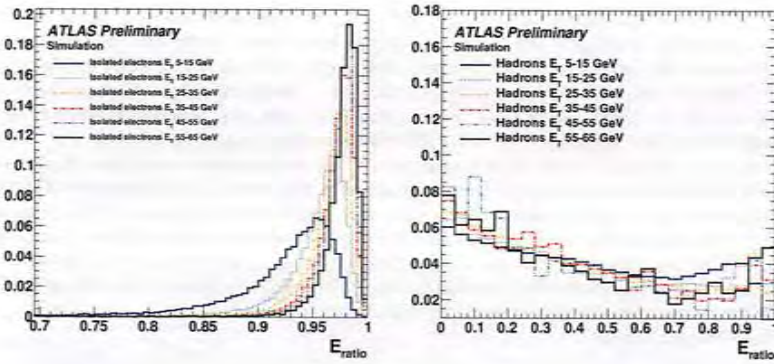


Figure 11: Ratio of the energy difference associated with the largest and second largest energy deposit over the sum of these energies for isolated electrons (left) and hadrons faking electrons (right) in various  $E_T$  bins

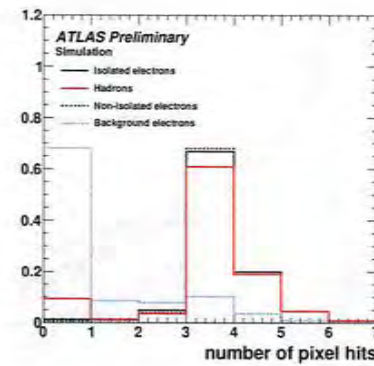


Figure 12: Number of pixel (left) and silicon hits (right) for isolated electrons and the main backgrounds to isolated electron studies.

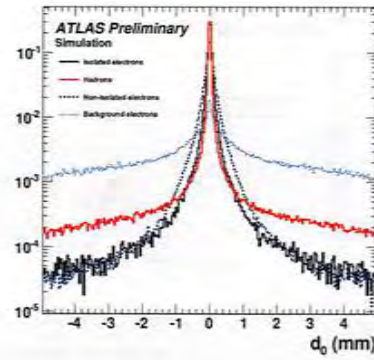
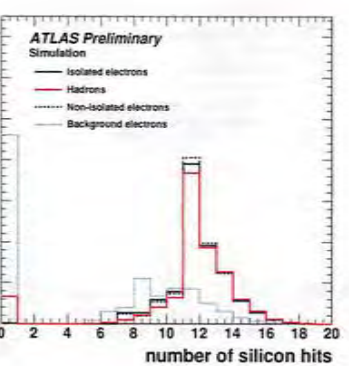
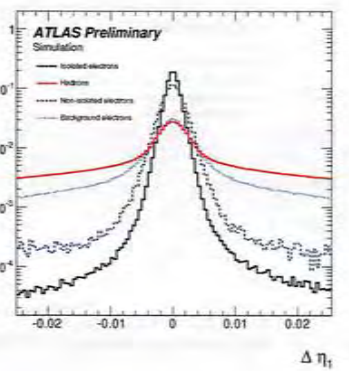


Figure 13: Impact parameter of electron track (left) and difference between cluster  $\eta$  and  $\eta$  of extrapolated track for isolated electrons and the main backgrounds to isolated electron studies.



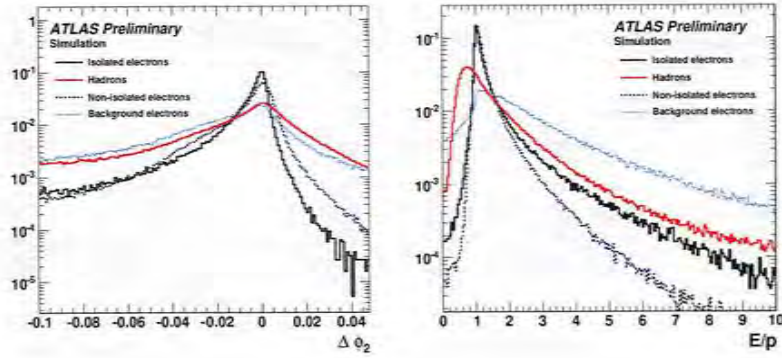


Figure 14: Difference between cluster  $\phi$  and  $\phi$  of the extrapolated track (left), ratio of  $E$  over  $p$  (right) for isolated electrons and the main backgrounds to isolated electron studies.

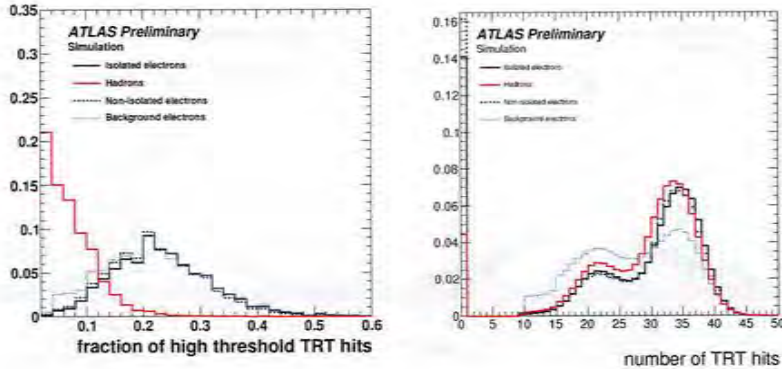


Figure 15: Fraction of high threshold TRT hits (left) and number of TRT hits (right)

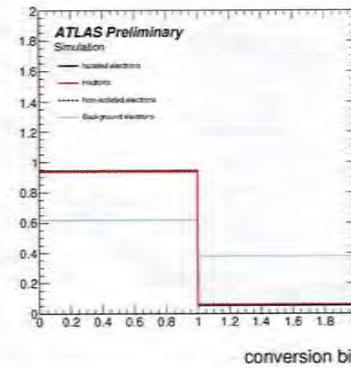


Figure 16: Conversion bit (is 1 if the electron candidate is considered a conversion), this particular variable is shown for all candidates passing the full set of cuts (tight) apart from the conversion bit

## 6 Recent changes in electron identification (based on the 2009/2010 LHC data-taking runs)

Since the very early data taking periods in 2009 and the first collisions at 900 GeV [6], the data/Monte-Carlo comparisons have highlighted discrepancies in the shower shape distributions. In particular, the electromagnetic showers are seen to be broader in data than in the Monte-Carlo, which translates into a shift in the relevant distributions ( $R_\eta$  and  $w_{\eta 2}$ ). This shift is consistently observed on pure hadronic background (on the very first electron candidates for example) as well as on isolated electrons from  $W$  or  $Z$  bosons decays (from tag and probe studies). The reason for this discrepancies is not yet clear, though it is believed to be related to the Geant 4 description of the electromagnetic calorimeter. Studies are ongoing on this issue. In order to maintain the robustness of the electron identification criteria in both the trigger and the offline selections, the cuts on  $R_\eta$  and  $w_{\eta 2}$  are loosened. The cut is placed on the tail of the relevant distributions from data, which thus reduces systematics due to a mismodeling of the shapes. In addition, the low  $p_T$  selection is improved based on tag and probe studies with  $J/\psi$  decaying to electrons. The probe electron efficiency and the trigger rates versus the shower shape cuts are studied to find the optimum between higher efficiency and acceptable trigger rates.

Other changes include:

- Modification of the hadronic leakage cut due to a change in the modeling of the hadronic calorimeter electronic noise. Based on early data, the electronic noise is now modeled using a double gaussian and is thus wider.
- The tight selection has been adapted to take into account disabled b-layer modules. If the tight candidate electron crosses a disabled b-layer module, it is kept, where as it was rejected in the previous definition of tight.

The conversion flag is set if the electron is identified as a conversion. This recovery procedure however did not check the status of the crossed b-layer. Thus tight electrons crossing disabled

b-layers were identified as single track conversions, and therefore they did not satisfy the standard isEM tight criteria. This problem is now corrected with the new definition of tight.

- As result of broader  $\Delta\eta$  and  $\Delta\phi$  distributions observed in data than in Monte-Carlo due to not yet optimal calo-ID alignment, the new tight selection applies only the looser medium  $\Delta\eta$  cut, while the  $\Delta\phi$  cut is removed from the selection. Improvements are expected on this issue in the near future.

The results for electron efficiency and jet rejection are given in section 8.1.2.

## 7 Electron isolation algorithm

The electron identification described so far does not include dedicated isolation cuts. Various analyses may require different isolation criteria of different tightness and therefore the isolation cuts are applied on top of the electron identification. Different calorimeter and tracking based isolation variables have been studied and optimised. They are used to define a set of reference cuts.

A calorimetric isolation discriminator is computed from the reconstructed energy in a cone of half opening angle  $R_0$  around the electron candidate direction, where the energy of the electron itself is excluded. While a larger cone will contain more energy in case of misidentified jets, a smaller cone is more robust against energy depositions from pile-up events. A cone with  $R_0 = 0.3$  has been found to give the best trade-off with high discrimination power and robustness against pile-up at the same time.

In addition, a tracking based discriminator is used, which is the summed scalar  $p_T$  of tracks in a cone of  $R_0 = 0.3$  around the electron. In contrast to the calorimetric isolation, neutral particles do not contribute to this quantity. The advantage, however, is that track quality criteria can be applied in order to reject tracks from secondary vertices. Track isolation considers tracks with  $p_T > 1$  GeV, a hit in the innermost pixel detector layer, at least 7 hits in silicon detectors and transverse and longitudinal impact parameter less than 1 mm. For tracks with  $\Delta R < 0.1$  with respect to the electron it is also required that they are not matched to a conversion vertex.

When applying cuts on the isolation variables, the dependence of the isolation variables on  $p_T$  and  $\eta$  is taken into account by separately optimising the cuts for different regions in  $p_T$  and  $|\eta|$ . Especially for higher  $p_T$  ranges, this procedure is limited by the statistics of the simulated jet sample. To further reduce correlation effects, the described isolation variables are divided by  $E_T$  (see Fig. 17).

The electrons which are used for the cut optimisation are required to pass the medium electron identification criteria. The optimisation is done in such a way that the efficiency for isolated electrons, with respect to the pre-selection, is constant in all ranges of  $p_T$  and  $|\eta|$ . Three sets of cuts that exploit calorimetric and tracking isolation variables are part of the recent software releases. Each of them allow to retain 99 %, 98 %, 95 % or 90 % efficiency for isolated electrons. The rejection factors of the isolation cuts in combination with the tight and medium electron identification criteria are discussed in the next section.

## 8 Expected electron reconstruction and identification performance

The expected performance of the ATLAS detector in terms of isolated electron efficiency and jet rejection is summarized here. The full coverage in  $p_T$  and  $\eta$  is studied via known Standard Model processes as well as more exotic models. For Standard Model processes, the electron efficiency is evaluated on the following Monte-Carlo samples:

- A Pythia  $Z \rightarrow ee$  sample with a one lepton filter requiring one electron above 0 GeV in  $p_T$  within  $|\eta| \leq 2.8$ .

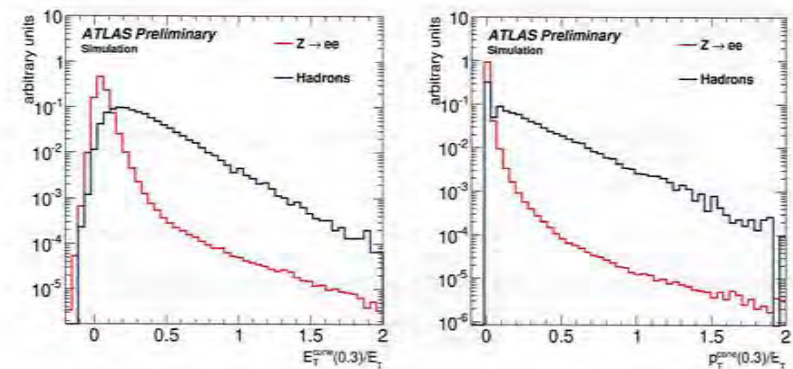


Figure 17: Calorimetric and tracking isolation energy normalised to the transverse energy,  $E_T^{\text{cone}}/E_T$  and  $p_T^{\text{cone}}/E_T$ , for a cone of  $R_0 = 0.3$ . The electron candidates are required to have a transverse energy larger than 15 GeV and to pass the medium electron identification. The samples used are a Pythia  $Z \rightarrow ee$  sample for the signal and a Pythia di-jet sample for the background.

- A  $H \rightarrow 4l$  sample with a Higgs boson generated at 130 GeV and a generator filter requiring 4 leptons (electrons or muons) with  $p_T > 5$  GeV within an  $|\eta|$  range of 10.
- A  $J/\psi \rightarrow ee$  sample with a generator filter requiring one electron above 3 GeV in  $p_T$  within  $|\eta| \leq 2.7$ .

The jet rejection is evaluated on the following samples:

- A filtered inclusive di-jet sample of the most important hard processes generated with Pythia including all hard QCD processes ( $q\bar{q} \rightarrow q\bar{q}$ ,  $q\bar{q} \rightarrow q\bar{q}$ ,  $q\bar{q} \rightarrow gg$ ,  $gg \rightarrow q\bar{q}$ ,  $gg \rightarrow gg$  and  $gg \rightarrow gg$ ), heavy flavor production ( $q\bar{q} \rightarrow Q\bar{Q}$ ,  $gg \rightarrow Q\bar{Q}$ ), prompt photon production ( $q\bar{q} \rightarrow g\gamma$ ,  $q\bar{q} \rightarrow q\gamma$ ) and W and Z production ( $q\bar{q} \rightarrow Z^0$ ,  $q\bar{q} \rightarrow W^\pm$ ). This sample has a jet filter applied at generator level. This filter sums the transverse energy of all stable truth particles (excluding muons and neutrinos) in a grid of  $0.12 \times 0.12$  in  $\eta \times \phi$  and looks for a transverse energy deposit greater than 17 GeV within an  $\eta$  range of 2.7.
- A minbias using the same jet filter as described above but with a transverse energy cut at 6 GeV.

Note that the Monte-Carlo used is not corrected for the observed broader shower shapes 6 and since the shift in the shower shapes seems to be consistent for hadron background as well as isolated electrons it is assumed that the all expected jet rejection numbers are underestimated on an un-corrected Monte-Carlo.

Common definitions for electron efficiency and jet rejection are used. The electron identification efficiency is defined as :

$$\epsilon_e^{\text{track}} = \frac{N_e^{\text{reco}}}{N_e^{\text{truth}}}, \quad (1)$$

where  $N_e^{\text{truth}}$  is the total number of true electrons and  $N_e^{\text{reco}}$  is the number of reconstructed signal electrons matched to true electrons and which pass certain identification cuts, within the same acceptance.

The quoted jet rejections are derived from di-jet samples (filtered at generation level) and are normalised with respect to the number of truth particle jets. The jet rejection is defined as :

$$R_{jet} = \frac{N_{\text{true jets}}}{N_{\text{fakes}}}, \quad (2)$$

where  $N_{\text{true jets}}$  is the number of true jets in the initial sample and  $N_{\text{fakes}}$  is the number of candidates which pass a certain selection. The filter at generation level sums the transverse energy of particles in a  $0.12 \times 0.12 \eta, \phi$  grid. Only the events passing the filter are going through the full simulation of the ATLAS detector.

Truth jets are defined by summing particle four-momenta within a cone of size  $\Delta R = 0.4$  and passing a 1 GeV transverse energy threshold. The number of truth jets per event is derived from a dedicated un-filtered sample of di-jets events. The total number of truth jets is then obtained through:

$$N_{\text{true jets}} = \frac{N_{\text{total}} \times F_{\text{jets}}}{\epsilon_{\text{filter}}}, \quad (3)$$

where  $N_{\text{total}}$  is the number of events passing the filter,  $\epsilon_{\text{filter}}$  the filter efficiency and  $F_{\text{jets}}$  the number of truth jets per generated event.  $F_{\text{jets}}$  was determined to be 0.53 for 10 TeV and 0.50 for 7 TeV samples.

Note that the samples used are simulated filtered di-jet events, where all main QCD hard processes, heavy quark production as well as (for the higher ET thresholds) the prompt photon and W, Z production are included.

## 8.1 High $p_T$ electrons: Standard Model processes

### 8.1.1 Results of standard selection

The efficiency for the cuts-based identification algorithm is evaluated on a  $Z \rightarrow ee$  inclusive sample and is shown in Fig. 18 for the three reference electron identification selections "loose", "medium" and "tight". The results in this section are based on  $\sqrt{s} = 10$  TeV Monte-Carlo samples and do not include the latest changes in electron identification described in Section 6. The efficiency on  $Z \rightarrow ee$  for  $E_T > 20$  GeV is given in Table 5. For  $E_T > 8$  GeV, efficiency numbers are derived from a  $H \rightarrow 4l$  sample and given in Table 6. It should be noted that the efficiency has significantly improved with respect to previous software releases. For similar rejection, the efficiency increases, in the "medium" selection, from 77.3% in previous publications [2] to 90.0% in the present note. This is due to the improvements in the reconstruction described in section 4 as well as the optimisations described in section 5.

Rejection numbers for  $E_T > 20$  GeV (in Table 5) come from a filtered dijet sample. A filtered minimum bias sample is used to derive the  $E_T > 8$  GeV numbers (in Table 6).

As can be seen from Table 5, the tight selection at high  $E_T$  has a rejection of  $(1.39 \pm 0.06) \times 10^5$  for an efficiency of 71.6 %. This is comparable to previously published expectations [2]. Removing the rejection of reconstructed photon conversions matched to the cluster, results in a loss in rejection of around 45 % for a gain in efficiency of around 3 % and the fraction of background electrons remaining after selection rises to 25 %.

It is interesting to examine the fraction of surviving electron candidates remaining after a corresponding selection criteria. It can be seen in Table 5, that after the tight selection, the largest background contribution to isolated electron from b(c) decays. The second largest contribution is equally shared between hadrons and background electrons from Dalitz decays or photon conversions originating from neutral pion decays. A partial explanation for this can be found in figures 2, 4, 6, 8 and 10 showing the shower shape distributions for b(c) electrons and background electrons coming from photon conversions or Dalitz decays. One can observe that b(c) electrons more closely resemble isolated Z electrons than hadron fakes or background electrons.

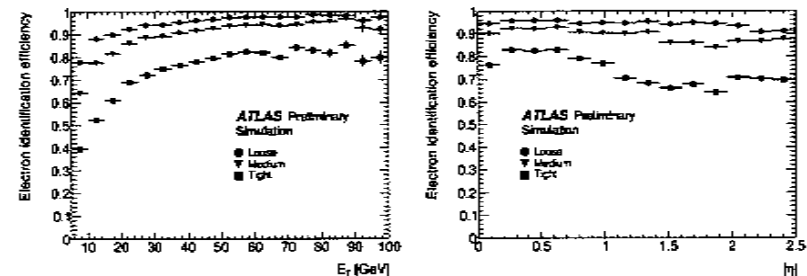


Figure 18: Electron efficiency vs  $E_T$  (left) and vs  $|\eta|$  (right) for the "loose", "medium" and "tight" selection for  $Z \rightarrow ee$

The default isolation criteria based on tracking and calorimeter variables has been optimised to keep 95% of isolated electrons from  $Z$  decays. Other optional isolation cuts have an efficiency of 99, 98 or 90%. Table 5 clearly shows that a cleaner isolated electron sample can be obtained by applying tighter isolation cuts. This is also illustrated in Fig. 19 where the inclusive electron  $p_T$  spectrum is shown for increasing levels of tightness. The Tight(+Iso90) line of Table 5 and Fig. 19 (bottom right) show that adding the very strict isolation to the tight selection increases the fraction of isolated electrons in the sample to 73.5% and thus makes it exceptionally pure.

Cuts	$E_T > 20$ GeV						
	Efficiency (%)	$J/\psi$ rej. (tot)	surviving candidates (%)				
	$Z \rightarrow ee, b,c \rightarrow e$	$\pm 0.03$	iso	non-iso	bkg	had	
Reco	97.58	-	$91.5 \pm 0.1$	0.1	0.8	23.3	75.8
Loose	94.32	$36.7 \pm 0.3$	$1065 \pm 5$	0.3	1.9	56.7	40.4
Medium	90.00	$31.5 \pm 0.3$	$6840 \pm 70$	6.0	9.9	50.5	33.4
+ isol. 99%	88.87	-	$10300 \pm 130$	9.2	7.6	56.2	27.0
+ isol. 98%	87.99	-	$13600 \pm 200$	11.7	5.8	58.7	23.8
+ isol. 95%	85.06	-	$20000 \pm 350$	16.0	3.5	60.5	20.0
+ isol. 90%	80.67	-	$27100 \pm 550$	16.9	2.6	60.7	16.8
Tight	71.59	$25.2 \pm 0.2$	$(1.39 \pm 0.06) \cdot 10^5$	29.9	44.9	11.4	13.8
+ isol. 99%	70.78	-	$(1.98 \pm 0.11) \cdot 10^5$	42.3	32.7	12.5	12.5
+ isol. 98%	70.16	-	$(2.50 \pm 0.15) \cdot 10^5$	51.6	24.1	12.3	12.0
+ isol. 95%	68.05	-	$(3.79 \pm 0.28) \cdot 10^5$	65.5	13.3	11.7	9.5
+ isol. 90%	64.83	-	$(5.15 \pm 0.45) \cdot 10^5$	73.5	8.3	11.0	7.2

Table 5: Expected jet rejections, isolated electron efficiencies and non-isolated electron efficiencies for the standard set of identification cuts and an  $E_T$ -thresholds of 20 GeV and  $|\eta| < 2.5$ . The total jet rejection includes hadron fakes and background electrons from photon conversions and Dalitz decays. The last four columns give the fraction of surviving electron candidates in the dijet sample after each selection level. The categories considered for the electron candidates are described in Section 5. The efficiencies are computed on a  $Z \rightarrow ee$  sample and rejections are computed on a filtered dijet sample. The quoted errors are statistical.

Cuts	$E_T > 8 \text{ GeV}$					
	Efficiency (%)		Jet rej. (tot)	surviving candidates (%)		
$H \rightarrow 4l$	$b, c \rightarrow e$			non-iso	bkg	had
$\pm 0.5$	$\pm 5$					
Reco	95.2	-	$179.8 \pm 0.2$	1.0	26.7	64.6
Loose	90.9	56	$870 \pm 5$	2.6	45.3	37.8
Medium	86.4	54	$4600 \pm 30$	13.7	27.4	58.9
+ isol. 99%	81.9	-	$5210 \pm 40$	13.6	27.2	59.1
+ isol. 98%	81.1	-	$6040 \pm 50$	13.9	27.2	58.8
+ isol. 95%	78.3	-	$8610 \pm 90$	14.7	27.6	57.6
+ isol. 90%	74.1	-	$11400 \pm 130$	15.1	27.7	57.1
Tight	70.4	42	$(4.55 \pm 0.10) \cdot 10^4$	54.0	10.1	35.8
+ isol. 99%	66.7	-	$(5.05 \pm 0.12) \cdot 10^4$	53.3	10.2	36.6
+ isol. 98%	66.0	-	$(5.85 \pm 0.15) \cdot 10^4$	53.7	9.8	36.4
+ isol. 95%	63.9	-	$(7.90 \pm 0.25) \cdot 10^4$	54.3	9.2	36.4
+ isol. 90%	60.7	-	$(1.00 \pm 0.05) \cdot 10^5$	54.3	9.1	36.6

Table 6: Expected jet rejections, isolated electron efficiencies and non-isolated electron efficiencies for the standard set of identification cuts and an  $E_T$ -thresholds of 8 GeV and  $|\eta| < 2.5$ . The total jet rejection includes hadron fakes and background electrons from photon conversions and Dalitz decays. The last four columns give the fraction of surviving electron candidates in the minimum bias sample after each selection level. The categories considered for the electron candidates are described in Section 5. Efficiencies are computed on a  $H \rightarrow 4l$  sample with a generated Higgs boson mass of 130 GeV and rejections are computed on a filtered minimum bias sample. The quoted errors are statistical.

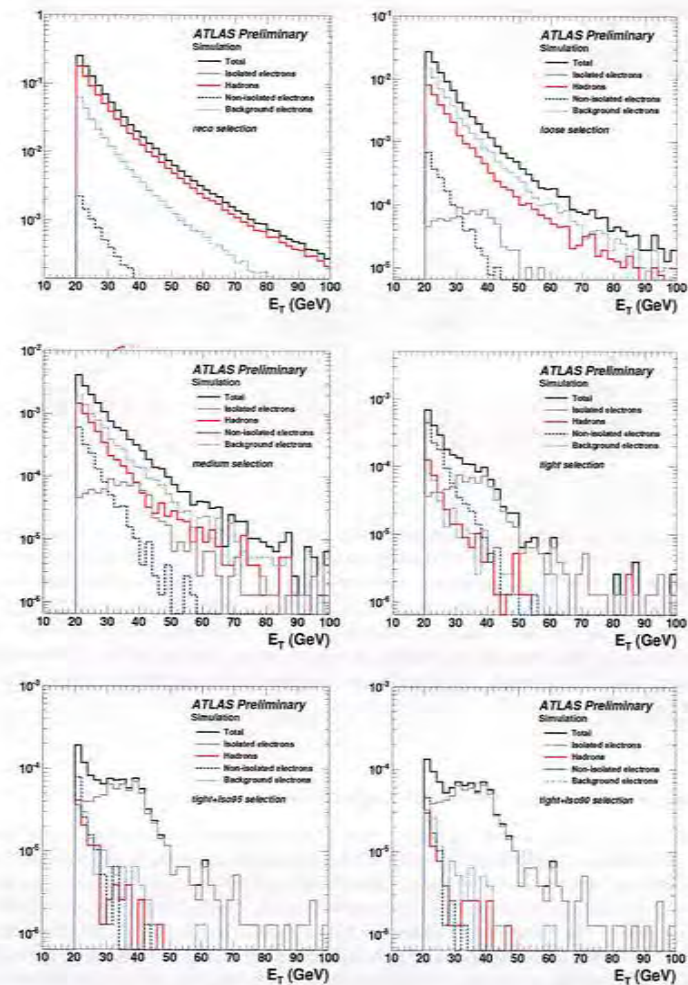


Figure 19: Cluster  $E_T$  distributions normalised to the number of reconstructed electron candidates showing the relative importance of all background contributions to isolated electron selections. The figures show all electron candidates (upper left), candidates after loose selection (upper right), candidates after medium selection (middle left) and candidates after tight selection (middle right). The two lower figures show electron candidates after tight selection and an isolation cut optimised for an efficiency of 95 % on a  $Z \rightarrow ee$  sample (left) and electron candidates after tight selection and an isolation cut of optimised for a 90 % efficiency (right). The sample used are simulated filtered di-jet events, where all main hard QCD processes as well as heavy quark production, prompt photons and W, Z production are simulated.

### 8.1.2 Results on recent modification of identification (based on 2009/2010 Run)

The efficiency and rejection numbers presented in Table 7 are based on 7 TeV center-of-mass Monte-Carlo samples. They are based on the more robust identification selection optimised on the latest data taken (see Section 6).

Cuts	$E_T > 20 \text{ GeV}$						
	Efficiency (%)		Jet rej. (tot)	surviving candidates (%)			
	$Z \rightarrow ee$	$Z \rightarrow ee$ (+ FSR)	iso	non-iso	bkg	had	
Reco	96.25	96.90	$87.3 \pm 0.1$	0.0	1.0	26.0	73.0
Loose	94.68	95.28	$614.3 \pm 1.5$	1.0	2.0	58.0	39.0
Medium	89.61	89.86	$4435 \pm 30$	3.0	9.0	57.0	31.0
+ isol. 99%	88.49	88.71	$6280 \pm 50$	5.0	7.0	61.0	27.0
+ isol. 98%	87.57	87.78	$8330 \pm 80$	6.0	6.0	63.0	25.0
+ isol. 95%	84.99	85.18	$13000 \pm 160$	10.0	4.0	64.0	22.0
+ isol. 90%	81.26	81.43	$17760 \pm 250$	12.0	4.0	65.0	19.0
Tight	72.77	72.81	$(4.9 \pm 0.1) \cdot 10^4$	16.0	39.0	22.0	23.0
+ isol. 99%	71.95	71.99	$(7.1 \pm 0.2) \cdot 10^4$	25.0	30.0	24.0	21.0
+ isol. 98%	71.27	71.31	$(9.4 \pm 0.3) \cdot 10^4$	31.0	24.0	25.0	20.0
+ isol. 95%	69.33	69.36	$(1.52 \pm 0.06) \cdot 10^5$	43.0	18.0	23.0	16.0
+ isol. 90%	66.50	66.53	$(2.10 \pm 0.10) \cdot 10^5$	52.0	14.0	22.0	12.0

Table 7: Expected jet rejections, isolated electron efficiencies for the robust set of identification cuts and an  $E_T$ -thresholds of 20 GeV. The total jet rejection includes hadron fakes and background electrons from photon conversions and Dalitz decays. The numbers are also given for loose truth matching where electrons matched to converted FSR photons from  $Z$  are counted in the efficiency calculation. The last four columns give the fraction of surviving electron candidates in the dijet sample after each selection level. The categories considered for the electron candidates are described in Section 5. The efficiencies are computed on a  $Z \rightarrow ee$  sample and rejections are computed on a filtered dijet sample. The quoted errors are statistical.

### 8.1.3 Possible further improvements of the tight selection

Studies are ongoing to further improve the tight selection, by, on one hand, adapting to a better understanding of the various distributions and, on the other hand, introducing new, possibly more optimal variables. The first variables that will be reintroduced in the tight selection are the tighter track matching variables that had initially been removed due to calo-ID misalignment. Moreover, cut optimisation is studied for variables like  $\Delta\phi$  and  $E/p$  (see Section 5.2 for variable definitions). Those two variables are especially affected by Bremsstrahlung and the possibility of using variables corrected for those effects is investigated. In particular, the correlation of  $E/p$  and  $\Delta\phi$  can be used to define a new, Bremsstrahlung corrected,  $E/p$  variable based on the measured  $E/p$ , the standard  $\Delta\phi$  between the extrapolated track and the electron cluster and the  $\Delta\phi$  between the track at the perigee and the cluster position. In addition, for the extrapolation to the calorimeter, the standard  $\Delta\phi$  could be improved by using the energy of the calorimeter instead of the track momentum in a simple extrapolation formula.

### 8.2 High $p_T$ electrons: Beyond the Standard Model processes

Searches beyond the Standard Model usually involve leptons of  $p_T$  well above the range used for Standard Model gauge boson physics where data-driven estimations of efficiency can be obtained with the tag-and-probe method. This section considers the electron identification efficiency for exotics ( $Z'$  and  $W'$ , both with a 1.5-TeV mass) and SUSY (SU4<sup>2</sup>, benchmark point in ATLAS for low-mass SUSY production) processes. The  $t\bar{t}$  sample with one lepton filter is also considered since it is the main background for SUSY searches. Table 8 shows the results for efficiency in these samples for  $E_T > 17 \text{ GeV}$ . Fig. 20 shows the Loose and Medium electron efficiency as a function of the electron  $p_T$ .

Cuts	$E_T > 17 \text{ GeV} ( \eta  < 2.5)$			
	SU4	$t\bar{t}$	$Z'(1.5 \text{ TeV}) \rightarrow ee$	$W'(1.5 \text{ TeV})$
Loose	$89.73 \pm 0.04$	$86.56 \pm 0.21$	$94.07 \pm 0.15$	$96.89 \pm 0.15$
Medium	$87.20 \pm 0.05$	$84.11 \pm 0.22$	$91.97 \pm 0.17$	$93.77 \pm 0.21$
Tight	$75.26 \pm 0.06$	$72.34 \pm 0.27$	$77.98 \pm 0.26$	$76.68 \pm 0.37$

Table 8: Electron identification efficiency for samples commonly used in searches beyond the Standard Model (see text).

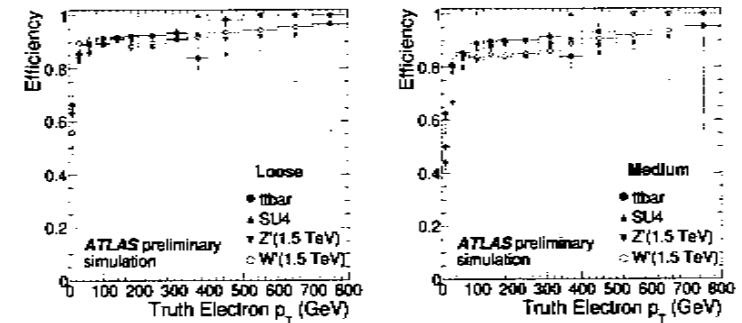


Figure 20: Electron identification efficiencies for Loose (left) and Medium (right) cuts as a function of the electron  $p_T$ . Results are shown for SU4,  $t\bar{t}$ ,  $Z'$  and  $W'$  samples.

As shown, differences of a few percent are found between these results and the reference values obtained with  $Z$  boson samples. For instance, the overall Medium electron efficiency for  $Z'$  and  $W'$  samples is more than 5% higher than for SUSY or  $t\bar{t}$ . Indeed, the results between the different samples can only be compared in bins of variables such as  $p_T$ ,  $\eta$  and isolation, since different topologies in the electron production for each physics process can lead to these differences once integrated over the whole phase space.

### 8.3 Low $p_T$ electrons from $J/\psi$

Table 9 shows the electron reconstruction and identification efficiency obtained for the different standard levels of cuts for electrons from  $J/\psi$ . The reconstruction efficiency is  $\sim 71\%$  for a transverse energy

<sup>2</sup>SU4 is low-mass mSUGRA point which is defined by the following parameters:  $m_0 = 200 \text{ GeV}$ ,  $m_{1/2} = 160 \text{ GeV}$ ,  $A_0 = 400 \text{ GeV}$ ,  $\tan\beta = 10$  and  $\mu > 0$ .

$E_T > 5$  GeV. For a tight selection it is  $\sim 45\%$  which correspond to  $\sim 62.8\%$  relative to the reconstruction efficiency. Fig. 21 shows the  $E_T$  and  $\eta$  dependence of the identification efficiency.

Sample	Selection level			
	Container	Loose	Medium	Tight
$\epsilon_e$	71.0	61.0 (85.9)	58.3 (82.1)	44.6 (62.8)

Table 9: Expected efficiencies  $\epsilon_e$  for electrons from the  $J/\psi$  sample for the different standard levels of cuts used for isolated electron identification. Results are given for electrons with transverse energy  $E_T > 5$  GeV and  $|\eta| < 2.47$ . Results in brackets are given with respect to the reconstruction efficiency. The statistical error is typically 0.1 %.

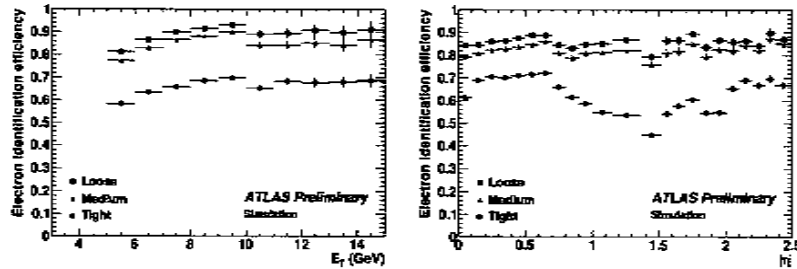


Figure 21: Electron identification efficiency for “loose”, “medium” and “tight” level selections normalised to all reconstructed electron candidates as a function of the cluster transverse energy (left) and the pseudorapidity (right) in  $J/\psi$  events.

## 9 Forward algorithm in high $\eta$ electron studies

The electron identification in the forward region ( $2.5 < |\eta| < 4.9$ ) is essential in many physics analyses, including electroweak measurements and new phenomena searches. In contrast to the central electron, the forward electron reconstruction uses only the information from the calorimeters as the tracking system is limited to  $|\eta| < 2.5$ . Obviously it is not possible to distinguish between electrons and photons. The forward algorithm is based on topological clusters measured in the various subdetectors of the forward calorimeters and provides energy and position measurement. The selection criteria for high  $\eta$  electrons are based on cluster moments and shower shapes which provide efficient identification due to the good transverse and longitudinal segmentation of the calorimeters. An electron candidate in the forward calorimeters is reconstructed if there is a cluster with  $E_T > 5$  GeV. The direction of the electron is defined by the barycenter of the cells belonging to the cluster in the calorimeter. The energy of the electron is determined by the sum of the cluster cells.

In order to distinguish electrons from hadrons the difference in the electromagnetic showers induced by the electrons and the hadronic showers induced by the hadron (e.g. pion) is exploited. These differences appear in the energy deposition and the shower shape of the two types of particles.

## 9.1 Optimisation

Most of the variables used as input to the cuts-based identification method are defined as the cluster moments or a combination of them. The cluster moment of degree  $n$  for a variable  $x$  is defined as:

$$\langle x^n \rangle = \frac{1}{E_{\text{norm}}} \times \sum_i E_i x_i^n, \quad (4)$$

where  $E_{\text{norm}} = \sum_i E_i$  and  $i$  is the cell index of the cluster.

For the electron identification, the following discriminating variables are studied:

- $r_i = |(\vec{x}_i - \vec{c}) \times \vec{s}|$ : Electromagnetic and hadronic showers have different shapes in both the transverse and the longitudinal directions. Hadronic showers are usually deeper and broader than electromagnetic showers. To evaluate the shower shapes in the transverse direction the second moment of the distance  $r_i$  of each cell  $i$  to the shower axis is used.  $\vec{c}$  is the center of the shower and  $\vec{s}$  is the shower axis.
- $lat_2/(lat_2 + lat_{\text{max}})$ : Normalized lateral moment, where  $lat_2$  is the second moment of the variable  $r_i$  for which it is imposed that the distance  $r = 0$  for the two most energetic cells. For  $lat_{\text{max}}$  it is imposed that  $r = 4$  cm for the two most energetic cells and  $r = 0$  for the remaining cells.
- $\lambda_i = (\vec{x}_i - \vec{c}) \cdot \vec{s}$ : To evaluate the shower shapes in the longitudinal direction the second moment of the distance of each cell  $i$  to the shower center is used.
- $long_2/(long_2 + long_{\text{max}})$ : Normalized longitudinal moment. It takes also into account the two most energetic cells.  $long_2$  the second moment of the variable  $\lambda_i$  for which the distance  $\lambda = 0$  for the two most energetic cells is used. For  $long_{\text{max}}$  we impose that  $\lambda = 10$  cm for the two most energetic cells and  $\lambda = 0$  for the remaining cells.
- $\frac{1}{E_{\text{norm}}} \times \sum_i E_i (E_i/V_i)$ : where  $V_i$  is the volume of the cell  $i$ . This variable represents the energy density. The EM shower is broader and deposits locally more energy than the hadronic shower.
- $f_{\text{max}}$ : Fraction of the energy in the most energetic cell of the cluster. By measuring the energy fractions deposited in the cells of a segmented calorimeter it is usually possible to distinguish incident hadrons from electrons and photons.
- $\lambda_{\text{cover}}$ : distance of the shower barycenter from the calorimeter front face measured along the shower axis. A combination of the optimal set of variables should be done from the list of the variables that are shown above. These variables are first classified with respect to their discriminating power. An iterative method was used where one iterates until the best possible efficiency is reached.
- For the early LHC running a robust set of variables (and cuts) is also needed. The variable distributions should ideally not depend too strongly on  $E_T$  and  $\eta$ . The first moment of the energy density variable

from the optimal list is not fulfilling this requirement (see Fig. 22). Only the remaining 6 variables are kept. Fig. 23 shows the lateral moment for the electrons signal from  $Z \rightarrow ee$  events and jet background from QCD induced events.

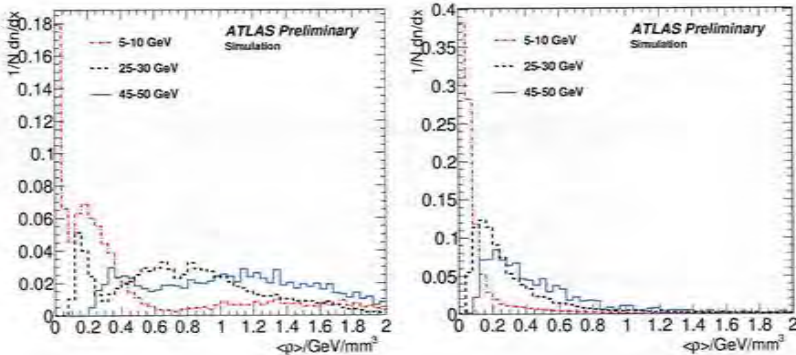


Figure 22: First energy density moment for the signal (left) and the background (right) in the EMEC, in different  $E_T$  bins.

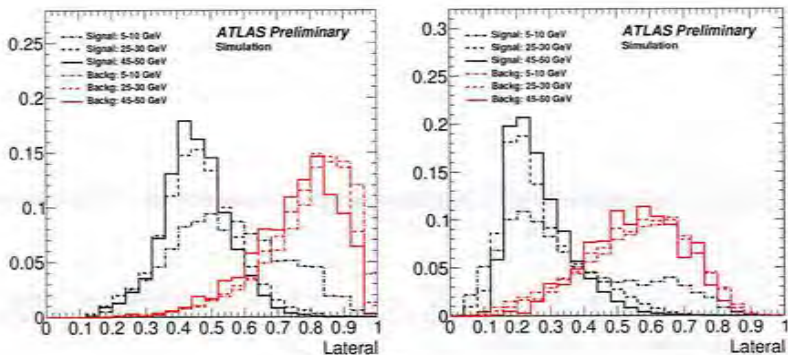


Figure 23: Lateral moment for the signal and the background in the EMEC (left) and in the FCal (right), in different  $E_T$  bins.

## 9.2 Expected performance

Two levels of selection for offline electrons are defined. Loose electrons (using a subset of the previously defined variables with mainly longitudinal and transverse shower profile variables) and tight electrons adding further requirements on shower shapes. The “loose” working point is defined at 74 % efficiency and the tight at 60 % with a fake rate of about 0.13 % and 0.06 % respectively. This performance is expected to yield a clean  $Z \rightarrow ee$  sample where one of the electrons is in the forward region. Fig. 24 shows the expected background contribution under the  $Z$  peak for one tight central electron and one loose forward electron. A significance ( $S/\sqrt{B}$ ) of 4 can be achieved for about  $300 \text{ pb}^{-1}$  of integrated luminosity.

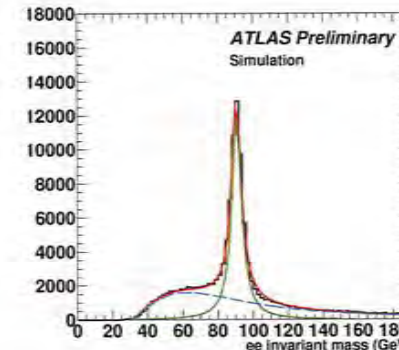


Figure 24: Di-electron invariant mass distribution in the  $Z \rightarrow ee$  channel (one tight central electron and loose forward electron). The fitted shapes of the signal (green) and QCD background (dashed blue) are shown.

## 10 Conclusion

The assessment of the expected electron performance in the ATLAS experiment over the full acceptance in  $\eta$  and  $p_T$  was performed using the latest reconstruction software and detailed geometry description of the detector. The electron trigger identification variables were described, the electron menus defined and the rates estimated. The offline electron reconstruction algorithms were summarized and the expected performance of the various levels of identification cuts estimated on known Standard Model as well as on more exotic processes. This includes a careful study of the calorimeter and tracking isolation criteria which play a central role in various analysis where different levels of isolation are required. The strict requirements for isolated electron searches are met through a combined reconstruction and identification effort over all calorimeter and tracking subdetectors. We find a mid-range  $p_T$  efficiency of around 70 % for a rejection of  $10^5$  for the central part of the detector (up to 2.5 in  $\eta$ ). This extends to the low  $p_T$  region where the modularity of the cuts allows to have similar rejection with only a small cost in efficiency or equivalent efficiency with slightly lower rejection. The forward region offers in addition an 80 % efficiency on  $Z$  boson electrons with good signal/background separation if one electron is required

to be in the central region. This latest estimation of the ATLAS detector performance in terms of electron reconstruction and identification confirms the design requirements. This has been achieved by careful improvements in the reconstruction and identification software adapting to the more accurate description of the detector in the simulation.

## References

- [1] ATLAS: *Detector and physics performance technical design report. Volume 1, section 7.4, Electron/Jet separation*, CERN-LHCC-99-14.
- [2] The ATLAS Collaboration, G. Aad et al., *Expected Performance of the ATLAS Experiment - Detector, Trigger and Physics*, arXiv:0901.0512 [hep-ex].
- [3] R. O. Duda and P. E. Hart, *Use of the Hough Transformation to Detect Lines and Curves in Pictures*, Commun. ACM (Association for Computing Machinery).
- [4] A. Hocker, P. Speckmayer, J. Stelzer, F. Tegenfeldt, and H. Voss, *TMVA, toolkit for multivariate data analysis with ROOT*, CERN-2008-001 .
- [5] The ATLAS Collaboration, G. Aad et al., *Expected photon performance in the ATLAS experiment*, ATL-PHYS-PUB-2011-007 .
- [6] The ATLAS Collaboration, G. Aad et al., *Electron and photon reconstruction and identification in ATLAS: expected performance at high energy and results at 900 GeV*, ATLAS-CONF-2010-005 .

3

3



# OBSERVE IT!

## ATLAS NOTE

ATLAS-CONF-2011-008  
February 16, 2011



### Determination of the muon reconstruction efficiency in ATLAS at the Z resonance in proton-proton collisions at $\sqrt{s} = 7$ TeV

The ATLAS collaboration

#### Abstract

This note presents a measurement of the muon reconstruction efficiency in p-p collision data collected by the ATLAS experiment at  $\sqrt{s} = 7$  TeV using muons from Z boson decays. The measurement is based on the tag-and-probe approach, using the full data sample collected in 2010 which corresponds to a total integrated luminosity of  $42 \text{ pb}^{-1}$ .

## 1 Introduction

Via its decay into two muons, the Z boson provides a clean source of muons which can be used to study the performance of the muon identification and reconstruction tools in ATLAS.

The aim of the present note is the comparison of muon reconstruction efficiencies predicted by the Monte-Carlo simulation with the efficiencies measured with experimental data in first pass reconstruction using muon pairs produced in the decays of Z bosons. The reconstruction efficiencies are determined using the so-called “tag-and-probe” method. Events are selected by applying strict selection criteria on one of the two muons, the tag, and loose criteria on the second muon, the probe, which is an inner detector track in this analysis. Due to the clean signature of these events such a selection suffers from only a very small background. The relative reconstruction efficiency is given by the fraction of probes which are reconstructed as a muon. The results are compared to simulation and correction factors provided for different geometrical and kinematic regions.

This study uses the full data sample of proton-proton collisions at 7 TeV centre of mass energy recorded in 2010 for which the inner detector (ID) and the muon spectrometer (MS) were fully operational. The sample corresponds to an integrated luminosity of  $42 \text{ pb}^{-1}$ . The efficiencies of two independent muon reconstruction algorithm chains in the prompt reconstruction of p-p collision data are studied. The chains are referred to as chain 1 (Staco) and chain 2 (Muld) in the following.

The note is structured as follows: after a description of the ATLAS detector and the muon reconstruction, the tag-and-probe method is explained. The method is then applied to simulated and experimental data including a discussion of systematic uncertainties on the efficiency measurements.

## 2 The ATLAS detector

A detailed description of the ATLAS Detector can be found elsewhere [1]. Muons are independently measured in the ID and in the MS.

The ID measures tracks up to  $|\eta| = 2.5$ <sup>1</sup> exploiting three types of detectors operated in a solenoidal magnetic field of 2 T: a silicon pixel detector closest to the interaction point, a silicon strip detector (SCT) surrounding the pixel detector, and a transition radiation straw tube tracker (TRT) as the outermost part of the ID.

The MS consists of three large air-core superconducting toroidal magnets (two end caps and one barrel) providing a field of approximately 0.5 T. The deflection of the muons in the magnetic field is measured via hits in three layers of precision drift tube (MDT) chambers for  $|\eta| < 2$  and two layers of MDT chambers in combination with one layer of cathode strip chambers (CSC) in the innermost end cap wheels of the MS, for  $2.0 \leq |\eta| < 2.7$ . Three layers of resistive plate chambers (RPC) in the barrel ( $|\eta| < 1.05$ ) and three layers of thin gap chambers (TGC) in the end caps ( $1.05 < |\eta| < 2.4$ ) provide the muon trigger and also measure the muon trajectory in the non-bending plane of the spectrometer magnets.

The ATLAS detector has a three-level trigger system: Level 1 (L1), Level 2 (L2), and the Event Filter (EF). The MS provides a L1 hardware muon trigger which is based on hit coincidences within different RPC or TGC detector layers inside programmed geometrical windows which define the muon  $p_T$ . The L2 and EF muon triggers perform a software confirmation of the L1 muon trigger, by applying a further  $p_T$  selection.

Figure 1 shows a schematic drawing of the ATLAS MS. The barrel muon chambers are installed in roughly cylindrical rings around the calorimeters. The end cap chambers are arranged in disks orthogonal to the proton beams. The BEE chambers are mounted on the end cap toroids. Large barrel chambers

<sup>1</sup> $\eta = -\ln(\tan(\theta/2))$ , where  $\theta$  is the polar angle measured from the beam line.

are mounted between the barrel toroid coils. Small barrel chambers are installed on and inside the toroid coils.

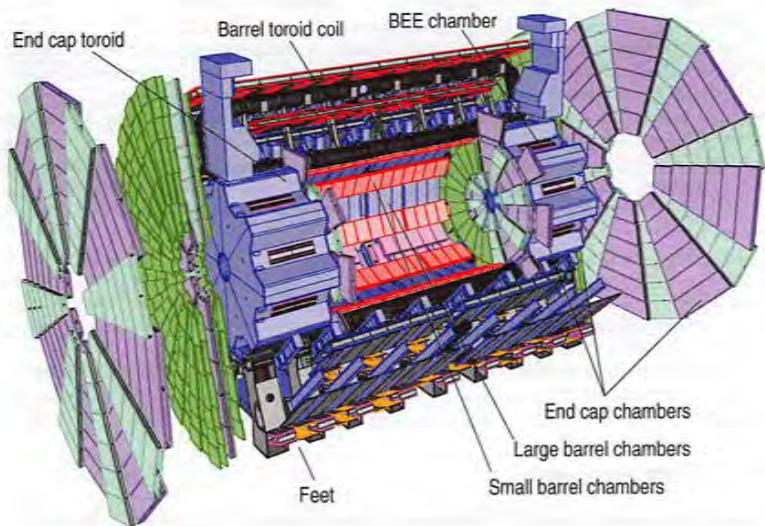


Figure 1: Schematic drawing of the ATLAS muon spectrometer

### 3 Detector map for muon efficiencies

In this note, the efficiency is calculated as a function of the muon transverse momentum, charge,  $\eta$  and  $\phi$ . The transverse momentum is divided into eight intervals between 20 GeV and 100 GeV with interval sizes chosen to achieve similar statistical uncertainties in all bins. The efficiency for  $p_T < 20$  GeV is studied with  $J/\psi \rightarrow \mu\mu$  decays [2]. To provide an efficiency measurement with good statistical precision, regions in  $\eta - \phi$  space are grouped such that they represent the geometrical configuration of the muon system. Ten different regions are used, corresponding to ten different physical regions in the MS [1]. Figure 2 shows the location of these regions in  $\eta - \phi$  space. In each of these regions the muon will traverse a particular set of detector layers. The ten detector regions are labeled and described below:

- Barrel large: large barrel stations.
- Barrel small: small barrel stations.
- Barrel overlap: overlap between small and large barrel stations.
- Feet: region of the feet supporting the detector; some chambers are missing in this region which makes the muon reconstruction more difficult.

- Transition: transition region between the barrel part and the end cap wheels.
- End cap small: small end cap sectors, MDT chambers.
- End cap large: large end cap sectors, MDT chambers.
- BEE: sectors containing BEE chambers.
- CSC small: small end cap sectors, CSC chambers, outside TRT acceptance.
- CSC large: large end cap sectors, CSC chambers, outside TRT acceptance.

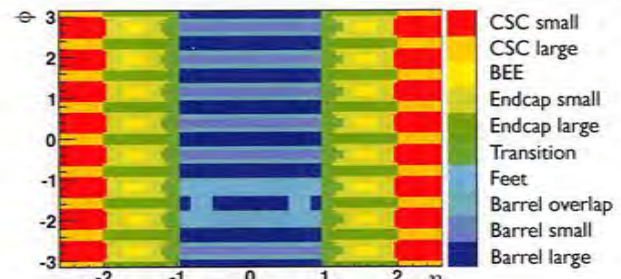


Figure 2: The detector regions. Regions in the  $\eta - \phi$  map with the same colour code are grouped into a single detector region.

### 4 Muon reconstruction in ATLAS

This note considers two types of muons reconstructed from measurements in the ID and MS.

**Combined muon (CB):** Track reconstruction is performed independently in the ID and MS, and a track formed from the successful combination of a MS track with an ID one.

**Segment tagged muon (ST):** A track in the ID is identified as a muon if the track extrapolated to the MS is associated with straight track segments in the precision muon chambers. In chain 2 the tagged tracks are refitted adding the MS segment information to improve their resolution.

Calorimetric information can also be used to tag ID tracks as muons. An ID track which can be matched with energy deposits in the calorimeters compatible with a minimum ionizing particle is called a *calorimeter tagged muon*. The performance of calorimeter tagged muons is not studied in the note, but calorimeter tagged muons have been used to check the results described in Sections 8 and 9.

Combined muons are the highest purity muon candidates. Their efficiency is determined mainly by the ability to form the independently reconstructed MS track, which varies with pseudorapidity and the azimuthal angle. This is most apparent in two regions:

- At  $\eta \sim 0$  the MS is only partially equipped with muon chambers to provide space for services of the ID and the calorimeters.
- In the transition region between the barrel and the end caps at  $|\eta| \sim 1.2$  only one chamber is traversed by muons in the MS due to staged end-cap chambers. So no stand-alone momentum measurement is available and the combined muon efficiency is decreased.

Segment-tagged muons are expected to have higher efficiency as they can recover muons which did not cross enough precision chambers to allow an independent momentum measurement in the MS. They are also needed to reconstruct low  $p_T$  muons which only hit the inner layer of the muon chambers [3].

In the present early phase of the LHC operation ATLAS uses two algorithm chains for reconstructing combined and segment-tagged muons. These follow different pattern recognition strategies and define the combined muon in slightly different ways [4]. In chain 1 it is required that the muon momentum is measured in both the ID and the MS. The momentum of the combined muon is then calculated as the weighted average of the ID and the MS stand-alone momentum measurements. The ID dominates the momentum measurements up to  $p_T \sim 50$  GeV; for  $50 \text{ GeV} < p_T < 100 \text{ GeV}$  the ID and MS measurements have similar weight; the MS dominates the measurement for  $p_T > 100 \text{ GeV}$ . In chain 2, instead of this statistical combination, a combined track fit to all muon hits in the ID and the MS is performed. This makes it possible to include also hit configurations in which no muon momentum measurement is possible in the MS alone. As a consequence more combined muons at  $|\eta| \sim 1.2$  are found in chain 2 than in chain 1. When a muon is reconstructed as both a combined and segment-tagged muon, only the combined muon is used in the analysis.

## 5 The tag-and-probe method

For this study, an unbiased muon sample with high transverse momentum is selected using  $Z \rightarrow \mu\mu$  decays. These events are selected by requiring one good muon, the tag, and one charged particle track measured by the ID, the probe. To reduce the backgrounds, the tag together with the probe has to match the signature of a  $Z$  boson decay i.e. the invariant mass of the pair has to be close to the nominal  $Z$  mass and the tracks must have opposite charge. To avoid any bias caused by the trigger, all tags are required to have triggered the data acquisition.

The efficiency is determined from the fraction of probes which are matched to a reconstructed muon. Despite the large data sample used, some bins in the efficiency map have low statistics. To avoid unphysical results, especially concerning the uncertainty calculation in bins with low statistics, the efficiencies are calculated with the Bayesian approach for a binomial distribution using a minimally informative (flat) prior, where flat prior means that *a priori* all efficiencies are equally probable [5]. Accordingly the efficiencies are calculated by:

$$\epsilon_{\text{true}} = \frac{\# \text{ successful matches} + 1}{\# \text{ trials} + 2}$$

## 6 Selection of tag-and-probe pairs

The selection is performed in three steps: selection of collision events, tag selection and probe selection. These steps are discussed below. A detailed overview of all cuts is given in Table I.

### 6.1 Collision event selection

The ID and MS, including their magnet systems, are required to have been fully operational for an event to be included in the analysis. Events must furthermore pass the muon trigger with the lowest

available transverse momentum threshold which was unprescaled. The events entering the efficiency measurements were recorded with an unprescaled muon trigger with a transverse momentum threshold well below the transverse momentum threshold of the tagged muon in the analysis. To ensure the event is a p-p collision at least one reconstructed primary vertex with at least three associated tracks is required.

All tracks considered in the analysis must have a minimum number of hits in the silicon detectors. Within the geometrical acceptance of the TRT a successful extension of the muon trajectory into that detector is enforced by requirements on the numbers of associated good TRT hits and TRT outliers. TRT outliers appear in two forms in the track reconstruction, as drift tube with a signal but not crossed by the near-by track or as a set of TRT measurements in the prolongation of a track which, however, failed to form a smooth trajectory together with the Pixel and SCT measurements. These quality cuts are put in place to suppress fake tracks and discriminate muons from hadrons.

### 6.2 Tag selection

Tags are defined as combined muons, separately for each of the two reconstruction chains. A combined muon has to pass the following cuts:

- the ID track on which the combined muon is based has to fulfil the track quality cuts listed above;
- the transverse momentum  $p_T$  is greater than 20 GeV;
- $|\eta| < 2.4$ , limited to the acceptance of the muon trigger system;
- longitudinal distance from primary vertex  $|z_0| < 10$  mm;
- additional muon quality requirements are imposed to remove a part of the background from decays in flight. These are applied only for chain 1, which had a looser selection of combined muon candidates during the commissioning with 2010 p-p collision data.
  - $\chi^2$  of the MS-ID match lower than 150 for 5 degrees of freedom;
  - if the momentum measured in the MS ( $p_T^{\text{MS}}$ ) is below 50 GeV the difference between the momenta measured in the ID ( $p_T^{\text{ID}}$ ) and  $p_T^{\text{MS}}$  normalized by  $p_T^{\text{ID}}$  must be larger than -0.4;
- the tagged muon must have triggered the data acquisition;
- the tag is isolated :  $\sum p_T(\Delta R < 0.4)/p_T(\text{muon}) < 0.2$  (with  $\Delta R := \sqrt{\Delta\eta^2 + \Delta\phi^2}$ ), where the sum extends over all charged particle tracks within a cone of 0.4 around the tag, excluding the charged particle track on which the tag is based.

### 6.3 Probe selection

Probes are defined as tracks, measured by the ID. They have to pass the following criteria :

- they fulfil the ID track quality criteria listed above;
- the  $p_T$  is greater than 20 GeV;
- $|\eta| < 2.5$ , limited to the coverage of the ID;
- longitudinal distance from primary vertex  $|z_0| < 10$  mm;
- they are isolated :  $\sum p_T(\Delta R < 0.4)/p_T(\text{muon}) < 0.2$ , where the sum extends over all charged particle tracks within a cone of 0.4 around the probe, excluding the probe itself;

- the tag and the probe must be associated to the same vertex;
- distance between tag and probe tracks in  $\phi > 2.0$ ;
- the invariant mass of the tag-and-probe pair is close to the nominal Z boson mass:  $|m_Z - m_{\text{TP}}| < 10 \text{ GeV}$ ;
- the probe and tag are oppositely charged.

#### 6.4 Probe - Muon matching

After selecting all tag-and-probe pairs an attempt is made to match the probe tracks to muons in the event. A match is considered successful if both have the same measured charge and are close in  $\eta - \phi$  space:  $\Delta R \leq 0.01$ .

### 7 Expectations from Monte-Carlo simulation

The efficiencies are measured relative to the efficiency of the ID, which is 100% within less than 1% statistical error [6]. Therefore all obtained efficiencies are taken to be absolute. The method is applied to simulated samples, to determine the influence of backgrounds on the efficiency determination and to derive scale factors, defined as the ratio between the efficiencies from data and Monte Carlo. As shown in [7], the tag-and-probe method determines the efficiency in simulated  $Z \rightarrow \mu\mu$  events correctly within errors.

The Monte Carlo samples used for these studies are generated by Pythia [8] using the ATLAS MC09 tune [9]. In these samples only a single interaction is simulated per bunch crossing. Six background channels were considered:  $Z \rightarrow \tau\tau$ ,  $W \rightarrow \mu\nu$ ,  $W \rightarrow \tau\nu$ , and production of  $b\bar{b}$ ,  $c\bar{c}$ , and  $t\bar{t}$  pairs. For the two QCD background channels a scale factor of 0.58 is applied to the cross section. This scale factor was measured in [10].

The background events can be split into two categories:

- Events in which the probe track is a muon. These background events do not bias the efficiency measurement.
- Event in which the probe track is not a muon. These events lead to an apparently reduced muon reconstruction efficiency. The measured reconstruction efficiency has to be corrected for the rate of these events.

The number of successful probe track to muon matches and the total number of probe tracks are counted for the  $Z \rightarrow \mu\mu$  signal and each of the six considered background samples. The efficiency is calculated from the sum of the successful and total trials, where the individual contributions are weighted according to the nominal cross-section of each sample.

If only the signal sample is considered, the efficiency is independent of  $p_T$  in the region under study. In the different detector regions (see Figure 3), the combined muon efficiencies vary between 90% and 98% in chain 1 and between 96% and 99% in chain 2, except for the large barrel region, for which the efficiency is only 92%. The region suffers most from the gap in the muon system around  $\eta \approx 0$  [1] which reduces the acceptance of the muon system. If the region  $|\eta| < 0.1$  is excluded from the efficiency calculation the efficiency in the Barrel large region rises significantly.

When the effect of the background contamination is taken into account, the calculated efficiency is lowered by  $\sim 1\%$  in total. The efficiency results for signal only and signal plus full background are shown in Figure 3. The drop in the efficiency is most pronounced in the low  $p_T$  bins, as displayed in Figure 3 (c,d). Background events with single high  $p_T$  muons will yield an efficiency of approximately

Collision Event Selection	
Data quality	muon Good Runs List [3]
Primary Vertex (PV) with $\geq 3$ tracks	$\geq 1$
ID Hit requirements for all tracks	
ID Si hit requirement	number of pixel hits $\geq 1$ , SCT hits $\geq 6$
TRT hit requirements: $ \eta  \leq 1.9$	Hits + Outliers > 5 & $\frac{\text{Outliers}}{\text{Hits+Outliers}} < 0.9$
TRT hit requirements: $ \eta  > 1.9$	if (Hits + Outliers > 5): $\frac{\text{Outliers}}{\text{Hits+Outliers}} < 0.9$
Tag Selection	
Kinematics	$p_T \geq 20 \text{ GeV} \&  \eta  \leq 2.4 \&  z_0  < 10 \text{ mm}$
Isolation	$\sum_{\text{tracks}} p_T^{\text{ID}} / p_T < 0.2$ tracks inside cone of 0.4 around tag
Muon Quality (chain 1 ONLY)	$\chi^2_{\text{match}} < 150$ if ( $p_T^{\text{MS}} < 50 \text{ GeV}$ ): $\frac{p_T^{\text{MS}} - p_T^{\text{ID}}}{p_T^{\text{ID}}} > -0.4$
Trigger:	
Period A-D	$p_T > 10 \text{ GeV}$ at level 1
Period E-F	$p_T > 10 \text{ GeV}$ at the Event Filter
Period G-H	$p_T > 13 \text{ GeV}$ at the Event Filter
Period I	$p_T > 13 \text{ GeV}$ at the Event Filter
Probe Selection	
Kinematics	$p_T \geq 20 \text{ GeV} \&  \eta  \leq 2.5 \&  z_0  < 10 \text{ mm}$
Isolation	$\sum_{\text{tracks}} p_T^{\text{ID}} / p_T < 0.2$ tracks inside cone of 0.4 around probe
Charge	$\text{charge}_{\text{Tag}} \cdot \text{charge}_{\text{Probe}} < 0$
$\Delta\phi(\text{Tag}, \text{Probe})$	$> 2.0$
Invariant mass	$ m_Z - m_{\text{TP}}  < 10 \text{ GeV}$
same vertex as Probe	$ z_{0_{\text{tag}}} - z_{0_{\text{probe}}}  < 3 \text{ mm}$
Probe - Muon matching	
$\Delta R$	$< 0.01$
Charge	same

Table 1: All cuts used in the efficiency measurement to select the tag and probe pairs and to match probes to muons are summarized.

zero. To quantify the impact of background events of category 2 on the measured muon reconstruction efficiency, the number of probe tracks which cannot be matched to a reconstructed muon in each background channel has been compared to the number of probes in the  $Z \rightarrow \mu\mu$  signal sample. The obtained fractions are summarized in Table 2.

Background	$Z \rightarrow \tau\tau$	$W \rightarrow \mu\nu$	$W \rightarrow \tau\nu$	$b\bar{b}$	$c\bar{c}$	$t\bar{t}$	Total
Category 2 background fraction (%)	0.02	0.30	0.07	0.22	0.08	0.03	0.72

Table 2: Fraction of category 2 background events in the final data sample after all selection cuts.

The largest background contributions are due to  $W$ , beauty, and charm decays. The QCD background increases with decreasing muon  $p_T$ . As a consequence the measured efficiency drops towards lower  $p_T$ .

A cross check of the simulated background contribution has been made by selecting like-charge tag and probe pairs. In simulation  $91 \pm 6$  and in data 75 pairs have been found. The ratio of like-charge to opposite-charge tag and probe pairs agrees very well between simulation (0.38%) and data (0.40%).

## 8 Results on experimental data

The efficiencies are determined using the full proton-proton sample recorded in 2010 and processed with the prompt reconstruction. The data corresponds to  $42 \text{ pb}^{-1}$  for which the MS and ID were fully operational and is divided into nine data taking periods, labeled A-I, of approximately one month length each. These coincide with periods of similar beam conditions in the LHC.

### 8.1 Efficiencies for combined muons.

Figure 4 shows the efficiency for combined muons as a function of  $p_T$  and detector region for data and simulation. The simulation includes all considered backgrounds. The scale factor defined as the ratio between data and Monte Carlo is displayed in the lower panel of each plot. It is on average  $0.9806 \pm 0.0024$  for chain 1 and  $0.9918 \pm 0.0020$  for chain 2, where the errors are only statistical. The largest deviation is found to be in the Transition region with a scale factor of 0.902 for chain 1 and 0.971 for chain 2. For chain 1 also the Feet and the BEE region show significantly lower efficiencies compared to the simulation with scale factors of 0.959 and 0.958, respectively. The efficiency drop in the BEE and the Feet regions are understood to arise from a poor alignment in this area. The efficiency drop in the Transition region is attributed to the limited accuracy of the magnetic field map used in the first-pass reconstruction of the ATLAS data in this region which leads to a small mismeasurement of the stand-alone muon momentum. The efficiency drops can be recovered by using muons which are tagged by only one muon station as is described in detail below.

The scale factors determined in bins of  $p_T$  agree within 1.5 standard deviations with the average scale factor for the algorithm in question. Hence it is sufficient to consider only the dependence on the different detector regions when applying the scale factors in a physics analysis.

The background corrected efficiencies for combined muons are shown in Figure 5. The background is estimated from Monte Carlo simulation, as described in the previous section. It is subtracted for every bin individually.

Table 3 summarises the background corrected efficiencies measured from data for the different data taking periods. The efficiencies as a function of time agree within the statistical uncertainties.

	Period	A-D	E	F	G	H	I
CB	$\epsilon_{\text{Chain 2}}$	0.946(19)	0.950(8)	0.960(6)	0.945(4)	0.955(4)	0.955(2)
	$\epsilon_{\text{Chain 1}}$	0.933(21)	0.896(10)	0.916(7)	0.919(5)	0.922(4)	0.925(3)
CB+ST	$\epsilon_{\text{Chain 2}}$	0.971(15)	0.985(5)	0.987(4)	0.979(3)	0.977(3)	0.980(1)
	$\epsilon_{\text{Chain 1}}$	0.971(15)	0.976(7)	0.974(5)	0.977(3)	0.974(3)	0.978(2)

Table 3: Background corrected reconstruction efficiencies for individual data taking periods. For each chain and muon definition the efficiency is consistent with being stable over the full run period. The statistical errors are shown in brackets.

### 8.2 Efficiencies for combined plus segment tagged muons.

The capability of recovering a part of the muon efficiency in the difficult detector regions by means of segment tagging is studied on the data by measuring the efficiency for combined plus segment-tagged muons. The same tag-and-probe method is used with the only difference that the probe is matched to a combined or segment-tagged muon. As combined muons are also reconstructed as segment tagged muons, combined muons which are rejected by the additional quality cuts for chain 1 enter the combined plus segment-tagged muon sample as tagged muons. Figure 6 shows the gain in efficiency when using segment-tagged muons in addition to the combined muons. The largest gains are in the ATLAS Feet (12 %) and Transition (18 %) regions of the detector for chain 1. For the chain 2 algorithm the gain is 3 % in the Feet and 5 % in the Transition region. In Figure 7 the efficiency for combined plus segment-tagged muons measured from data is compared to the Monte Carlo expectations and scale factors are derived. The scale factors for combined plus segment-tagged muons are 0.9990(16) for chain 1 and 1.0006(15) for chain 2 after background correction. The increase of the scale factor compared to the ones for combined muons only is 1.8% for chain 1 and 0.9% for chain 2.

## 9 Systematic Uncertainties

Uncertainties on the background contributions and due to the finite resolution of the detector are considered as systematic uncertainties.

The uncertainty due to the finite resolution of the detector is estimated by varying the selection cuts when determining the efficiency from Monte Carlo simulated data. The cuts on the mass window around the  $Z$  mass and the cut on the transverse momentum of the tag are each varied within their resolution. Other cuts are varied by  $\pm 10\%$ . The resulting change in the scale factors is quoted as systematic uncertainty. The amount of simulated background was varied by  $\pm 10\%$  and the resulting differences in the scale factors are considered as additional systematic uncertainties. A variation of  $\pm 10\%$  was chosen as it corresponds to the statistical uncertainty of the measurement of like-charge tag and probe pairs presented earlier in this note. Furthermore the uncertainty of the measurement of electro-weak and QCD background contributions in [11] also show an uncertainty of  $\sim 10\%$ .

The systematic uncertainties on the total scale factors for combined muons are summarised in Table 4. The individual systematic uncertainties are considered to be uncorrelated and are added in quadrature to obtain the total systematic uncertainty. For values which result from an up- and downwurd variation the larger value is quoted and used. The largest deviation arises from the variation of mass window followed by the variation of the background contamination and the variation of the probe isolation.

As the same tag-and-probe selection is used for the measurement of the CB+ST muon efficiency, the same systematic uncertainties are expected for the corresponding scale factors.

The background corrected efficiencies presented in this note have also been compared to the efficiencies which are obtained when the background is suppressed by an order of magnitude by requiring the

probe track to be a calorimeter tagged muon. The results of both methods agree within the systematic error of the method described in the note which is 0.2%.

Cut	Variation	absolute difference of SF from nominal	
		Chain 1, SF = 0.9806	Chain 2 SF = 0.9918
Probe isolation	0.2 → 0.18	0.0009	0.0009
Mass window	10 GeV → 8 GeV	0.0014	0.0013
$\Delta\phi$	2.0 → 2.2	0.0003	0.0003
$p_T$ (Tag)	20 GeV → 22 GeV	0.0006	0.0006
Probe TRT outlier frac.	0.9 → 0.7	0.0001	0.0001
MC Background	+ 10%	0.0007	0.0008
Total		0.0020	0.0019

Table 4: Contributions to the total systematic uncertainty in the CB muon efficiency measurement. For the total uncertainty only the largest deviation of an upward/downward variation is considered. The individual uncertainties are treated as fully uncorrelated and are added in quadrature.

## 10 Summary

The muon reconstruction efficiency for two different ATLAS reconstruction chains has been determined with the tag-and-probe method using events in which Z bosons decay into muon pairs. The efficiencies are determined from the p-p collision data collected with the ATLAS detector in 2010 and are compared to the efficiencies determined from the Monte Carlo simulation. The efficiency is measured as a function of  $p_T$  and in different detector regions. The measurement of the total reconstruction efficiency shows systematical and statistical errors of 0.002, where the largest systematic errors result from the influence of the mass window on the scale factors.

The muon reconstruction efficiency is found to be well above 92%, as predicted by the Monte-Carlo simulation. The average scale factor between experimental data and Monte Carlo simulations for combined muons from Z boson decays has been measured to be 0.9806(31) for chain 1 and 0.9918(28) for chain 2. Within one standard deviation all scale factors binned versus  $p_T$  agree with these values. The binning with respect to the different detector regions reveals significantly lower efficiencies for combined muons in data compared to the Monte Carlo simulation in the Transition region for both algorithms as well as in the Fiducial and BEE region for chain 1. The measured combined plus segment tagged efficiencies are in agreement with the Monte-Carlo predictions.

## References

- [1] ATLAS Collaboration, G. Aad et al., *The ATLAS Experiment at the CERN Large Hadron Collider*, JINST 3 (2008) S08003.
- [2] ATLAS Collaboration, *A measurement of the ATLAS muon efficiency using J/psi decays*, ATLAS conference note (in preparation).
- [3] ATLAS Collaboration, *Muon Reconstruction Performance*, ATLAS-CONF-2010-064 (Jul, 2010).
- [4] T. A. Collaboration, *Muon Performance in Minimum Bias pp Collision Data at  $\sqrt{s} = 7$  TeV with ATLAS*, Tech. Rep. ATLAS-CONF-2010-036, CERN, Geneva.
- [5] Rubin, *Bayesian Data Analysis*. Chapman & Hall/CRC, 2004.
- [6] ATLAS Collaboration, *Performance of the ATLAS Inner Detector Track Reconstruction*, ATLAS conference note (in preparation).
- [7] ATLAS Collaboration, G. Aad et al., *Expected performance of the ATLAS experiment: detector, trigger and physics*, arXiv:0901.0512, CERN-OPEN-2008-020 (2009).
- [8] T. Sjostrand, S. Mrenna, and P. Z. Skands, *PYTHIA 6.4 Physics and Manual*, JHEP 05 (2006) 026.
- [9] ATLAS Collaboration, G. Aad et al., *Measurement of underlying event characteristics using charged particles in pp collisions at  $\sqrt{s} = 900$ GeV and 7 TeV with the ATLAS detector*, arXiv:1012.0791 (2010).
- [10] ATLAS Collaboration, *Measurement of the  $W \rightarrow l\nu$  production cross-section and observation of  $Z \rightarrow ll$  production*, Tech. Rep. ATLAS-CONF-2010-051, CERN, Geneva.
- [11] ATLAS Collaboration, *Measurement of the  $W \rightarrow l\nu$  and  $Z/\gamma^* \rightarrow ll$  production cross sections in proton-proton collisions at  $\sqrt{s} = 7$  TeV with the ATLAS detector*, arXiv:1010.2130 (2010).

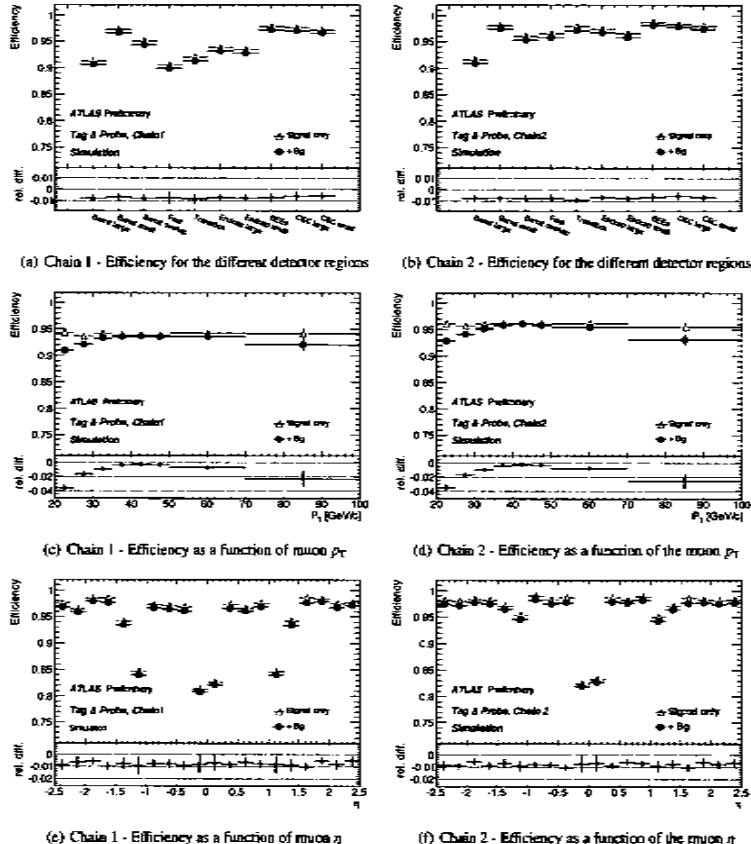


Figure 3: Measured efficiencies for combined muons from Monte Carlo simulated data for chain 1 and chain 2. Triangles correspond to signal only. Black dots correspond to signal plus all studied background contributions.

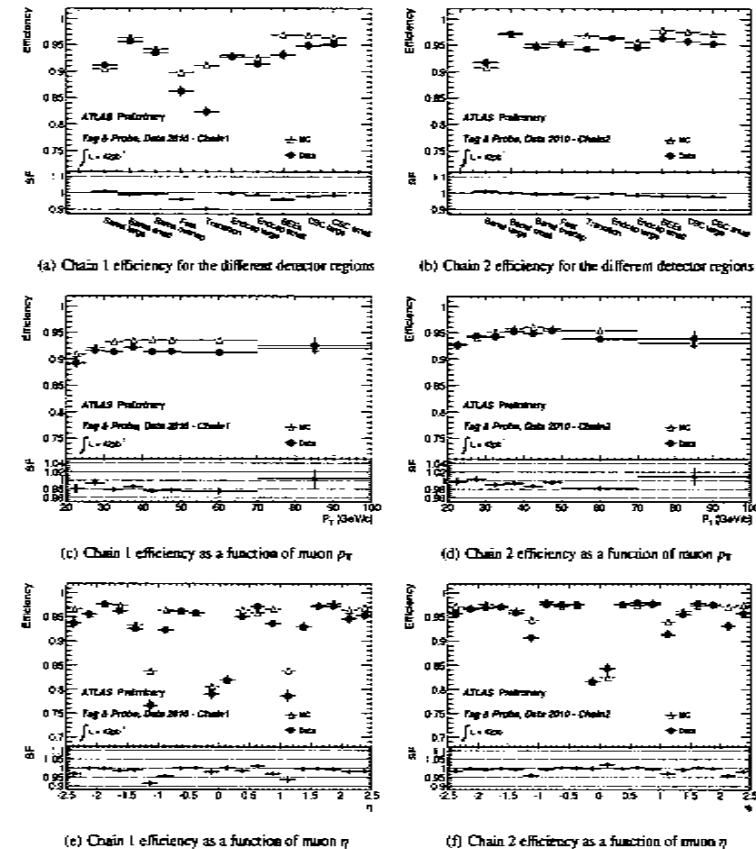
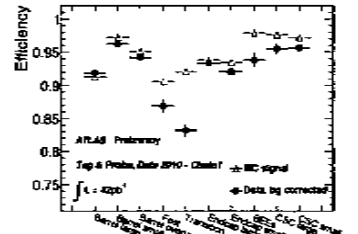
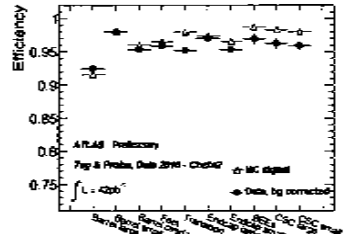


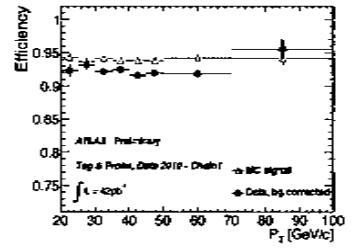
Figure 4: Reconstruction efficiencies and scale factors for combined muons. The efficiency for the two reconstruction chains, obtained from data (dots) and Monte Carlo simulation (open triangles) including backgrounds, are shown in the upper part of each figure. The corresponding scale factors are shown in the lower part.



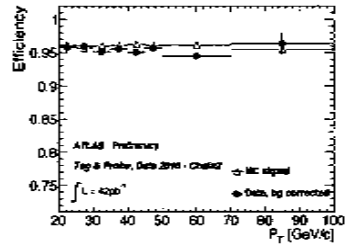
(a) Chain 1 efficiency for the different detector regions.



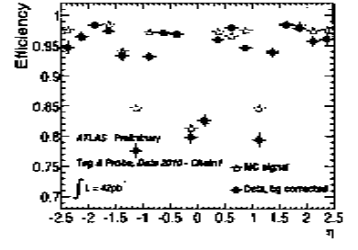
(b) Chain 2 efficiency for the different detector regions.



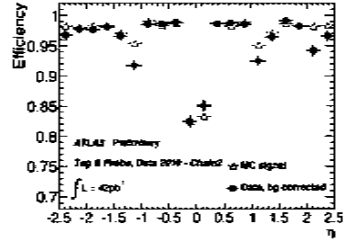
(c) Chain 1 efficiency as a function of muon  $p_T$ .



(d) Chain 2 efficiency as a function of muon  $p_T$ .

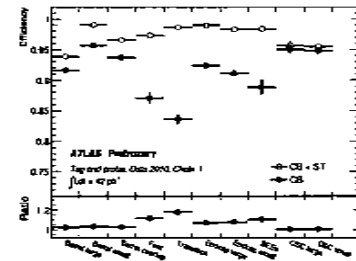


(e) Chain 1 efficiency as a function of muon  $\eta$ .

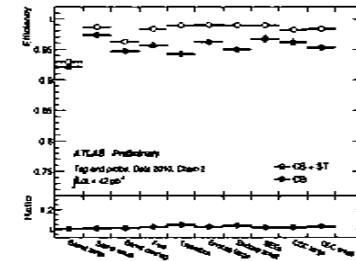


(f) Chain 2 efficiency as a function of muon  $\eta$ .

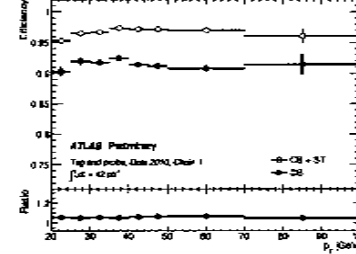
Figure 5: Background corrected efficiencies for combined muons for the two reconstruction chains, obtained from data (dots) and Monte Carlo simulation (open triangles).



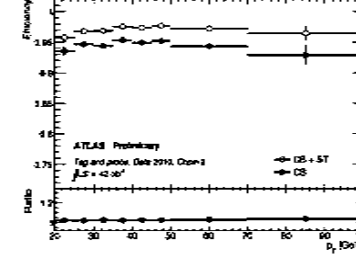
(a) Chain 1 efficiency for the different detector regions.



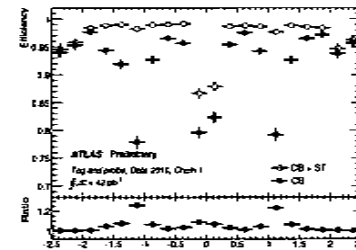
(b) Chain 2 efficiency for the different detector regions.



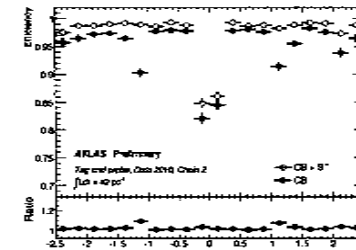
(c) Chain 1 efficiency as a function of muon  $p_T$ .



(d) Chain 2 efficiency as a function of muon  $p_T$ .

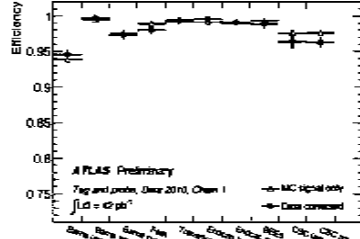


(e) Chain 1 efficiency as a function of muon  $\eta$ .

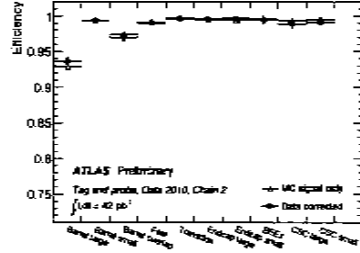


(f) Chain 2 efficiency as a function of muon  $\eta$ .

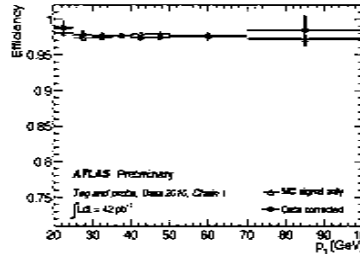
Figure 6: Efficiencies for combined plus segment-tagged muons (open circles) in comparison to those for combined muons only (dots). The relative gain is shown in the lower part of each figure.



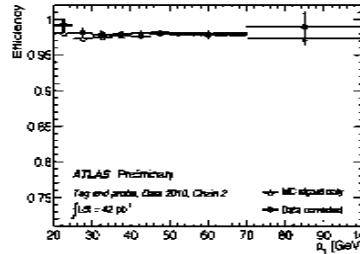
(a) Chain 1 efficiency for the different detector regions



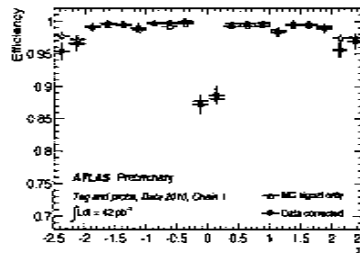
(b) Chain 2 efficiency for the different detector regions



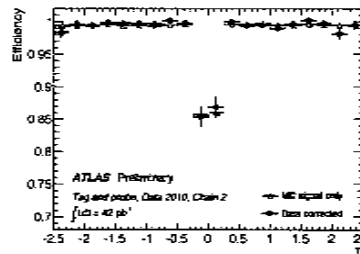
(c) Chain 1 efficiency as a function of muon  $p_T$



(d) Chain 2 efficiency as a function of muon  $p_T$



(e) Chain 1 efficiency as a function of muon  $\eta$



(f) Chain 2 efficiency as a function of muon  $\eta$

Figure 7: Efficiencies for combined plus segment-tagged muons, obtained from data with background correction (dots) and Monte Carlo simulation of the signal (open triangles).



M efficiency





## ATLAS NOTE

ATLAS-CONF-2011-063



### Muon reconstruction efficiency in reprocessed 2010 LHC proton-proton collision data recorded with the ATLAS detector

The ATLAS collaboration

#### Abstract

This note presents measurements of the muon reconstruction and isolation efficiencies based on an analysis of  $Z \rightarrow \mu^+\mu^-$  decays in an integrated luminosity of  $40 \text{ pb}^{-1}$  of  $\sqrt{s} = 7 \text{ TeV}$  proton-proton collision data recorded with the ATLAS detector in 2010. The data entering the analysis were reprocessed with an optimized ATLAS reconstruction software and improved detector calibration and alignment.

## 1 Introduction

The ATLAS detector has been designed for efficient muon detection and high momentum resolution. The good relative momentum resolution of  $< 3.5\%$  up to transverse momenta  $p_T \sim 200 \text{ GeV}$  and  $< 10\%$  up to  $p_T \sim 1 \text{ TeV}$  is achieved by a combination of measurements from the inner detector and the muon spectrometer [1]. The complementarity of these measurements can be exploited to provide measurements of the muon reconstruction efficiencies in both of these tracking systems. In the present note, the muon reconstruction efficiencies are measured with  $Z \rightarrow \mu^+\mu^-$  decays in which one of the decay muons is reconstructed in both systems and the other is identified by just one of the systems in order to probe the efficiency of the other. This so-called “tag-and-probe method” was successfully applied to the first pass reconstruction of the ATLAS proton-proton collision data recorded in 2010 at a centre-of-mass energy of  $7 \text{ TeV}$  [2]. The subject of this note is the muon reconstruction and muon isolation efficiency achieved after the reprocessing of the same data with optimized reconstruction software and improved detector calibration and alignment.

## 2 The ATLAS detector

A detailed description of the ATLAS detector can be found elsewhere [1]. Muons are independently measured in the inner detector (ID) and in the muon spectrometer (MS).

The ID measures tracks up to  $|\eta| = 2.5$ <sup>1</sup> exploiting three types of detectors operated in a solenoidal magnetic field of  $2 \text{ T}$ : a silicon pixel detector closest to the interaction point, a silicon strip detector (SCT) surrounding the pixel detector, and a transition radiation straw tube tracker (TRT) covering  $|\eta| < 2.0$  as the outermost part of the ID. The innermost layer of the pixel detector is referred to as the B-layer.

The MS consists of three large air-core superconducting toroidal magnet systems (two endcaps and one barrel) providing a field of approximately  $0.5 \text{ T}$ . The deflection of the muon trajectories in the magnetic field is measured via hits in three layers of precision drift tube (MDT) chambers for  $|\eta| < 2$  and two layers of MDT chambers in combination with one layer of cathode strip chambers (CSC) in the innermost endcap wheels of the MS, for  $2.0 \leq |\eta| < 2.7$ . Three layers of resistive plate chambers (RPC) in the barrel ( $|\eta| < 1.05$ ) and three layers of thin gap chambers (TGC) in the endcaps ( $1.05 < |\eta| < 2.4$ ) provide the muon trigger and also measure the muon trajectory in the non-bending plane of the spectrometer magnets.

The ATLAS detector has a three-level trigger system: level 1 (L1), level 2 (L2), and the event filter (EF). The MS provides a L1 hardware muon trigger which is based on hit coincidences within different RPC or TGC detector layers inside programmed geometrical windows which define the muon  $p_T$ . The L2 and EF muon triggers perform a software confirmation of the L1 muon trigger, by using refined  $p_T$  measurements from the precision chambers.

Figure 1 shows a schematic drawing of the ATLAS MS. The barrel muon chambers are installed in roughly cylindrical rings around the calorimeters. The endcap chambers are arranged in disks orthogonal to the proton beams. The BEE chambers are mounted on the endcap toroids. Large barrel chambers are mounted between the barrel toroid coils. Small barrel chambers are installed on and inside the toroid coils.

## 3 Detector map for muon efficiencies

As in [2], the efficiency is calculated as a function of the muon  $p_T$ ,  $\eta$  and azimuthal angle,  $\phi$ . The available statistics was sufficient to measure the muon efficiency in eight transverse momentum bins

<sup>1</sup> $\eta = -\ln(\tan(\theta/2))$ , where  $\theta$  is the polar angle measured from the beam line.

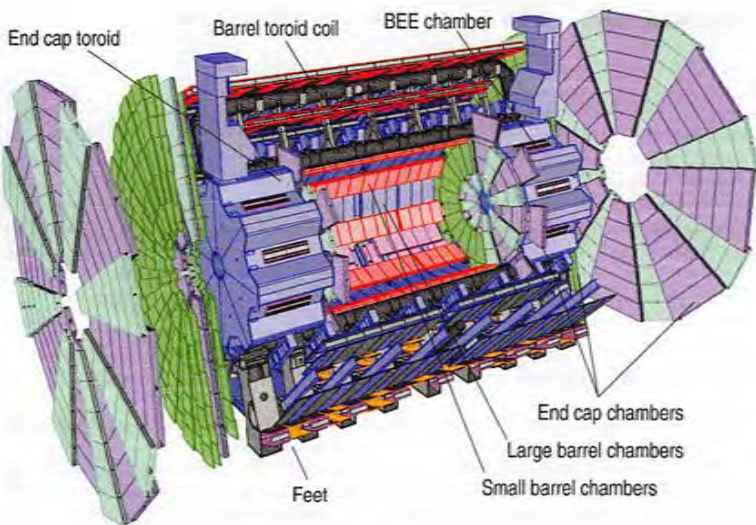


Figure 1: Schematic drawing of the ATLAS muon spectrometer

between 20 GeV and 100 GeV. The regions in  $\eta - \phi$  space are grouped in a manner that follows the spectrometer configuration. Ten different regions are used, corresponding to ten different physical regions in the MS [1]. Figure 2 shows their locations in  $\eta - \phi$  space. In each of these the muon will traverse a particular set of detector layers. The ten regions are labelled and described below:

- barrel large: large barrel stations;
- barrel small: small barrel stations;
- barrel overlap: overlap between small and large barrel stations;
- feet: region of the feet supporting the detector; some chambers are missing in this region which makes the muon reconstruction more difficult;
- transition: transition region between the barrel part and the endcap wheels;
- endcap small: small endcap sectors, MDT chambers;
- endcap large: large endcap sectors, MDT chambers;
- BEE: sectors containing barrel extended endcap chambers;
- CSC small: small endcap sectors, CSC chambers, outside TRT acceptance;
- CSC large: large endcap sectors, CSC chambers, outside TRT acceptance.

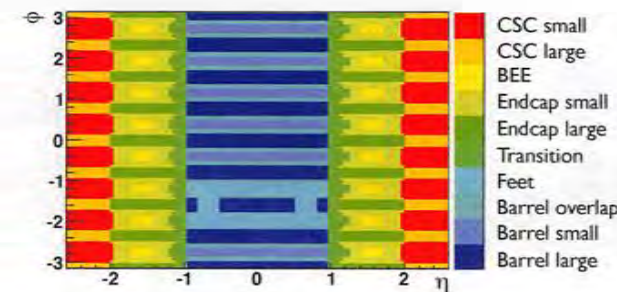


Figure 2:  $\eta - \phi$  map of the coverage of the ten detector regions.

#### 4 Muon identification in ATLAS

This note makes use of three classes of muons:

**Stand-alone (SA) muon:** The muon trajectory is only reconstructed in the MS. The direction of flight and the impact parameter of the muon at the interaction point are determined by extrapolating the spectrometer track back to the beam line taking the energy loss of the muon in the calorimeters into account;

**Combined (CB) muon:** Track reconstruction is performed independently in the ID and MS, and a track is formed from the successful combination of a MS track with an ID one;

**Segment tagged (ST) muon:** A track in the ID is identified as a muon if the track extrapolated to the MS is associated with straight track segments in the precision muon chambers.

The goal of the note is the measurement of the reconstruction efficiency for combined and segment tagged muons. Stand-alone muons are employed to measure the muon reconstruction efficiency in the inner detector as described in Section 5.

CB muons are the highest purity candidates. The efficiency for their reconstruction is determined mainly by the ability to form the independently reconstructed MS track, which varies with  $\eta$  and  $\phi$ . This is most apparent in two regions:

- At  $\eta \sim 0$  the MS is only partially equipped with muon chambers to provide space for services of the ID and the calorimeters.
- In the transition region between the barrel and the endcaps at  $|\eta| \sim 1.2$  only one chamber is traversed by muons in the MS, due to staged endcap chambers. So no stand-alone momentum measurement is available and the CB muon efficiency is decreased.

The algorithms for ST muons have higher efficiency than those for CB muons as they can recover muons which did not cross enough precision chambers to allow an independent momentum measurement in the MS. They are also needed to reconstruct low  $p_T$  muons which only reach the inner layer of the muon chambers [3].

Staco = Chain 1  
Mu Id = Chain 2

In the present early phase of the LHC operation ATLAS uses two algorithm chains for reconstructing ST and CB muons, namely chain 1 (Staco) and chain 2 (MuId). These follow different pattern recognition strategies and define the CB muon in slightly different ways [4]. In chain 1 it is required that the muon momentum is measured in both the ID and the MS. The momentum of the CB muon is then calculated as the weighted average of the ID and the MS stand-alone momentum measurements. The ID dominates the measurement up to  $p_T \sim 80$  GeV in the barrel and  $p_T \sim 20$  GeV in the endcaps. For higher  $p_T \lesssim 100$  GeV the ID and MS measurements have similar weight while the MS dominates at  $p_T \gtrsim 100$  GeV. In chain 2, instead of this statistical combination, a combined track fit to all muon hits in the ID and the MS is performed. The fit procedure includes recovery of missing or wrongly assigned spectrometer hits, most frequently arising from missing or low quality MS information in the transverse projection. A small fraction of combined muon tracks are formed from MS tracks without a momentum measurement (such as found in the transition region). When a muon is reconstructed as both a CB and ST muon, only the CB muon is used in the analysis.

#### 4.1 Major changes to the first pass reconstruction software

The combined reconstruction algorithm of chain 1 has been improved compared to the version used in the first pass reconstruction in 2010. In that version, the association of stand-alone muons with inner detector tracks was performed by comparing the momentum of the stand-alone muon with the momentum of the inner detector track taking into account the corresponding uncertainties of the momentum measurements. As the estimate of the energy at the beam line for low-energy stand-alone muons has a large uncertainty due to the significant energy loss fluctuations of the muon in the calorimeters, the combination of a low-energy MS track with a high momentum ID track can satisfy the matching criteria. This incorrect association is avoided in the improved version of the chain 1 algorithm by also checking whether the inner detector track extrapolated into the MS can be geometrically matched with the MS track.

#### 5 The tag-and-probe method

$$\epsilon_{\text{reco}} = \epsilon_{\text{ID}} \times \epsilon_{\text{MS}} \times \epsilon_{\text{match}}$$

The reconstruction efficiency for CB or ST muons is the product of the muon reconstruction efficiency in the ID, the reconstruction efficiency in the MS, and the matching efficiency between the ID and MS measurements. Therefore it is possible to study the full reconstruction efficiency by measuring these individual efficiencies. The tag-and-probe method is sensitive to either the inner detector efficiency or the MS and matching efficiency.

In the tag-and-probe method,  $Z \rightarrow \mu^+ \mu^-$  decays are selected by requiring two oppositely charged isolated tracks with a dimuon invariant mass near the mass of the  $Z$  boson. One of the tracks must be a CB muon. This track is called the "tag muon". The other track, the so-called "probe", must be a stand-alone muon if the ID efficiency is to be measured. If the MS and matching efficiency is to be measured the other track must be an inner detector track. The ID reconstruction efficiency is the fraction of stand-alone muon probes which can be associated to an inner detector track. The MS and matching efficiency is the fraction of ID probes which can be associated to a CB or ST muon. The impact of background events on the efficiency measurements is discussed in Section 6.6.

#### 6 Selection of tag-and-probe pairs

The selection is performed in three steps: selection of collision events, tag selection and probe selection. These steps are discussed below. A detailed overview of the selection criteria is given in Table 1.

tag  
CB  
probe  
SA  $\leftarrow \epsilon_{\text{ID}}$   
idtrack  $\leftarrow \epsilon_{\text{MS}}$   
 $\epsilon_{\text{MS}}$

Collision Event Selection	
Data quality	muon Good Runs List [3]
Primary vertex (PV) with $\geq 3$ tracks	$\geq 1$
ID Hit requirements	number of B layer hits > 0, pixel hits $\geq 2$ , SCT hits $\geq 6$
ID Si hit requirement	Hits + Outliers > 5 & $\frac{\text{Outliers}}{\text{Hits+Outliers}} < 0.9$
TRT hit requirements: $ \eta  \leq 1.9$	if (Hits + Outliers > 5): $\frac{\text{Outliers}}{\text{Hits+Outliers}} < 0.9$
TRT hit requirements: $ \eta  > 1.9$	
Tag Selection	
Kinematics	$p_T \geq 20$ GeV & $ \eta  \leq 2.4$ & $ z_0  < 10$ mm
Isolation	$\sum_{\text{tracks}} p_T^{ID}/p_T < 0.2$ tracks inside cone of 0.4 around tag
Trigger:	
Period A-D	$p_T > 10$ GeV at level 1
Period E-F	$p_T > 10$ GeV at the event filter
Period G-I	$p_T > 13$ GeV at the event filter
Probe Selection	
Kinematics	$p_T \geq 20$ GeV & $ \eta  \leq 2.5$ & $ z_0  < 10$ mm
Isolation	$\sum_{\text{tracks}} p_T^{ID}/p_T < 0.2$ tracks inside cone of 0.4 around probe
Charge	Opposite charges of tag and probe
$\Delta\phi(\text{Tag}, \text{Probe})$	$> 2.0$
Invariant mass	$ m_Z - m_{\text{TP}}  < 10$ GeV
same vertex as Probe	$ z_{0_{\text{tag}}} - z_{0_{\text{probe}}}   < 3$ mm
Probe - Muon matching	
$\Delta R$	$< 0.01$
Charge	same

Table 1: All cuts used to select the tag and probe pairs and to match probes to muons are summarized. The ID hit requirements are restricted to the instrumented areas; dead or missing sensors crossed by a track are counted as hits.

#### 6.1 Collision event selection

The ID and MS, including their magnet systems, have to be fully operational for an event to be included in the analysis. Events must pass the lowest  $p_T$  threshold muon trigger that was unprescaled. The thresholds of the selected triggers ranged from 10 to 13 GeV and were well below the transverse momentum threshold of the tag muon in the analysis. To include only proton-proton collision events, a reconstructed primary vertex with at least three associated tracks is required.

#### 6.2 Inner detector track selection

All tracks considered in the analysis must have a minimum number of hits in the silicon detectors. Dead or missing sensors crossed by a track are counted as hits. Within the geometrical acceptance of the TRT a successful extension of the muon trajectory into that detector is enforced by requirements on the numbers of associated good TRT hits and TRT outliers. TRT outliers appear in two forms in the track reconstruction, as a straw tube with a signal but not crossed by the near-by track or as a set of TRT measurements in the prolongation of a track which, however, failed to form a smooth trajectory together with the pixel and SCT measurements. These quality cuts are put in place to suppress fake tracks and

discriminate against muons from hadron decays. Combined and segment-tagged muons which do not fulfil the ID hits requirements are rejected in the analysis.

### 6.3 Tag selection

Tag muons are defined as combined muons from the primary vertex, separately for each of the two reconstruction chains. A combined muon has to pass the following cuts:

- the ID track on which the combined muon is based has to fulfil the track hit cuts listed in Table 1;
- $p_T \geq 20$  GeV;
- $|\eta| \leq 2.4$ , limited to the acceptance of the muon trigger system;
- longitudinal distance from primary vertex  $|z_0| < 10$  mm;
- the tag muon must have triggered the data acquisition;
- isolation:  $\sum p_T(\Delta R < 0.4)/p_T(\text{tag}) < 0.2$  (with  $\Delta R := \sqrt{\Delta\eta^2 + \Delta\phi^2}$ ), where the sum extends over all tracks within a cone of 0.4 around the tag, excluding the track on which the tag is based.

### 6.4 Probe selection

Probes are either stand-alone muons or inner detector tracks depending on which efficiency measurement is being performed. They have to pass the following criteria :

- ID probes must fulfil the ID track hit criteria listed in Table 1;
- $p_T > 20$  GeV;
- $|\eta| < 2.5$ , limited to the coverage of the ID;
- longitudinal distance from primary vertex  $|z_0| < 10$  mm;
- isolation:  $\sum p_T(\Delta R < 0.4)/p_T(\text{probe}) < 0.2$ , where the sum extends over all tracks within a cone of 0.4 around the probe, excluding the probe itself;
- the tag and the probe must be associated to the same vertex;
- azimuthal separation of tag and probe tracks,  $\Delta\phi > 2.0$ ;
- the invariant mass of the tag-and-probe pair is close to the nominal  $Z$  mass:  $|m_Z - m_{\text{TP}}| < 10$  GeV;
- the tag and the probe are oppositely charged.

The additional quality requirements used in [2] to reject bad matches of stand-alone muons with inner detector tracks in chain 1 are no longer needed in the improved version of that combined reconstruction algorithm.

### 6.5 Probe - muon matching

After selecting all tag-and-probe pairs an attempt is made to match the probe tracks to muons in the event. A match between an ID probe and a muon is considered successful if they have the same measured charge and are close in  $\eta$ - $\phi$  space:  $\Delta R \leq 0.01$ . A match between a SA muon probe and an ID track is considered successful if  $\Delta R \leq 0.05$ .

### 6.6 Purity of the selected sample

According to Monte Carlo studies, 99.3% of the selected events with an inner detector probe contain dimuon decays of  $Z$  bosons; the background events are  $Z \rightarrow \tau^+\tau^-$ ,  $W^+ \rightarrow \mu^+\nu_\mu$ ,  $W^+ \rightarrow \tau^+\bar{\nu}_\tau$ ,  $b\bar{b}$ ,  $c\bar{c}$ , and  $t\bar{t}$  as shown in [2]. The presence of background events leads to an apparently lower measured muon efficiency. This is visible in the plots of Figure 3 which, for CB muons using ID probes, shows the effect of the backgrounds on the measured efficiency in bins of detector region,  $p_T$ , and  $\eta$ . Figures 3(c) and (d) show that the background mainly contributes to the region of low transverse momenta of the probe muons and is negligible for  $p_T \geq 30$  GeV. The background contamination is below 0.1% for selected events with a stand-alone muon probe.

## 7 Measured muon reconstruction efficiencies

### 7.1 Inner detector reconstruction efficiency

As discussed earlier, and illustrated in Figure 3, the efficiency for the combined muon reconstruction varies with the detector region, and with  $p_T$  in the range below 6 GeV [5]. In contrast, the ID muon efficiency is independent of  $\phi$  and  $p_T$ [1]. It shows a small  $\eta$  dependence as illustrated in Figure 4. The small efficiency drops at  $\eta \sim 0$  and  $\eta \sim 1$  are caused by the ID hit requirements listed in Table 1. At  $\eta \sim 0$  ID tracks which pass through the dead region near the middle of the TRT barrel straws produce no TRT hits. At  $|\eta| \sim 1$  there is a small region in the transition between the barrel and endcaps of the ID in which muons cross less than 6 SCT sensors. The measured ID muon reconstruction efficiency agrees with the Monte-Carlo prediction within the statistical errors of less than 1 %. The measured ID efficiency is  $(0.991 \pm 0.001)$  on average due to the hit requirements imposed on the ID muon tracks. The results are independent of the choice of the algorithm chain for the stand-alone muon.

### 7.2 Combined muon reconstruction efficiency

Figure 5 shows the efficiency for CB muons as a function of  $p_T$ , the detector region, and  $\eta$  for data and simulation, relative to the ID efficiency. The simulation includes all considered backgrounds. The scale factor, defined as the ratio between data and Monte Carlo, is displayed in the lower panel of each plot. The mean value of the  $\eta$  dependent scale factor curve is  $0.989 \pm 0.003$  for chain 1 and  $0.995 \pm 0.002$  for chain 2, where the errors are statistical. The 1% deviation from 1 in overall efficiency scale factor of chain 1 is caused by the efficiency scale factor of 0.94 in the transition region. The efficiency drop in the transition region is attributed to the limited accuracy of the magnetic field map used in the reconstruction of the ATLAS data in this region which leads to a small mismeasurement of the stand-alone muon momentum. The efficiency drops can be recovered by using muons which are tagged by only one muon station as described in detail below.

The scale factors determined in bins of  $p_T$  agree, within 1.5 standard deviations, with the average scale factor for the algorithm in question.

The background-corrected efficiencies for CB muons are shown in Figure 6. The background is estimated from Monte Carlo simulation, as described in Section 6.6. It is subtracted for every bin individually. The average CB muon reconstruction efficiency is  $0.928 \pm 0.002$  for chain 1 and  $0.958 \pm 0.001$  for chain 2. The difference in efficiency between the two chains arises mainly from more stringent requirements on the reconstructed MS tracks considered for identifying a muon as combined muon in chain 1.

### 7.3 Efficiencies for combined plus segment tagged muons.

The degree to which some muon efficiency, in detector regions with partial muon coverage, can be recovered using segment tagging, has been studied by measuring the efficiency for CB plus ST muons. The same tag-and-probe method is used with the only difference that the probe is matched to a CB or ST muon. Figure 7 shows the measured combined plus segment tagged muon efficiencies as functions of the detector region,  $p_T$ , and  $\eta$ , in comparison with the combined muon efficiencies. The gain in efficiency when using ST muons in addition to the CB muons is presented in the lower panels of the plots. These are largest in the ATLAS feet (13 %) and transition (15%) regions of the detector for chain 1. For the chain 2 algorithm the largest gain is 3 % in the feet and BEE regions. Figures 7(c) and (d) show that the two chains have similar overall efficiencies for combined plus segment tagged muons,  $0.970 \pm 0.001$  for chain 1 and  $0.980 \pm 0.001$  for chain 2.

In Figure 8 the efficiency for CB plus ST muons measured from data is compared to the Monte Carlo expectations and scale factors are derived. Remarkable agreement between the measured and predicted efficiencies is achieved. The scale factors for CB plus ST muons are  $1.003 \pm 0.002$  for chain 1 and  $1.004 \pm 0.002$  for chain 2.

## 8 Measurement of the muon isolation efficiency

A powerful tool for rejecting muons from hadron decays in the tag-and-probe efficiency measurement is isolation. It is therefore desirable to quantify the reliability of the Monte-Carlo prediction of the isolation efficiency. This is studied using the same event selection as was used for the efficiency measurements, up to the selection of the tag muon. In this case, the probe muon is defined as an isolated CB muon with  $p_T > 20$  GeV that fulfils the ID hit requirements of Table 1. We consider track isolation and calorimeter isolation:

- Track isolation:  $\sum p_T(\Delta R < 0.4(0.3))/p_T(\mu) < 0.2$  or  $0.1$ , where the sum extends over all charged particle tracks within a cone of  $0.4(0.3)$  around the probe, excluding the probe itself;
- Calorimeter isolation: the transverse energy deposition in the calorimeter ( $E_T$ ) in a cone of size  $\Delta R < 0.4(0.3)$  around the muon is less than  $0.2p_T(\mu)$  or  $0.1p_T(\mu)$ . The calorimeter isolation energy is corrected for the muon energy loss.

Figure 9 compares the distributions of the measured isolation variables for the probe muons with the Monte-Carlo prediction. The excellent agreement between the experimental and simulated distributions leads to a reliable prediction of the isolation efficiency which is defined as the fraction of probe muons passing a given set of isolation cuts. The measured isolation efficiencies and the corresponding Monte Carlo predictions are compared for chain 1 in Figure 10; the results for chain 2 are consistent. Experimental and simulated data agree within errors. The isolation efficiency in the  $Z \rightarrow \mu^+\mu^-$  selection under study is well modelled by the ATLAS Monte Carlo simulation. The efficiency drops at low  $p_T(\mu)$  are mainly caused by the fact that the track  $p_T$  sums and  $E_T$ , which depend only weakly on  $p_T(\mu)$ , are divided by  $p_T(\mu)$ , leading to isolation variables that rise with decreasing  $p_T(\mu)$ . They are also partially due to the background which populates the low  $p_T(\mu)$  region.

## 9 Summary

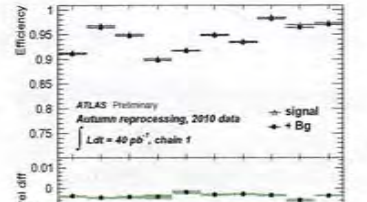
The muon reconstruction and isolation efficiency has been studied with  $Z \rightarrow \mu^+\mu^-$  decays for an integrated luminosity of  $40 \text{ pb}^{-1}$  of proton-proton collision data recorded with the ATLAS detector in 2010.

The muon reconstruction efficiency is measured to be  $> 96\%$  and agrees with the Monte-Carlo prediction to within less than 1%. The measurement of the isolation efficiency is in excellent agreement with the Monte-Carlo prediction.

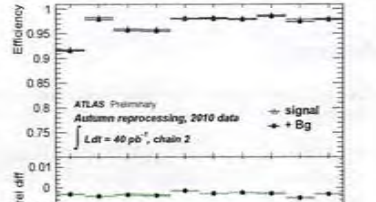
## References

- [1] ATLAS Collaboration, *The Atlas Experiment at the CERN Large Hadron Collider*, JINST 3 (2008) S08003.
- [2] ATLAS Collaboration, *Determination of the muon reconstruction efficiency in ATLAS at the Z resonance in proton-proton collisions at  $\sqrt{s}=7$  TeV*, ATLAS-CONF-2011-008, CERN, Geneva, 2011.
- [3] ATLAS Collaboration, *Muon Reconstruction Performance*, ATLAS-CONF-2010-064, CERN, Geneva, 2010.
- [4] ATLAS Collaboration, *Muon Performance in Minimum Bias pp Collision Data at  $\sqrt{s} = 7$  TeV with ATLAS*, ATLAS-CONF-2010-036, CERN, Geneva, 2010.
- [5] ATLAS Collaboration, *A measurement of the ATLAS muon efficiency using J/ψ decays*, ATLAS-CONF-2011-021, CERN, Geneva, 2011.

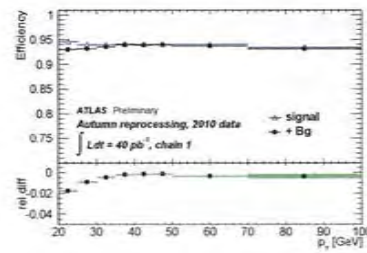
$$\sum_{\text{MS}}^{\text{CB}} + \sum_{\text{match}}^{\text{CB}}$$



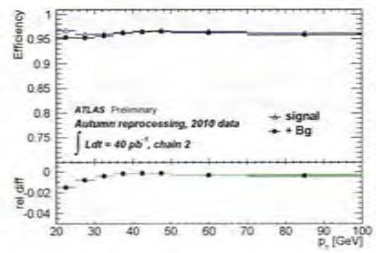
(a) Chain 1 efficiency for the different detector regions



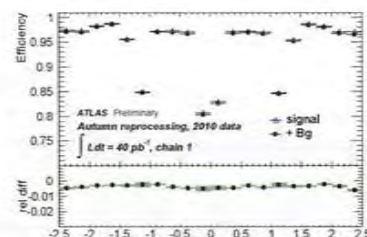
(b) Chain 2 efficiency for the different detector regions



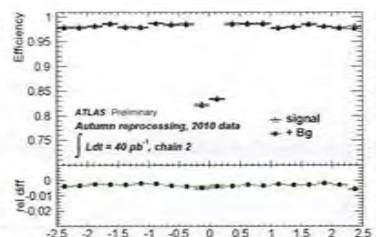
(c) Chain 1 efficiency as a function of muon  $p_T$



(d) Chain 2 efficiency as a function of the muon  $p_T$



(e) Chain 1 efficiency as a function of muon  $\eta$



(f) Chain 2 efficiency as a function of the muon  $\eta$

Figure 3: Measured efficiencies for combined muons from Monte Carlo simulated data for chain 1 and chain 2 using ID probes. The triangles correspond to efficiencies determined from the  $Z \rightarrow \mu^+ \mu^-$  sample only, while the black dots show the efficiencies obtained with the tag-and-probe method when backgrounds are included.

$$\epsilon_{ID}$$

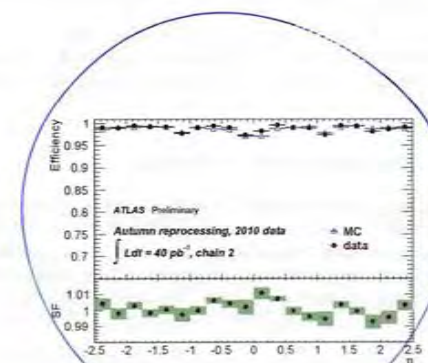


Figure 4: Comparison of the measured ID muon reconstruction efficiency as a function of  $\eta$  with the Monte-Carlo prediction. The scale factors, defined as the ratios of the measured and the predicted efficiencies, are consistent with unity to within the uncertainties, which are less than about 1%. The inefficiencies are created by the hit requirements imposed on the ID tracks.

$$\epsilon_{ID}$$

Avg 98.8%

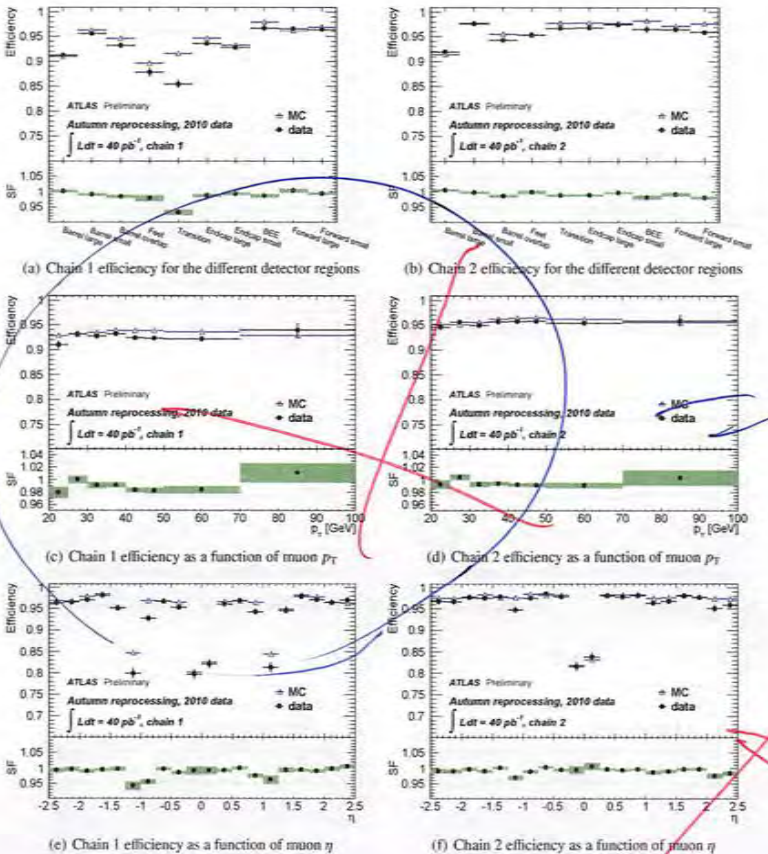


Figure 5: Reconstruction efficiencies and scale factors for CB muons. The efficiencies for the two reconstruction chains, obtained from data (dots) without background correction and Monte Carlo simulation (open triangles) including backgrounds, are shown in the upper part of each figure. The corresponding scale factors are shown in the lower part.

12

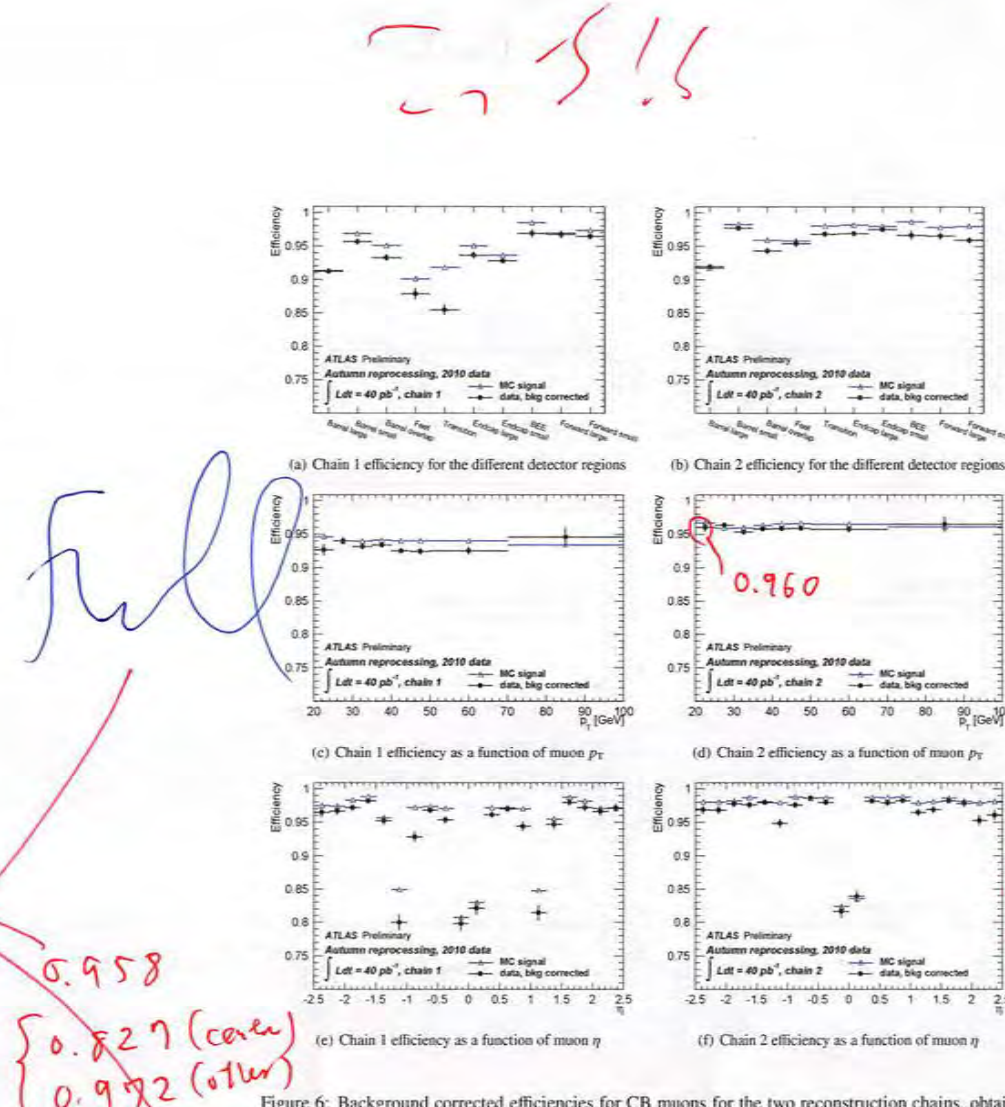


Figure 6: Background corrected efficiencies for CB muons for the two reconstruction chains, obtained from data (dots) and Monte Carlo simulation (open triangles).

13

$\mathcal{E}_{\text{full}}^{\text{CB+ST}}$

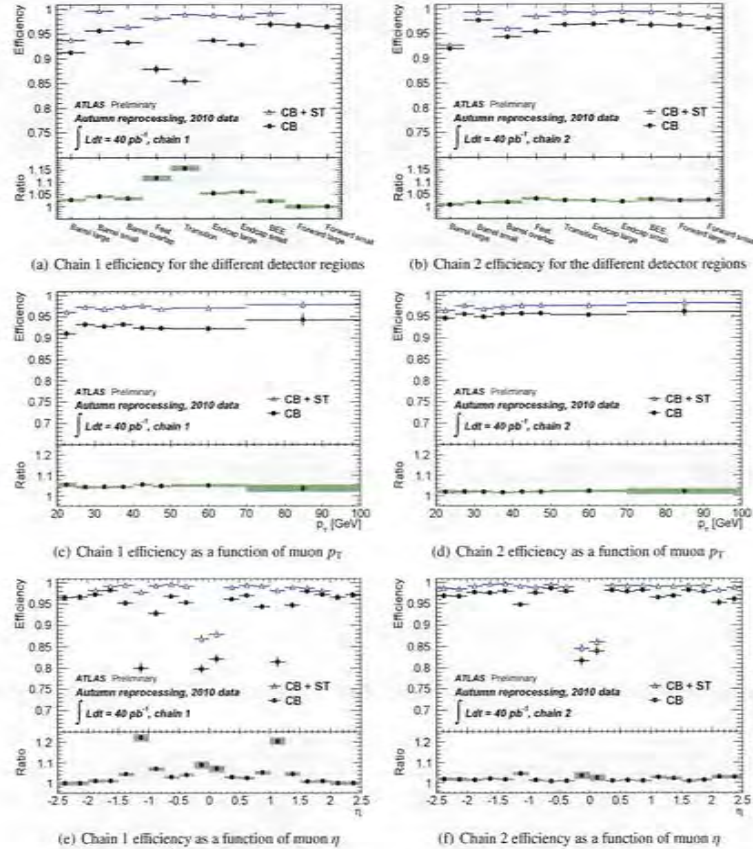


Figure 7: Efficiencies for CB plus ST muons (open circles) in comparison to those for CB muons only (dots). The relative gain is shown in the lower part of each figure.

$\mathcal{E}_{\text{CB}}, \mathcal{E}_{\text{ST+CB}}$

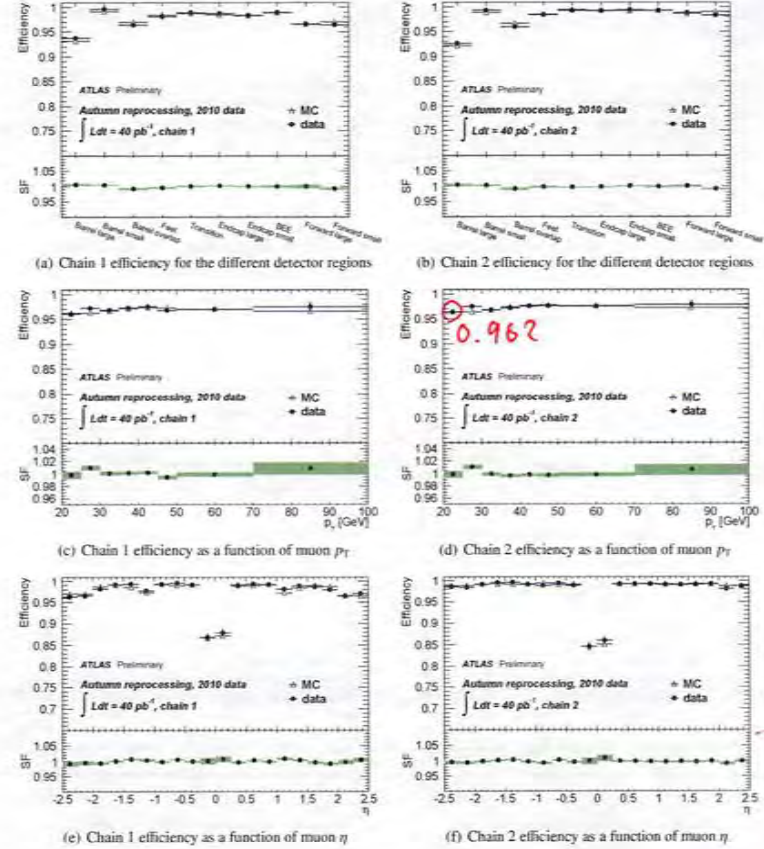


Figure 8: Efficiencies for CB plus ST muons, obtained from data with background correction (dots) and Monte Carlo simulation of the signal (open triangles).

0.976  
(Conf 0.852  
other 0.990)

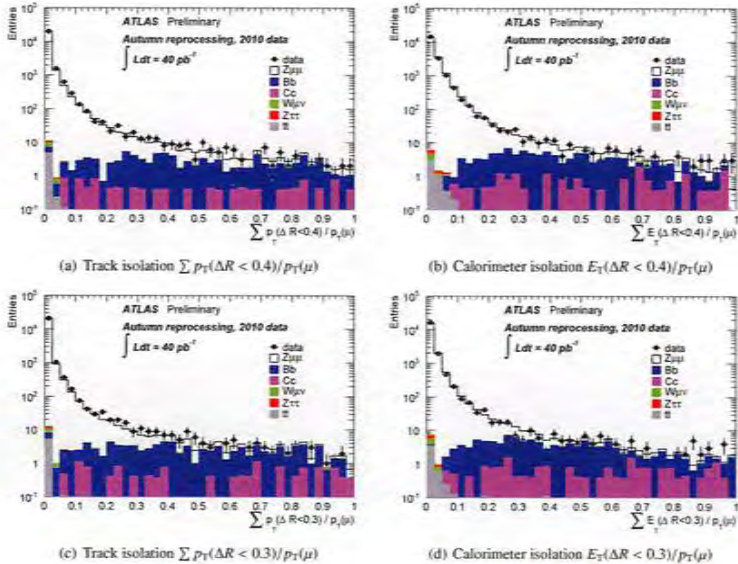


Figure 9: Comparison of the measured track and calorimeter isolation distributions of the probe muon with the Monte-Carlo prediction for two different cone sizes.

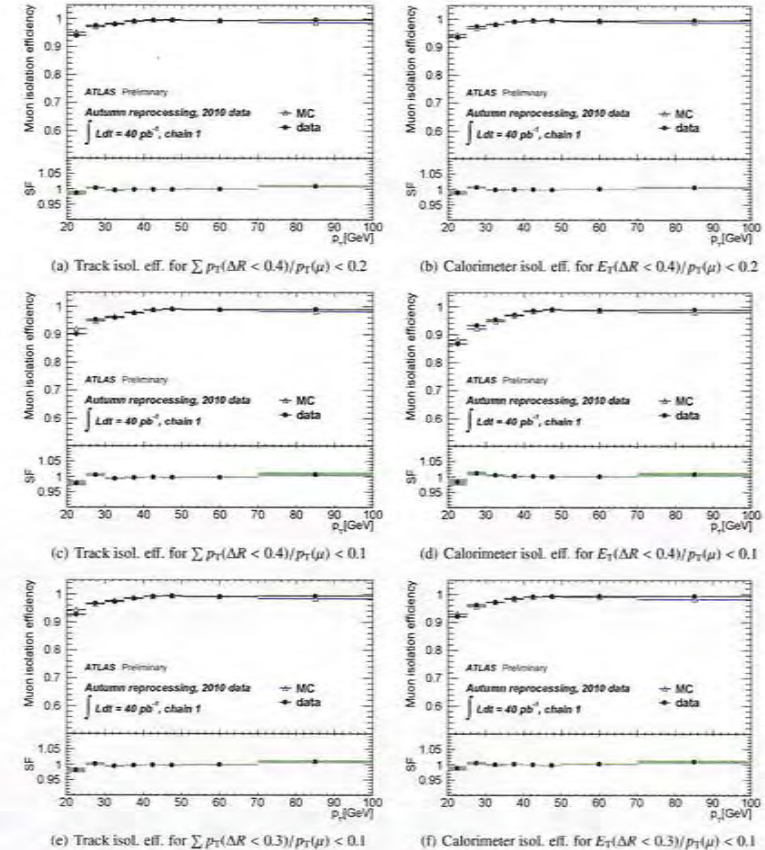


Figure 10: Muon isolation efficiency in  $Z \rightarrow \mu^+ \mu^-$  events for different isolation requirements. The Monte-Carlo prediction includes  $Z$  signal and background processes.

Eisal

3

3

ESF in small  $p_T$  case



## ATLAS NOTE ATLAS-CONF-2012-125

August 27, 2012



### A measurement of the muon reconstruction efficiency in 2010 ATLAS data using $J/\psi$ decays

The ATLAS Collaboration

#### Abstract

A measurement of the ATLAS muon reconstruction efficiency based on the *tag-and-probe* method using muons from decays of  $J/\psi$  mesons is presented. The data sample, corresponding to  $40 \text{ pb}^{-1}$  of  $pp$  collisions data at  $\sqrt{s} = 7 \text{ TeV}$ , was collected during the 2010 run. These results improve the previous determination of the reconstruction efficiency at low transverse momenta thanks to a better statistical precision and to lower systematic uncertainties.

## 1 Introduction

This note describes a measurement of the offline muon reconstruction efficiency at low transverse momenta using  $40 \text{ pb}^{-1}$  of data collected by ATLAS during the 2010  $pp$  run of LHC. The ATLAS detector is described in detail elsewhere [1]. This measurement is based on the so-called *tag-and-probe* method at the  $J/\psi$  resonance; the basic analysis strategy has already been applied in previous preliminary determinations of the muon reconstruction efficiency based on  $3.1 \text{ pb}^{-1}$  [2].

In this procedure, muon pairs are selected by requiring a well reconstructed muon, the *tag*, and an Inner Detector (ID) track, the *probe*, forming a system with invariant mass consistent with a  $J/\psi \rightarrow \mu^+ \mu^-$  decay. The probes, selected without using the Muon Spectrometer (MS) information, provide an unbiased muon sample that can be used to measure the muon reconstruction efficiency with respect to the ID tracking efficiency.

The method suffers from background muons that originate from decays in flight of light mesons as well as from semileptonic  $b$ - and  $c$ -hadron decays. When those muons are identified as tags, they may combine with ID tracks to form a dimuon system with invariant mass close to the  $J/\psi$  mass. With additional requirements on the energy deposit in the calorimeters associated to the ID probe tracks, a sample of probes with a low background contamination can be selected. These calorimeter-tagged (CT) probes allow a measurement of the Muon Spectrometer track reconstruction efficiency that is almost free of the biases induced by the background subtraction.

A study of the muon efficiency at larger  $p_T$ , exploiting the  $Z \rightarrow \mu^+ \mu^-$  decay, is reported in [3].

Two reconstruction chains, with similar features, are implemented in the ATLAS offline software and used for physics analyses. They are referred as chain 1 and chain 2. Two categories of muons are reconstructed in ATLAS using the Muon Spectrometer information. Combined (CB) muons require the reconstruction of tracks in the MS and in the ID with parameters compatible within the measurement errors. Including segment-tagged (ST) muons [4] in a sample provides additional efficiency, especially for low- $p_T$  muons, which do not cross enough MS precision chambers to allow an independent momentum measurement in the Muon Spectrometer. The muon reconstruction efficiency is measured for the implementation of both classes of muons in the two reconstruction chains. It should be noticed that the boundary between the CB and ST muon categories is actually different in the two chains. In chain 1 a CB muon requires a track in the MS, providing a standalone momentum measurement in addition to a direction determination, which matches an ID track; the parameters measured in the two subdetectors are then averaged by weighting each component with the appropriate covariance matrix. A CB muon in chain 2 is defined by a successful fit of hits in both the ID and MS to a single track. In most cases, the MS hits belong to an independent MS track. It is possible, however, that hits from an ID track and a matching MS segment are successfully fitted to a common track - such an object is classified as a CB muon in chain 2.

The typical strategy pursued in ATLAS physics analyses for improving the agreement between data and simulation is to apply corrective factors to the simulation for the detector, reconstruction and trigger efficiencies derived from control samples in the data. The muon reconstruction efficiency is tuned to data by applying  $p_T$ - and  $\eta$ -dependent scaling factors (s.f.) defined as the ratio of the efficiency measured in data and the efficiency measured in simulation in the appropriate  $\eta \times p_T$  interval. This study is applied to simulated  $J/\psi \rightarrow \mu^+ \mu^-$  decays, in addition to data, to serve the purpose of providing the measurement of the muon reconstruction efficiency scaling factor in the low- $p_T$  regime.

## 2 Monte Carlo samples

A sample of five million multijet events with direct production of a  $J/\psi$  meson in the hard scattering and subsequent decay of the  $J/\psi$  into muons was generated with PYTHIA 6.4 [5] using the color-octet

model[6]. The sample covers the muon phase space from very low to intermediate (10 GeV) transverse momenta, since no filtering on the muon momentum is applied. In order to enhance the statistics in the higher  $p_T$  region, the previous sample was supplemented by a sample, generated with PYTHIA 6.4 [5], of one million  $b\bar{b}$  events containing two muons of  $p_T > 2.5$  GeV. The two MC samples were passed through a simulation of the ATLAS detector [7] based on GEANT4 [8, 9], reconstructed with the same software as real data and weighted according to their cross sections.

### 3 Selection of Tag-and-Probe pairs

Events were selected online with single muon triggers.

Good detector conditions for tracking and muon reconstruction were explicitly required and events with collisions were selected by requiring at least one reconstructed primary vertex built from three or more tracks. During 2010 the rate of pile-up of multiple collisions in the same bunch crossing was very low and of no relevance for this measurement. In a given event, the primary interaction vertex is defined as the vertex whose constituent tracks have the highest sum of  $p_T$ -squared.

Tag muons satisfied the following requirements<sup>1</sup>:

- must be CB;
- must be associated to a good quality ID track (see the definition of 'good quality' below);
- $p_T > 4$  GeV,  $|\eta| < 2.5$ ;
- distance of closest approach to the primary vertex in the transverse plane  $|d_0| < 0.3$  mm, in the longitudinal coordinate  $|z_0| < 1.5$  mm and significance on the impact parameters  $|d_0|/\sigma(d_0) < 3$  and  $|z_0|/\sigma(z_0) < 3$ ;
- consistent with being the muon that fired the trigger. This was checked by requiring that the reconstructed muon was crossing the  $\eta$ - $\phi$  region in the MS corresponding to the *region of interest* (RoI) [1] where a single muon trigger signature was reconstructed. The typical size of a level 1 muon RoI is  $0.1 \times 0.1$  in  $\eta \times \phi$ ; this is fixed in the barrel region and variable in the endcaps.

Probe tracks were required to satisfy the following requirements:

- $p > 3$  GeV,  $|\eta| < 2.5$  and good track quality;
- $\chi^2/\text{ndof}$  ( $\chi^2$  normalized to the number of degrees of freedom) of the fit to a common vertex of the probe and the tag tracks smaller than 6;
- distance from the tag  $\Delta R = \sqrt{(\Delta\phi)^2 + (\Delta\eta)^2} < 3.5$ .

Tracks were tested against these kinematic requirements using parameters calculated using inner detector measurements alone.

The lower bound on the momentum of the selected probes was motivated by the consideration that muons typically lose 3 GeV of energy whilst crossing the calorimetry, and therefore a muon with  $p < 3$  GeV has little chance of reaching the MS.

<sup>1</sup>Track parameters are expressed in the ATLAS right-handed coordinate system with origin at the nominal interaction point (IP) in the center of the detector and the z-axis along the beam pipe. The x-axis points from the IP to the center of the LHC ring, and the y-axis points upward. Cylindrical coordinates ( $R, \phi$ ) are used in the transverse plane,  $\phi$  being the azimuthal angle around the beam pipe. The pseudorapidity is defined in terms of the polar angle  $\theta$  as  $\eta = -\ln \tan(\theta/2)$  and  $p_T$  is the momentum component transverse to the beam line.

In each event, all tag-and-probe combinations were considered. In the high multiplicity of LHC events, an ID track can pass all the selection criteria in association with more than one tag. The probability of such occurrence is found to be below 0.6% over the whole data taking period. In such cases, in order to avoid testing the muon reconstruction result more than once for the same probe, a unique probe-to-tag association was chosen based on the minimum  $\chi^2$  of the common vertex fit.

The quality requirements for ID tracks, applied both to the tag and the probe, are listed below:

- at least one hit in the innermost layer of the Pixel detector was required, if the track was expected to intersect this detector layer;
- the sum of the number of pixel hits and of dead pixel sensors crossed by the track was required to be greater than one;
- the sum of the number of SCT (SemiConductor Tracker) hits and of the number of dead SCT sensors crossed by the track was required to be greater than six;
- the number of missing pixel layers (i.e. crossed by the track but without hits associated to the track) plus the number of missing SCT layers was not allowed to exceed one;
- for  $|\eta| < 1.9$ , the total number of Transition Radiation Tracker (TRT) hits was required to be  $n_{\text{TRT}}^{\text{tot}} > 5$ ;
- for the case  $n_{\text{TRT}}^{\text{tot}} > 5$ , the fraction of outlier TRT hits was required to be  $n_{\text{TRT}}^{\text{out}}/n_{\text{TRT}}^{\text{tot}} < 90\%$ . TRT outliers are measurements associated to the ID track that either appear in a drift tube not crossed by the track or belong to a set of TRT measurements that failed to form a smooth trajectory together with the Pixel and SCT measurements.

Finally, in order to minimize any residual trigger bias induced by event topologies with nearby tag-and-probe tracks overlapping the same RoI, the following cut was applied:

$$|\eta_{\text{tag}} - \eta_{\text{probe}}| > 0.5 \text{ or } |\phi_{\text{tag}} - \phi_{\text{probe}}| > 0.22. \quad (1)$$

The above selection resulted in  $6 \times 10^6$  tag-and-probe pairs in the invariant mass range  $2 < m < 4$  GeV.

### 4 Efficiency measurement

The selected tag-and-probe pairs were divided into two categories, those in which the probe was reconstructed as a muon by the algorithm (matched) and those in which the probe was not reconstructed as a muon (unmatched). Figure 1 shows a typical invariant mass distribution for the two categories of tag-and-probe pairs, using a selection of probes in a narrow  $p_T$  interval (3-4 GeV). The distribution is displayed separately for probes classified as matched and unmatched for CB and CB+ST chain 2 muons. A matched probe for the CB algorithm will contribute also to the sample of matched probes for the CB+ST algorithm; an unmatched probe for the CB algorithm may or may not be reconstructed as a ST muon and, therefore, it may or may not contribute to the sample of unmatched probes for the CB+ST category. The distribution of matched probes shows a clean peak at the  $J/\psi$  mass with low background while the distribution of unmatched probes has a peak on top of a large background. The sample of probes reconstructed as CB or ST muons is larger than the sample of probes reconstructed as CB muons because the segment tagging algorithms are more efficient than the combined algorithms at the low values of transverse momentum of the probes contributing to the invariant mass distribution shown in the plot.

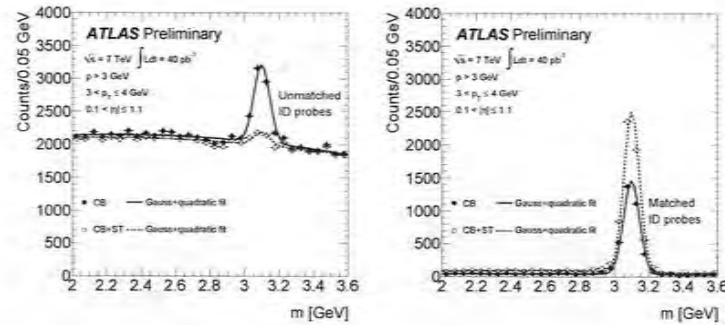


Figure 1: Invariant mass of the unmatched (left plot) and matched (right plot) tag-and-probe pairs for CB (solid circles) and CB+ST (open circles) muons of chain 2 for  $0.1 < |\eta| < 1.1$  and  $3 < p_T < 4 \text{ GeV}$ . The curves show the fits described in the text.

The reconstruction efficiency is given by the ratio of the number of events in the peak of the matched distribution to the total number of events in the two mass peaks. It has been derived from a binned maximum log-likelihood fit, performed simultaneously on the two distributions, with the following parameterization:

$$\begin{aligned} \text{Matched } f_M(m) &= N_{\text{tot}} \epsilon G(m; \mu_M, \sigma_M) + P_M(m), \\ \text{Unmatched } f_U(m) &= N_{\text{tot}} (1 - \epsilon) G(m; \mu_U, \sigma_U) + P_U(m), \end{aligned}$$

where  $G(m; \mu, \sigma)$  is a Gaussian distribution with mean  $\mu$  and width  $\sigma$  normalized to unit integral, used to describe the signal, and  $P$  is a polynomial function used to describe the background. The main parameters extracted from the fit are the number of signal tag-and-probe pairs  $N_{\text{tot}}$  and the reconstruction efficiency  $\epsilon$ .

This procedure allows for the proper evaluation of the efficiency and its uncertainty taking the background subtraction procedure into account, thanks to the simultaneous fit of signal and background components in the two statistically independent samples.

The mean and width of the Gaussian distributions (free parameters in the fit) were constrained to have the same values for both unmatched and matched distributions and a second-order polynomial was used to model the background. The assumption of comparable width on the  $J/\psi$  peak for the two cases of probes reconstructed and not reconstructed as muons was motivated by the consideration that the efficiency measurement was performed in bins of  $\eta \times p_T$  and therefore the ID resolution was rather uniform in each measurement and not significantly correlated with the ability of reconstructing a muon. When the two peaks were fitted independently, values for the widths compatible within the statistical errors were obtained. The quadratic modeling of the background was found to provide a good description of the background shape in the invariant mass range considered here.

Muon reconstruction efficiency and scale factors were measured as a function of  $p_T$  in five intervals of absolute pseudorapidity of the probes, based on a coarse definition of homogeneous MS regions:

- $|\eta| < 0.1$ , the  $\eta = 0$  crack region;
- $0.1 < |\eta| < 1.1$ , the barrel region;
- $1.1 < |\eta| < 1.3$ , the transition region between the barrel and the end-cap;
- $1.3 < |\eta| < 2.0$ , the end-cap region;
- $2.0 < |\eta| < 2.5$ , the forward region.

A schematic view of a quarter of the Muon Spectrometer layout in the  $r - z$  plane can be seen in Figure 2.

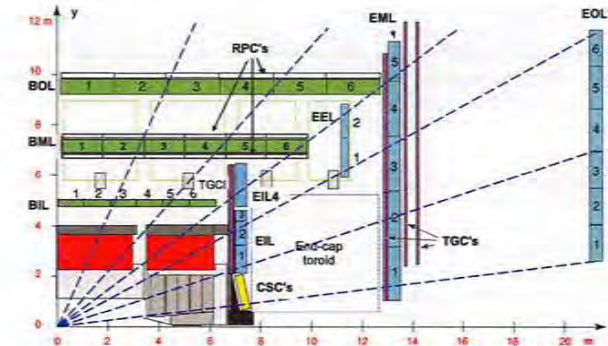


Figure 2: A  $r - z$  view of the layout of the Muon Spectrometer. Stations of Monitored Drift Tubes (in green in the barrel and light-blue in the endcaps) are arranged in three layers to provide a measurement of the muon momentum in the magnetic field. At  $|\eta| = 0$  a small acceptance hole, related to services, can be observed. The installation of the chambers denoted as EEL in the plot was not completed before the 2010 data taking, leading to a reduced acceptance in the region  $1.1 < |\eta| < 1.3$ . In the forward region,  $2.0 < |\eta| < 2.5$ , Cathod Strip Chambers (in yellow), instead of Monitored Drift Tubes provide the precision tracking in the innermost layer of the MS.

## 5 Systematic checks and uncertainties

Several checks were performed to study the dependence of the results on analysis details and assumptions:

1. *Signal shapes*: the means and the widths of the two Gaussian functions in the fit were allowed to vary independently.
2. *Background shape*: a linear background function was used in the fit, instead of the quadratic one; in this case the fit was performed in the reduced mass range of  $2.7 - 3.5 \text{ GeV}$ .
3. *Alternative fit*: an independent fit to the matched and the total (matched + unmatched) distributions, rather than to matched and unmatched, was used and the efficiency estimated as the ratio of the signal normalization in the two distributions; while this option does not provide an easy

Staco  $\epsilon_{ID}$

2-10 GeV

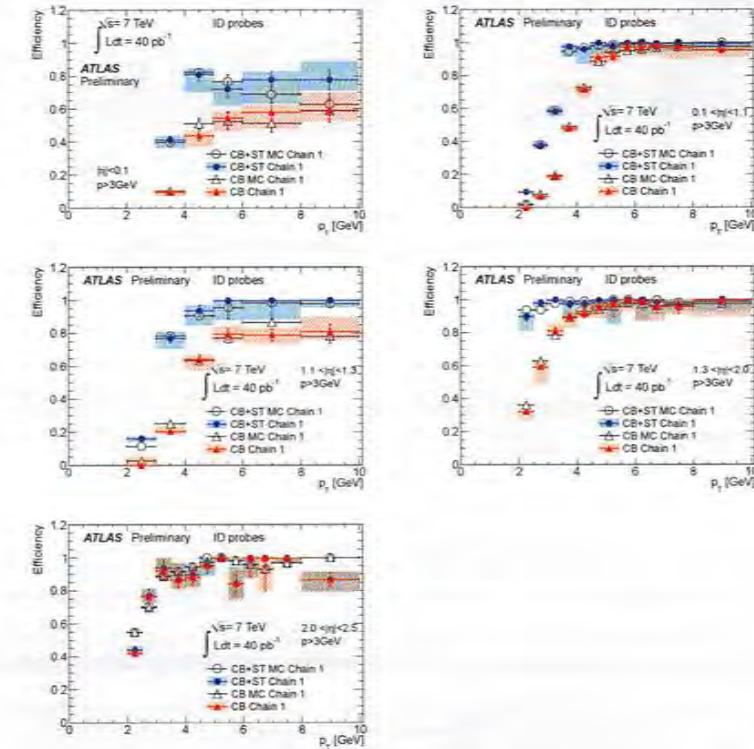


Figure 3: Efficiency for CB and CB+ST muons of chain 1 as a function of  $p_T$  for five bins in  $|\eta|$  for data and MC. The error bars represent the statistical uncertainties while the band around the data points represents the statistical and systematic uncertainties added in quadrature.

propagation of the uncertainty from the background subtraction and does not directly account for the correlation of the two samples, it profits from the high stability of the two simpler fits, whereas the default method may need some care in the choice of the initial conditions, in particular in case of very high efficiency or low overall statistics.

The three variations discussed above gave results which deviate from the baseline by comparable amounts. In general, the linear background option tends to overestimate the background under the signal Gaussian of the unmatched probes, leading to typically higher efficiency values. On the other hand using independent widths for the signal components over a quadratically modeled background in case of high efficiency tends to overestimate the signal of unmatched probes, resulting in lower values of the efficiency. The maximal positive and negative variations among checks 1 to 3 were assigned as systematic uncertainties and added in quadrature to the statistical uncertainty to obtain the total upper and lower uncertainties respectively. The systematic uncertainties were found to be typically  $\leq 5\%$ , with bin by bin variations depending on background conditions, statistics and, sometimes, data fluctuations enhancing the discrepancies between the results from the various fit methods.

## 6 Reconstruction efficiency with respect to ID tracks

Figures 3 and 4 show the efficiency for chain 1 and chain 2 with respect to ID tracks with  $p > 3$  GeV as a function of the probe  $p_T$  for the five bins in  $|\eta|$ . The efficiency is measured in  $p_T$  bins of typical width equal to 0.5 GeV starting from  $p_T$  as low as 2 GeV. In the central  $\eta$  region, the general requirement on the minimum momentum of the probe ( $p > 3$  GeV) does not allow an efficiency measurement for  $p_T < 3$  GeV. Overall, the Monte Carlo simulation is found to provide a good description of the efficiency measured in data.

The two reconstruction chains exhibit a comparable performance. The main features of the muon reconstruction efficiency, already observed in [2], are dictated by the MS geometry and acceptance. In both chains, the ST algorithm is shown to recover efficiency with respect to the CB algorithm at low  $p_T$  and in regions with limited instrumentation ( $|\eta| < 0.1$  and  $1.1 < |\eta| < 1.3$ ). In the central crack region, muons with  $p_T$  in the range 4 – 5 GeV have a slightly higher probability to be reconstructed than higher  $p_T$  muons thanks to the magnetic field which pushed them into the instrumented region. The main differences between the efficiencies of the two reconstruction chains are due to specific choices in their respective algorithms. Chain 2 exhibits a slightly higher efficiency than chain 1 in a few cases. In the barrel, in the  $p_T$  range 2 – 4 GeV, the efficiency of chain 2 is higher both for the CB+ST and CB muon categories. In the endcaps, the CB algorithm of chain 2 appears more efficient than the corresponding algorithm of chain 1 at low  $p_T$ . Finally, the CB efficiency plateau in the barrel-endcap transition is higher for chain 2 than chain 1. The main reason for the somewhat higher efficiency of the CB algorithm of chain 2 lies in the different definition of CB muons adopted in the two chains (discussed in Section 1). Finally, the efficiency of chain 1 in the forward region is similar for the CB and the CB+ST categories because the ST algorithm was not enabled for ID tracks with  $|\eta| > 2$ .

## 7 Calorimeter-tagged muons

The uncertainty on the reconstruction efficiency measurement described above is dominated by the statistical and systematic contribution from the large background in the unmatched sample. The background can be significantly suppressed if the probes are selected among calorimeter-tagged muons. The calo-tagging algorithm flags ID tracks as calorimeter-tagged muons by using the energy deposit in the calorimeter as a discriminant variable. During 2010 it was optimized to identify muons of  $p_T$  as low

MuID EID  
2 - 10 GeV

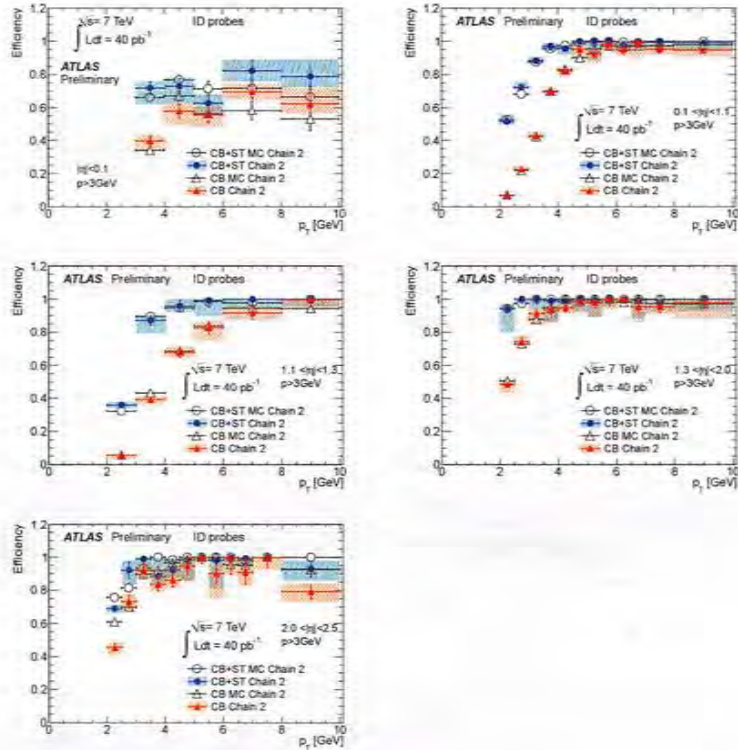


Figure 4: Efficiency for CB and CB+ST muons of chain 2 as a function of  $p_T$  for five bins in  $|\eta|$  for data and MC. The error bars represent the statistical uncertainties while the band around the data points represents the statistical and systematic uncertainties added in quadrature.

track isolation	Track $ \eta $ range	Cuts
	$ \eta  \leq 2.5$	$\sum_{0.45} p_T^{iso}/p_T \leq 8$
energy isolation	$ \eta  \leq 1.5$	$E_T^{iso,0.4}/p_T \leq 3 \text{ AND } E_T^{iso,0.4} \leq 17 \text{ GeV}$
	$1.5 <  \eta  < 1.8$	$E_T^{iso,0.4}/p_T \leq 1.4 \text{ AND } E_T^{iso,0.4} \leq 10 \text{ GeV}$
	$1.8 \leq  \eta  \leq 2.5$	$E_T^{iso,0.4}/p_T \leq 1.6 \text{ AND } E_T^{iso,0.4} \leq 13 \text{ GeV}$

Table 1: Isolation requirements applied to calo-tagged muons as a pre-selection (track isolation) and post-selection (energy isolation).

as 2 GeV with good efficiency and purity; this allowed the measurement of the muon reconstruction efficiency with respect to calo tagged muons in the same kinematic range explored with ID probes.

The calo-tagged muon selection is based on a pre-selection of ID tracks satisfying a loose isolation criterion in the ID defined in terms of the scalar sum of the  $p_T$  of tracks collected in a cone of half-aperture  $\Delta R = 0.45$  around the candidate CT muon. Two algorithms for muon identification in the calorimeter are implemented. The first one, cut-based, uses the energy measured in the calorimeter cells crossed by the track in each longitudinal compartment of the calorimeter. This energy is required to fall within well defined intervals, which are tuned with the purpose of discriminating the small signal from a single penetrating ionizing particle, like a muon, from electron and hadron signatures. Loose and tight energy intervals are defined for a more efficient or more pure selection. The second algorithm is based upon a likelihood-ratio (*LHR*) discriminant which tests the consistency of the observed total energy deposit around the track direction in the calorimeter with the expected energy loss from a minimum ionizing particle. Tracks with  $p_T \geq 4 \text{ GeV}$  are classified as calo-tagged muons if the cut-based selection with loose cuts or the *LHR*-based selection is passed. Tracks with  $p_T < 4 \text{ GeV}$  are required to pass the tight cut-based selection in order to enter the calo-tagged muon candidate sample. Finally, in order to reduce the contamination from non-isolated hadrons, the sample of muon candidates identified in the calorimeter is subject to a final cleanup based on a calorimetric isolation requirement: the total energy deposited in a cone of half-aperture 0.4 around the direction of the track extrapolated to the calorimeter entrance, corrected for the expected muon energy loss contribution, is required to be smaller than  $\eta$ -dependent absolute and relative thresholds listed in table 1.

## 8 Reconstruction efficiency with respect to calorimeter-tagged probes

The muon reconstruction efficiency measurement reported in section 6 was repeated with the only difference in the analysis procedure being that the probes were additionally required to have been identified as a muon by the calo-tagging algorithm.

The mass distributions for tag-and-probe pairs, where the probe is calo-tagged, are shown in Figure 5 for probes matched and unmatched to offline reconstructed muons.

Figures 6 and 7 show the turn-on of the efficiency for CB and CB+ST muon reconstruction as a function of  $p_T$  in the five  $|\eta|$  regions, obtained using CT probes. In all of these cases, the Monte Carlo simulation reproduces the data well.

The efficiency measurement obtained using CT probes is found to be in agreement, within systematic uncertainties, with the measurement obtained using the larger statistics of ID probes, which suffers from a much larger background. The consistency of the results provides further confidence on the estimate of the systematic uncertainties on the measurement and on the general robustness of the procedure.

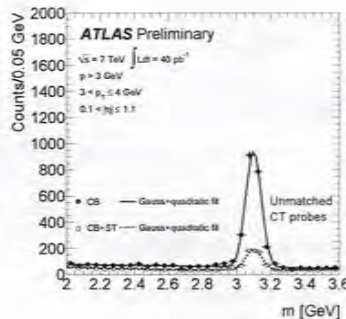


Figure 5: Invariant mass of the unmatched (left plot) and matched (right plot) tag-and-probe pairs for CB (solid circles) and CB+ST (open circles) muons of chain 2 for  $0.1 < |\eta| < 1.1$  and  $3 < p_T < 4 \text{ GeV}$ . The probes are selected among calorimeter-tagged muons. The curves show the fits described in the text.

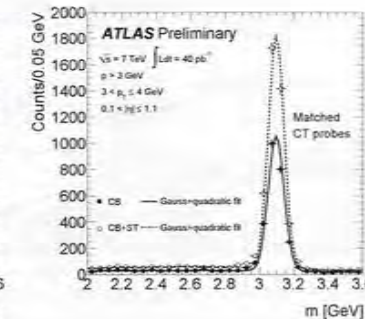
## 9 Charge dependence

Due to the toroidal magnetic field of the ATLAS MS, muons with positive (negative) charge are bent towards regions at larger (smaller) values of  $\eta$ . At a given  $\eta$ , a muon of low  $p_T$  crosses a different number of measurement layers depending on its charge. This effect introduces a charge dependence of the muon reconstruction efficiencies, as first reported in [2]. As long as the ATLAS detector is symmetric with respect to  $\eta = 0$ , the efficiency depends only on  $q \times \eta$ , where  $q$  is the muon charge.

Figures 8 and 9 show the reconstruction efficiency as a function of  $q \times \eta$  for two  $p_T$  regions:  $2 < p_T < 6 \text{ GeV}$  and  $p_T > 6 \text{ GeV}$  for the two chains. In the first region a strong asymmetry between positive and negative  $q \times \eta$  is observed for CB muons. For CB+ST muons the asymmetry is lower since in this case it is sufficient to find a segment in the inner MS stations, which are located at a position where the muon trajectory has not yet been significantly bent by the toroidal magnetic field. Most of the asymmetry for CB+ST muons is in the largest  $|\eta|$  bin. The  $q \times \eta$  dependence is well reproduced by the simulation. No significant asymmetry is observed in the high- $p_T$  region for CB+ST muons.

## 10 Data-MC scale factors

MC scaling factors are used in physics analyses to correct for the mis-modeling of the reconstruction performance in simulation. They are defined as  $s.f. = \epsilon_{\text{data}}/\epsilon_{\text{MC}}$ , where  $\epsilon_{\text{data}}$  and  $\epsilon_{\text{MC}}$  are the efficiencies measured in data and MC. The scale factors in the plateau of the efficiency ( $p_T > 6 \text{ GeV}$ ) obtained by applying the same tag-and-probe selection and efficiency determination in data and MC are shown in Figure 10 for chain 1 (left) and for chain 2 (right), both for the case of ID and CT probes. The error bars account for the statistical and systematic uncertainties on the efficiency measured in data and for the statistical error on the efficiency estimated in the simulation. In the MC, the systematic error on the efficiency arising from the background shape modeling has been neglected, because the limited background has a negligible systematic impact on the result. Results from ID probes and CT probes are in good agreement.



Stars  
Ecalotes  
2-12GeV

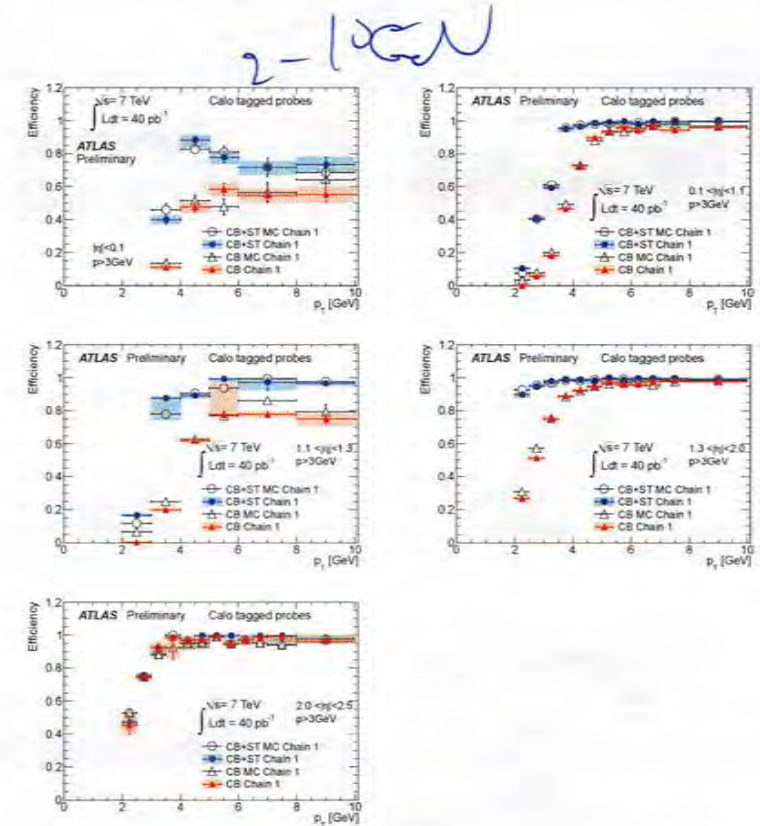


Figure 6: Efficiency for CB and CB+ST muons of chain 1 with respect to calorimeter-tagged muons as a function of  $p_T$  for five bins in  $|\eta|$  for data and MC. The error bars represent the statistical uncertainties while the band around the data points represents the statistical and systematic uncertainties added in quadrature.

$\mu_{\text{ad}}$

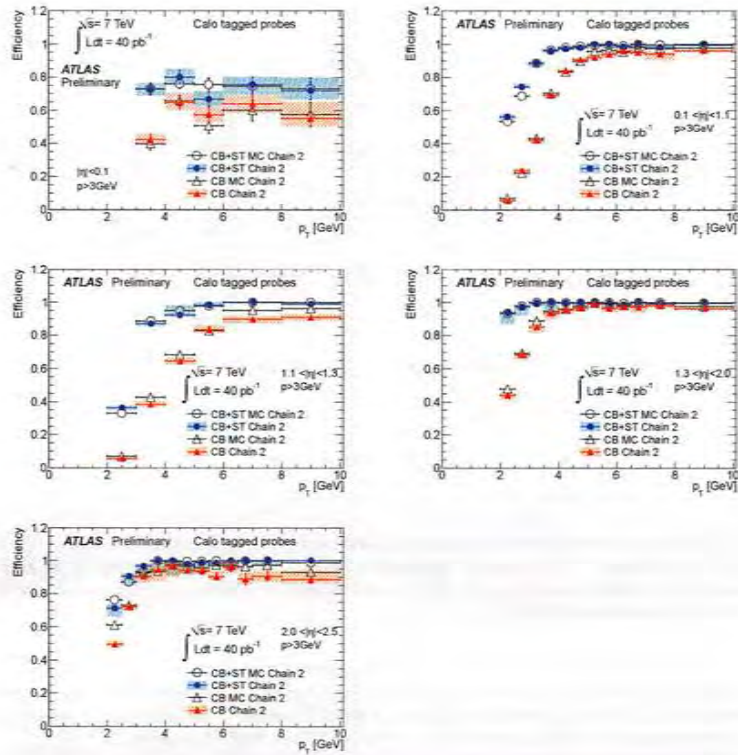


Figure 7: Efficiency for CB and CB+ST muons of chain 2 with respect to calorimeter-tagged muons as a function of  $p_T$  for five bins in  $|\eta|$  for data and MC. The error bars represent the statistical uncertainties while the band around the data points represents the statistical and systematic uncertainties added in quadrature.

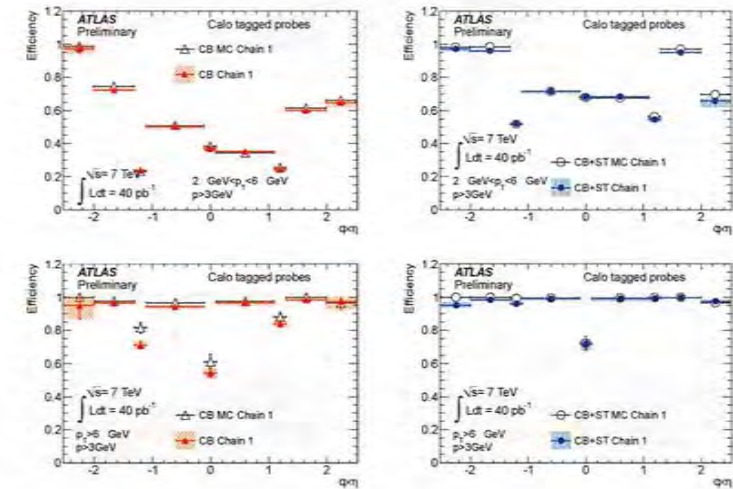


Figure 8: Efficiency for CB (left) and CB+ST (right) muons of chain 1 as a function of  $q \times \eta$  for data and MC. The upper plots are for the  $p_T$  range  $2 < p_T < 6$  GeV. The lower plots are for  $p_T > 6$  GeV. Statistical uncertainties are added in quadrature to the systematic uncertainties.

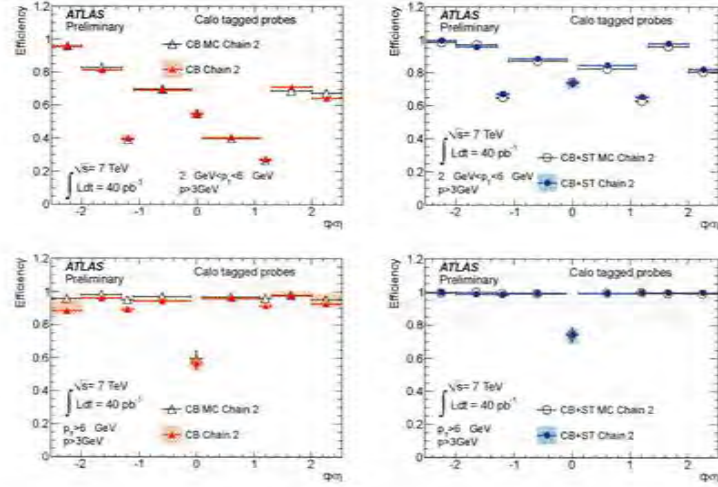


Figure 9: Efficiency for CB (left) and CB+ST (right) muons of chain 2 as a function of  $q \times \eta$  for data and MC. The upper plots are for the  $p_T$  range  $2 < p_T < 6$  GeV. The lower plots are for  $p_T > 6$  GeV. Statistical uncertainties are added in quadrature to the systematic uncertainties.

chain 1 CB+ST			chain 1 CB			
	s.f.	(stat.)	(syst.)	s.f.	(stat.)	(syst.)
$ \eta  \leq 0.1$	1.071	$\pm 0.065$	$^{+0.120}_{-0.098}$	0.860	$\pm 0.074$	$^{+0.103}_{-0.085}$
$0.1 <  \eta  \leq 1.1$	1.008	$\pm 0.000$	$^{+0.002}_{-0.006}$	0.993	$\pm 0.008$	$\pm 0.008$
$1.1 <  \eta  \leq 1.3$	0.992	$\pm 0.012$	$^{+0.017}_{-0.019}$	0.949	$\pm 0.034$	$^{+0.059}_{-0.068}$
$1.3 <  \eta  \leq 2.0$	0.999	$\pm 0.007$	$\pm 0.005$	0.996	$\pm 0.008$	$\pm 0.009$
$2.0 <  \eta  \leq 2.5$	0.987	$\pm 0.015$	$^{+0.037}_{-0.012}$	0.987	$\pm 0.015$	$^{+0.034}_{-0.011}$
chain 2 CB+ST			chain 2 CB			
	s.f.	(stat.)	(syst.)	s.f.	(stat.)	(syst.)
$ \eta  \leq 0.1$	1.024	$\pm 0.062$	$^{+0.101}_{-0.089}$	0.963	$\pm 0.081$	$^{+0.143}_{-0.108}$
$0.1 <  \eta  \leq 1.1$	1.005	$\pm 0.000$	$^{+0.005}_{-0.007}$	0.985	$\pm 0.008$	$^{+0.007}_{-0.010}$
$1.1 <  \eta  \leq 1.3$	0.990	$\pm 0.007$	$^{+0.007}_{-0.003}$	0.946	$\pm 0.017$	$^{+0.024}_{-0.023}$
$1.3 <  \eta  \leq 2.0$	1.002	$\pm 0.002$	$^{+0.003}_{-0.007}$	0.987	$\pm 0.009$	$^{+0.010}_{-0.009}$
$2.0 <  \eta  \leq 2.5$	1.013	$\pm 0.000$	$^{+0.008}_{-0.006}$	0.953	$\pm 0.023$	$^{+0.059}_{-0.019}$

Table 2: CB and CB+ST reconstruction efficiency scale factors, for both reconstruction chains. Only CT probes with  $p_T > 8$  GeV are used. Statistical and systematic uncertainties are shown separately. Asymmetric statistical errors are quoted, since upward fluctuations of the measurement are constrained by the physical boundary of full efficiency.

Additionally, Figure 11 shows the scale factor as a function of  $p_T$  in the end-cap region, chosen as an example, for both chain 1 (left) and chain 2 (right); scale-factors are consistent with one in the whole  $p_T$  range, demonstrating a good MC description of the turn-on region. The same level of consistency between measurements on data and MC predictions is observed in the other  $\eta$  regions.

Measurements of muon reconstruction efficiency in a different kinematic domain are described in [3]. These are based on the tag-and-probe method applied to  $Z \rightarrow \mu\mu$  decays; the minimum  $p_T$  of the probes is 20 GeV and the probes (ID tracks) are required to be isolated in the inner tracker; in particular, the scalar sum of the  $p_T$  of tracks in a cone of size  $\Delta R=0.4$  around the probe is required to be lower than 20% of the probe  $p_T$ . As the results obtained here are for low- $p_T$  muons embedded in jets where  $J/\psi$  mesons are produced, the measurements obtained with calo-tagged muon probes (which satisfy some minimal isolation criteria, as described in table 1) were used for comparison with the  $Z$  results. The asymptotic values of the scale factors (obtained for CT muons with  $p_T > 8$  GeV) are summarized in table 2 and shown in Figure 12 for the five  $\eta$  regions. In this kinematic regime the background contribution is expected to be small and correspondingly the systematic uncertainties on background modeling is reduced. The scale factors in table 2 are in agreement with the results presented in [3] and demonstrate

a good modeling of the efficiency in simulation. For CB+ST muons the scale factors are always very close to one. The muon CB reconstruction algorithms exhibit scale factors compatible with one, within the uncertainty of the measurement, but with slightly larger deviations than observed in the CB+ST case; the most significant deviation is found in the barrel-endcap transition region for chain 2, where the ratio of efficiency measured in data and in MC is two standard deviations below one.

## 11 Calo-tagging efficiency

The  $J/\psi$  tag-and-probe selection based on ID probes can also be used to measure the calo-tagging efficiency. The analysis procedure closely followed the muon reconstruction efficiency measurement. In this case, ID probes were used and the two samples of probes satisfying or failing the calo-tagging criteria were built. The same fit procedures described in section 4 was applied.

The resulting efficiencies for the calo-tagging algorithm are shown in Figure 13. The discontinuous trend of the efficiency observed around 4 GeV, well reproduced in the simulation, is clearly related to the transition between the two different identification regimes implemented by the algorithm in order to achieve a good fake rejection up to very low transverse momenta. The calo-tagging efficiency is generally increasing with  $p_T$  in all regions of the detector. The highest efficiency is achieved in the central pseudorapidity region where the hadronic activity registered by the ATLAS calorimeter is low compared to other detector regions. In the end-cap and forward regions the probes are surrounded by more dense multijet activity producing an increasingly lower calo-tagging efficiency as  $|\eta|$  increases. In these regions, the MC predicts typically a calo-tagging efficiency for  $p_T > 4$  GeV higher than observed in data, suggesting a mis-modeling of the jet activity and pileup.

## 12 Conclusions

Muons from  $J/\psi$  decays have been used to measure the low- $p_T$  muon reconstruction efficiency in ATLAS. The data sample corresponds to an integrated luminosity of  $40 \text{ pb}^{-1}$  collected in 2010.

The reconstruction efficiency is well described by the Monte Carlo simulation for all algorithms based on the Muon Spectrometer and all algorithm families. For  $p_T > 6$  GeV the reconstruction efficiency is above 98% and the scale factor, defined as the ratio of data and MC efficiencies, are compatible with one within the errors. The results of this analysis are in good agreement with the scale factor measurements obtained with the tag-and-probe method at the  $Z$  resonance [3].

Additionally, a data-driven measurement of the calo-tagging efficiency is presented based on a tag-and-probe method at the  $J/\psi$  resonance. Overall, a good agreement between data and simulation is observed with some discrepancies in the end-cap and forward regions where the MC prediction is most sensitive to the modeling of the low- $p_T$  physics.

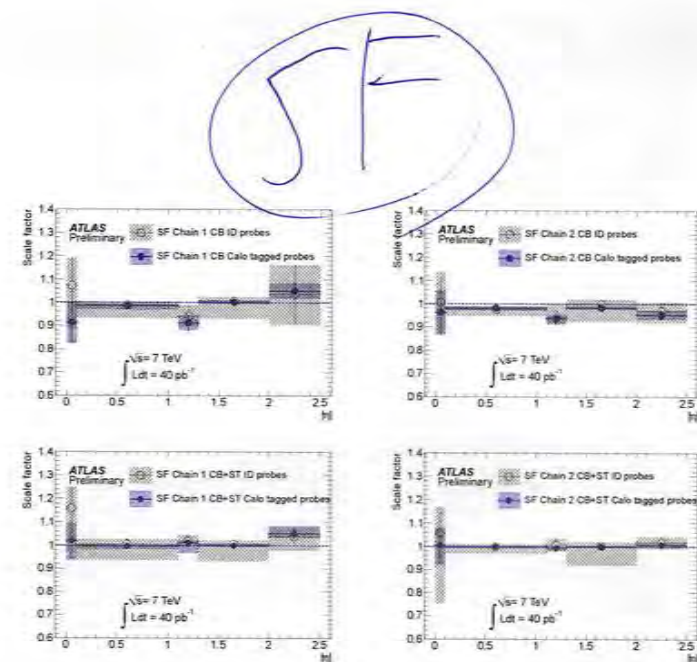


Figure 10: Efficiency scale factors, for both reconstruction chains, in the region of the efficiency plateau ( $p_T > 6$  GeV) for CB and CB+ST muons measured for ID and CT probes. The error bars represent the statistical errors and the shaded areas correspond to the total uncertainties, computed as the sum in quadrature of the statistical and systematic errors.

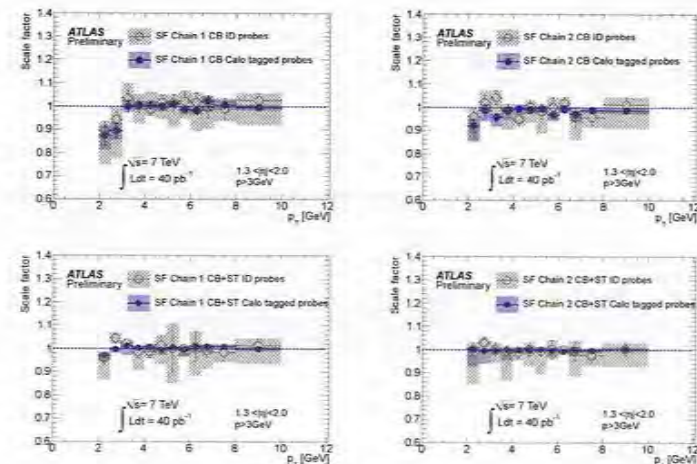


Figure 11: Efficiency scale factors, for both reconstruction chains, in the end-cap region for CB and CB+ST muons measured for ID and CT probes. The error bars represent the statistical errors and the shaded areas correspond to the total uncertainties, computed as the sum in quadrature of the statistical and systematic errors.

Physics off

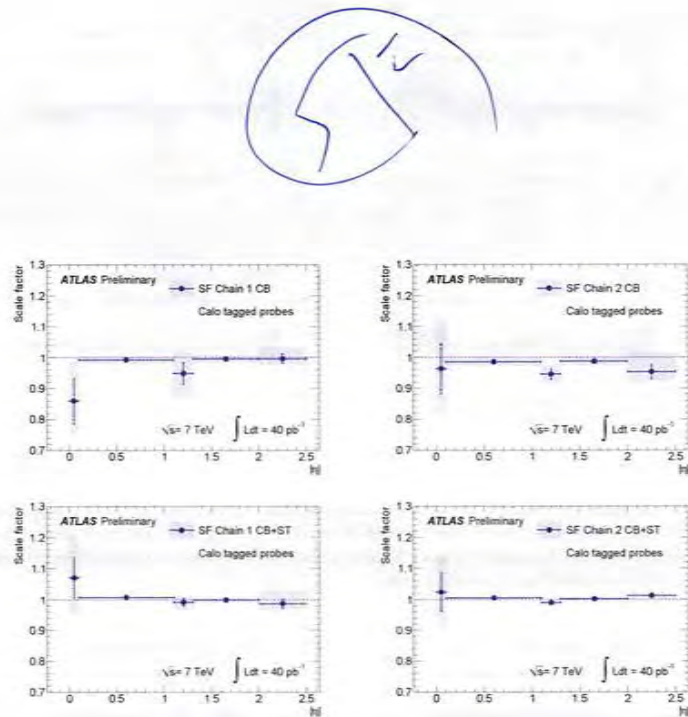


Figure 12: Efficiency scale factors, for both reconstruction chains, for  $p_T > 8$  GeV for CB and CB+ST muons measured only using CT probes. The error bars represent the statistical errors and the shaded areas correspond to the total uncertainties, computed as the sum in quadrature of the statistical and systematic errors.

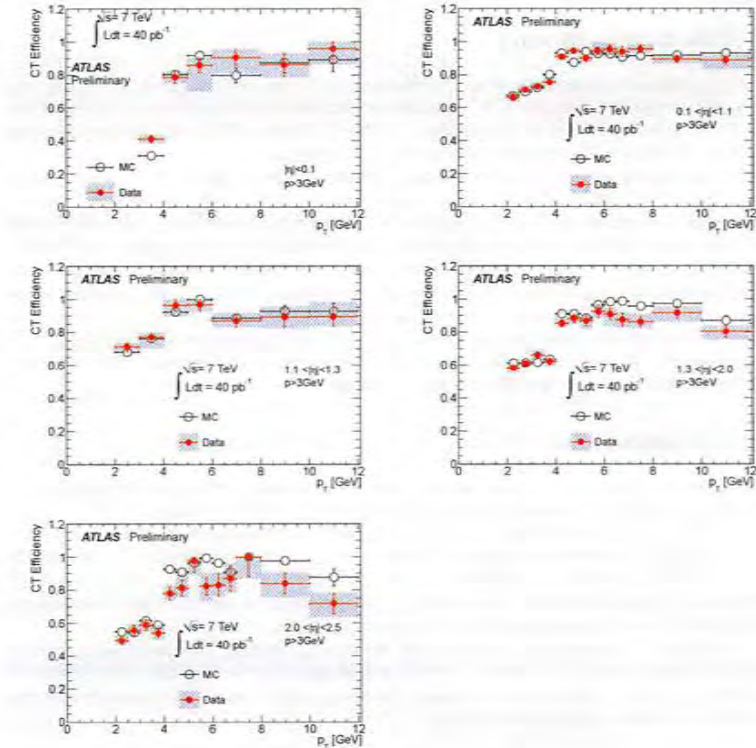


Figure 13: Calo-tagging efficiency as a function of  $p_T$  for five bins in  $|\eta|$  for data and MC. The error bars represent the statistical uncertainties while the band around the data points represents the statistical and systematic uncertainties added in quadrature.

## References

- [1] ATLAS Collaboration, *The ATLAS Experiment at the CERN Large Hadron Collider*, JINST **3** (2008) S08003.
- [2] ATLAS Collaboration, *A measurement of the ATLAS muon reconstruction and trigger efficiency using  $J/\psi$  decays*, ATLAS-CONF-2011-021 (2011).
- [3] ATLAS Collaboration, *Muon reconstruction efficiency in reprocessed 2010 LHC p-p collision data recorded with the ATLAS detector*, ATLAS-CONF-2011-063 (2011).
- [4] ATLAS Collaboration, *Muon Reconstruction Performance*, ATLAS-CONF-2010-064 (2010).
- [5] T. Sjostrand, S. Mrenna, and P. Z. Skands, *PYTHIA 6.4 Physics and Manual*, JHEP **05** (2006) 026.
- [6] P. Nason, et al., *Bottom production, Standard Model Physics (and more) at the LHC*, 231, Geneva, 1999, arXiv:hep-ph/0003142.
- [7] ATLAS Collaboration, *The ATLAS Simulation Infrastructure*, Eur. Phys. J. **C70** (2010) 823–874, arXiv:1005.4568.
- [8] S. Agostinelli et al., *Geant4: a simulation toolkit*, Nuclear Instrument and Methods A **506** (2006) no. 3, 250 –303.
- [9] J. Allison et al., *Geant4 developments and applications*, Nuclear Science, IEEE Transactions on **53** (2006) no. 1, 270 –278.

C

C

# Plots of Muon Performance in 2012 Data

O. Kortner, M. Vanadia for the MCP working group

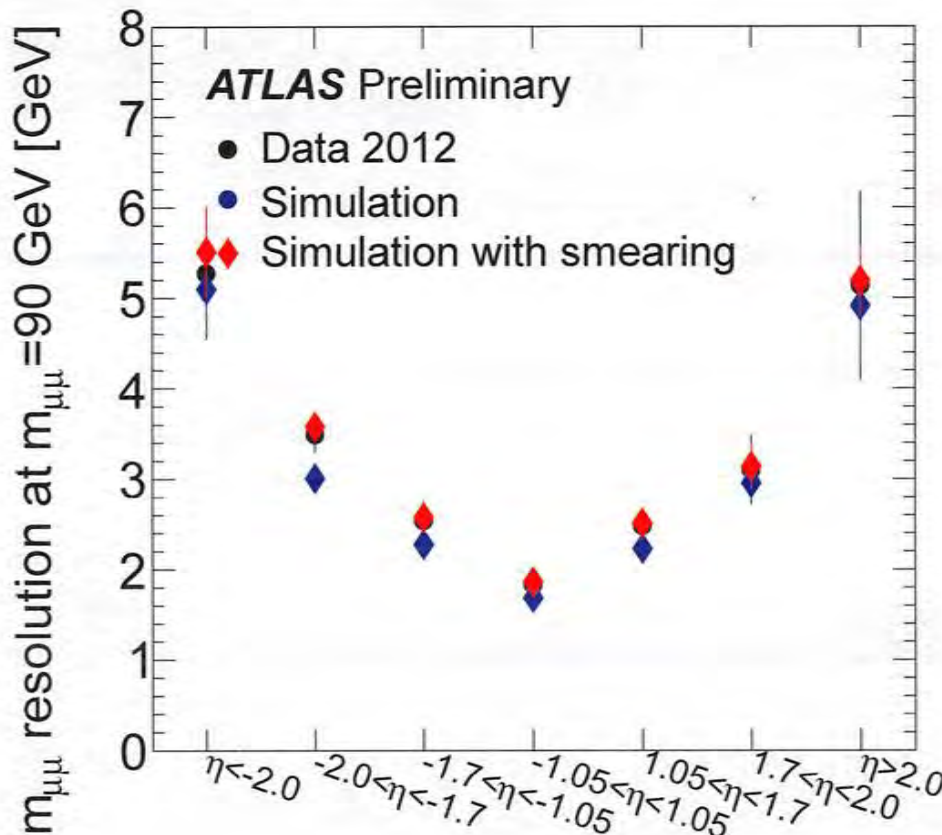
Max-Planck-Institut für Physik

June 4, 2012

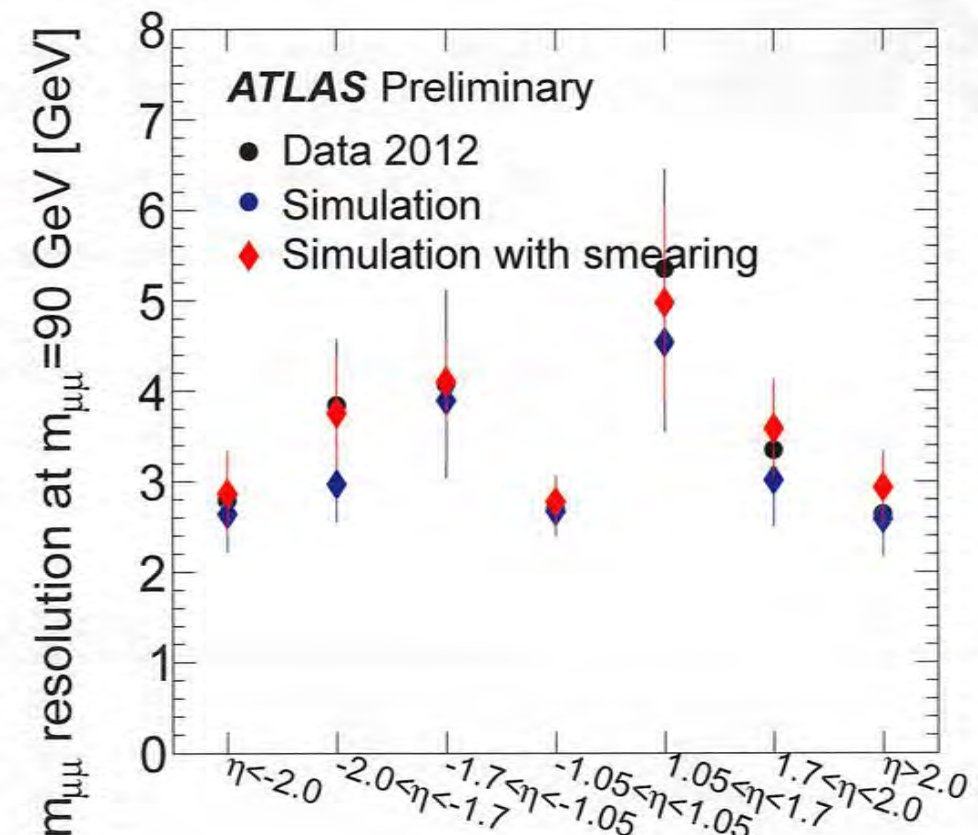
## Subdetector resolution

Plots produced on 2012 period A,  $824 \text{ pb}^{-1}$

Inner detector resolution



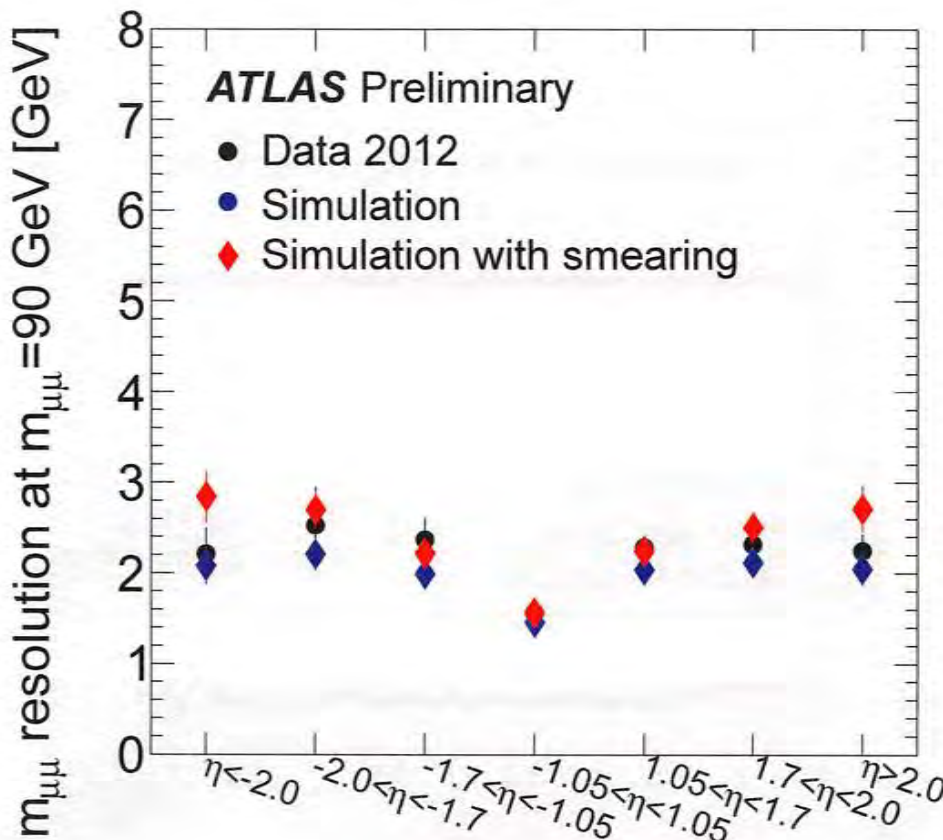
Muon spectrometer resolution



- The resolution is the width of a Gaussian which is convoluted with the di-muon mass resolution at generator level.
- The fit is performed in the mass window  $m_{\mu\mu} \in [75 \text{ GeV}, 105 \text{ GeV}]$ .
- Error bars are the sum of the statistical error and the absolute value of the change of the resolution when the fit range is reduced to  $m_{\mu\mu} \in [82 \text{ GeV}, 100 \text{ GeV}]$ .

## Combined resolution

Plots produced on 2012 period A,  $824 \text{ pb}^{-1}$   
Combined muon resolution



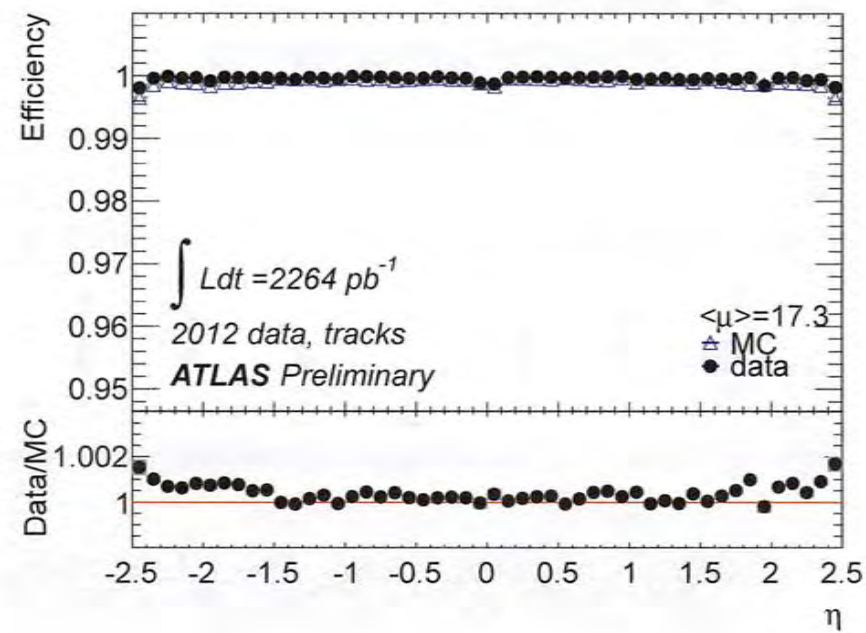
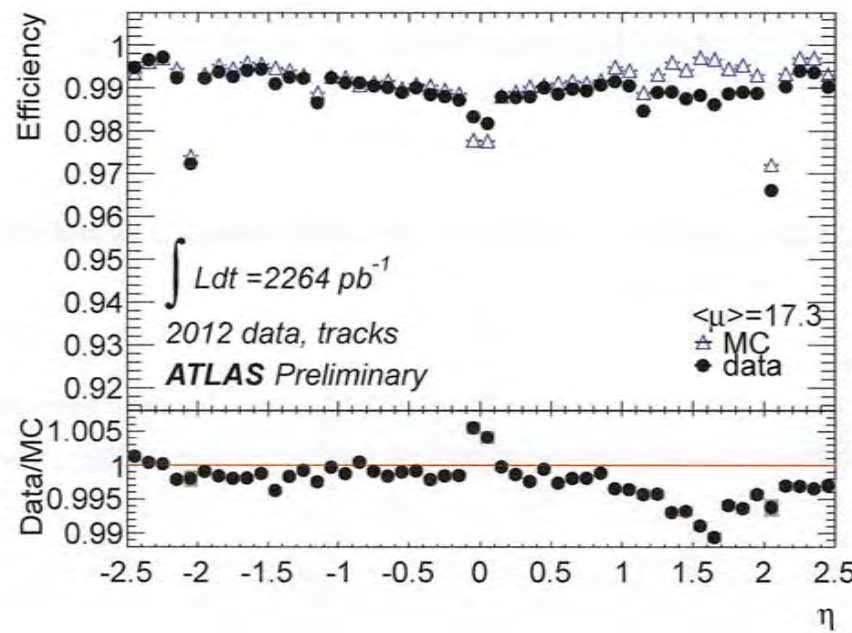
Details about the smearing procedure can be found under these links:

- <https://atlas.web.cern.ch/Atlas/GROUPS/PHYSICS/CONF-2011-046>
- <https://twiki.cern.ch/twiki/bin/view/AtlasProtected/>

- The resolution is the width of a Gaussian which is convoluted with the di-muon mass resolution at generator level.
- The fit is performed in the mass window  $m_{\mu\mu} \in [75 \text{ GeV}, 105 \text{ GeV}]$ .
- Error bars are the sum of the statistical error and the absolute value of the change of the resolution when the fit range is reduced to  $m_{\mu\mu} \in [82 \text{ GeV}, 100 \text{ GeV}]$ .

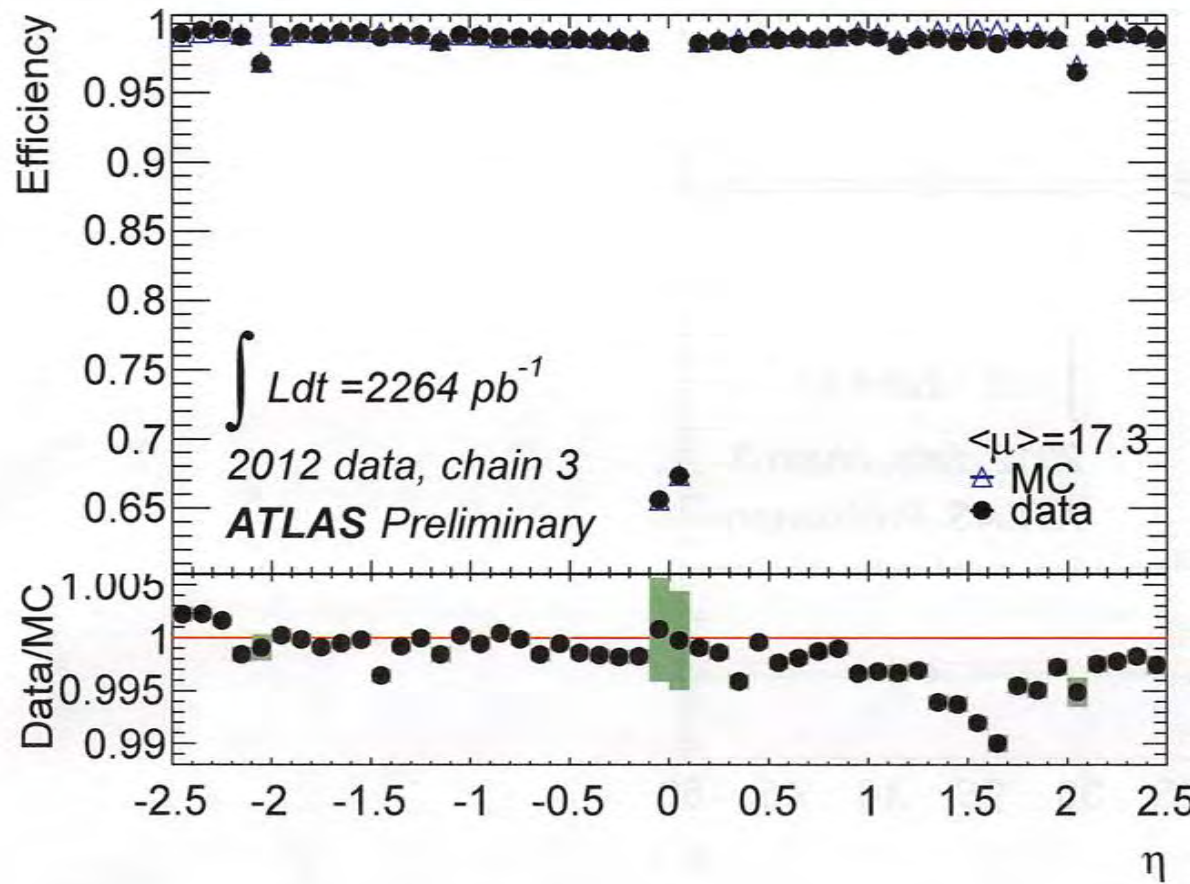
## ID reconstruction efficiency

ID tracks, plots produced on Period A + B up to run 203636  
with additional inner detector hit requirements without additional ID hit requirements



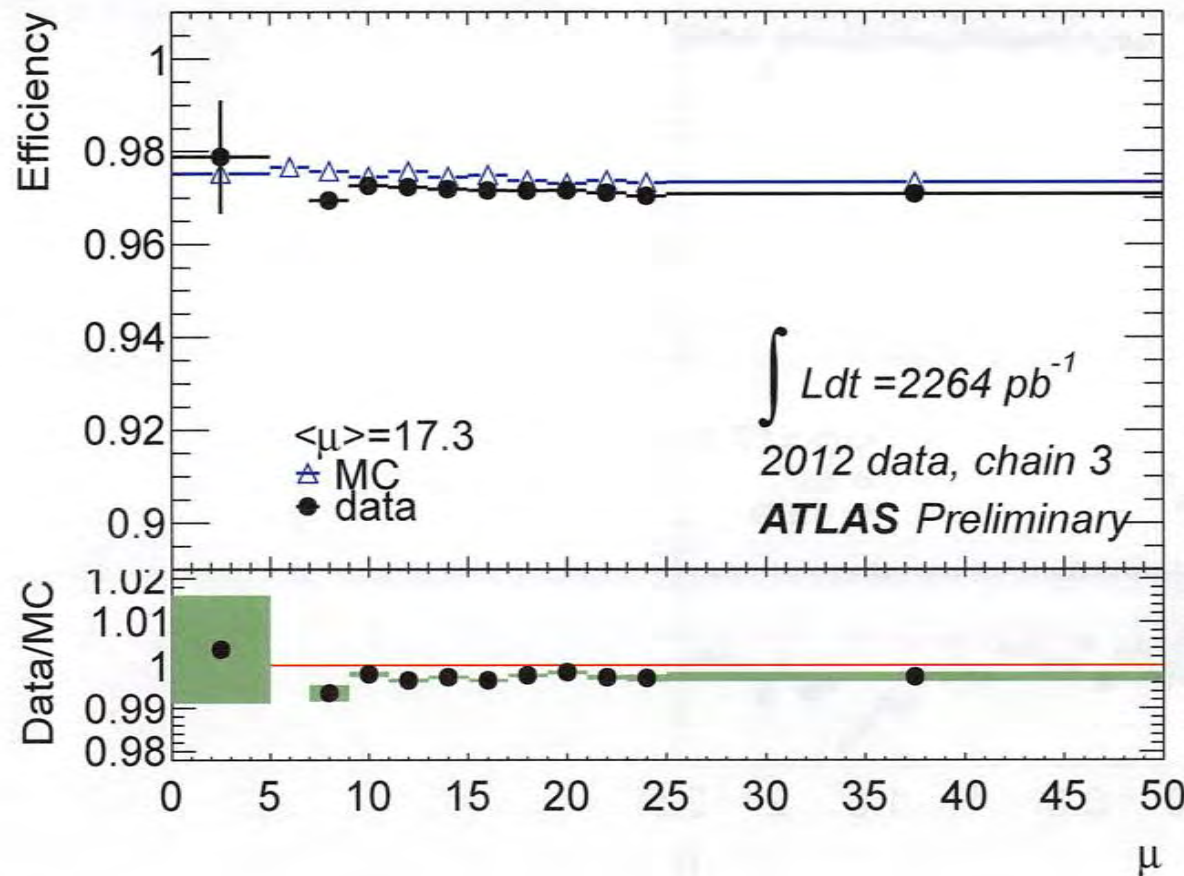
## Reconstruction efficiency vs $\eta$

Combined+Segment Tagged muons; plot produced on Period A + B up to run 203636



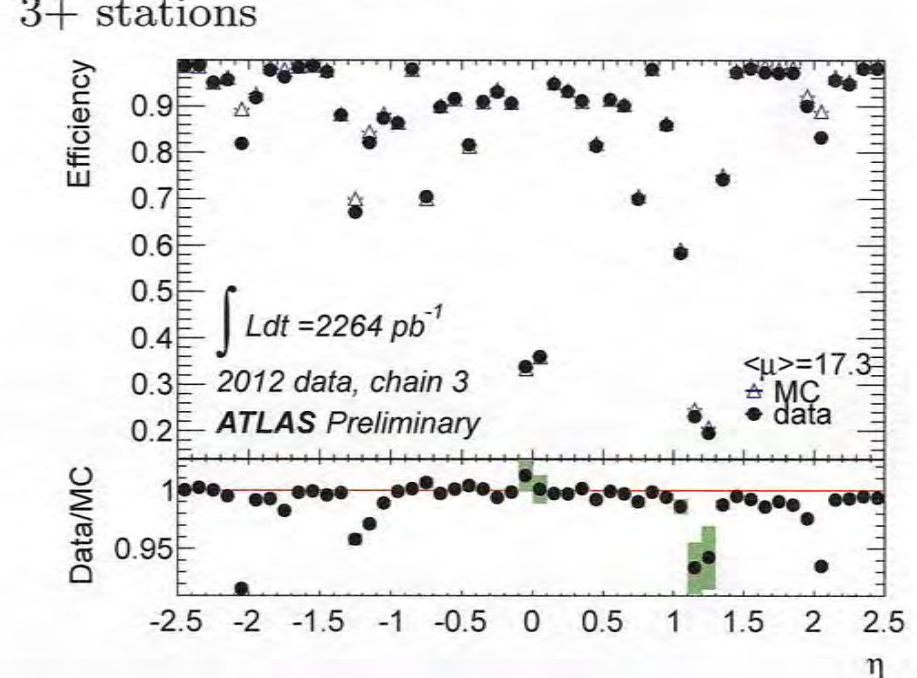
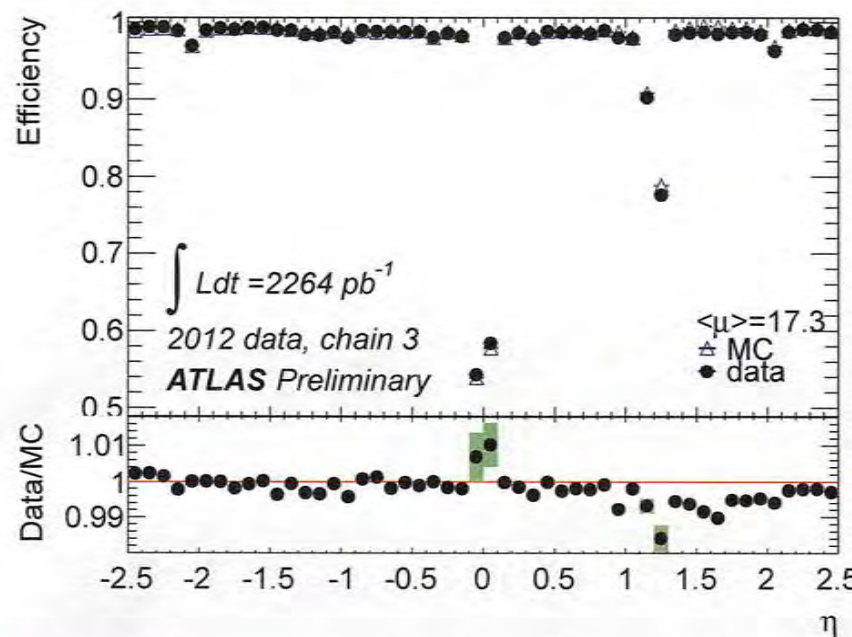
## Reconstruction efficiency vs $\mu$

Combined+Segment Tagged muons; plot produced on Period A + B up to run 203636

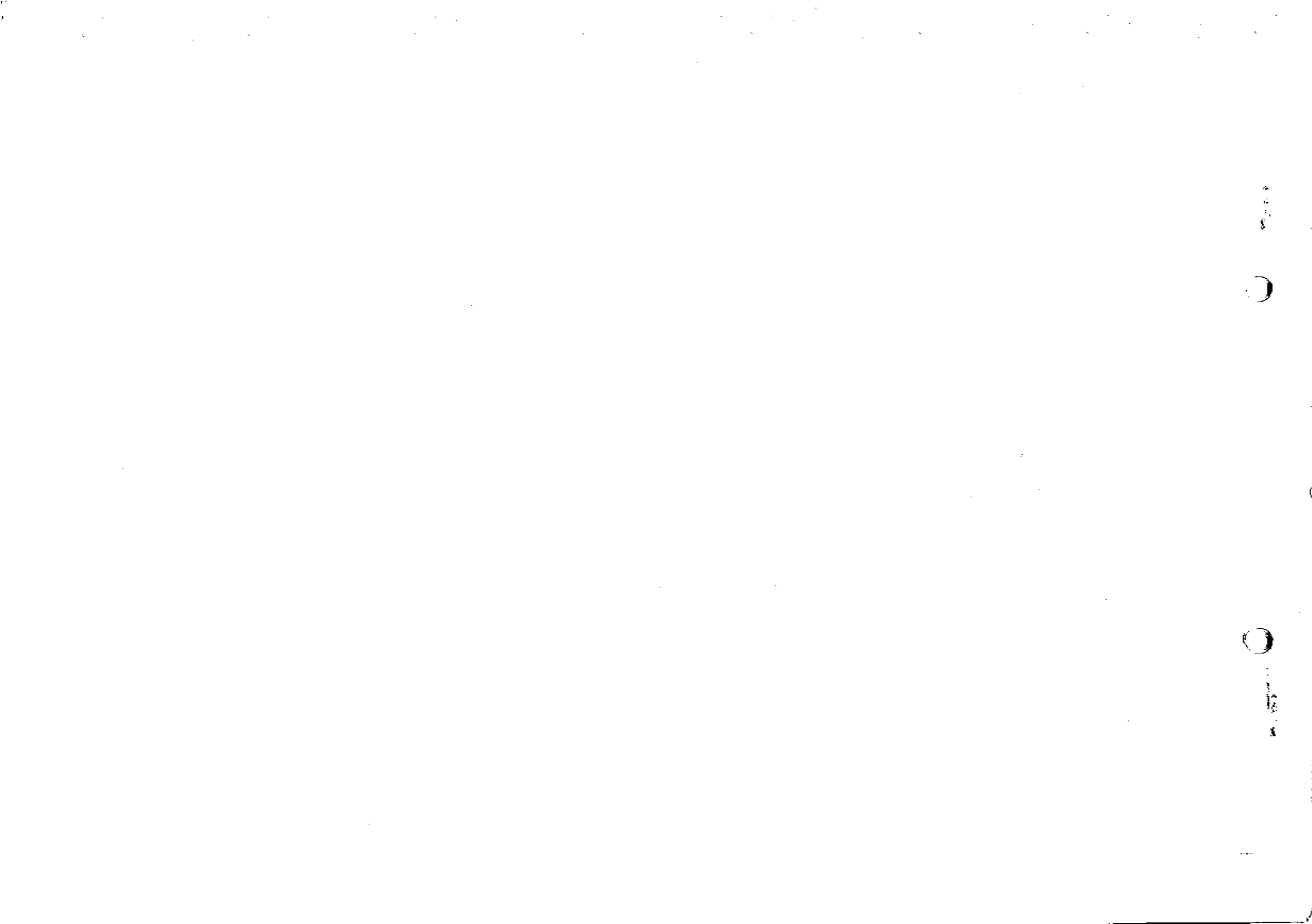


## Reconstruction efficiency for 2 stations and 3 stations

Combined muons; plots produced on Period A + B up to run 203636  
2+ stations



As the EE muon chambers have only been fully installed on side C, not A, there is an efficiency drop at  $\eta \sim 1.2$  causing a larger statistical uncertainty.





## ATLAS NOTE

ATLAS-CONF-2011-046

March 22, 2011



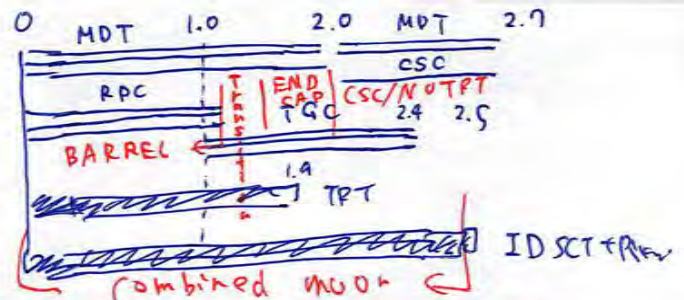
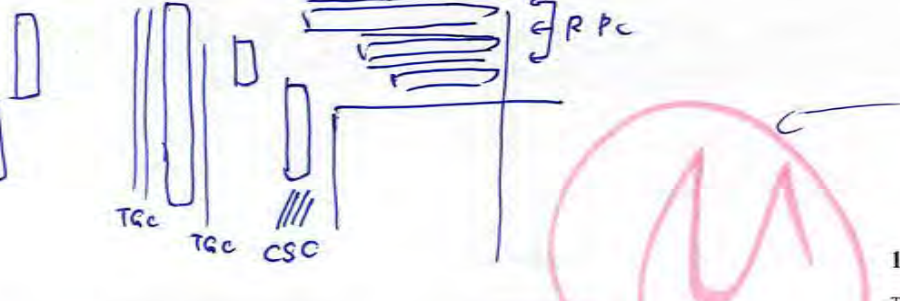
### ATLAS Muon Momentum Resolution in the First Pass Reconstruction of the 2010 $p\text{-}p$ Collision Data at $\sqrt{s} = 7 \text{ TeV}$

The ATLAS Collaboration

2011 - 608

#### Abstract

A measurement of the muon momentum resolution is presented for the first pass reconstruction of ATLAS  $p\text{-}p$  collision data in 2010, which uses preliminary calibration and alignment constants. The measurement is based on a sample of  $40 \text{ pb}^{-1}$  of LHC  $p\text{-}p$  collision data at  $\sqrt{s} = 7 \text{ TeV}$  collected with muon triggers. The momentum resolution is extracted from the width of the di-muon mass distribution in  $Z \rightarrow \mu\mu$  decays and the comparison of the independent measurements of muons from  $Z \rightarrow \mu\mu$  and  $W \rightarrow \mu\nu_\mu$  decays provided by the two ATLAS tracking systems, the Inner Detector and Muon Spectrometer. This note documents the status of the muon system performance used in 2010 physics analyses.



## 1 Introduction

The physics programme of the ATLAS experiment [1] at the LHC includes investigations of many processes with final state muons. The ATLAS detector is equipped with a Muon Spectrometer (MS) optimized to provide a momentum measurement with a relative resolution designed to be better than 3% over a wide  $p_T$  range and 10% at  $p_T = 1 \text{ TeV}$ , where  $p_T$  is the muon momentum component in the plane transverse to the beam axis. The momentum in the MS is measured from the deflection of the muon trajectory in the magnetic field generated by a system of air-core toroid coils. The MS track is reconstructed using three layers of precision drift tube (MDT) chambers in the pseudorapidity<sup>1</sup> range  $|\eta| < 2.0$  and two layers of MDT chambers behind one layer of cathode strip chambers (CSC) for  $2.0 \leq |\eta| < 2.7$ . Large and small MDT and CSC chambers alternate to cover the full angle in the transverse plane,  $\phi$ , following the azimuthal segmentation of the toroid magnet system. Three layers of resistive plate chambers (RPC) in the barrel region ( $|\eta| < 1.05$ ) and three layers of thin gap chambers (TGC) in the end-caps ( $1.0 < |\eta| < 2.4$ ) provide fast response to select events with muons in the final state *in real-time*, forming the ATLAS level-1 muon trigger. The trigger chambers also measure the muon trajectory in the non-bending (longitudinal) plane of the spectrometer magnets.

An additional determination of the muon momentum is provided by the Inner Detector (ID) for  $|\eta| < 2.5$ . The ID is composed of three detectors providing coordinate measurements for track reconstruction inside a solenoidal magnetic field of 2 T. A silicon pixel detector is mounted close to the interaction point and is surrounded by a silicon strip detector (SCT). The outermost part is a transition radiation straw tube tracker (TRT) whose full coverage is given up to  $|\eta| = 1.9$  in pseudorapidity. Muons entering this analysis are reconstructed as *combined muons*. The underlying muon identification is described in [2] and relies on the principle that first separate tracks are measured in ID and MS before the two tracks are reconstructed as a single trajectory with higher momentum resolution than each of the individual tracks could achieve.

This note documents the muon momentum resolution in the first pass reconstruction of  $p\text{-}p$  collision data collected in 2010 corresponding to an integrated luminosity of  $40 \text{ pb}^{-1}$ . The first pass reconstruction uses preliminary calibration and alignment, therefore it is expected that the measured resolution is poorer than its design value estimated from simulation. The momentum resolution is measured from the width of the di-muon invariant mass distribution in  $Z \rightarrow \mu\mu$  decays and from comparisons of the individual ID and MS momentum determination for *combined muons* from  $W \rightarrow \mu\nu_\mu$  decays.

## 2 Parametrization of the momentum resolution as a function of transverse momentum and pseudorapidity

The relative resolution on the momentum measurement,  $\frac{\sigma(p)}{p}$ , is dictated by different effects related to the amount of material that the muon traverses, the spatial resolution of the individual track points and the degree of internal alignment of the two subsystems (see also [3, 4]). The ATLAS MS is designed to provide a uniform momentum resolution as a function of the pseudorapidity. For a given value of  $\eta$ , the resolution can be parametrized in the following way as a function of the transverse component  $p_T$ :

$$\frac{\sigma(p)}{p} = \frac{p_0^{\text{MS}}}{p_T} \oplus p_1^{\text{MS}} \oplus p_2^{\text{MS}} \cdot p_T \quad (1)$$

where  $p_0^{\text{MS}}$ ,  $p_1^{\text{MS}}$  and  $p_2^{\text{MS}}$  are coefficients related to the energy loss in the calorimeters material, multiple scattering and intrinsic resolution terms, respectively. For the ID a similar parametrization can be found. In this case the curvature measurement depends on the track length of the muon in the active material,

<sup>1</sup>The pseudorapidity  $\eta = -\ln(\tan(\theta/2))$ , where  $\theta$  is the polar angle measured from the beam line.

which is reduced close to the edge of the TRT fiducial volume. This translates into a uniform response in the central part and a rapidly worsening resolution beyond this region. The following approximate parametrization of the resolution<sup>2</sup> is used:

$$\frac{\sigma(p)}{p} = p_1^{ID} \oplus p_2^{ID} p_T \quad (2)$$

for fixed  $\eta$  and  $|\eta| < 1.9$ . For  $|\eta| > 1.9$  and using the muon polar angle  $\theta$  it is

$$\frac{\sigma(p)}{p} = p_1^{ID} \oplus p_2^{ID} p_T \frac{1}{\tan^2(\theta)} \quad (3)$$

By considering *combined muons* the analysis is limited to the ID geometrical acceptance ( $|\eta| < 2.5$  for a precise momentum measurement). Four regions in pseudorapidity are distinguished for which we expect to have different resolutions in the ID and MS:

- *Barrel* – covering  $0 < |\eta| < 1.05$ ,
- *Transition region* – covering  $1.05 < |\eta| < 1.7$ ,
- *End-caps* – covering  $1.7 < |\eta| < 2.0$  and
- *CSC/no TRT* – covering  $2.0 < |\eta| < 2.5$ .

There are four regions each for  $\eta > 0$  and  $\eta < 0$ . All  $\eta$  regions are studied individually with  $Z \rightarrow \mu\mu$  decays to probe for a possible  $\eta$  asymmetry in the momentum resolution before combining results for positive and negative  $\eta$ . In addition to the  $\eta$ -dependence the muon momentum resolution in the MS varies also with the azimuthal angle  $\phi$ . Given the limited statistics available, this variation is neglected in the present analysis and the resolution is integrated over  $\phi$ .

### 3 Data and Monte Carlo samples

The results documented in this note are based on an integrated luminosity of  $40 \text{ pb}^{-1}$ , obtained with stable LHC beams in the period March to October 2010.

Events are selected on-line by the ATLAS muon trigger chain [5]: no  $p_T$  threshold requirement is applied at level-1 and an inclusive trigger sample is used for these performance studies. Events have been accepted for this analysis if the ID and MS detectors were in optimal data-taking conditions and both magnet systems were on. For the analysis with single muons from  $W$  boson decays we also require the calorimeters to be in optimal data-taking conditions: this additional requirement reduces the integrated luminosity to  $29 \text{ pb}^{-1}$ .

Experimental data are compared to Monte Carlo simulations of signal and background processes. The simulated processes are generated with Pythia [6], passed through the full simulation of the ATLAS detector based on Geant4 [7, 8], the trigger simulation and the same reconstruction chain used for data. For the signal we use samples of  $W$  and  $Z$  boson decays into muons, without any additional kinematic filters at the generation or simulation stage. The different background sources used are described in Section 5.3. The simulation describes the performance of a perfectly calibrated and aligned ATLAS detector. Studies with cosmic rays [9] showed shortcomings in the simulation of the intrinsic resolution and module misalignment, neither of which are corrected for in the current simulation. Inactive or non-installed detector parts are modeled by masking or omitting the corresponding components, respectively.

The  $p\text{-}p$  collision and simulated datasets were processed offline with a single version of the reconstruction software. In particular, we report results based on the 2010 first pass ATLAS reconstruction which used preliminary calibration and alignment for the ID and MS.

<sup>2</sup> $p_1^{ID}$  and  $p_2^{ID}$  are the multiple scattering and intrinsic resolution terms, respectively

## 4 Event selection

Collision events are selected by requiring at least one reconstructed Primary Vertex (PV) with a position  $|z_{\text{PV}}| < 150 \text{ mm}$  relative to the nominal interaction point and at least 3 ID tracks associated with the PV. Each of the 3 tracks should have at least 1 hit in the pixel detector and at least 6 hits in the SCT. Specific additional requirements for each decay channel, both at the muon and event level, are described in the following paragraphs.

### 4.1 Muon selection

To select collision events with muon final state we require *combined muons* [2] with:

- At least 1 hit in the pixel detector, 6 hits in the SCT and a number of hits in the TRT compatible with its coverage in pseudorapidity,
- Pseudorapidity  $|\eta| < 2.5$ .

### 4.2 Selection of $Z \rightarrow \mu\mu$ decays

We select  $Z \rightarrow \mu\mu$  decays by applying the following requirements:

- Exactly two combined muons, with opposite electric charge, each satisfying the requirements discussed in Section 4.1;
- Each of the selected muons should have a transverse momentum  $p_T > 20 \text{ GeV}$  and a direction within the same  $\eta$  region, as defined in Section 2.

### 4.3 Selection of $W \rightarrow \mu\nu_\mu$ decays

The sample of  $W \rightarrow \mu\nu_\mu$  decays was selected with the following requirements, which were optimized for the measurement of the  $W$  boson production cross-section from leptonic decays [10]:

- At least one isolated muon with  $p_T > 10 \text{ GeV}$ : a muon is considered isolated if the sum of the transverse momenta of the (non-muon) tracks in a cone of  $\sqrt{\Delta\eta^2 + \Delta\phi^2} = 0.4$  around the muon is less than 20% of the muon  $p_T$ ;
- A missing transverse energy  $E_T^{\text{miss}}$ , measured using both the calorimetric and muon energy measurements, of at least  $25 \text{ GeV}$ ;
- A reconstructed  $W$  boson transverse mass

$$M_T(W) = \sqrt{2(p_T^\mu)(E_T^{\text{miss}})[1 - \cos(\phi^\mu - \phi^{E_T^{\text{miss}}})]} \quad (4)$$

larger than  $40 \text{ GeV}$ .

This selection suppresses the muon background from decays in flight and heavy flavor decays in jets.

## 5 Combined fit to the muon resolution components and comparison with results from cosmic ray data

The processes  $Z \rightarrow \mu\mu$  and  $W \rightarrow \mu\nu_\mu$  are sensitive to the momentum resolution through two quantities:

- the width of the reconstructed di-muon invariant mass peak at the Z pole, which is a convolution of the natural width of the Z boson and the muon momentum resolution;
- the difference of the independent momentum measurements of the ID and MS for combined muons in selected  $W \rightarrow \mu\nu_\mu$  events; this difference is sensitive to the quadratic sum of the ID and MS momentum resolutions.

This section discusses first the individual performance of the two quantities and then presents the technique to parameterize both with a single resolution function for each tracking system. This combination of two independent channels also increases the statistical sensitivity of the momentum resolution on the expected  $p_T$  and  $\eta$  dependence. Once the actual resolution parameters are measured, correction parameters are provided for the simulated muon  $p_T$  to reproduce the data. Such corrections are needed in order to accurately measure analysis-level quantities based on the muon  $p_T$ . These include, for example, an event selection acceptance and the muon contribution to the calculation of the event missing transverse energy.

### 5.1 Di-muon invariant mass distribution at the Z pole

The resolution contribution to the relative invariant mass width is studied as a function of the  $\eta$  region in cases where both muons are reconstructed in that  $\eta$  region (see event selections in Section 4.2). The di-muon invariant mass distributions are obtained separately from MS and ID track parameters and integrated over all muon  $p_T$  values. They are then fitted using a convolution of the Z lineshape and two Gaussian functions modelling the detector resolution effects. The two Gaussians are centered at 0. While the full fit range is from 60 to 120 GeV, one core Gaussian is constrained to contain 85% of the di-muon pairs. This value corresponds to the fraction of muons contained within the core Gaussian in the simulation, where the fit was applied without constraint. The Z lineshape, including the Z boson natural width, a photon radiation term and the interference term [11], is given by:

$$f(x) = A \left( \frac{1}{x^2} \right) + B \left( \frac{(x^2 - \bar{x}^2)}{(x^2 - \bar{x}^2)^2 + \sigma_x^2 \bar{x}^2} \right) + C \left( \frac{x^2}{(x^2 - \bar{x}^2)^2 + \sigma_x^2 \bar{x}^2} \right) \quad (5)$$

where  $x$  indicates the reconstructed di-muon invariant mass  $M_{\mu\mu}$ ,  $A$ ,  $B$  and  $C$  as well as  $\sigma_x$  are fixed parameters, determined from the invariant mass of the muon pair at particle level before detector simulation, while  $\bar{x}$  is a free parameter in the fit. The fit function is validated by investigating how well it describes the true Z boson lineshape in simulation. It is also verified that, if left free to fluctuate, the estimates for  $A$ ,  $B$  and  $C$  are unbiased.

The mass resolution, i.e.  $\sigma(M)$  of the core Gaussian in the fit, is shown in Figure 1 as a function of  $\eta$  region for the MS (left) and ID (right). Variations in  $\eta$  of the detector material, magnetic field bending power and detector acceptance create a structure in the simulated mass resolution that is symmetric in  $\eta$ . The data show the same symmetric structure with the exception that the ID momentum resolution shows an absolute asymmetry in the di-muon invariant mass resolution of about 4% in the region  $|\eta| > 2.0$  between positive and negative  $\eta$ . This corresponds to about a 60% fractional difference in resolution between the two sides. The effect is due to a different level of ID misalignment on the two sides, already observed in [12] (see e.g. Figure 5b). This issue was solved for the reprocessing of the full 2010 dataset [13].

An overall discrepancy between simulated and measured resolution is observed in all detector regions. It is partly understood as a result of the limited accuracy with which the calibration and alignment constants were known prior to the first pass reconstruction. For the MS also the material distribution and magnetic field description can, if inaccurate, contribute to a larger resolution at low momenta. The agreement between data and Monte Carlo in the  $|\eta| < 1.05$  region of both tracking systems is of the

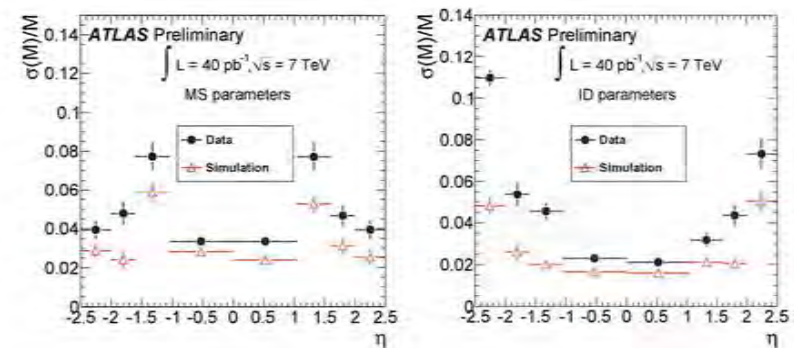


Figure 1: Resolution contribution  $\sigma(M)$  to the relative di-muon invariant mass width in data (circles) and simulation (open triangles) as a function of  $\eta$  region, for the MS (left) and the ID (right) part of combined muon pairs.

same kind as that observed with cosmic ray events [3, 4]. The disagreement for the other regions, which had a smaller exposure to cosmic ray muons, is discussed in detail at the end of Section 5.2.

The value of the fitted invariant mass at the Z pole is sensitive to possible shifts in the momentum scale. The accuracy of the momentum scale is probed by measuring the average deviation of the measured invariant mass from the Z mass world average, which is shown in Figure 2 for combined muons in data and simulation. It is obtained for each of the four  $\eta > 0$  and  $\eta < 0$  regions and averaged over all muon  $p_T$  values. A good agreement with the Z mass world average ( $M(Z) = 91.1876$  GeV [14]) is observed, except for the two regions within  $-2.5 < \eta < -1.7$ . There an offset of up to 1.5% is present which is not modelled by simulation. This offset has been further studied by measuring the average deviation separately in the ID and MS. It can be explained by an asymmetry in the magnetic field between the positive and negative end-caps that is taken into account in a more recent version of the track reconstruction code.

### 5.2 Quadratic sum of the momentum resolution of the Muon Spectrometer and the Inner Detector from $W \rightarrow \mu\nu_\mu$ decays

Another way of measuring the muon momentum resolution is to use the redundancy in the ATLAS tracking systems, by comparing the independent momentum measurements for events with single muons. A relative difference in momentum is defined as

$$\rho := \frac{p_{\text{ID}} - p_{\text{MS}}}{p_{\text{ID}}} \quad (6)$$

where  $p_{\text{ID}}$  denotes the momentum measurement in the ID and  $p_{\text{MS}}$  the momentum measured by the MS and extrapolated to the interaction point, taking energy loss into account. As a result the expectation value for  $\rho$  is 0 and the width of the distribution is determined by the quadratic sum of the resolutions of the two detectors. Depending on the region of the pseudorapidity and the range of  $p_T$ , this quantity is dominated by the ID or MS contribution. The use of single muons allows us to probe the quadratic sum of the resolutions of the two detectors as a function of  $p_T$  from  $\approx 20$  GeV up to about 120 GeV.

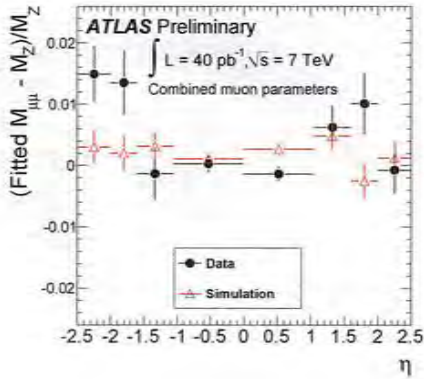


Figure 2: Average deviation of the measured invariant mass from the  $Z$  mass world average as function of  $\eta$  region to which the two combined muons are associated. The fitted value corresponds to the  $\bar{x}$  in Equation 5. The error bars for both data (circles) and simulation (open triangles) are statistical only.

To extract the resolution as a function of the muon  $p_T$  and  $|\eta|$  the  $p$  distribution is fitted with a normal distribution, in a range of  $\pm 1$  r.m.s. from the mean of the data distribution. Using about 70 000 selected  $W \rightarrow \mu\nu_\mu$  decays, the sample is large enough to perform the fitting procedure in six  $p_T$  bins: 20–25 GeV, 25–35 GeV, 35–45 GeV, 45–55 GeV, 55–70 GeV,  $>70$  GeV. The fitted resolution sum values as a function of  $p_T$  are shown in Figure 3. Once more the four pseudorapidity regions described in Section 2 are studied, confirming the observation from the  $Z \rightarrow \mu\mu$  decays that the discrepancy between data and simulation is larger in the high  $|\eta|$  regions.

In summary, when looking at the muon momentum resolution using the first pass reconstruction with preliminary calibration and alignment constants, the performance in data is worse than in simulation. The barrel region has been studied extensively using cosmic rays in the past [4, 3]: for both ID and MS, residual miscalibrations and misalignment in data reduce the agreement with the simulation. An additional discrepancy between data and simulation in the MS, coming from the term constant in  $p_T$ , is also observed and is being investigated. In the ID, for the end-caps, the use of preliminary alignment constants in this reconstruction pass introduces some disagreements with respect to expectations. For the MS, the alignment and calibration in the end-caps instrumented with MDT chambers are observed to be essentially similar to the barrel. For the CSC/no-TRT region the 2010  $p\text{-}p$  collisions are the first data that allow the reconstruction performance for high- $p_T$  tracks to be studied in detail. The limitations of the initial detector positioning used by the first pass reconstruction become visible as a discrepancy between the simulated and measured resolutions. This difference rises with  $p_T$ , as shown in Figure 3, and is attributed to the quality of the internal ID and MS alignment.

### 5.3 Input quantities to the combined fit

To measure the overall resolution and to determine the corrections needed for simulation we use the following inputs:

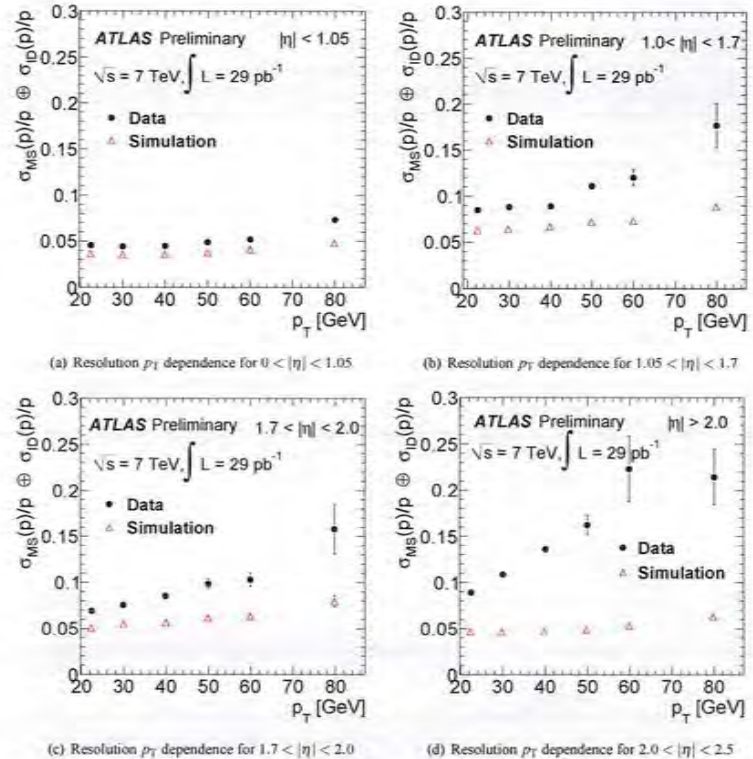


Figure 3: Sum in quadrature of the MS and ID resolutions as a function of muon  $p_T$ , for the four pseudorapidity regions. Data, selected according to the requirements in the text (dots) are compared with signal  $W \rightarrow \mu\nu_\mu$  Pythia Monte Carlo simulation (open triangles) [6, 7]. This quantity accumulates the alignment and calibration effects from both tracking systems, therefore any discrepancy between data and simulation is expected to shrink when more detailed alignment and calibration corrections are made in subsequent analysis.

- The di-muon invariant mass in the  $Z$  boson mass region;
- The MS-to-ID curvature difference weighted by the muon electric charge,  $(\frac{g_B}{p_T} - \frac{g_M}{p_T})$ . The weighting by the electric charge disentangles systematic effects of the curvature due to local misalignments from the overall intrinsic resolution, reducing the bias on the estimation of the resolution and correction parameters.

For the simulation, we consider contributions from the  $Z$  and  $W$  boson decays into muons and the following background processes: Drell-Yan di-muon production,  $t\bar{t}$ , where one or two muons are generated,  $Z \rightarrow \tau\tau$  and  $W \rightarrow \tau\nu$ ; and heavy flavour decays ( $b\bar{b}$ ,  $c\bar{c}$ ) with one or two muons in the final state. Events and muons are selected as described in Section 4. In addition, it is required for data and simulation that the event be triggered by the level-1 muon trigger and a uniform  $p_T$  threshold of 10 GeV is applied to the muon candidate from the trigger chain in order to guarantee an unbiased determination of the correction parameters. For the  $W \rightarrow \mu\nu_\mu$  events entering the combined fit the  $p_T$  cut is tightened to 25 GeV as a measure to improve the stability of the combined fit. The difference between reconstructed and true momentum resolution on simulation was examined and showed a Gaussian distribution with highly suppressed tails in the  $p_T$  and  $\eta$  ranges considered.

#### 5.4 Combined fitting technique

The measurements of the MS and ID momentum resolution are obtained using a Monte Carlo template technique: a series of distributions of  $\sigma(M)$  and  $\rho$  are created for various momentum resolution values and then matched to the one in data. For the MS the transformation is the following:

$$p'_T(MS) = p_T(MS) (1 + \Delta(MS)) \quad (7)$$

where

$$\Delta(MS) = f(0, 1) \Delta p_1^{MS} + f(0, 1) \Delta p_2^{MS} p_T \quad (8)$$

$p'_T(MS)$  indicates the simulated muon  $p_T$  after applying the corrections  $\Delta p_1^{MS}$ , while  $f(0, 1)$  is a normally distributed random number with mean 0 and width 1.

For the ID the rescaled  $p_T$  is expressed in the same way :

$$p'_T(ID) = p_T(ID) (1 + \Delta(ID)) \quad (9)$$

where

$$\Delta(ID) = f(0, 1) \Delta p_1^{ID} p_T \quad (|\eta| < 1.9) \quad (10)$$

$$\Delta(ID) = f(0, 1) \Delta p_1^{ID} p_T / \tan^2(\theta) \quad (|\eta| > 1.9)$$

$p'_T(ID)$  indicates the simulated muon  $p_T$  after applying the corrections  $\Delta p_1^{ID}$  and  $\theta$  is the muon polar angle. The values of the additional resolution  $\Delta(ID), \Delta(MS)$  are obtained from a  $\chi^2$  minimisation fit to the overall spectrum (sum of all inputs for ID and MS and in the various  $|\eta|$  regions). The variation of the  $p_T^{DMS}$  parameters is performed by rescaling the simulated muon  $p_T$ .

An iterative smearing procedure is performed in which first we correct the  $p_T$  of single muons and pairs of muons from  $Z$  boson decays in the barrel region. Then the additional corrections are extracted for events in which one of the two muons or both fall in the  $|\eta| > 1.05$  range.

#### 5.5 External constraints to the combined fit

In the fitting procedure, additional knowledge is introduced from independent studies, both for the ID and the MS. This reduces the correlation among the multiple scattering and the detector resolution terms in the fit, resulting in smaller uncertainties on the fitted parameters. The way this external knowledge is translated into fit constraints is described in Section 5.6.

#### 5.5.1 Multiple scattering in ID and MS

For the ID, the correction to the multiple scattering term in the ID,  $\Delta p_1^{ID}$ , is constrained around an expected value of zero, using the uncertainty on the ID material budget. The latter has been probed by the results on the  $K^0_s$  reconstructed mass (sensitive to energy loss corrections) [15], the  $J/\psi$  width [16] and the resolution on the transverse impact parameter for low  $p_T$  ID tracks [17]. The material uncertainty from these studies is transformed in an approximation into 5% uncertainty on the multiple scattering correction term for  $|\eta| < 2.0$ , and 10% for  $|\eta| > 2.0$ .

For the MS, the multiple scattering term,  $\Delta p_2^{MS}$ , is a free parameter of the fit. The energy loss of muons is mainly concentrated in the calorimetry and has been measured in [9]. Its contribution to the overall MS resolution in the transverse momentum range from 20 to 100 GeV is negligible and therefore no additional contribution for the energy loss in the calorimetry,  $\Delta p_0^{MS}$ , is included.

#### 5.5.2 MS alignment

In treating the corrections to the MS, where the  $\Delta p_1^{MS}$  and  $\Delta p_2^{MS}$  are highly correlated (up to 80% correlation) in the  $p_T$  region of interest, we apply our best estimate of the initial alignment accuracy. This is the result of commissioning studies from 2009 and 2010, on a large sample of cosmic ray events and samples of straight tracks obtained in periods of collision data taken with no magnetic field in the muon system. The estimated accuracy is shown in Table 1 for the various  $|\eta|$  regions. Such figures reflect results from different sources: for the MDT barrel region they come essentially from studies with cosmic ray muons [3] and are monitored with the relative optical alignment system; for the transition region and for the end-caps our current knowledge comes mainly from the optical system and is confirmed by a study with straight cosmic muon tracks, though statistically limited. About 10% of the chambers in the transition region are not monitored with alignment sensors. Their position is currently known at the level of about 1 mm. The position of the CSC chambers has been measured with straight muon tracks and found to agree within 700  $\mu\text{m}$  with the positions used in track reconstruction.

This information can be translated directly into a constraint on the correction to the intrinsic resolution term in the MS,  $\Delta p_2^{MS}$ , by making use of the formula for the track sagitta:

$$\Delta s [\mu\text{m}] \approx \frac{0.3}{8} B[\text{T}] L[\text{m}]^2 \Delta p_2^{MS} [\text{TeV}^{-1}] \cdot 10^3 \quad (11)$$

where  $\Delta s$  is the difference in sagitta from a correction  $\Delta p_2^{MS}$ , in a magnetic field of intensity  $B$ , given a track length  $L$ . The uncertainty on  $\Delta p_2^{MS}$  is propagated directly from the uncertainty on the alignment accuracy using the above formula. The resulting constraints on  $\Delta p_2^{MS}$  are summarized in Table 1. Since the statistical power of the measurement is not yet sufficient to probe the fraction of chambers in the

$\eta$ region	Accuracy on alignment ( $\mu\text{m}$ )	Constraint on $\Delta p_2^{MS}$ ( $\text{TeV}^{-1}$ )
barrel	$100 \pm 20$	$0.20 \pm 0.04$
transition	$100 \pm 50$	$0.20 \pm 0.07$
end-caps	$100 \pm 50$	$0.20 \pm 0.07$
CSC+TRT	$700 \pm 200$	$0.7 \pm 0.2$

Table 1: Alignment accuracy for the various regions of the MS corresponding to the 2010 first pass reconstruction. These values are obtained from the cosmic ray data and collision runs with no toroidal magnetic field ("straight track runs"). They are used to constrain the amount of correction needed on simulation to reproduce the MS intrinsic resolution term on data.

transition region whose alignment is determined with a less good accuracy (1 mm), we study the muon momentum resolution for that region as a whole. A systematic uncertainty on the measurement of the resolution in data is quoted to quantify this effect.

### 5.6 Combined fit results

The constraints on the  $\Delta p_t$  parameters from Section 5.5 are applied in the combined fit by adding a penalty term  $\sum_i (\frac{\Delta p_i - \alpha_i}{\sigma_i})^2$  to the total  $\chi^2$  being minimized. Here  $\alpha_i$  is the expectation value and  $\sigma_i$  the associated uncertainty for each of the constrained  $\Delta p_t$  parameters. For the alignment accuracy in the MS they are the ones of Table 1. For the ID multiple scattering, the expected value  $\alpha$  is set to 0. The value of  $\sigma_\alpha$  is the needed absolute correction corresponding to a 5% (10%) relative deviation of  $p_1^{ID}$  from the Monte Carlo value for  $|\eta| < 2.0$  ( $|\eta| > 2.0$ ). The  $\Delta p_2^{ID}$  for the CSC/no-TRT region is obtained using the parameterization of Equation 3.

The fitted corrections parameters are provided in Table 2 together with their statistical and systematic uncertainties. The latter are discussed in the next section. For the  $\Delta p_2^{ID}$  parameter Equation 3 is used in the CSC/no-TRT region and Equation 2 for the other regions.

$\eta$ region	MS		ID	
	$\Delta p_1^{MS}$ (%)	$\Delta p_2^{MS}$ ( $\text{TeV}^{-1}$ )	$\Delta p_1^{ID}$ (%)	$\Delta p_2^{ID}$ ( $\text{TeV}^{-1}$ )
barrel	$2.60 \pm 0.10 \pm 0.04$	$0.21 \pm 0.05 \pm 0.01$	$0.03 \pm 0.32$	$0.396 \pm 0.044 \pm 0.008$
transition	$6.95 \pm 0.23^{+0.39}_{-0.09}$	$0.193 \pm 0.09^{+0.06}_{-0.15}$	$0.03 \pm 0.54^{+0.10}_{-0.09}$	$0.900 \pm 0.091^{+0.09}_{-0.09}$
end-caps	$3.45 \pm 0.35 \pm 0.05$	$0.21 \pm 0.12 \pm 0.01$	$0.04 \pm 0.58$	$1.324 \pm 0.045 \pm 0.013$
CSC/no TRT	$4.05 \pm 0.61 \pm 0.22$	$0.90 \pm 0.19 \pm 0.16$	$0.07 \pm 0.50$	$0.129 \pm 0.004 \pm 0.001$

Table 2: Set of corrections to be applied to the  $p_T$  parameterization of the simulated resolution in the MS and ID to reproduce the one in data. For example, in the MS barrel region the simulated multiple scattering term needs to be increased by an absolute 2.6% to match the one in data. The first uncertainty is statistical, the second one the quadratic sum of all systematic uncertainties. The statistical uncertainty is rescaled as explained in Section 5.7. The systematic uncertainties are discussed in Section 5.7 and their individual values are provided in Table 4.

The values of the correction parameters quantify the increase in momentum resolution in data when compared to simulation. The full parametrization of the experimental momentum resolution is obtained by adding quadratically the uncorrected simulated resolution terms of Equations 1–3 and the corresponding corrections from Table 2. The uncertainties are directly propagated from those of the correction parameters and the statistical errors on the uncorrected Monte Carlo resolution. The results for the full parametrization are listed in Table 3.

### 5.7 Systematic error sources

Given the uncertainty on the current knowledge of the material budget in the ID, the results of the resolution fit are tested by constraining the multiple scattering correction in the ID to the expected value and standard deviation as in Section 5.6. In the transition region some chambers in the MS are known to be less well aligned than others, therefore the effect of applying a uniform constraint to  $\Delta p_2^{MS}$  is also investigated.

The first effect (ID multiple scattering constraint) is evaluated by performing the fit for the  $\Delta p_1^{MS}$ ,  $\Delta p_2^{MS}$  and  $\Delta p_1^{ID}$  parameters after fixing  $\Delta p_2^{ID}$  to the absolute value of Table 4, corresponding to a relative

$\eta$ region	MS			ID	
	$p_0^{MS}$ (TeV)	$p_1^{MS}$ (%)	$p_2^{MS}$ ( $\text{GeV}^{-1}$ )	$p_1^{ID}$ (%)	$p_2^{ID}$ ( $\text{TeV}^{-1}$ )
barrel	$0.23 \pm 0.01$	$3.75 \pm 0.10$	$0.24 \pm 0.04$	$1.60 \pm 0.32$	$0.49 \pm 0.04$
transition	0	$8.80 \pm 0.46$	$0.30 \pm 0.16$	$2.60 \pm 0.54$	$0.95 \pm 0.10$
end-caps	0	$4.77 \pm 0.35$	$0.23 \pm 0.12$	$3.40 \pm 0.58$	$1.39 \pm 0.05$
CSC/no TRT	$0.17 \pm 0.02$	$4.87 \pm 0.65$	$0.90 \pm 0.25$	$4.10 \pm 0.50$	$0.140 \pm 0.004$

Table 3: Resolution parameterization as defined in Equations 1–3 in the MS and ID. The measurements are obtained by adding the correction parameters in quadrature to the uncorrected momentum resolution from simulation.

5% (10%)  $\sigma$ . The systematic uncertainty on the other corrections is taken as the difference of each fitted value with respect to the baseline case.

The systematic uncertainty originated by imposing a single constraint to  $\Delta p_2^{MS}$  from the alignment accuracy in the transition region is also quantified. About 30% of the muons in the transition region have  $1.05 < |\eta| < 1.2$ , corresponding to the less well known part of the geometry. To assess the correctness of the  $(100 \pm 50)\mu\text{m}$  accuracy assumed for the whole region in the baseline analysis, all muons within the latter  $\eta$  range are removed and the fit is repeated. The additional systematic uncertainty for the transition region is shown in Table 4.

Finally, residual shape mismodeling in the simulation or incompatibilities with the constraints are accounted for by rescaling the statistical uncertainty  $\sigma_{\text{stat}}$  returned by the baseline fit. Both effects would produce a  $\chi^2/N_{\text{d.o.f.}}$  (with  $N_{\text{d.o.f.}}$  the overall number of degrees of freedom) different from 1; therefore we use as statistical uncertainty the quantity  $\sigma'_{\text{stat}} = \sigma_{\text{stat}} \sqrt{\chi^2/N_{\text{d.o.f.}}}$  [14]. Values of  $\chi^2/N_{\text{d.o.f.}}$  between 1.1 and 1.5 are used, depending on the  $\eta$  region.

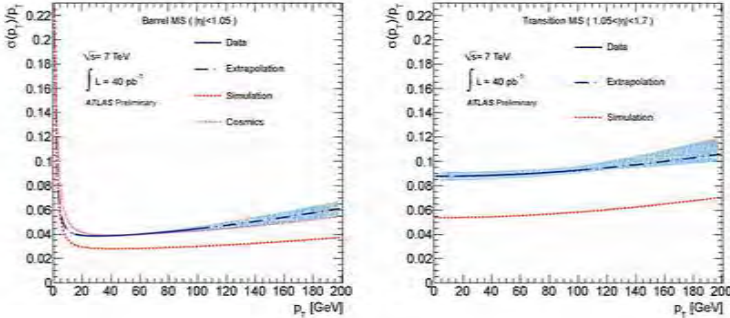
In this context, an additional check of the goodness of the constraints from the external alignment accuracy is performed. This is not considered in the evaluation of the systematic uncertainties, but rather as an independent control. The gaussian constraint of Section 5.6 is completely removed and  $\Delta p_2^{MS}$  is left to vary freely in the fit. A  $\chi^2$  minimization for the unconstrained  $\Delta p_2^{MS}$  is performed. The  $\Delta p_2^{MS}$  corresponding to the minimum  $\chi^2$  and the bounds of the  $2\sigma$  interval are the following:

- Barrel:  $\Delta p_2^{MS}(\chi^2_{\min}) = 0.25 \text{ TeV}^{-1}$ ;  $2\sigma$  interval = [0.05, 0.40]
- Transition:  $\Delta p_2^{MS}(\chi^2_{\min}) = 0.25 \text{ TeV}^{-1}$ ;  $2\sigma$  interval = [0.0, 0.3]
- End-caps:  $\Delta p_2^{MS}(\chi^2_{\min}) = 0.0 \text{ TeV}^{-1}$ ;  $2\sigma$  interval = [0.0, 0.3]
- CSC/no TRT:  $\Delta p_2^{MS}(\chi^2_{\min}) = 0.2 \text{ TeV}^{-1}$ ;  $2\sigma$  interval = [0.0, 0.4]

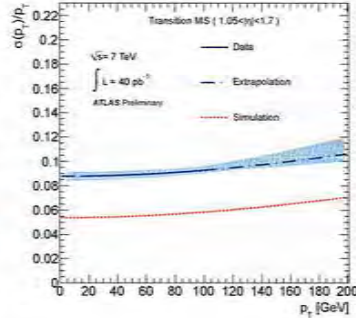
The test proves the fit consistency with the external alignment constraints imposed; furthermore it shows the sensitivity of a fully free fit to the  $\Delta p_2^{MS}$  parameter in the  $p_T$  range probed with the available data sample.

### 5.8 Measured resolutions as a function of $p_T$

The parametrized resolution as a function of  $p_T$  for the four  $\eta$  regions, obtained using the values of the parameters from the combined fits, are shown separately in Figures 4 and 5 for the MS and the ID, respectively. The resolution curves for experimental data are compared to those from the uncorrected parameters obtained for the simulation. The results of the analysis on collision data is also compared with the resolution curves obtained from analysis of cosmic ray muons [3]. Results using cosmic rays

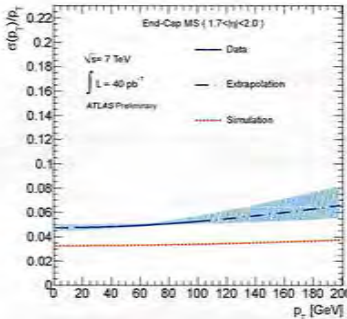


(a) MS resolution  $p_T$  curve for  $0 < |\eta| < 1.05$



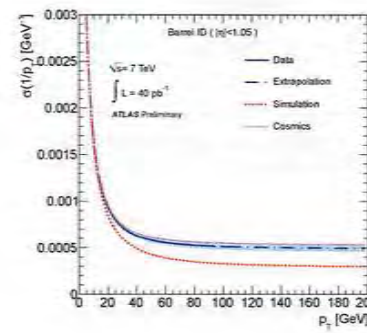
(c) MS resolution  $p_T$  curve for  $1.7 < |\eta| < 2.0$

(b) MS resolution  $p_T$  curve for  $1.05 < |\eta| < 1.7$

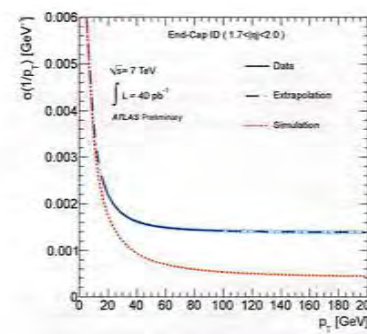


(d) MS resolution  $p_T$  curve for  $2.0 < |\eta| < 2.5$

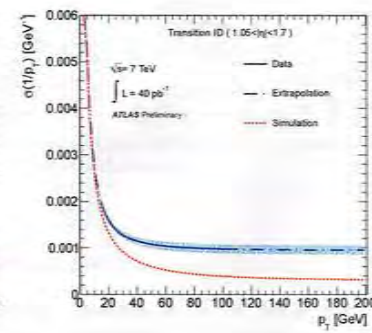
Figure 4: Resolution curve from the fitted parameter values of the MS in collision data and simulation as a function of the muon  $p_T$ , for the different  $\eta$  regions of the detector. The solid blue line shows determinations based on data and is continued as dashed line for the extrapolation to  $p_T$  ranges not accessible in this analysis. The shaded band represents the sum in quadrature of the statistical and systematic uncertainties. For the case of the barrel, a comparison with the curve obtained from the fitted parameters from cosmic ray data is overlaid for comparison.



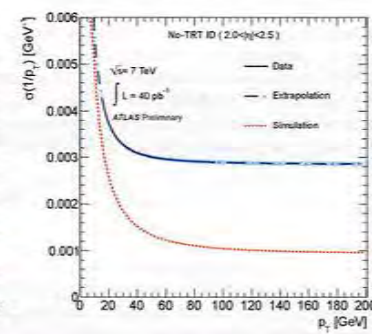
(a) ID resolution  $p_T$  curve for  $0 < |\eta| < 1.05$



(c) ID resolution  $p_T$  curve for  $1.7 < |\eta| < 2.0$



(b) ID resolution  $p_T$  curve for  $1.05 < |\eta| < 1.7$



(d) ID resolution  $p_T$  curve for  $2.0 < |\eta| < 2.5$

Figure 5: Resolution curve on the curvature,  $\sigma(1/p_T)$ , from the fitted parameter values of the ID in collision data and simulation as a function of the muon  $p_T$  for the different  $|\eta|$  regions. The solid blue line shows measurements on data and is continued as dashed line for the extrapolation to  $p_T$  ranges not accessible in this analysis. The shaded band represents the sum in quadrature of the statistical and systematic uncertainties.

Source	$\eta$ region	MS		ID	
		$\Delta p_T^{MS}$ (%)	$\Delta p_T^{MS}$ ( $\text{TeV}^{-1}$ )	$\Delta p_T^{ID}$ (%)	$\Delta p_T^{ID}$ ( $\text{TeV}^{-1}$ )
ID mult. scattering	barrel	$\pm 0.041$	$\pm 0.006$	0.51 (fixed)	$\pm 0.008$
	transition	$\pm 0.00$	$\pm 0.057$	0.83 (fixed)	$\pm 0.000$
	end-caps	$\pm 0.05$	$\pm 0.009$	1.09 (fixed)	$\pm 0.013$
	CSC/no TRT	$\pm 0.22$	$\pm 0.16$	2.20 (fixed)	$\pm 0.0002$
MS alignment ( $1.05 <  \eta  < 1.2$ )	transition	+0.8	-0.14	-0.1	+0.05

Table 4: Systematic uncertainty on the correction parameters, divided by source.  $\Delta p_T^{ID}$  indicated as fixed are set to the value in the table, corresponding to the Monte Carlo value of  $\Delta p_T^{ID} + 1\sigma$ , following the procedure described in Section 5.7.

are only available for the MS barrel region and show a good agreement with the presented results for  $p_T$  larger than 20 GeV. At lower transverse momenta the cosmic ray results are biased by the fluctuations in the muon energy loss. The associated systematic uncertainty is of the same order as the disagreement between the cosmic ray and the collision results in Figure 4.

### 5.9 Correction formula for combined muons

The combined muon momentum measurement is determined by the relative weights of the ID and MS momentum measurements in the track fit. Due to the large amount of calorimeter material between ID and MS, the two measurements can be treated as uncorrelated. Therefore, starting from the corrected ID and MS  $p_T$  measurements in Monte Carlo, we can correct the combined muon  $p_T(CB)$  in the simulation and obtain a new measurement,  $p_T'(CB)$ . The new Monte Carlo measurement is the linear combination of the MS and ID contributions, weighted by the MS and ID resolutions:

$$p_T'(CB) = p_T(CB) \left[ 1 + \frac{\frac{\Delta p_T(MS)}{\sigma(MS)}}{\frac{\Delta p_T(ID)}{\sigma(ID)}} \right]. \quad (12)$$

where  $\Delta(MS, ID)$  is the overall correction to the simulated MS or ID  $p_T$ , from Equations 7 and 9; and  $\sigma(MS, ID)$  are the values for the resolution at that  $p_T(MS, ID)$ , taken from Table 3.

The results of the correction of the Monte Carlo simulation for the MS, ID and combined momentum measurement, compared with data for the di-muon invariant mass in the Z region are shown in the Appendix.

## 6 Conclusions

A determination of the muon momentum resolution is presented for the full integrated luminosity of  $40 \text{ pb}^{-1}$   $p\text{-}p$  collision data collected in 2010 with the ATLAS detector. Different physics channels have been used to evaluate the resolution as a function of the muon  $p_T$  and  $\eta$ , for both the muon spectrometer and the inner detector. Combining all the information, the momentum scale and resolution were measured on the experimental data and compared to simulation. A correction function is presented which allows the muon momentum resolution in simulation to model closely the one in data over a wide range of momenta.

The results show that the expected resolution on simulation is not yet fully achieved with the use of preliminary alignment and calibration constants in the first-pass reconstruction. Subsequent analysis of the muon momentum resolution indicates that the resolution is improved when more detailed alignment and calibration corrections are made.

## References

- [1] ATLAS Collaboration, *The ATLAS Experiment at the CERN Large Hadron Collider*, **JINST** **3** (2008) S08003.
- [2] ATLAS Collaboration, *Determination of the muon reconstruction efficiency in ATLAS at the Z resonance in  $p\text{-}p$  collisions at  $\sqrt{s} = 7 \text{ TeV}$* , ATLAS-CONF-2011-008 (2011).
- [3] ATLAS Collaboration, *Commissioning of the ATLAS Muon Spectrometer with Cosmic Rays*, **Eur. Phys. J. C** **70** (2010) 875.
- [4] ATLAS Collaboration, *The ATLAS Inner Detector commissioning and calibration*, **Eur. Phys. J. C** **70** (2010) 787.
- [5] ATLAS Collaboration, *Performance of the ATLAS Muon Trigger in  $p\text{-}p$  collisions at  $\sqrt{s} = 7 \text{ TeV}$* , ATLAS-CONF-2010-095 (2010).
- [6] T. Sjöstrand, S. Mrenna, and P. Skands, *PYTHIA 6.4 Physics and Manual*, **JHEP** **05** (2006) 026.
- [7] ATLAS Collaboration, *The ATLAS Simulation Infrastructure*, **Eur. Phys. J. C** **70** (2010) 823.
- [8] GEANT-4 Collaboration, S. Agostinelli et al., *Geant4: A simulation toolkit*, **Nucl. Instrum. Meth. A** **506** (2003).
- [9] ATLAS Collaboration, *Studies of the performance of the ATLAS detector using cosmic-ray muons*, acc. by **Eur. Phys. J.** (2011), arXiv:1011.6665 [physics.ins-det].
- [10] ATLAS Collaboration, *Measurement of the  $W \rightarrow \ell\nu$  and  $Z/\gamma^* \rightarrow \ell\ell$  production cross sections in proton-proton collisions at  $\sqrt{s} = 7 \text{ TeV}$  with the ATLAS detector*, **JHEP** **12** (2010) 060.
- [11] R. K. Ellis, W. J. Stirling, and B. R. Webber, *QCD and Collider Physics*, Cambridge University Press, Cambridge, UK, 1996.
- [12] ATLAS Collaboration, *Alignment Performance of the ATLAS Inner Detector Tracking System in 7 TeV proton-proton collisions at the LHC*, ATLAS-CONF-2010-067 (2010).
- [13] ATLAS Collaboration, *Alignment of the ATLAS Inner Detector Tracking System with 2010 LHC proton-proton collisions at  $\sqrt{s} = 7 \text{ TeV}$* , ATLAS-CONF-2011-012 (2011).
- [14] Particle Data Group Collaboration, K. Nakamura et al., *Review of Particle Properties*, **J. Phys. G** **37** (2010) 075021.
- [15] ATLAS Collaboration, *Study of the Material Budget in the ATLAS Inner Detector with  $K_s^0$  decays in collision data at  $\sqrt{s} = 900 \text{ GeV}$* , ATLAS-CONF-2010-019 (2010).
- [16] ATLAS Collaboration,  *$J/\psi$  Performance of the ATLAS Inner Detector*, ATLAS-CONF-2010-078 (2010).

- [17] ATLAS Collaboration, *Tracking Studies for b-tagging with 7 TeV Collision Data with the ATLAS Detector*, ATLAS-CONF-2010-070 (2010) .

## Appendix

### Validation of the simulation smearing

To indicate the goodness of the simulation corrections provided in Section 5, Figure 6 shows the distribution of the di-muon invariant mass in the Z region after applying the corrections. The comparison displays good agreement between data and Monte Carlo simulation.

### In perspective: first results with reprocessed data

In this note the muon resolution was measured in the 2010 data processed with the first-pass ATLAS reconstruction, using the preliminary calibration and alignment constants for both ID and MS detectors. The reprocessing of the whole 2010 dataset completed lately indicates that, making use of more refined knowledge of the alignment, calibration and magnetic field layout, a better performance and a more satisfying agreement with expectations is achieved. To illustrate the subsequent improvements, Figure 7 shows the reconstructed di-muon invariant mass around the Z pole, comparing combined muon tracks in first-pass reconstruction and reprocessing. The better agreement between data and simulation is mainly the result of the improved alignment. Further improvements are expected for the 2011 data taking due to additional refinements of the detector calibration and alignment.

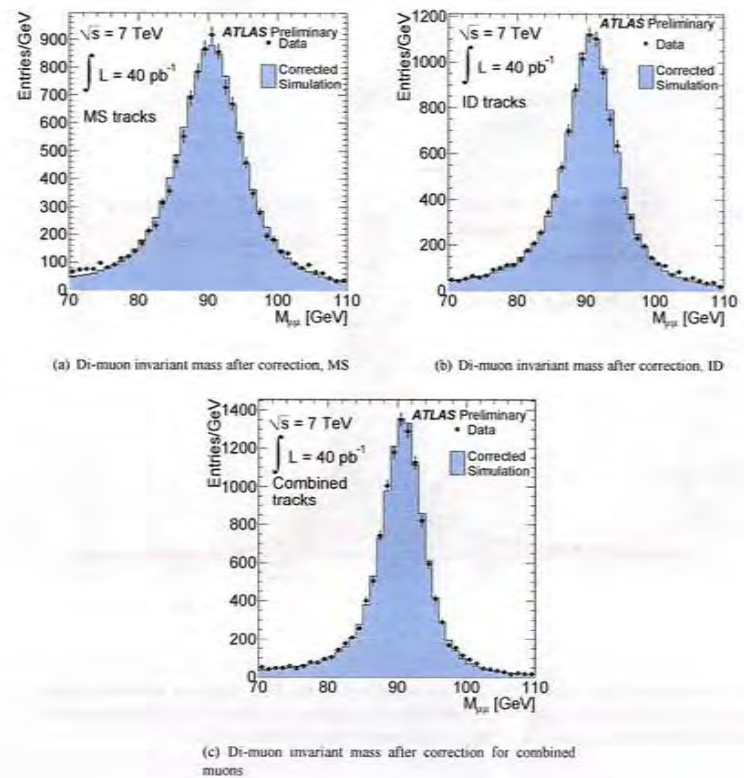


Figure 6: Di-muon invariant mass comparison in the Z boson mass range between collision data (dots) and simulation (full histogram), after correcting the simulated muon  $p_T$  by the parameters derived in this study. The distributions are integrated over the full range of  $\eta$ . From top left to bottom: MS, ID and combined measurements are shown.

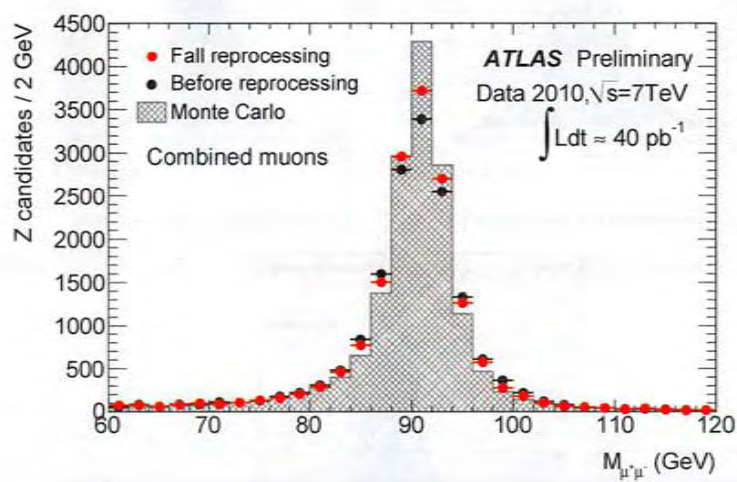


Figure 7: Di-muon invariant mass in the  $Z$  boson mass region, for data processed with the prompt reconstructions (black dots), the Fall 2010 reprocessing (red dots) and simulation (grey full histogram). Combined measurements are shown. The integrated luminosity corresponds to  $40\text{pb}^{-1}$ .

Eff in small  $p_T$  region OBSOLETE



## ATLAS NOTE

ATLAS-CONF-2011-021

March 11, 2011



### A measurement of the ATLAS muon reconstruction and trigger efficiency using $J/\psi$ decays

The ATLAS collaboration

#### Abstract

We present a measurement of the ATLAS muon reconstruction and trigger efficiencies using decay muons from the  $J/\psi$  resonance. The measurement is based on the “tag and probe” method and uses a sample of  $p$ - $p$  collisions at a center-of-mass energy of  $\sqrt{s} = 7$  TeV, corresponding to an integrated luminosity of  $3.1 \text{ pb}^{-1}$ .

To be submitted to *next conference*

## 1 Introduction

This note describes a measurement of the muon identification efficiency in the first-pass reconstruction of ATLAS data and the trigger efficiency of the ATLAS detector for muons with low transverse momentum,  $p_T$ . The efficiencies were determined using the so-called “tag and probe” method at the  $J/\psi$  resonance. In this method muon pairs are selected by requiring a well reconstructed muon, the “tag”, and an inner detector (ID) track, the “probe”, consistent with coming from a  $J/\psi \rightarrow \mu^+ \mu^-$  decay. In this way the “probes” are selected independently of the ATLAS muon spectrometer (MS) and can be used to measure the efficiency for reconstructing a muon based on the MS. The reconstruction efficiency could be measured with this method up to  $p_T = 12$  GeV. With additional requirements on the energy deposit in the calorimeters associated to the probe tracks, the background could be reduced significantly and the measurement could be extended to  $p_T = 20$  GeV.

This study was performed with a sample of  $p$ - $p$  collisions at  $\sqrt{s} = 7$  TeV, collected in the period April-August 2010, corresponding to an integrated luminosity of  $3.1 \text{ pb}^{-1}$ . The efficiencies presented in this note are currently used in the measurement of the  $J/\psi$  production cross section [1] based on the same data sample.

A study of the muon efficiency at larger  $p_T$ , exploiting the  $Z$  resonance is reported in [2]. Early results on the performance of the ATLAS muon system have been presented in [3].

## 2 The ATLAS Detector

A detailed description of the ATLAS Detector can be found elsewhere [4]. Muons are independently measured in the ID and in the MS.

The ID measures tracks up to a pseudorapidity  $|\eta| = 2.5$  exploiting three types of detectors operated in a solenoidal magnetic field of 2 T: a silicon pixel detector closest to the interaction point, a silicon strip detector (SCT) surrounding the pixel detector, and a transition radiation straw tube tracker (TRT) as the outermost part of the inner detector.

The MS consists of large air-core superconducting toroidal magnets, providing a field of approximately 0.5 T. The deflection of the muons in the magnetic field is measured by three layers of precision drift tube (MDT) chambers for  $|\eta| < 2.0$  and, for  $2.0 < |\eta| < 2.7$ , by two layers of MDT chambers in combination with cathode strip chambers (CSC) as the inner layer.

Three layers of resistive plate chambers (RPC) in the barrel ( $|\eta| < 1.05$ ) and three layers of thin gap chambers (TGC) in the end-caps ( $1.05 < |\eta| < 2.4$ ) provide the muon trigger and also measure the muon trajectory in the non-bending plane of the spectrometer magnets.

The ATLAS detector has a three-level trigger system: level 1 (L1), level 2 (L2), and the Event Filter (EF). The MS provides a L1 hardware muon trigger which is based on hit coincidences within different RPC or TGC detector layers inside programmed geometrical windows which define the muon  $p_T$ . The L2 and EF muon triggers perform a software validation of the L1 muon trigger using additional information from MDT and CSC chambers and from the ID, applying a further  $p_T$  selection.

## 3 Classification of reconstructed muons

Three kinds of reconstructed muons are considered in this note:

- **Combined (CB)** muons, obtained from the combination of tracks reconstructed independently in the MS (stand-alone muons) and in the ID;
- **Segment tagged (ST)** muons, obtained from ID tracks that, extrapolated to the MS, are associated with track segments in the muon chambers.

- **Calorimeter tagged (CT) muons**, obtained by matching ID tracks with an energy deposition in the calorimeters compatible with a minimum ionizing particle. These are used in place of ID tracks to reduce the background in the “tag and probe” method.

CB muons are the highest purity muon candidates. ST muons give additional efficiency as they can recover muons which did not cross enough precision chambers to allow an independent momentum measurement in the MS. Typical cases are low  $p_T$  muons that only reach the inner layer of precision chambers or less instrumented detector regions.

Two independent reconstruction chains, each implementing CB and ST muons, are used in ATLAS [5]: chain 1 (or Staco) and chain 2 (or MuId). This redundancy allows a cross check of the performances of the reconstruction algorithms and is particularly useful in the first phase of the LHC operation.

Efficiencies for four categories of reconstructed muons are presented in this note:

- **CB, chain 1**: CB muons from chain 1 with the  $\chi^2$  of the MS-ID combination lower than 150 for 5 degrees of freedom. In contrast to other studies [2], no cut on the relative momentum difference between the ID and the MS tracks was applied; the effect of this cut on the efficiency was found to be negligible in the low- $p_T$  region studied in this analysis;
- **CB + ST, chain 1**: all CB muons from chain 1 plus ST muons from chain 1 not associated to a CB muon from the same reconstruction chain;
- **CB, chain 2**: all CB muons from chain 2;
- **CB + ST, chain 2**: all candidates belonging to the previous category plus ST muons not associated to a CB muon from the same reconstruction chain. The algorithm used in this analysis for chain 2 ST muon finding differs from that used in other studies [2] since it is optimised for muon identification at low  $p_T$ .

#### 4 Monte Carlo samples and expectations

A Monte Carlo (MC) sample of five million prompt  $J/\psi$  events with subsequent decay into muons was generated with PYTHIA 6.4 [6] using the PYTHIA implementation of the colour-octet model. It was then passed through a detailed simulation of the ATLAS detector [7] based on GEANT4 [8, 9] and reconstructed with the same reconstruction programs as real data.

The reconstruction efficiencies obtained from analysis of the Monte Carlo sample are shown in Figure 1 as a function of  $p_T$  and  $\eta$  for CB and CB+ST muons from chain 1. The most discernible features are the areas of lower efficiency at fixed  $\eta$  that result from the crack in the MS at  $\eta \approx 0$  for the passage of services and from the barrel/end-cap transition region at  $|\eta| \approx 1.2$  where the chamber configuration and the magnetic field are rather non-uniform. Another clearly visible feature of Figure 1 is that, for  $|\eta| < 2.0$ , the CB+ST muons start to be efficient at lower  $p_T$  with respect to CB muons since they include muons reaching only the inner layer of muon chambers in the MS. For  $|\eta| > 2.0$  the CB and CB+ST efficiency are very similar since cases with only one segment in the CSC chambers, which correspond to the inner layer of precision chambers in this region, are not considered for ST muons. This motivates the binning used in this note for the reconstruction efficiency determination. The data are separated into five pseudorapidity intervals according to the different MS regions:

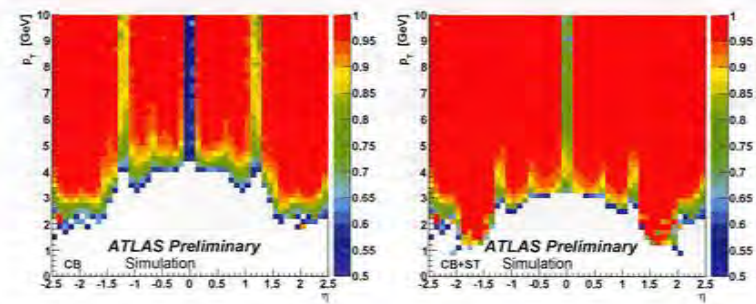


Figure 1: The muon reconstruction efficiency from Monte Carlo for CB (left) and CB+ST (right) muons of the reconstruction chain 1. The efficiency is shown as a function of  $\eta$  and  $p_T$  for efficiency values above 0.5.

- $|\eta| < 0.1$ , the  $\eta = 0$  crack region;
- $0.1 < |\eta| < 1.1$ , the barrel region;
- $1.1 < |\eta| < 1.3$ , the transition region between the barrel and the end-cap;
- $1.3 < |\eta| < 2.0$ , the end-cap region;
- $2.0 < |\eta| < 2.5$ , the forward region.

#### 5 Selection of Tag and Probe pairs

Events were selected online with a single-muon trigger chain. At level 1 the events were taken by the lowest possible L1 trigger threshold, “L1\\_MU0”. At L2 and at the EF, a CB muon was required, with minimum- $p_T$  thresholds of 4, 6 or 10 GeV. As the luminosity increased during the data taking, the two lower  $p_T$  thresholds were prescaled. Approximately 35% of the integrated luminosity used in this analysis was collected with the lowest unrescaled threshold of  $p_T > 4$  GeV, 50% with  $p_T > 6$  GeV and 15% with  $p_T > 10$  GeV. For the first part of the considered period, corresponding to  $\approx 1.5\%$  of the integrated luminosity, the events were selected online using the L1 trigger only.

Good collision events were selected by requiring at least one reconstructed primary vertex with three or more associated good ID tracks, where a good ID track was defined by having:

- $\geq 1$  pixel hits;
- $\geq 6$  SCT hits;
- for  $|\eta| < 1.9$ : total number of TRT hits  $n_{\text{TRT}}^{\text{tot}} > 5$ ;
- for  $n_{\text{TRT}}^{\text{tot}} > 5$ : fraction of outlier TRT hits  $n_{\text{TRT}}^{\text{out}}/n_{\text{TRT}}^{\text{tot}} < 90\%$ . TRT outliers are measurements associated to the ID track that either appear in a drift tube not crossed by the track or belong to a set of TRT measurements that failed to form a smooth trajectory together with the Pixel and SCT measurements.

A tag muon was defined to have:

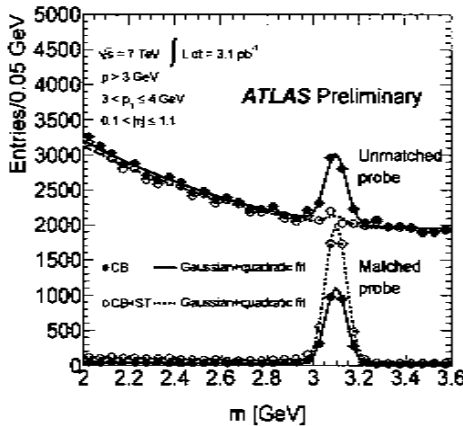


Figure 2: Invariant mass of the unmatched (upper points) and matched (lower points) tag-probe pairs for CB (filled circles) and CB+ST (empty circles) muons of chain 1 for  $0.1 < |\eta| < 1.1$  and  $3 < p_T < 4$  GeV. The curves show the fits described in the text.

- a CB muon associated to a good ID track defined as above;
- $p_T > 4$  GeV,  $|\eta| < 2.5$ ;
- distance of closest approach to the primary vertex in the transverse plane  $|d_0| < 0.3$  mm and in the longitudinal coordinate  $|z_0| < 1.5$  mm. Distance of closest approach significances  $|z_0|/\sigma(d_0) < 3$  and  $|z_0|/\sigma(z_0) < 3$ ;
- the tag muon is consistent with being the muon that fired the trigger. This was checked by requiring that the reconstructed muon is consistent with passing through the  $\eta\phi$  region in the MS (the “region of interest” [4]) corresponding to the trigger muon.

Probes were selected as any good ID track, as defined above, with

- $p > 3$  GeV,  $|\eta| < 2.5$ ;
- the probe and the tag track can be refitted to a common vertex with  $\chi^2/\text{ndof} < 6$ ;
- distance between tag and probe  $\Delta R = \sqrt{(\Delta\phi)^2 + (\Delta\eta)^2} < 3.5$ .

All possible tag-probe combinations are used in the analysis. The above selection results in  $2.6 \times 10^6$  tag-probe pairs in the invariant mass range  $2.0 < m < 3.6$  GeV, including 276 cases in which the same probe enters in two different pairs.

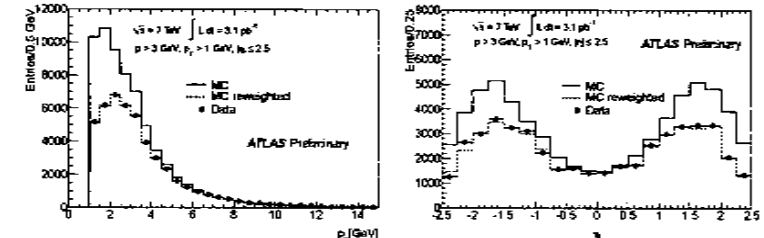


Figure 3: Distribution of probes, after background subtraction, in  $p_T$  (left) and  $\eta$  (right), for data, MC, and reweighted MC. Tags were selected using chain 1.

## 6 Efficiency measurement

To measure the reconstruction efficiency of a particular algorithm, the tag-probe pairs were divided into two categories, those in which the probe was reconstructed as a muon by the algorithm (matched) and those in which the probe was not reconstructed as muon (unmatched). Figure 2 shows the invariant mass distribution for pairs with the probe in the transverse momentum and pseudorapidity region  $3 < p_T < 4$  GeV and  $0.1 < |\eta| < 1.1$ . The mass distribution is shown separately for probes classified as matched and unmatched with respect to CB and to CB+ST chain 1 muons. The distribution of matched probes shows a clear peak at the  $J/\psi$  mass with low background while the distribution of unmatched probes has a peak on top of a large background.

The reconstruction efficiency was obtained as the ratio of the number of events in the peak of the matched distribution to the total number of events in the two mass peaks. A  $\chi^2$  fit was performed simultaneously on the two distributions, with the following parametrizations:

$$\begin{aligned} \text{Matched } f_U(m) &= N_{\text{tot}} \epsilon G(m; \mu_M, \sigma_M) + P_M(m) \\ \text{Unmatched } f_U(m) &= N_{\text{tot}} (1 - \epsilon) G(m; \mu_U, \sigma_U) + P_U(m) \end{aligned}$$

where  $G(m; \mu, \sigma)$  is a Gaussian distribution with mean  $\mu$  and standard deviation  $\sigma$ , used to describe the signal peak, and  $P$  is a polynomial function used to describe the background. The main parameters extracted from the fit are the number of tag-probe pairs in the signal peak  $N_{\text{tot}}$  and the reconstruction efficiency  $\epsilon$ . The mean and width of the two Gaussian distributions were forced to be the same and second-order polynomials were used for the background.

The MC sample was used to compare the efficiencies obtained with the method described above to the true efficiency, defined as the probability for a true muon matched to a reconstructed ID track to be also reconstructed as a CB or CB+ST muon. The differences were found to be always smaller than 1%. It should be noted that this check does not test the background subtraction procedure since the background is almost absent in the  $J/\psi$  MC sample.

Figure 3 shows the number of probes after background subtraction as a function of  $p_T$  and  $\eta$  for data and MC. The MC distribution differs significantly from the data, being more populated at low  $p_T$  and large  $|\eta|$ . This difference is ascribed to several origins: the lack of non-prompt  $J/\psi$  production in the MC sample (i.e.  $J/\psi$ s from beauty decays), possible deficiencies of the physics model, and a distortion caused by the trigger requirements applied on the tag muon in the data but not in the MC.

For a precise comparison of the efficiencies calculated in data and MC it is important that the underlying probe distributions agree. For this reason the MC tag-probe pairs have been reweighted according to the data/MC ratio calculated in small two-dimensional bins in  $\eta$  and  $p_T$ , using a simple sideband subtraction to extract the  $J/\psi$  yield for the data. The probe distributions after reweighting are also shown in Figure 3.

## 7 Systematic checks and uncertainties

A number of checks have been performed to study the dependence of the results on analysis details and assumptions (the abbreviations in parentheses are used later in Table 1):

1. Signal shapes (s1): the mean and the widths of the two Gaussian functions in the fit were allowed to vary independently.
2. Background shape (s2): a linear background function was used in the fit, instead of the quadratic one, and the fit was performed in a reduced mass range of 2.7 – 3.5 GeV.
3. Alternative fit (s3): a simultaneous fit to the matched and the total (matched + unmatched) distributions, rather than to matched and unmatched, was used to enhance the fit stability.
4. Trigger matching: the bias introduced by the trigger was studied by applying a different criterion, based on a  $\Delta R$  cut, to associate the tag muon to the trigger muon. The effect was negligible.
5. Other signal extraction methods: to reduce the dependence on the functional form used in the fit, the efficiency was also calculated using sideband subtraction. The analysis was also repeated using the sPlot [10] technique. No significant variation of the efficiency was observed.
6. Dependence on probe selection: the dependence on the probe selection was tested by reducing the background by requiring an energy deposit in the calorimeter compatible with a muon. No significant variation of the efficiency was observed. Further studies with a calorimeter-based probe selection are presented in Section 10.
7. Dependence on the impact parameter cuts: the dependence on the fraction of prompt and non-prompt  $J/\psi$  in the sample was checked by loosening the cuts on the track  $d_0$  and  $z_0$  in the selection of the tag muon. No significant variation of the efficiency was observed.
8. Period dependence: the data sample was split in two different periods; the results were compatible within the statistical uncertainties.

The maximal positive and negative variations among checks 1 to 3 were considered as systematic uncertainties and added in quadrature to the statistical uncertainty to obtain the total upper and lower uncertainties.

The efficiency measured in a given bin of  $p_T$  and  $\eta$  depends on the underlying probe distribution within that bin. Therefore the measured efficiency applies only to a sample of muons with the same  $p_T$  and  $\eta$  distribution as the probes. In addition to the sources of systematic error described above, the uncertainty from the underlying probe distribution was included when comparing the result with MC (s4). This uncertainty was evaluated by using different procedures to reweight the MC probe distribution. The weights applied to the MC were calculated using alternative methods to extract the  $J/\psi$  signal (the same fit used for the efficiency measurement or a simpler sideband subtraction) and using different binnings in  $p_T$  and  $\eta$ . The variations were in general within 2%.

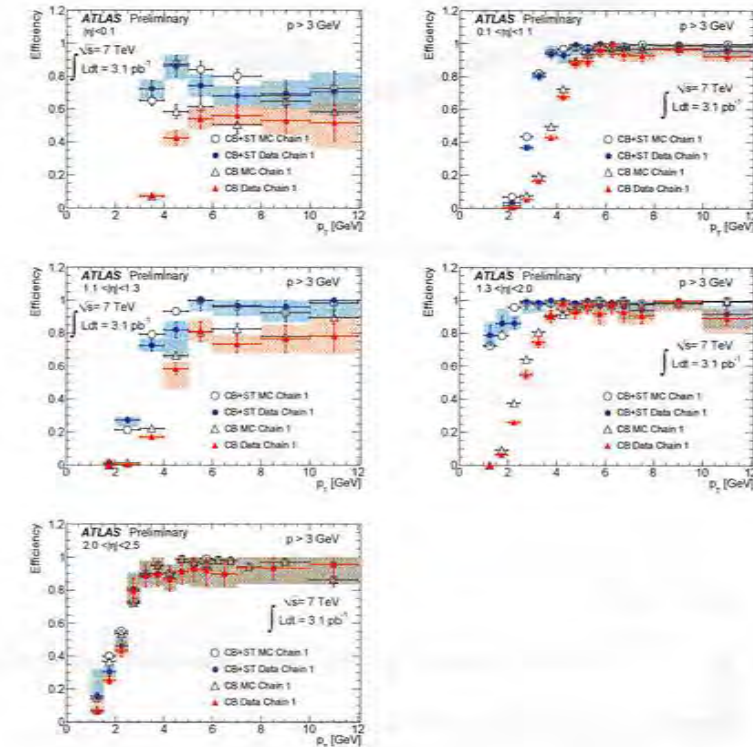


Figure 4: Efficiency for CB and CB+ST muons of chain 1 as a function of  $p_T$  for five bins in  $|\eta|$  for data and MC. The error bars represent the statistical uncertainties while the band around the data points represents the statistical and systematic uncertainties added in quadrature.

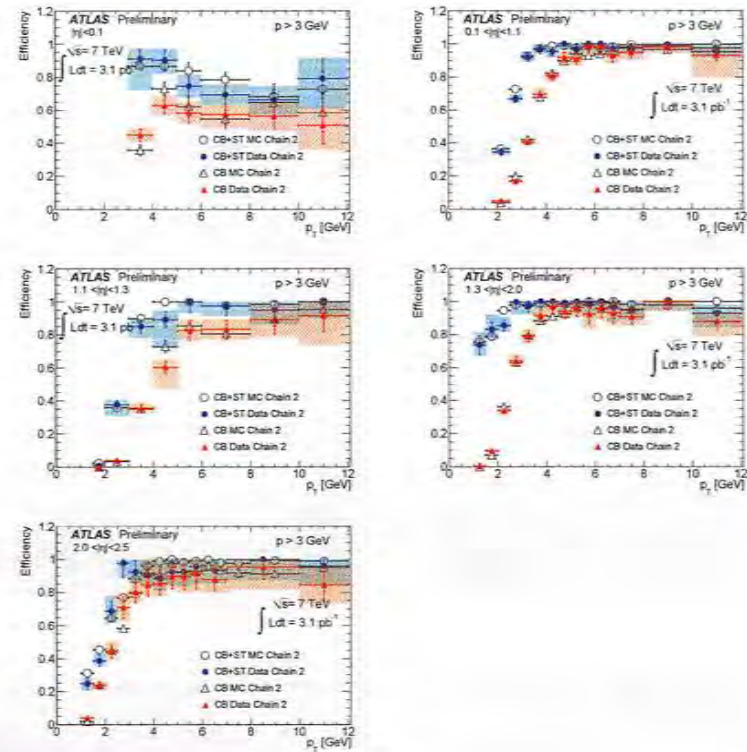


Figure 5: Efficiency for CB and CB+ST muons of chain 2 as a function of  $p_T$  for five bins in  $|\eta|$  for data and MC. The error bars represent the statistical uncertainties while the band around the data points represents the statistical and systematic uncertainties added in quadrature.

## 8 Reconstruction efficiency with respect to ID tracks

Figure 4 shows the efficiency for chain 1 with respect to ID tracks with  $p > 3$  GeV as a function of the probe  $p_T$  for the five bins in  $|\eta|$ . As expected, the efficiency for CB+ST muons is larger than for CB muons at low  $p_T$  and in the  $\eta$  ranges corresponding to the less instrumented regions ( $|\eta| < 0.1$  and  $1.1 < |\eta| < 1.3$ ). In the forward region ( $2.0 < |\eta| < 2.5$ ) CB and CB+ST have similar efficiencies. The requirement  $p > 3$  GeV only affects the two bins with  $p_T < 3$  GeV in the region  $0.1 < |\eta| < 1.1$  and the bin with  $p_T < 2$  GeV in the region  $1.1 < |\eta| < 2.0$ . The efficiency plateau is reached for  $p_T > 5$  GeV for CB muons and  $p_T > 3.5$  GeV for CB+ST muons in the barrel region, while it starts earlier in the end-caps. In the range  $|\eta| < 0.1$  the efficiency is larger for  $p_T$  in the range  $4 - 5$  GeV than at larger  $p_T$  since low- $p_T$  tracks have more chances to be bent away from the  $\eta = 0$  crack. In the range  $1.3 < |\eta| < 2.0$ , the efficiency for CB+ST muons is above 70% for  $p_T > 1$  GeV. The simulation describes the data well.

Figure 5 shows the efficiency for chain 2. Also in this case the agreement between data and MC is very good.

The Data/MC scale factors, defined as s.f. =  $\epsilon_{\text{data}}/\epsilon_{\text{MC}}$ , where  $\epsilon_{\text{data}}$  and  $\epsilon_{\text{MC}}$  are the measured efficiencies for data and MC, are given in Table I for the plateau region  $p_T > 6$  GeV.

## 9 Charge dependence

Due to the toroidal magnetic field of the ATLAS MS, muons with positive (negative) charge are bent towards larger (smaller)  $\eta$ . This effect introduces a charge dependence of the muon reconstruction and trigger efficiencies, which is particularly relevant at very large  $|\eta|$ , where muons of one charge may be bent outside the detector geometrical acceptance, and at low  $p_T$ , where muons of one charge may be bent back before reaching the middle or outer MS stations.

As an illustration, Figure 6 shows the measured efficiency as a function of  $\eta$  for CB muons of chain 1. The charge dependence of the efficiency is reversed between the two sides of ATLAS: the efficiency for positively charged muons is larger for  $\eta < 0$  than for  $\eta > 0$ , since at  $\eta < 0$  ( $> 0$ ) they are bent away from (towards) the beamline, while the opposite holds for negatively charged muons. Therefore, as long as the ATLAS detector is symmetric with respect to  $\eta = 0$ , the efficiency depends only on  $q \times \eta$ , where  $q$  is the muon charge. Figures 7 (chain 1) and 8 (chain 2) show the reconstruction efficiency as a function of  $q \times \eta$  for two  $p_T$  regions:  $1 < p_T < 6$  GeV and  $p_T > 6$  GeV. In the first region a strong asymmetry between positive and negative  $q \times \eta$  is observed for CB muons. For CB+ST muons the asymmetry is lower since in this case it is sufficient to find a segment in the inner MS stations, which are located at a position where the muon trajectory has not yet been significantly bent by the toroidal magnetic field. Most of the asymmetry for CB+ST muons is in the largest  $|\eta|$  bin. The  $q \times \eta$  dependence is well reproduced by the simulation. No significant asymmetry is observed in the high- $p_T$  region.

## 10 Reconstruction efficiency with respect to calorimeter-tagged muons

At large  $p_T$  the uncertainty of the reconstruction efficiency measurement described above is dominated by the statistical contribution from the background in the unmatched sample. The background can be significantly suppressed using CT muons as probes instead of ID tracks. The CT efficiency for muons from  $J/\psi$  decays is around 90%. The same analysis as described above was repeated with the difference that the probe was required to be a CT muon. This allows a precise measurement of the probability that a CT muon is also reconstructed as a CB or CB+ST muon. A cut of  $p_T > 4$  GeV was applied by the CT muon algorithm, as the background contamination of CT muons increases rapidly at lower  $p_T$ . The mass distributions for tag-probe pairs with matched and unmatched probes are shown in Figure 9. As the background is small and linear to a good approximation, a simple sideband subtraction was used to

	$ \eta $ range	s.f.	$\pm$ stat.	+syst..	-syst..	s1	s2	s3	s4
Chain 1 CB	0.0 : 0.1	1.022	0.084	0.025	-0.042	-0.035	0.004	-0.027	$\pm 0.024$
	0.1 : 1.1	0.973	0.018	0.022	-0.001	0.009	0.016	0.021	$\pm 0.001$
	1.1 : 1.3	0.909	0.050	0.022	-0.007	0.008	0.021	0.001	$\pm 0.007$
	1.3 : 2.0	0.951	0.023	0.037	-0.075	-0.075	0.037	-0.025	$\pm 0.001$
	2.0 : 2.5	0.976	0.056	0.040	-0.013	-0.012	0.040	0.008	$\pm 0.003$
Chain 1 CB+ST	0.0 : 0.1	0.958	0.155	0.009	-0.019	-0.018	0.004	-0.005	$\pm 0.008$
	0.1 : 1.1	0.989	0.017	0.015	-0.001	<10 <sup>-3</sup>	0.015	0.015	$\pm 0.001$
	1.1 : 1.3	1.024	0.046	0.015	-0.020	-0.015	0.007	0.005	$\pm 0.013$
	1.3 : 2.0	0.970	0.024	0.036	-0.066	-0.065	0.035	-0.023	$\pm 0.006$
	2.0 : 2.5	0.976	0.050	0.040	-0.013	-0.012	0.040	0.008	$\pm 0.003$
Chain 2 CB	0.0 : 0.1	0.930	0.080	0.059	-0.073	-0.042	0.007	-0.034	$\pm 0.059$
	0.1 : 1.1	0.982	0.018	0.024	-0.002	0.008	0.017	0.024	$\pm 0.002$
	1.1 : 1.3	0.969	0.049	0.021	-0.020	-0.020	0.021	-0.004	$\pm 0.001$
	1.3 : 2.0	0.962	0.024	0.036	-0.072	-0.072	0.036	-0.022	$\pm 0.004$
	2.0 : 2.5	0.963	0.053	0.050	-0.029	-0.027	0.050	-0.023	$\pm 0.008$
Chain 2 CB+ST	0.0 : 0.1	0.922	0.057	0.022	-0.023	-0.009	0.004	<10 <sup>-3</sup>	$\pm 0.021$
	0.1 : 1.1	0.992	0.017	0.012	<10 <sup>-3</sup>	<10 <sup>-3</sup>	0.012	0.012	<10 <sup>-3</sup>
	1.1 : 1.3	1.001	0.045	0.007	-0.012	-0.011	0.005	0.003	$\pm 0.005$
	1.3 : 2.0	0.972	0.023	0.028	-0.063	-0.063	0.028	-0.027	$\pm 0.003$
	2.0 : 2.5	0.996	0.050	0.015	-0.020	-0.012	0.015	-0.020	$\pm 0.003$

Table 1: Data/MC scale factors for  $p_T > 6$  GeV in different intervals of  $|\eta|$ . The table shows the scale factor (s.f.), the statistical uncertainty, the total positive and negative systematic uncertainties and the contributions to the systematic uncertainty from individual sources described in the text: signal shape (s1), background shape (s2), alternative fit (s3), and MC reweighting (s4).

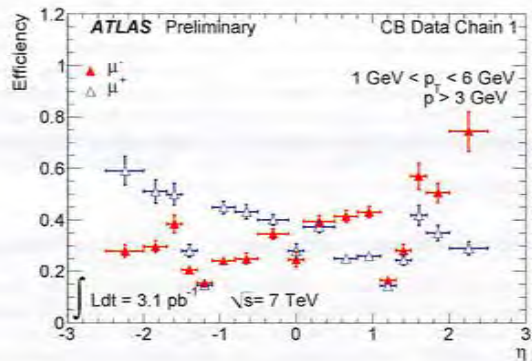


Figure 6: Efficiency for CB muons of chain 1 as a function of  $\eta$ , separately for  $\mu^+$  and  $\mu^-$ . Only statistical uncertainties are shown.

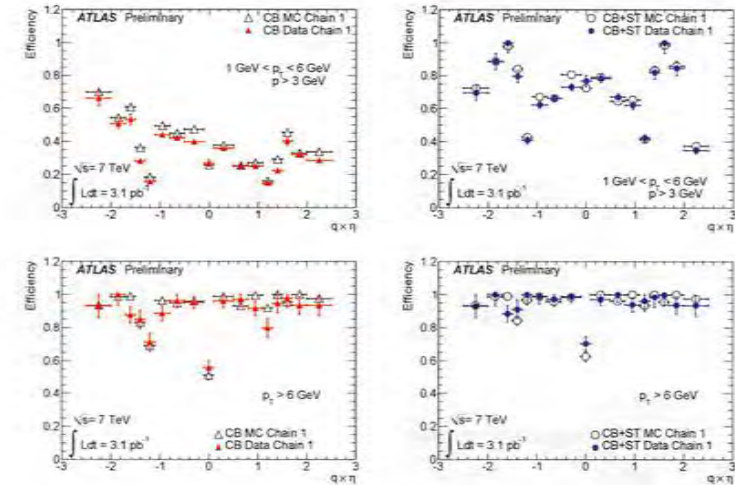


Figure 7: Efficiency for CB (left) and CB+ST (right) muons of chain 1 as a function of  $q \times \eta$  for data and MC. The upper plots are for the  $p_T$  range  $1 < p_T < 6 \text{ GeV}$ . The lower plots are for  $p_T > 6 \text{ GeV}$ . Only statistical uncertainties are shown.

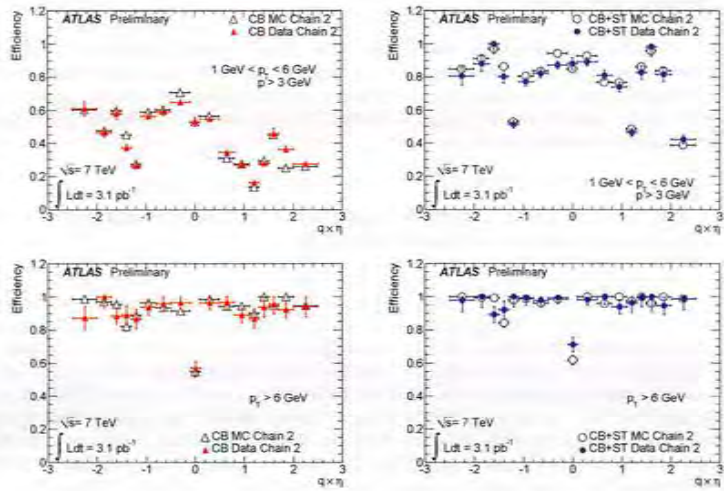


Figure 8: Efficiency for CB (left) and CB+ST (right) muons of chain 2 as a function of  $q \times \eta$  for data and MC. The upper plots are for the  $p_T$  range  $1 < p_T < 6$  GeV. The lower plots are for  $p_T > 6$  GeV. Only statistical uncertainties are shown.

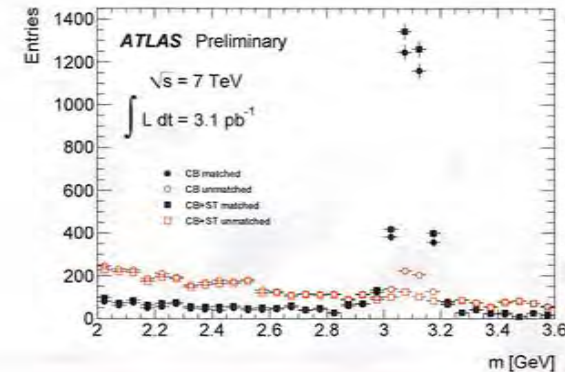


Figure 9: Invariant mass using calorimeter-tagged muons as probes for unmatched and matched tag-probe pairs for CB (filled circles) and CB+ST (empty circles) muons of chain 1 for  $0.1 < |\eta| < 1.1$  and  $p_T > 4$  GeV.

determine the signal yield using the mass range  $2.95 - 3.25$  GeV for the signal region,  $2.65 - 2.95$  GeV and  $3.25 - 3.55$  GeV for the sidebands. No reweighting of the MC probe distribution was needed since the probe distribution was reasonably described by MC.

The efficiency for CB muons with respect to CT muons is shown in Figures 10 and 11 and compared to the MC results. The following systematic uncertainties were considered:

1. Signal extraction: the signal region was widened to  $2.9 - 3.3$  GeV and the sidebands moved to  $2.5 - 2.9$  and  $3.3 - 3.7$  GeV;
2. Tag muon selection: the trigger matching criteria and the  $p_T$  cut on the tag muon were varied, producing negligible effects on the efficiency;
3. MC probe distribution: the  $\eta$  distribution was reweighted by varying by 33% the weight of muons in the end-caps, to allow for differences between data and MC similar to those observed in Figure 3. The effect on the plateau efficiency was  $\leq 0.1\%$ .

The effects of the above variations were added in quadrature to the statistical uncertainty to produce the total error bars.

At large  $p_T$  the efficiency reaches a plateau of  $\approx 94\%$  ( $99\%$ ) for CB (CB+ST) muons for both chains. Data and MC agree to within 2%. The data/MC scale factors are given in Table 2 for  $p_T > 6$  GeV and the full pseudorapidity range,  $|\eta| < 2.5$ . These scale factors are in agreement with those for the efficiencies calculated with respect to ID tracks presented in Table 1. The average scale factors obtained in the analysis of high- $p_T$  muons from  $Z \rightarrow \mu\mu$  decays [2] are also reported in Table 2, showing good agreement between the two analyses.

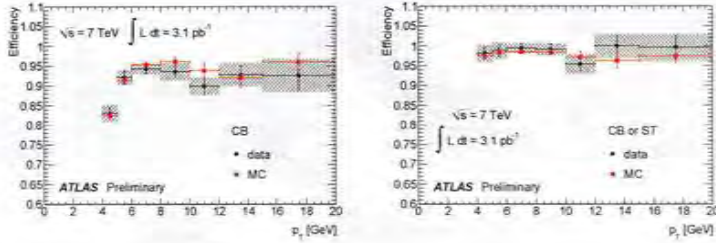


Figure 10: Efficiency of CB (left) and CB+ST (right) muons with respect to calorimeter-tagged muons for chain 1 as a function of  $p_T$  for the full range of  $\eta$ . Results for Data and MC are shown. The error bars represent the statistical uncertainties while the band around the data points represents the statistical and systematic uncertainties added in quadrature.

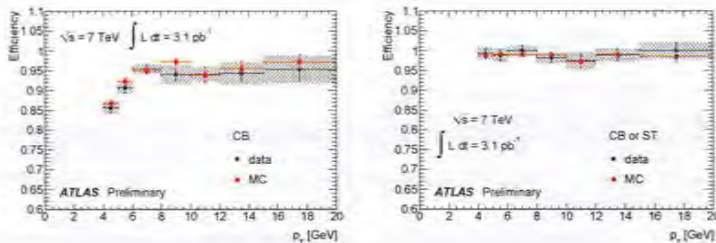


Figure 11: Efficiency of CB (left) and CB+ST (right) muons with respect to calorimeter-tagged muons for chain 2 as a function of  $p_T$  for the full range of  $\eta$ . Results for Data and MC are shown. The error bars represent the statistical uncertainties while the band around the data points represents the statistical and systematic uncertainties added in quadrature.

Algorithm	s.f.	$\pm$ stat.	$\pm$ syst.	s.f.@Z	$\pm$ stat.
chain 1	CB	0.980	0.007	0.9806	0.0024
	CB+ST	1.009	0.004	0.9990	0.0016
chain 2	CB	0.993	0.007	0.9918	0.0020
	CB+ST	1.011	0.003	1.0006	0.0015

Table 2: Scale factors (s.f.) for the efficiency with respect to calorimeter-tagged muons for the full pseudorapidity range  $|\eta| < 2.5$  and  $p_T > 6$  GeV. The last two columns show the scale factors obtained from the analysis of  $Z \rightarrow \mu\mu$  decays [2].

## 11 Trigger efficiency

The “tag and probe” method was also used to measure the trigger efficiency relative to reconstructed muons. The trigger efficiency measurement follows the same approach as the measurement of the reconstruction efficiency, with the main difference being that reconstructed muons are used as a probe. This study also uses the same sample and triggers used in the  $J/\psi$  cross section measurement [1]. Two kinds of trigger efficiencies have been measured:

- $\epsilon(L1 | rec)$ : the probability for a reconstructed muon to pass the level 1 trigger;
- $\epsilon(L2 \& EF | L1 \& rec)$ : the probability for a reconstructed muon accepted by the L1 trigger to pass a particular  $p_T$  threshold at level 2 and in the Event Filter.

Figure 12 shows  $\epsilon(L1 | rec)$  for the lowest L1 threshold (“L1\_MU0”) with respect to chain 1 muons for the regions covered by the RPC ( $|\eta| < 1.05$ ) and the TGC ( $1.05 < |\eta| < 2.4$ ) trigger chambers. The efficiency at plateau ( $p_T > 8$  GeV) is  $\approx 80\%$  (76%) for CB (CB+ST) muons in the barrel and  $\approx 95\%$  (93%) in the end-cap, in agreement with studies based on inclusive muon samples [11]. The lower efficiency in the barrel region is mainly due to the geometrical acceptance of the trigger systems that have inefficient regions corresponding to support structures of the ATLAS detector. The L1 efficiency for CB muons is higher than for CB+ST muons, in particular at low  $p_T$ . This is because the L1 trigger chambers are placed close to the second layer of MDT chambers in the MS. CB muons, that require segments in at least two MDT layers to be reconstructed, are typically made of muons that reach the middle stations, while ST muons, at low  $p_T$ , are typically made of muons reaching only the inner MDT stations, therefore missing the trigger chambers.

The efficiency  $\epsilon(L2 \& EF | L1 \& rec)$  is shown in Figure 13 for two  $p_T$  thresholds,  $p_T > 4$  GeV (“EF\_mu4”) and  $p_T > 6$  GeV (“EF\_mu6”). The efficiency above the nominal threshold is 90% or larger.

## 12 Conclusions

Muons from  $J/\psi$  decays have been used to measure the reconstruction and trigger efficiencies of the ATLAS detector for low- $p_T$  muons, using a data set corresponding to an integrated luminosity of  $3.1\text{pb}^{-1}$ .

The reconstruction efficiency is well described by the Monte Carlo simulation. For  $p_T > 6$  GeV the reconstruction efficiency is above 98% and the scale factor, defined as the ratio of data and MC efficiencies ranges from 0.98 to 1.01 depending on the particular type of reconstruction considered.

The efficiency was also measured for the level 1 trigger and for level 2 and event filter triggers used in the  $J/\psi$  cross section analysis [1]. The L1 trigger efficiencies, measured using CB reconstructed tracks, reach a plateau value of 80% in the barrel and 95% and endcap region for  $p_T > 8$  GeV. The L2 and EF efficiency, above the applied  $p_T$  thresholds, is above 90%.

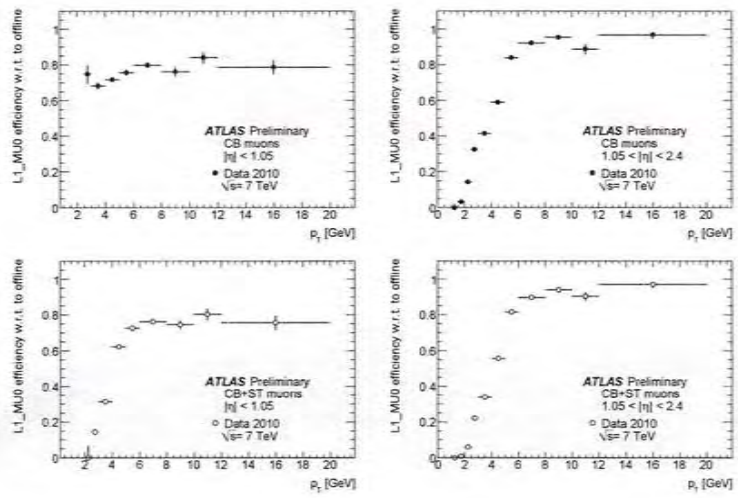


Figure 12: Efficiency  $\epsilon(L1 | rec)$  for the L1 trigger “L1\_MU0” with respect to reconstructed chain 1 muons, CB (upper plots) muons as a function of  $p_T$  for the trigger barrel (left) and end-cap (right) regions. The lower plots show the efficiencies for CB+ST muons.

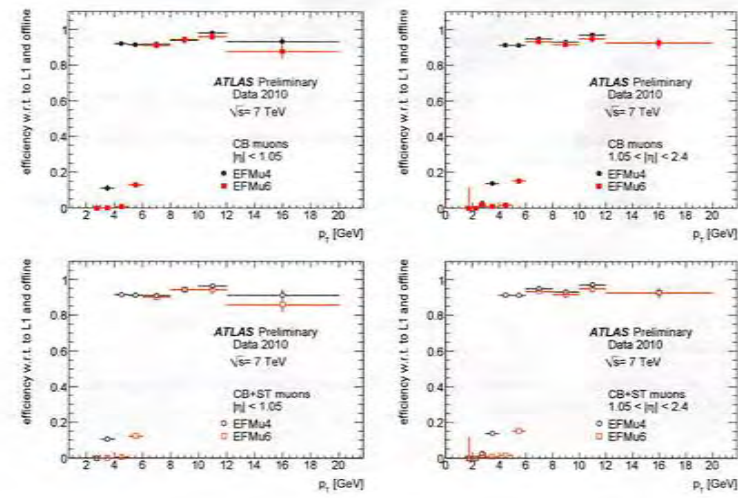


Figure 13: Efficiency  $\epsilon(L2 \& EF | L1 \& rec)$  for the L2 and Event Filter trigger  $p_T$  thresholds of 4 and 6 GeV with respect to reconstructed chain 1 CB (upper plots) and CB+ST (lower plots) muons that passed the L1 trigger.

## References

- [1] ATLAS Collaboration, *Measurement of the differential cross sections for the  $J/\psi \rightarrow \mu^+ \mu^-$  resonance and the non-prompt  $J/\psi$  cross section fraction with  $p\bar{p}$  collisions at  $\sqrt{s} = 7 \text{ TeV}$* , article in preparation (2011).
- [2] ATLAS Collaboration, *Determination of the muon reconstruction efficiency in ATLAS at the Z resonance in proton-proton collisions at  $\sqrt{s} = 7 \text{ TeV}$* , ATLAS-CONF-2011-008 (2011).
- [3] ATLAS Collaboration, *Muon Reconstruction Performance*, ATLAS-CONF-2010-064 (2010).
- [4] ATLAS Collaboration, G. Aad et al., *The ATLAS Experiment at the CERN Large Hadron Collider*, JINST 3 (2008) S08003.
- [5] ATLAS Collaboration, *Muon Performance in Minimum Bias  $p\bar{p}$  Collision Data at  $\sqrt{s} = 7 \text{ TeV}$  with ATLAS*, ATLAS-CONF-2010-036 (2010).
- [6] T. Sjostrand, S. Mrenna, and P. Z. Skands, *PYTHIA 6.4 Physics and Manual*, JHEP 05 (2006) 026.
- [7] ATLAS Collaboration, G. Aad et al., *The ATLAS Simulation Infrastructure*, Eur. Phys. J. C70 (2010) 823–874, arXiv:1005.4568.
- [8] S. Agostinelli et al., *G4ant4: a simulation toolkit*, Nuclear Instrument and Methods A 506 (2006) no. 3, 250–303.
- [9] J. Allison et al., *G4ant4 developments and applications*, Nuclear Science, IEEE Transactions on S3 (2006) no. 1, 270–278.
- [10] M. Pivk and F. Le Diberder, *sPlot: a statistical tool to unfold data distributions*, arXiv:0402083v3.
- [11] ATLAS Collaboration, *Performance of the ATLAS Muon Trigger in  $p\bar{p}$  collisions at  $\sqrt{s} = 7 \text{ TeV}$* , ATLAS-CONF-2010-095 (2010).